Conformation-dependent excited state properties in extended π-conjugated systems: Static and dynamics studies

A thesis submitted by

Palak Mandal

to

Indian Institute of Technology Guwahati

in fulfillment of the requirements for the degree of

Doctor of Philosophy

Department of Chemistry

Indian Institute of Technology Guwahati

Guwahati 781039

INDIA

March 2026

Conformation-dependent excited state properties in extended π-conjugated systems: Static and dynamics studies

Doctoral Thesis

Author:

Palak Mandal
Roll No. 216122025

Supervisor:
Dr. Aditya N. Panda

Department of Chemistry
Indian Institute of Technology Guwahati
Guwahati 781039
INDIA

March 2026

Declaration

I, Palak Mandal, declare that this thesis titled, "*Conformation-dependent excited state properties in extended π-conjugated systems: Static and dynamics studies*" and the work presented in it are my own. I confirm that this work was done by me during the period from July 2021 to March 2026 in candidature for the degree of Doctor of Philosophy at Indian Institute of Technology Guwahati under the guidance and supervision of Dr. Aditya N. Panda, Professor, Department of Chemistry. Any part of this thesis has not previously been submitted for a degree or any other qualification at this Institution or any other university/institution. Where I have consulted the published work of others, this is always clearly attributed. I have acknowledged all main sources of help.

Signed:

Palak Mandal

Date:

Certificate

This is to certify that the thesis titled "*Conformation-dependent excited state properties in extended π-conjugated systems: Static and dynamics studies*" submitted for the award of degree of Doctor of Philosophy by **Palak Mandal** is the record of research work carried out by him during the period July 2021 to March 2026 under my guidance and supervision. This work has not formed the basis for the award of any degree, diploma, associateship, fellowship or other titles in this Institution or in any other university/institution.

Signed:

Dr. Aditya N. Panda

Professor

Date:

Acknowledgements

I would like to take this opportunity to express my gratitude to everyone who has accompanied me on my academic journey. First and foremost, I extend my sincere thanks to my supervisor, Prof. Aditya Narayan Panda, for giving me the opportunity to work in his research group. I deeply appreciate the immense knowledge he has imparted to me and his continuous support and encouragement. His patience, rigour, and integrity have profoundly influenced my path. It is a true blessing to have worked under his guidance. I will always cherish my experience as part of his group.

I would like to thank my doctoral committee members, **Prof. Manabendra Sarma**, **Prof. Ashish Kumar Gupta**, and **Dr. Rajiv K. Kar** for their insightful comments, valuable suggestions and encouragements.

I acknowledge financial support from the Indian Institute of Technology (IIT) Guwahati, and am grateful to the Department of Chemistry for the opportunity to work as a research scholar in this department. I am thankful to IIT Guwahati for the computational resources provided through Param-Ishan and Param-Kamrupa.

I extend my gratitude to my labmates Mohd. Shavez, Bishwanath, Iban, Derreck, Priyanka, Gargi, and Smiti for their constructive discussions, suggestions, and cooperation in the lab.

I also wish to thank my friends Roop, Srijan, Malay, Nandini, Subham, and Deepak for their support and companionship throughout my PhD journey.

Last but not least, my heartfelt appreciation goes to my family, especially my parents, my wife, and my brother, whose unwavering support and encouragement have been my foundation.

Synopsis

In recent years, conjugated oligomers and polymers have attracted significant attention as promising alternatives to inorganic materials for electronic devices (such as in photovoltaic cells, light-emitting diodes, and field-effect transistors), primarily because of their distinctive optoelectronic properties. These organic materials are lightweight, inexpensive to process, and mechanically flexible; however, their performance and efficiency are still behind those of inorganic electronic devices. The performance and efficiency of organic-based electronic devices are governed by several factors, notably the molecular architecture, which influences excited-state phenomena such as charge separation, energy transfer, exciton localization and delocalization, and charge recombination. Therefore, understanding molecular-level structure-property relationships is essential for designing materials with improved performance for efficient organic electronics. Computational explorations are of great help at this point to have a good molecular-level understanding of the statics and dynamics of the underlying processes. Keeping this in mind, in this thesis, we report on excited-state processes, including exciton localization and delocalization, *intra-* and *inter*-molecular charge transfer (CT), and excimer formation, which are examined for different conformational isomers of specific molecular systems using computational approaches. For the investigation of exciton localization and delocalization, two conformers of 2-Phenylpyridine oligomers, namely linear and helical structures, are analyzed. Non-adiabatic surface-hopping dynamics simulations are performed using the semiempirical time-dependent density functional tight-binding (TD-DFTB) method to investigate localization and delocalization. Additionally, static electronic-structure calculations are carried out using the algebraic diagrammatic construction to the second order (ADC(2)) method for the three distinct isomers of 2-Phenylpyridine oligomers. Following 2-Phenylpyridine, the next chapter reports on the differences in the excited states of ***trans*** and ***cis***-2,2′-bipyridine oligomers. In another case, analysis of *intra-* and *inter*-molecular CT is performed on four conformers of azulene-fused anthracene and naphthalene and their π-stacked dimers. This part of the work involves excited-state characterization at the ADC(2) level, followed by time-dependent density functional theory (TD-DFT) studies employing DFT functionals such as CAM-B3LYP, SCS-ωB2GP-PLYP, and SCS-RSX-QIDH. Excimer formation is explored in covalently linked azulene-fused anthracene by considering two conformers that differ in the mode of fusion of the azulene units with the anthracene cores. A chapter-wise overview of the thesis is presented below.

Chapter 1: Introduction

Chapter 1 provides a brief description of the role of the molecular structures and their respective excited states on the performance of the organic devices. The description mainly focuses on local, CT, charge-separated, and excimer states and on how these states evolve across different molecular conformers, using a few examples. The aim and scope of the present thesis work are also discussed at the end of the chapter.

Chapter 2: Methodology

This chapter presents the theoretical and computational techniques employed to investigate excited-state phenomena. It begins with the time-independent Schrödinger equation, the central equation of quantum mechanics, which provides information about a system's electronic state. The fundamental concepts of Hartree–Fock theory, which form the basis for many advanced methods, are then introduced. Single-reference approaches such as density functional theory (DFT), time-dependent DFT (TDDFT), second-order Møller–Plesset perturbation theory (MP2), and ADC(2) are covered in this chapter. Semiempirical methods, including DFTB and its time-dependent extension, TD-DFTB, are also discussed. For the treatment of excited-state dynamics, mixed quantum–classical approaches, notably the trajectory surface hopping, are also discussed.

Chapter 3: Conformational effect on the excitonic states of $(\mathbf{PhPy})_{n=1-5}$ oligomers

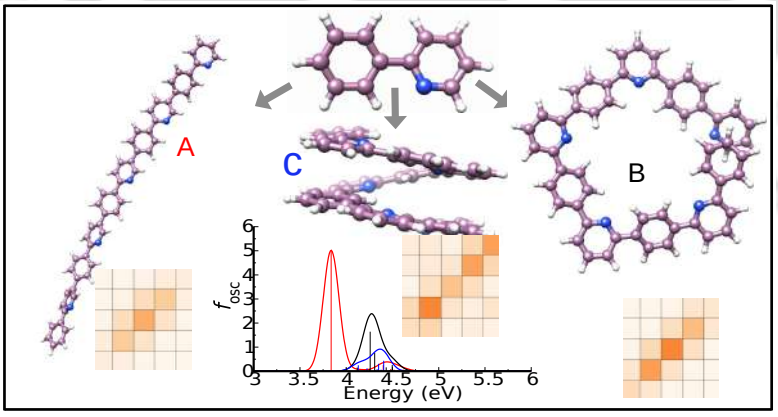

In this chapter, we report on the effect of different conformations of 2-Phenylpyridine oligomers ($(\mathbf{PhPy})_{n=1-5}$) on the excited state properties. The computational studies were carried out at the RI-ADC(2)/def2-TZVP level of theory, considering the three conformers, namely **A** (linear), **B** (helical), and **C** (helical). The differences in the geometries of the three conformers are reflected in the UV and CD spectra. The UV

spectra of conformer **A** show high-intensity peaks compared to the results for conformers **B** and **C**, for each oligomer. While the helical oligomers of conformers **B** and **C** show high-intensity CD bands, the intensities of CD bands for all the oligomers of conformer **A** are weaker. Analysis of the properties of the first five excited states in **(PhPy)**$_5$ reveals that these are partially charge-transfer states.

Chapter 4: Confirmation-driven localization and delocalization of exciton in 2-phenyl-pyridine oligomers: surface-hopping dynamics

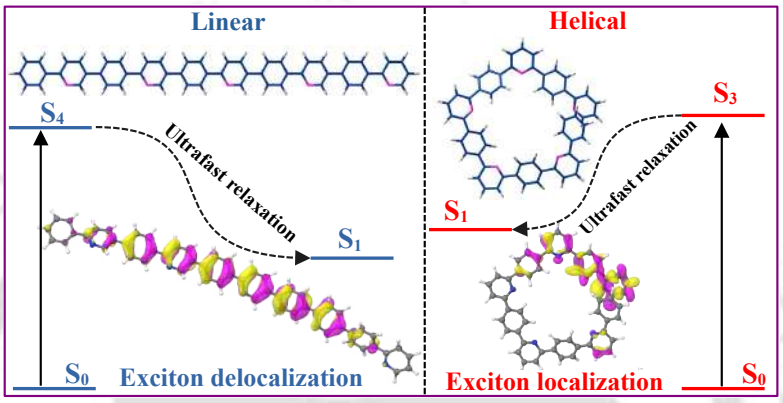

In this chapter, we report on our investigation of the exciton localization and delocalization processes in two 2-Phenylpyridine oligomers, one linear (**(PhPy)**$_5$**-A**) and the other helical (**(PhPy)**$_5$**-B**), using the non-adiabatic surface-hopping dynamics method. The dynamics studies were carried out in combination with the semi-empirical TD-DFTB method and Tully's fewest-switches surface-hopping method. Post-dynamics calculations were carried out at the RI-ADC(2) level of theory for characterizing the excited states. Upon photo-excitation, the two conformers undergo ultrafast internal conversion within 10-100 fs from the high-energy excited state S_4/S_3 to the lower energy S_1 state. The excited state relaxation results in delocalization of the exciton over multiple monomeric units in the linear conformer **(PhPy)**$_5$**-A**, while the exciton is localized over a single monomeric unit in the helical conformer **(PhPy)**$_5$**-B**.

Chapter 5: Contrasting the excited state properties in 2, 2′-bipyridine oligomers

In this chapter, we present conformation-dependent photo-physical and excited state properties of ***trans***- and ***cis***-bipyridine oligomers at the RI-ADC(2)/def2-TZVPD level. The UV spectra of oligomers of **meta** conformer show high-intensity and red-shifted UV bands compared to **ortho** and **para** oligomers. The CD spectra of **para** oligomers show

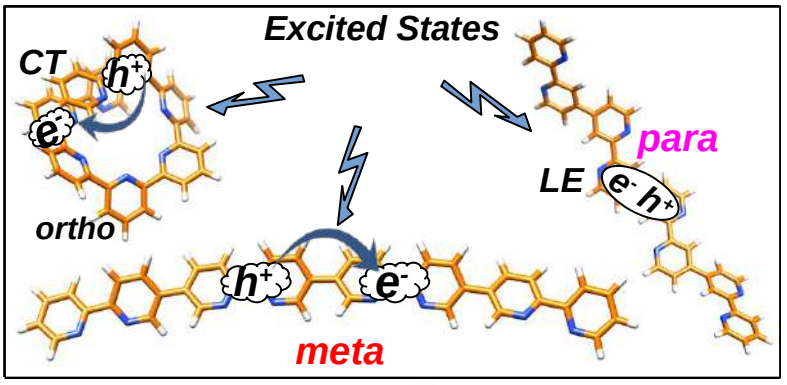

intense CD bands compared to **ortho** and **meta** oligomers in the case of ***trans***- structures. In contrast, oligomers of each conformer of ***cis***- structures show high-intensity CD bands. The characterization of the first five excited states in $(\mathbf{BPY})_2$ and $(\mathbf{BPY})_4$ reveals that these are mainly LE states in dimer (ω_{CT}=0.06-0.32), whereas for tetramer, the ω_{CT} values range from 0.17 to 0.53, indicating the possibility of partial CT characteristics of these states. These observations are also explained using the natural transition orbitals and *e*-*h* correlation plots.

Chapter 6: Insight into the excited states in monomers and π-stacked dimers of azulene-fused acenes

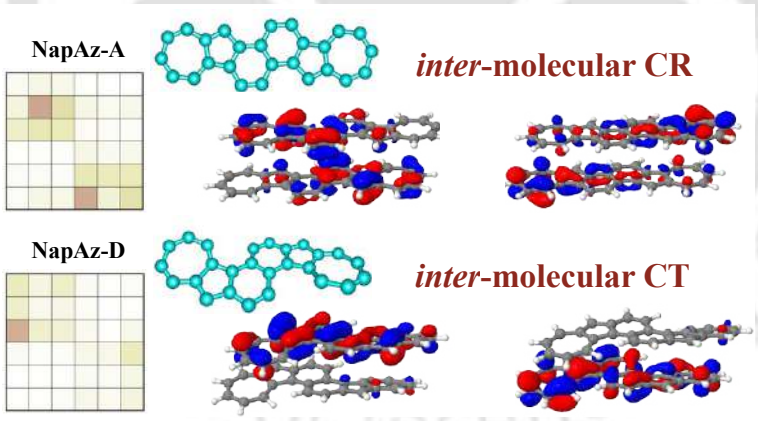

In this chapter, the nature of the excited states in monomers and π-stacked dimers of azulene-fused naphthalene and anthracene systems, focusing on the interplay between conformational isomers and excited state properties, is reported. For the monomers, the states with CT characters are different in naphthalene- and anthracene-based systems. In π-stacked dimers, a few of the excited states are of the charge resonance (CR) type in conformers **NapAz-A**, **NapAz-B**, and **NapAz-C**, and intermolecular CT type in

NapAz-D. Overall, among the three DFT functionals considered (CAM-B3LYP, SCS-ωB2GP-PLYP, and SCS-RSX-QIDH), CAM-B3LYP was found to reproduce well the SCS-ADC(2) excited results in both monomers and π-stacked dimers.

Chapter 7: Conformation-induced excimer formation in covalently-linked dimer of azulene-fused anthracene

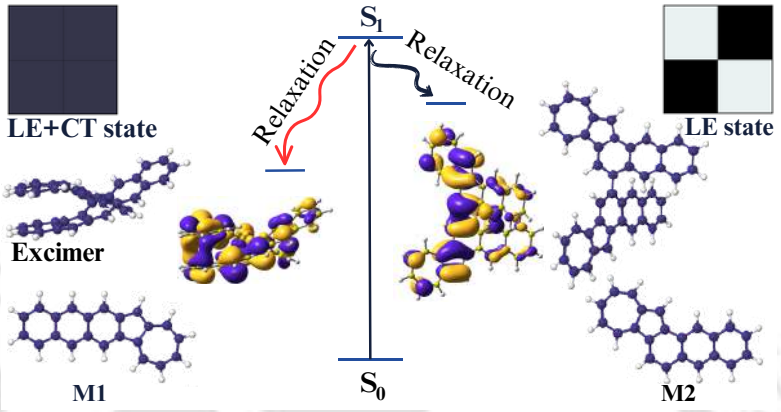

In this chapter, we explore the possibility of excimer formation in covalently linked azulene-fused anthracenes, considering two different conformational isomers, **M1** and **M2**, using the MP2 and ADC(2) methods. In conformer **M1**, the azulene units are oriented towards each other, leading to excimer formation in the S_1 state. This is confirmed by the orbital overlap of the azulene units and the CT character of the S_1 state. In contrast, conformer **M2**, in which the azulene rings are oriented away from each other, shows minimal changes in the excited-state geometry relative to the ground state, preserving the CT features.

Chapter 8: Summary and conclusions

The last chapter of the thesis gives an overview of the present work and the scope for future work.

Published/submitted articles:

1. **Mandal, P.**; Panda, A. N. Conformation-driven (de)localization of exciton in 2-phenylpyridine oligomers: non-adiabatic surface hopping dynamics, *Chem. Commun.* **2026**, 62, 5447-5451.
2. **Mandal, P.**; Panda, A. N. Conformation-Induced Excimer Formation in Covalently Linked Dimer of Azulene-Fused Anthracene, *J. Phys. Chem. A* **2025**, 129(35), 8085–8092.
3. **Mandal, P.**; Panda, A. N. Insight into the Excited States in Monomers and π-Stacked Dimers of Azulene-Fused Acenes: ADC(2) and TD-DFT Studies, *J. Phys. Chem. A* **2025**, 129(4), 1085–1098.
4. **Mandal, P.**; Panda, A. N. Contrasting the excited state properties of different conformers of trans- and cis-2, 2′-bipyridine oligomers in the gas phase, *Phys. Chem. Chem. Phys.* **2024**, 26, 2646–2656.
5. **Mandal, P.**; Panda, A. N. Conformational Effect on the Excitonic States of 2-Phenylpyridine Oligomers: Ab Initio Studies and Analysis, *J. Phys. Chem. A* **2023**, 127(38), 7898–7907.

Conferences/workshops attended:

1. **Theoretical Chemistry Symposium (TCS-2023)**, IIT Madras
2. Summer School on **MACHINE LEARNING & DEEP LEARNING (2023)** conducted jointly by the **Centre for Intelligent Cyber Physical Systems (CI-CPS) and Technology Innovation Hub (TIH) Division of IITG Technology Innovation & Development Foundation (TIDF)**
3. **LaTeX Workshop- 2023**, IIT Guwahati
4. **Frontiers in Chemical Science (FICS-2024)**, IIT Guwahati
5. **Symposium on Theoretical Chemistry (STC-2025)**, Freie University Berlin, Germany

Contents

List of Figures

List of Tables

Abbreviations

ϵ	epsilon
θ	theta
ω	omega
Ω	Omega
π	pi
Ψ	Psi
ψ	psi
μ	mu
λ	lambda
ϕ	Uppercase phi
φ	Lowercase phi
ν	nu
χ	chi
∇	operator
Å	Angstrom
%	Percentage
E_{g}	Excitation energy
E_{g}^{1}	First excitation energy
λ_{em}	Emission energy
HF	Hartree-Fock
MP	Møller-Plesset
MO	Molecular orbital
BO	Born-Oppenheimer
TD	Time dependent
DFT	Density functional theory
CAM	Coulomb-attenuating method
GGA	Generalized gradient approximation
HOMO	Highest occupied molecular orbital

LUMO	Lowest unoccupied molecular orbital
PT	Proton transfer
f_{osc}	Oscillator strength
LC	long-range corrected
UV	Ultraviolet
LE	Locally excited
CT	Charge transfer
NTO	Natural transition orbital
ADC(2)	Second order algebraic diagrammatic construction
CC2	Second order coupled-cluster
ω_{CT}	Charge transfer
ISC	Intersystem crossing
IC	Internal conversion

Chapter 1

Introduction

Conjugated oligomers and polymers possess unique optical and electronic properties that arise from the delocalization of π-electrons across their molecular structures. This delocalization allows for efficient light absorption, charge and energy transfer, charge separation, recombination, localization, and delocalization of excitons, etc., making them suitable for various applications in the field of organic electronics such as organic light-emitting diodes (OLEDs),[1–3] organic photovoltaics (OPVs),[4–6] and organic field-effect transistors (OFETs)[4,7,8] and other applications. These organic material-based electronic devices have several advantages over their inorganic counterparts, including low cost, lightweight design, and mechanical flexibility. These characteristics of organic material-based electronic devices make them complementary to inorganic photovoltaic technologies for various applications, such as portable power sources and building-integrated photovoltaics.

However, in many cases, the molecules in the organic layer exhibit structural flexibility, producing pronounced coupling between electronic and nuclear degrees of freedom.[9–11] As a result, the excited-state properties and deactivation mechanisms become conformation-dependent,[12–14] and in particular, modes such as backbone torsions and bond-length alternation dictate outcomes.[15] Torsional motion can help in bringing the excited states closer to each other,[16,17] which may enhance the non-adiabatic coupling, eventually either facilitating the relaxation process or opening up different channels. As these processes occur on a femtosecond to picosecond timescale, understanding conformation-dependence of the excited-state properties and relaxation pathways is of paramount importance to understand their behavior in the active layer.

Below, we provide a brief overview of the existing literature on this topic. This is followed by the last section, which shows the aim and scope of the present thesis work.

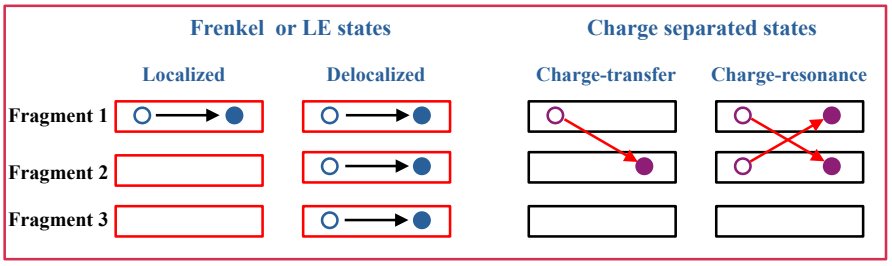

FIGURE 1.1: Schematic representation of different types of excited states of a molecular system consisting of three fragments. Blank and filled circles represent the hole and the electron, respectively.

1.1 Types of excited states and their dependence on molecular conformations

Characterization of electronic excitations is important for investigating excited states, as it provides valuable insights into the optical and electronic properties of materials. Excited states can be classified into four types, as shown in Figure 1.1.[18–20] Considering a system consisting of three fragments, a localized Frenkel or locally excited (LE) state occurs when the excitation is confined to a single fragment (first column of Figure 1.1). When these local excitations on individual fragments couple together, they lead to a delocalized LE state (second column of Figure 1.1). Conversely, a charge-transfer (CT) state is formed when an electron is transferred from one fragment to another during an excitation (third column of Figure 1.1). Finally, a charge-resonance (CR) state is depicted in the last column of Figure 1.1, resulting from the linear combination of two CT states with electron transfer occurring in opposite directions. In particular, the CT state plays a crucial role in governing a variety of charge-carrier generation processes. For example, the energy loss during the charge generation process in OPVs can be minimized by tuning the energies of the CT state and the band gap (E_g).[21] In addition, the relative energetic ordering of the CT, LE, and singlet-correlated triplet pair (^{1}(TT)) states also plays a vital role in the singlet fission (SF) process.[22] In recent years, SF has been extensively studied as a mechanism for carrier multiplication in OPVs.[23] In the SF process, a singlet exciton is converted into two triplet excitons.[23,24] Typically, the SF process proceeds via the formation of a ^{1}(TT) state through direct two-electron transfer from the local excited singlet state.[24] However, mechanisms are also reported where the ^{1}(TT) is formed via the

CT state, either through charge hopping or the CT-mediated superexchange mechanism, depending on the relative energetics of the LE, CT, and ^{1}(TT) states.[22]

The excimer state also plays a crucial role in controlling the efficacy of electronic devices.[25–27]. An excimer is a dimeric complex formed by two identical molecules in an excited state, stabilized through interactions between neighboring chromophores.[28–31] Typically, the excimer state is a mixed electronic state that includes contributions from both LE and CT states.[31] This mixed state acts as a low-energy exciton trap, thereby diminishing the performance of OPVs. This happens when the rate of excimer formation exceeds the rate of desired photo-physical processes, such as SF, charge transfer, and exciton diffusion.[25–27,32,33] However, the excimer state also has the potential to facilitate CS processes.[34,35] For example, excimer-mediated intramolecular charge transfer is observed in a cofacially stacked perylene bisimide pair.[34] Moreover, there are also examples reported where this state mediates the SF process when it interacts with the ^{1}(TT) state.[36,37]

The excited-state properties of conjugated systems are significantly influenced by their distinct geometrical architectures, which ultimately affect device performance.[13,38–42] For example, oligophenylene can exist in three different isomeric forms *ortho*-, *meta*-, and *para*- oligophenylene,[13,43–46] and these three isomers show different optoelectronic properties. The *para*-isomer shows red-shifted fluorescence spectrum with increasing oligomer chain length,[13,16,46] while in the case of the *ortho*-oligomer, the fluorescence energy increases with chain length.[13,47,48] On the other hand, for the *meta*- isomer, the variation in the fluorescence energy remains independent of the chain length.[13,49] In addition, the cyclic forms of the *para*-oligophenylene are also reported, known as [n]cycloparaphenylenes (CPPs).[12,50,51] In CPPs, the energy of the band gap increases with the chain length, which is exactly opposite to its linear counterpart.[12] Apart from this, these two conformers (linear *para*-oligophenylene and CPP) also exhibited different extents of exciton delocalization upon photoexcitation.[52] The cyclic forms of oligothiophene have also been reported[53], and it has been observed that the energy of the absorption maxima of cyclo[n]thiophene is nearly equal to that of a linear oligothiophene

containing n/2 thiophene units.[54] In linear polythiophene, photoexcitation induces dynamic planarization (torsional relaxation) within a few tens of picoseconds, resulting in the delocalization of excitons across multiple thiophene units. However, in cyclothiophene, conformational disorder prevents the complete delocalization of excitons along the entire cyclic backbone.[14] Oligofurans have received comparatively limited attention in the literature owing to their inferior photostability.[55,56] However, a recent study demonstrated the existence and relevance of a helical conformer that exhibits inherent photostability.[57] In oligofuran, the *syn* arrangement of the furan units gives rise to helical isomers, whereas the *anti* arrangement results in a linear structure. The helical isomer showed blue-shifted absorption maxima relative to the corresponding linear isomer.[57]

Studies examining the impact of different conformations on charge-carrier generation processes, including photo-induced symmetry-breaking charge separation (SB-CS),[58,59] have also been reported. Recently, Konar et al. investigated the impact of regioisomers on SB-CS, considering different regioisomers of the dimer of *ortho*-functionalized perylene monoimide (PMI)-acetylene units connected via a phenyl bridge at *ortho*-, *meta*-, and *para*- positions.[60] Among these, the *ortho*-bridged isomer displayed noticeably distinct optical properties, with a very fast CS rate (80.2 ps) upon photoexcitation. Hariharan and co-workers[61] demonstrated, both experimentally and theoretically, the orientation-dependence of SB-CS of two monomeric units, linear and angular, in perylenediimide dimers. In these systems, the lower coulombic coupling interactions due to the angular orientation led to faster CS in the angular form compared to its linear counterpart. Xia and co-workers have demonstrated that the *para*-isomer of an N-annulated perylene diimide dimer, bridged by a phenylene unit, exhibits faster CS dynamics compared to the corresponding *meta*-isomer.[42] This explained the reason behind the higher PCE value in the *para* isomer-based OPV device over the *meta* counterpart.[41]

1.2 Aim and scope of the present work

As discussed above, the relationship between structural variation and its influence on excited-state processes, including excited-state CT and excimer formation, is complex,

and it is important to gain a fundamental understanding of excited states across different molecular configurations. In this context, computational studies using various advanced quantum chemical methods are useful for exploring the different molecular conformations of conjugated systems and their excited-state properties. In this thesis work, we have chosen to explore the excited-state processes in extended π-conjugated systems, including oligomers of 2-Phenylpyridine and 2,2′-Bipyridine, and acene derivatives, considering their different molecular conformations. The growing interest in heterocyclic-based conjugated oligomers in organic electronics device applications,[62–74] motivated us to design 2-Phenylpyridine oligomers and study their excited-state properties for further development in the field of organic electronics. In this work, we have constructed various conformers during the design of the 2-Phenypyridine oligomers and studied their excited states, including vertical excitation energies and exciton localization and delocalization, using the non-adiabatic surface-hopping dynamics method. For the excited-state dynamics calculations, we employed the semiempirical time-dependent density functional tight-binding (TD-DFTB) method, aiming to keep computational cost low. To further extend our understanding of conformation-dependent excited-state properties in oligomers, along similar lines, we have considered different conformers (*ortho*-, *meta*-, and *para*-) of *cis*- and *trans*-2,2′-Bipyridine oligomers and reported their excited states.

For oligoacene derivatives, we have chosen azulene-fused acenes. The fusion of an azulene moiety to acenes yields all-carbon polycyclic aromatic hydrocarbons that retain chemical stability while exhibiting desirable optoelectronic properties[75–80] These derivatives have been shown to exhibit better performance in semiconducting materials. The literature showed that there is a possibility of obtaining different conformational isomers depending on the fusion mode of azulene to the acene unit.[81,82] However, most research on azulene-fused acenes has focused primarily on single-molecule systems, potentially overlooking important conformational aspects. In this thesis work, we examine four distinct conformers, each differing in the fusion patterns of azulene with naphthalene and anthracene units. We also consider their π-stacked dimers to investigate both *intra*- and *inter*molecular CT. Additionally, we also explore how the fusion mode of azulene influences the excited-state relaxation process through excimer formation in a covalently linked dimer of azulene-fused acenes. Again, the aim of this work is to design a more

robust molecular system that has the potential to be a better candidate as SF materials with greater chemical stability.

Chapter 2

Theoretical and computational methodologies

This chapter discusses the theoretical and computational methods employed to investigate the excited-state process examined in this thesis. We begin with the central equation of quantum mechanics, the time-independent Schrödinger equation, which describes the stationary states of a system. We then present Hartree–Fock theory, which forms the basis for many advanced approximation schemes. Additionally, we discuss post-Hartree–Fock methods, such as Møller-Plesset perturbation theory. Following this, we discussed density functional theory (DFT) and its time-dependent analog, time-dependent DFT (TD-DFT). We also present the algebraic diagrammatic construction (ADC) scheme, along with the tight-binding approximation of DFT and TD-DFT approaches. Finally, we discuss 1TDM analysis regarding the excited-state characterization, followed by an exploration of the non-adiabatic dynamics approach.

2.1 The time-independent Schrödinger equation

For a molecular system containing n electrons and N nuclei, the total energy can be determined by solving the time-independent Schrödinger equation (SE), which is expressed as

$$\hat{H}\Psi_i = E_i\Psi_i \tag{2.1}$$

or

$$\hat{H}\Psi_i(\mathbf{r}_1, \mathbf{r}_2, \ldots, \mathbf{r}_n, \mathbf{R}_1, \mathbf{R}_2, \ldots, \mathbf{R}_N) = E_i\Psi_i(\mathbf{r}_1, \mathbf{r}_2, \ldots, \mathbf{r}_n, \mathbf{R}_1, \mathbf{R}_2, \ldots, \mathbf{R}_N) \tag{2.2}$$

In this expression, $\hat{H}$ is the Hamiltonian (total energy) operator, Ψ_i is the wave function corresponding to molecular state (i), and E_i is the total energy associated with that state. The wave function Ψ_i depends on both the electronic coordinates (r) and the nuclear coordinates (R). The Hamiltonian operator $\hat{H}$ written as the sum of the kinetic-energy operator $\hat{T}$ and the potential-energy operator $\hat{V}$, as follows[83]

$$\hat{H} = -\sum_{i=1}^{n} \frac{1}{2}\nabla_i^2 - \sum_{A=1}^{N} \frac{1}{2M_A}\nabla_A^2 - \sum_{i=1}^{n}\sum_{A=1}^{N} \frac{Z_A}{\mathbf{r}_{iA}} + \sum_{i=1}^{n}\sum_{j>i}^{n} \frac{1}{\mathbf{r}_{ij}} + \sum_{A=1}^{N}\sum_{B>A}^{N} \frac{Z_A Z_B}{R_{AB}}. \quad (2.3)$$

In Eq. 2.3, the first and second terms represent the kinetic energies of the electrons and nuclei, respectively. The third term describes the Coulomb attraction between electrons and nuclei, the fourth term accounts for electron–electron repulsion, and the last term corresponds to the repulsive interaction between nuclei. Here, M_A represent the mass of the nucleus A, Z_A and Z_B are the atomic number of nuclei A and B, respectively. $\mathbf{r}_{ij}$, $\mathbf{r}_{iA}$ and $\mathbf{R}_{AB}$ are the distances between i^{th} and j^{th} electrons, between i^{th} electron and A^{th} nucleus, and between A^{th} and B^{th} nuclei, respectively.

2.2 The Born Oppenheimer approximation

The Born-Oppenheimer (BO) approximation is a fundamental concept that enables an analytical solution to the SE. The key idea behind the BO approximation is that in a molecule, the mass of the atomic nuclei is much greater than that of the electrons. Because of this, the nuclei move much more slowly than the electrons, and this allows us to treat the electrons as if they are moving in a field of fixed nuclei. Within this approximation, we can neglect the second term in the equation Eq. 2.3, which represents the kinetic energy of the nuclei. Additionally, the nuclei-nuclei repulsion term (the fifth term) can be considered constant. The remaining terms in Eq. 2.3 constitute what is called the electronic Hamiltonian, which describes the motion of n electrons in the field of N point charges and can be written as[83]

$$\hat{H}_{elec} = -\sum_{i=1}^{n} \frac{1}{2}\nabla_i^2 - \sum_{i=1}^{n}\sum_{A=1}^{N} \frac{Z_A}{\mathbf{r}_{iA}} + \sum_{i=1}^{n}\sum_{j>i}^{n} \frac{1}{\mathbf{r}_{ij}} \quad (2.4)$$

Within the BO approximation, the total wave function can be expressed as a product of a nuclear and an electronic wave function as follows:

$$\Psi_i(\mathbf{r}_1, \mathbf{r}_2, \ldots, \mathbf{r}_n, \mathbf{R}_1, \mathbf{R}_2, \ldots, \mathbf{R}_N) = \Psi_{elec}(\mathbf{r}_1, \mathbf{r}_2, \ldots, \mathbf{r}_n; \mathbf{R}_1, \mathbf{R}_2, \ldots, \mathbf{R}_N) \times \Psi_{nucl}(\mathbf{R}_1, \mathbf{R}_2, \ldots, \mathbf{R}_N) \quad (2.5)$$

Here, the electronic wave function $\Psi_{elec}(\mathbf{r}_i; \mathbf{R}_A)$ represents the electronic motion, depending explicitly on the electronic coordinates and parametrically on the nuclear coordinates. Solving the SE for $\hat{H}_{elec}$ and Ψ_{elec} yields the electronic energy:

$$\hat{H}_{elec}\Psi_{elec} = E_{elec}\Psi_{elec} \quad (2.6)$$

In this expression, the electronic energy E_{elec} or $E_{elec}(\mathbf{R}_A)$ depends parametrically on the nuclear coordinates. This parametric dependence implies that for each distinct nuclear configuration, the electronic wave function Ψ_{elec} is a different function of the electronic coordinates. Consequently, the total energy of a molecule at a fixed nuclear arrangement must also include the nuclear–nuclear repulsion contribution:

$$E_{total} = E_{elec} + \sum_{A=1}^{N} \sum_{B>A}^{N} \frac{Z_A Z_B}{R_{AB}}, \quad (2.7)$$

2.3 The Hartree-Fock theory

The Hartree–Fock (HF) theory, commonly known as the HF approximation, is central to quantum chemistry and forms the foundation for many highly accurate quantum chemical methods. In the HF formalism, the complicated many-electron problem is transformed into an effective one-electron problem, in which electron–electron repulsion is treated in an averaged manner.

Within this approach, the total electronic wave function Ψ_{elec} describing an n-electron system is expressed as a Slater determinant (SD) of spin orbitals $\Phi_i(\mathbf{r}_n)$, which satisfies the Pauli exclusion principle by constructing the appropriate antisymmetric linear

combination of all spin orbitals, written as

$$\Psi(\mathbf{r}_1, \mathbf{r}_2, \ldots, \mathbf{r}_n) = \frac{1}{\sqrt{n!}} \begin{vmatrix} \Phi_1(\mathbf{r}_1) & \Phi_2(\mathbf{r}_1) & \ldots & \Phi_M(\mathbf{r}_1) \\ \Phi_1(\mathbf{r}_2) & \Phi_2(\mathbf{r}_2) & \ldots & \Phi_M(\mathbf{r}_2) \\ \vdots & \vdots & \ddots & \vdots \\ \Phi_1(\mathbf{r}_n) & \Phi_2(\mathbf{r}_n) & \ldots & \Phi_M(\mathbf{r}_n) \end{vmatrix}, \tag{2.8}$$

or equivalently,

$$\Psi(\mathbf{r}_1, \mathbf{r}_2, \ldots, \mathbf{r}_n) = |\Phi_1(\mathbf{r}_1)\, \Phi_2(\mathbf{r}_2) \ldots \Phi_M(\mathbf{r}_n)\rangle\,. \tag{2.9}$$

Here, $\frac{1}{\sqrt{n!}}$ is the normalization constant, and the number of spin orbitals M is given by $M = \frac{n}{2}$ for even n and $M = \frac{n+1}{2}$ for odd n. Each spin orbital $\Phi_i(\mathbf{r}_n)$ incorporates both the spatial and spin parts of an electron, e.g., $\Phi_1(\mathbf{r}_1) = \Phi(1)\,\sigma(1)$, where the spin function σ corresponds to either the α- or β-spin state.

By using the SD, the HF equation can be written as

$$f(i)\,\Phi(\mathbf{r}_i) = E_i\,\Phi(\mathbf{r}_i), \tag{2.10}$$

where f is the effective one-electron operator, known as the Fock operator, written as

$$f(i) = -\frac{1}{2}\nabla_i^2 - \sum_{A=1}^{N} \frac{Z_A}{\mathbf{r}_{iA}} + v^{\mathrm{HF}}(i), \tag{2.11}$$

and $v^{\mathrm{HF}}(i)$ is the HF mean-field potential. The HF mean-field potential represents the average potential acting on the ith electron due to the presence of all the other electrons in the system. Therefore, the Fock operator depends on its own eigenfunctions, making the HF equation non-linear. It is therefore solved iteratively by employing the self-consistent field procedure.

2.4 Post-Hartree-Fock theory

The HF method does not account for electron correlation effect; for this reason, many quantum chemical methods have been developed, including the Møller-Plesset perturbation theory.

2.4.1 Møller-Plesset perturbation theory

In 1934, Møller and Plesset described how the HF ground state energy can be corrected by accounting for the electron pair correlation in terms of second-order perturbation theory.[84] This approach is now known as the Møller-Plesset (MP) perturbation theory. In MP theory, the HF Hamiltonian is considered as the zeroth-order reference, denoted as $\hat{H}_{HF}$ or $\hat{H}^0$, and can be written as a sum of one-electron Fock operators $f(p)$ as follows:

$$\begin{aligned} \hat{H}_{HF} &= \hat{H}^0 \\ &= \sum_p \hat{f}(p) \\ &= \sum_p \hat{h}(p) + \sum_{p,i} [\hat{J}_i(p) - \hat{K}_i(p)] \end{aligned} \tag{2.12}$$

where $\hat{h}(p)$ represents the one-electron operator containing the kinetic and electron-nuclear repulsion term of electron p, $\hat{J}_i(p)$, and $\hat{K}_i(p)$ are the Coulomb and exchange operators, respectively. The $\hat{J}_i(p)$ and $\hat{K}_i(p)$ operator expressed in terms of spin orbitals Φ_i as

$$\hat{J}_i(1)\Phi_j(1) = \left[\int d\mathbf{r}_2 \Phi_i^*(2) \frac{1}{\mathbf{r}_{12}} \Phi_i(2) \right] \Phi_j(1) \tag{2.13}$$

and

$$\hat{K}_i(1)\Phi_j(1) = \left[\int d\mathbf{r}_2 \Phi_i^*(2) \frac{1}{\mathbf{r}_{12}} \Phi_j(2) \right] \Phi_i(1). \tag{2.14}$$

If $\hat{\Psi}^0$ is the HF ground state wave function, then the corresponding eigenvalue is given by the sum of orbital energies E_i as follows:

$$E^0 = \sum_i^n E_i \tag{2.15}$$

$$\hat{H}^0\hat{\Psi}^0 = E^0\hat{\Psi}^0 \tag{2.16}$$

Now, if we define $\hat{H}$ as the exact Hamiltonian, which contains the exact electron-electron repulsion term, then the perturbation operator $\hat{V}$ can be written as

$$\begin{aligned}\hat{V} &= \hat{H} - \hat{H}^0 \\ &= \sum_{p\geq q}\frac{1}{r_{pq}} - \sum_{p,i}[\hat{J}_i(p) - \hat{K}_i(p)]\end{aligned} \tag{2.17}$$

Therefore, the first-order correction to the ground state energy E^0 can be written as

$$\begin{aligned}E^1 &= E^{(1)}_{MP} \\ &= \langle\Phi^{(0)}|\hat{V}|\Phi^{(0)}\rangle = V_{00} = -\frac{1}{2}\sum_{ij}\langle ij||ij\rangle\end{aligned} \tag{2.18}$$

where the double bar integral represents the two-electron antisymmetric integral defined as follows:

$$\begin{aligned}\langle ij||kl\rangle &= \langle ij|kl\rangle - \langle ij|lk\rangle \\ &= \int\int d\mathbf{r}_1\ d\mathbf{r}_2\ \phi_i^*(\mathbf{r}_1)\phi_j^*(\mathbf{r}_2)\frac{1}{\mathbf{r}_{12}}[\phi_k(\mathbf{r}_1)\phi_l(\mathbf{r}_2) - \phi_k(\mathbf{r}_2)\phi_l(\mathbf{r}_1)].\end{aligned} \tag{2.19}$$

Therefore, MP1 energy is simply the HF energy, indicating that the HF is correct up to the first order of the MP theory

$$E(\text{HF}) = E(\text{MP1}) = \sum_i^{occ}\epsilon_i - \frac{1}{2}\sum_{ij}^{occ}\langle ij||ij\rangle \tag{2.20}$$

The second-order correction to the ground state is given by the following equation:

$$E^{(2)}_{MP} = \sum_{j\neq 0}\frac{\langle\Phi_j|\hat{V}|\Phi_0\rangle\langle\Phi_0|\hat{V}|\Phi_j\rangle}{E_0 - E_j} \tag{2.21}$$

where Φj is a multiply excited determinant and an eigen function of $\hat{H}_{HF}$ with eigen value E_j. However, from Brillouin's theorem[85] it is concluded that only the double excitation determinant has non-zero $\hat{V}$ matrix elements with Φ_0, therefore only the double excitations contribute to $E_{MP}^{(2)}$. Considering this, the Eq. 2.21 takes the following form:

$$E_{MP}^{(2)} = \frac{1}{4}\sum_{ij}^{occ}\sum_{ab}^{vir}\langle ij||ab\rangle a_{ij}^{ab} \tag{2.22}$$

with

$$a_{ij}^{ab} = \left(\epsilon_i + \epsilon_j - \epsilon_a - \epsilon_b\right)^{-1}\langle ab||ij\rangle. \tag{2.23}$$

where ϵ_i and ϵ_j energies of occupied spin orbitals ϕ_i and ϕ_j, respectively, and ϵ_a and ϵ_b are the energies corresponding to the virtual spin orbitals.

2.5 Density functional theory

The central concept of density functional theory (DFT) is that the electronic energy of a system can be expressed as a functional of the electron probability density ρ.[86] In this context, W. Kohn and L. J. Sham[87] showed that the ground-state energy of an n-electron system can be written as

$$\begin{aligned} E[\rho] = -\frac{1}{2}\sum_{i=1}^{n}\int \psi_i^*(\mathbf{r}_1)\nabla_i^2\psi_i(\mathbf{r}_1)d\mathbf{r}_1 - \sum_{I=1}^{N}\frac{Z_I}{\mathbf{r}_{I1}}\rho(\mathbf{r}_1)d\mathbf{r}_1 \\ +\frac{1}{2}\int\frac{\rho(\mathbf{r}_1)\rho(\mathbf{r}_2)}{\mathbf{r}_{12}}d\mathbf{r}_1 d\mathbf{r}_2 + E_{\mathrm{XC}}[\rho(\mathbf{r})] \end{aligned} \tag{2.24}$$

where ψ_i $(i = 1, 2, \ldots, n)$ are the one-electron spatial orbitals, referred to as Kohn-Sham (KS) orbitals, and $\rho(\mathbf{r})$ is the total electron density at a point $\mathbf{r}$, which is given by

$$\rho(\mathbf{r}) = \sum_{i=1}^{n}|\psi_i(\mathbf{r})|^2 \tag{2.25}$$

In Eq. 2.24, the first term corresponds to the kinetic energy of the electrons; the second term describes the electron–nucleus interaction energy summed over N nuclei with nuclear charges Z_I; the third term represents the Coulomb interaction between charge

distributions located at $\mathbf{r}_1$ and $\mathbf{r}_2$; and the final term is the exchange–correlation (XC) energy, $E_{\mathrm{XC}}[\rho(\mathbf{r})]$. The $E_{\mathrm{XC}}[\rho(\mathbf{r})]$ is also a functional of the density and incorporates all non-classical electron–electron interactions.

The KS orbitals are obtained by solving the following KS equation for the one-electron orbitals $\psi_i(\mathbf{r}_1)$:

$$\Big\{ -\frac{1}{2}\nabla_i^2 - \sum_{I=1}^{N} \frac{Z_I}{\mathbf{r}_{I1}} + \int \frac{\rho(\mathbf{r}_2)}{\mathbf{r}_{12}} d\mathbf{r}_2 + V_{\mathrm{XC}}(\mathbf{r}_1) \Big\} \psi_i(\mathbf{r}_1) = \varepsilon_i \psi_i(\mathbf{r}_1) \tag{2.26}$$

where ε_i are the KS orbital energies and V_{XC} is the XC potential, which is a functional derivative of the exchange–correlation energy:

$$V_{\mathrm{XC}} = \frac{\delta E_{\mathrm{XC}}[\rho(\mathbf{r})]}{\delta \rho(\mathbf{r})} \tag{2.27}$$

The KS equations are solved self-consistently. Starting from an initial guess for the electron density ρ, one first evaluates $E_{\mathrm{XC}}[\rho]$, and then computes V_{XC} as a function of $\mathbf{r}$. This yields an initial set of KS orbitals by solving the KS equations. These orbitals are then used to construct an improved density from Eq. 2.25. The procedure is iterated until both the electron density and the XC energy are converged.

2.5.1 The exchange-correlation (XC) functionals

The primary source of error in DFT arises from the approximate nature of the XC functional. Numerous schemes have been developed for accounting for the correct XC energy, ranging from the local-density approximation (LDA) and generalized gradient approximation (GGA) to meta-GGA and, more recently, hybrid and double-hybrid functionals with range separation. The functional form of the hybrid XC functional, which contains exact exchange from HF and XC energy from DFT, can be written as

$$E_{\mathrm{XC}}^{\mathrm{hybrid}} = a E_{\mathrm{X}}^{\mathrm{exact}} + (1-a) E_{\mathrm{X}}^{\mathrm{DFT}} + E_{\mathrm{C}}^{\mathrm{DFT}} \tag{2.28}$$

where a represents the mixing coefficient, $E_{\mathrm{X}}^{\mathrm{exact}}$ is the HF exchange energy, and $E_{\mathrm{X}}^{\mathrm{DFT}}$ and $E_{\mathrm{c}}^{\mathrm{DFT}}$ are exchange and correlation energies from DFT, respectively. Among various hybrid functionals, the Becke's three-parameter Lee-Yang-Parr (B3LYP)[88,89] is the most widely used DFT functional for predicting the ground state properties, and the mathematical form of this functional can be written as

$$E_{\mathrm{XC}}^{\mathrm{B3LYP}} = a_0 E_{\mathrm{X}}^{\mathrm{exact}} + (1-a_0)E_{\mathrm{X}}^{\mathrm{LSDA}} + a_{\mathrm{b}}E_{\mathrm{X}}^{\mathrm{B88}} + a_{\mathrm{c}}E_{\mathrm{c}}^{\mathrm{LYP}} + (1-a_{\mathrm{c}})E_{\mathrm{c}}^{\mathrm{LSDA}} \tag{2.29}$$

where $E_{\mathrm{X}}^{\mathrm{LSDA}}$ and $E_{\mathrm{c}}^{\mathrm{LSDA}}$ are the local spin density approximation exchange and correlation energies, respectively, $E_{\mathrm{X}}^{\mathrm{B88}}$ is the Becke's 1988 gradient corrected exchange energy,[90] $E_{\mathrm{c}}^{\mathrm{LYP}}$ is the correlation energy by Lee, Yang, and Parr,[91] and three mixing parameters a_0, a_b, and a_c are stands for "3" in the B3LYP functional. However, the conventional hybrid functionals often struggle in the description of long-range electron correlation, which leads to errors in describing the CT states in conjugated molecular systems.[92–95] To address this issue, many long-range corrected (LC) DFT functionals, including CAM-B3LYP and ωB97XD, have been developed.[96–101] In these LC functionals, the exchange function $-\frac{1}{r_{12}}$ is separated into two components: short-range and long-range, as follows:

$$\frac{1}{r_{12}} = \frac{1-erf\,(\mu r_{12})}{r_{12}} + \frac{erf\,(\mu r_{12})}{r_{12}}. \tag{2.30}$$

In this equation, the first term accounts for the short-range interaction and the second term represents the long-range interaction. The key idea behind this LC functional scheme is that the DFT exchange is included via a short-range term, while the long-range exchange is described by HF exchange. The parameter μ in Eq.2.30 determines the balance between the DFT and HF exchange.

Furthermore, a large number of double hybrid (DH)[102,103] and range-separated (RS) DH[104–111] functionals have also been developed, providing promising results. The general expression of the DH functionals can be written as

$$E_{\mathrm{XC}}^{\mathrm{DH}} = a_x E_{\mathrm{X}}^{\mathrm{exact}} + (1-a_x)E_{\mathrm{X}} + a_{\mathrm{c}}E_{\mathrm{X}}^{\mathrm{PT2}} + (1-a_{\mathrm{c}})E_{\mathrm{c}} \tag{2.31}$$

and the range-separated functionals

$$E_{\mathrm{XC}}^{\mathrm{RS-DH}} = a_x E_{\mathrm{X}}^{\mathrm{exact}} + (1-a_x)E_{\mathrm{X}}^{\mathrm{exact}}(\omega) + (1-a_x)E_{\mathrm{X}} \\ -(1-a_x)E_{\mathrm{X}}(\omega) + a_{\mathrm{c}}E_{\mathrm{X}}^{\mathrm{PT2}} + (1-a_{\mathrm{c}})E_{\mathrm{c}} \tag{2.32}$$

where $E_{\mathrm{X}}^{\mathrm{PT2}}$ is the correlation energy obtained using the second-order perturbation theory, and ω is the range-separating parameter.

2.6 Time-dependent density functional theory

Time-dependent density functional theory (TD-DFT)[112–114] is a useful technique for investigating the response of molecular systems to electric and magnetic fields. In particular, it enables the calculation of excitation energies, absorption spectra, and linear and nonlinear response properties, such as polarizability and hyperpolarizability. The TD-DFT equation in KS formalism has the same basic structure as Eq. 2.26, with a time-dependent external potential, and can be expressed as

$$\left\{ -\frac{1}{2}\nabla_i^2 - \sum_{I=1}^{N}\frac{Z_I}{\mathbf{r}_{I1}} + \int \frac{\rho(\mathbf{r}_2,t)}{\mathbf{r}_{12}}\,d\mathbf{r}_2 + V_{\mathrm{ext}}(\mathbf{r}_1,t) + V_{\mathrm{XC}}(\mathbf{r}_1,t) \right\}\psi_i(\mathbf{r}_1,t) = \\ i\frac{\partial}{\partial t}\psi_i(\mathbf{r}_1,t) \tag{2.33}$$

where V_{ext} denotes the external potential (for example, oscillating electric and magnetic fields), which is time-dependent. The V_{XC}, the KS orbitals ψ_i, and the electron density $\rho(\mathbf{r})$ are all time-dependent. The time-dependent electron density is obtained from the KS orbitals according to

$$\rho(\mathbf{r},t) = \sum_{i=1}^{n} \left|\psi_i(\mathbf{r},t)\right|^2. \tag{2.34}$$

The time-dependent KS (TD-KS) Eq. 2.33 can be solved in two ways: using real-time integration[115] and linear-response (LR)[116–118] approaches. Among these two approaches, the LR theory is the popular method used for solving the TD-KS equation. The LR theory considered that in the presence of a small perturbation, the density responds

linearly. For a sufficiently well-behaved perturbing potential, the density can be expanded in a perturbing potential as

$$\rho(\mathbf{r},t) = \rho^0(\mathbf{r}) + \rho^{(1)}(\mathbf{r},t) + \rho^{(2)}(\mathbf{r},t) + \rho^{(3)}(\mathbf{r},t) + \dots \tag{2.35}$$

where $\rho^{(1)}$ is component of $\rho(\mathbf{r},t)$, which depends linearly to perturbation $V_{\text{ext}}^{(1)}$, $\rho^{(2)}$ depends quadratically, etc. The small perturbation leads us to consider only the first-order term

$$\begin{aligned} \rho(\mathbf{r},t) &= \rho^0(\mathbf{r}) + \rho^{(1)}(\mathbf{r},t) \\ \Rightarrow \rho^{(1)}(\mathbf{r},t) &= \rho(\mathbf{r},t) - \rho^0(\mathbf{r}) = \delta\rho(\mathbf{r},t) \end{aligned} \tag{2.36}$$

This first-order change in density ($\delta\rho$) and external potential (δV_{ext}) is connected as follow[118]

$$\delta\rho(\mathbf{r},t) = \int_{-\infty}^{t} dt' \int dr' \chi(\mathbf{r},\mathbf{r}',t-t')\delta V_{\text{ext}}(\mathbf{r}',t') \tag{2.37}$$

where $\chi(t-t')$ is the density-density response function of the system. Equivalently, one can also write the linear change in the density for a non-interacting system as

$$\delta\rho(\mathbf{r},t) = \int_{-\infty}^{t} dt' \int dr' \chi_{\text{S}}(\mathbf{r},\mathbf{r}',t-t')\delta V_{\text{S}}(\mathbf{r}',t') \tag{2.38}$$

where $\chi_s(\mathbf{r},\mathbf{r}',t-t')$ is the response function related to the wave function of the system of non-interacting electrons and δV_{S} represents the first-order change in the KS potential. This first-order change in KS potential can be written as

$$\delta V_{\text{S}} = \delta V_{\text{ext}} + \delta V_{\text{H}} + \delta V_{\text{XC}} \tag{2.39}$$

where

$$\begin{aligned} \delta V_{\text{H}}(\mathbf{r},t) &= \int d\mathbf{r}' \frac{\delta\rho(\mathbf{r}',t)}{\mathbf{r}-\mathbf{r}'} \\ \delta V_{\text{XC}}(\mathbf{r},t) &= \int d\mathbf{r}' f_{\text{XC}}(\mathbf{r},\mathbf{r}',t-t')\delta\rho(\mathbf{r}',t'), \quad f_{XC}(\mathbf{r},\mathbf{r}',t-t') = \int \frac{\delta V_{\text{XC}}(\mathbf{r},t)}{\delta\rho(\mathbf{r}',t')}. \end{aligned} \tag{2.40}$$

and f_{XC} is known as exchange-correlation kernel. Using the above equations, one gets the following Dyson-type equation for LR-TDDFT in the frequency space[118]

$$(1 - \hat{\chi}_S(\omega) f_{\mathrm{HXC}})\hat{\chi}(\omega) = \chi_S(\omega) \tag{2.41}$$

where $f_{\mathrm{HXC}} = \dfrac{\delta V_{\mathrm{H}(\omega)}}{\delta\rho(\omega)} + \dfrac{\delta V_{\mathrm{XC}(\omega)}}{\delta\rho(\omega)}$. The excitation energy can be obtained by solving the following eigenvalue problem

$$(1 - \hat{\chi}_S(\omega) f_{\mathrm{HXC}})X(\omega) = \omega X(\omega) \tag{2.42}$$

and the usual Casida form is obtained by expanding Eq. 2.42 in the KS spin orbital basis, which can be written as

$$\begin{vmatrix} A(\omega) & B(\omega) \\ -B^*(\omega) & -A^*(\omega) \end{vmatrix} \begin{vmatrix} X(\omega) \\ Y(\omega) \end{vmatrix} = \omega \begin{vmatrix} X(\omega) \\ Y(\omega) \end{vmatrix}, \tag{2.43}$$

where ω is the excitation energy. The matrix elements $A(\omega)$ and $B(\omega)$ are written in terms occupied (i, j) and virtual (a, b) orbitals as

$$\begin{aligned} A_{ia,jb}(\omega) &= \delta_{ij}\delta_{ab}(\varepsilon_a - \varepsilon_i) + (ia||jb) \\ B_{ia,jb}(\omega) &= (ia||bj), \end{aligned} \tag{2.44}$$

where the two-center integrals $(ia||jb)$ involve Coulomb and exchange-correlation kernels (f_{HXC}).

2.7 Algebraic diagrammatic construction (ADC) scheme

The algebraic diagrammatic construction (ADC) schemes are *ab initio* methods for calculating correlated excited states.[119–121] The derivation of ADC schemes originates from the many-body Green's function theory, where a diagrammatic perturbation theory is applied to construct a consistent level of approximation for the propagator.[119] An alternative route for deriving ADC schemes via the intermediate-state representation (ISR) formalism also exists and does not require knowledge of the propagator.[122–124] In general,

the ADC schemes are the Hermitian eigenvalue problem and can be written as

$$\mathrm{MX} = \mathrm{X}\Omega, \quad \mathrm{XX}^{\dagger} = 1 \tag{2.45}$$

where Ω is the diagonal matrix of vertical excitation energies, M is the shifted Hamiltonian matrix, and X is the matrix of eigenvectors. The shifted Hamiltonian M is represented by the standard MP Hamiltonian $\hat{H}$ shifted by the ground state energy $E_0^{MP_n}$. In the ISR formalism, this shifted Hamiltonian is written in terms of the intermediate state (IS) basis as follows:

$$(\mathrm{M})_{IJ} = \langle \tilde{\Psi}_I | H - E_0^{MP_n} | \tilde{\Psi}_J \rangle \tag{2.46}$$

where $\tilde{\Psi}_J$ is an IS basis. In ADC schemes, the key step is to generate the IS basis functions. This process involves two steps: in the first step, the correlated excited state basis function is obtained from the correlated ground state of MP$_n$ ($\tilde{\Psi}_0^{MP_n}$) by applying the physical excitation operator as follows

$$\bar{\Psi}_J = \hat{C}_J \Psi_0^{MP_n} \tag{2.47}$$

where $\hat{C}_J$ denotes the physical excitation operator. The correlated excited state basis functions $\bar{\Psi}_J$ are not orthogonal and can be orthogonalized via the Gram-Schmidt procedure, which leads to the final IS basis as follows:

$$\bar{\Psi}_J \xrightarrow{Gram-Schmidt} \tilde{\Psi}_J \tag{2.48}$$

By employing these IS basis functions in Eq. 2.46, one can get the corresponding ADC matrix, and the solving the Eq. 2.45 by diagonalization results in excitation energies. The order of the ADC schemes depends on the MP$_n$, for example, if we used the MP2 ground state wave function ($\Psi_0^{MP_2}$) and energy ($E_0^{MP_2}$) then ADC(2) is obtained.

2.8 Density functional tight binding (DFTB) and time-dependent density functional tight binding (TD-DFTB)

The density functional tight-binding (DFTB) method[125–127] can be interpreted as an approximate formulation of DFT at the GGA level. In this approach, the total energy of the system is written as a second-order expansion of the KS-DFT total energy functional (Eq. 2.26) around a suitably chosen reference electron density, ρ_0. The ground-state density, $\rho(\mathbf{r})$, is then written as a sum of this reference density and a fluctuation term,

$$\rho(r) = \rho_0 + \delta\rho \tag{2.49}$$

The total energy functional in Eq. 2.24 is then expanded in a Taylor series with respect to $\delta\rho$ as[128]

$$E^{DFTB}[\rho_0 + \delta\rho] = E^0[\rho_0] + E^1[\rho_0, \delta\rho] + E^2[\rho_0, (\delta\rho)^2] + E^3[\rho_0, (\delta\rho)^3] \tag{2.50}$$

with the individual terms given by

$$\begin{aligned}
E^0[\rho_0] &= \frac{1}{2}\sum_{AB}\frac{Z_A Z_B}{R_{AB}} - \frac{1}{2}\int\int\frac{\rho(\mathbf{r}_1)\rho(\mathbf{r}_2)}{\mathbf{r}_{12}}d\mathbf{r}_1 d\mathbf{r}_2 - \int V_{\mathrm{XC}}[\rho_0]\rho(\mathbf{r}_1)d\mathbf{r}_1 + E_{XC}[\rho_0] \\
E^1[\rho_0, \delta\rho] &= \sum_i n_i\langle\Psi_i|\hat{H}[\rho_0]|\Psi_i\rangle, \\
E^2[\rho_1, \delta\rho^2] &= \frac{1}{2}\int\int\left(\frac{1}{\mathbf{r}_{12}} - \frac{\delta^2 E_{XC}[\rho]}{\delta\rho(\mathbf{r}_1)\delta\rho(\mathbf{r}_2)}\bigg|_{\rho_0}\right)\delta\rho(\mathbf{r}_1)\delta\rho(\mathbf{r}_2)d\mathbf{r}_1 d\mathbf{r}_2, \\
E^3[\rho_1, \delta\rho^3] &= \frac{1}{6}\int\int\int\frac{\delta^3 E_{XC}[\rho]}{\delta\rho(\mathbf{r}_1)\delta\rho(\mathbf{r}_2)\delta\rho(\mathbf{r}_3)}\bigg|_{\rho_0}\delta\rho(\mathbf{r}_1)\delta\rho(\mathbf{r}_2)d\mathbf{r}_1 d\mathbf{r}_2 d\mathbf{r}_3
\end{aligned} \tag{2.51}$$

In the first-order implementation of DFTB, usually called DFTB1,[125,126,129] the zeroth- and first-order terms of Eq. 2.50 are taken into account, and the corresponding KS orbitals are expanded in a linear combination of atomic orbitals (LCAO),

$$\Psi_i = \sum_\mu c_{\mu i}\phi_\mu \tag{2.52}$$

where ϕ_μ denote the atomic basis functions. In addition, a two-center approximation is applied to the Hamiltonian operator $\hat{H}[\rho_0]$. The atomic orbital set ϕ_μ is obtained from DFT by solving the following atomic KS equation with an additional confinement potential[130] $\left(\frac{r}{r_0}\right)^m$,

$$\left[-\frac{1}{2}\nabla_i^2 + V_{\text{eff}}[\rho^{atom}] + \left(\frac{r}{r_0}\right)^m\right]\phi_\mu = \varepsilon_\mu \phi_\mu, \tag{2.53}$$

where V_{eff} is the effective KS atomic potential. Using the LCAO basis, the DFTB Hamiltonian can be written as

$$\begin{aligned} \hat{H}^0_{\mu v} &= \langle \phi_\mu | \hat{H}[\rho_0] | \phi_v \rangle \\ &\approx \langle \phi_\mu | -\frac{1}{2}\nabla_i^2 + V[\rho_A + \rho_B] | \phi_v \rangle, \quad \mu \in A, v \in B, \end{aligned} \tag{2.54}$$

where $V[\rho_A + \rho_B]$ denotes the KS potential within the two-center approximation.[125] $E^0[\rho_0]$ is approximated by a sum of pairwise repulsive potentials,

$$E^0[\rho_0] \approx E_{\text{rep}} = \frac{1}{2}\sum_{AB} V^{rep}_{AB}. \tag{2.55}$$

Therefore, the DFTB1 total energy can be expressed as[125]

$$E^{DFTB1} = \sum_i \sum_{AB} \sum_{\mu,v} n_i c_\mu c_v \hat{H}^0_{\mu v} + \frac{1}{2}\sum_{AB} V^{rep}_{AB} \tag{2.56}$$

Within the DFTB1 formalism, integral tables for $\langle \phi_\mu | \hat{H}[\rho_0] | \phi_v \rangle$ and $\langle \phi_\mu \phi_v \rangle$ are generated at different interatomic distances and orientations for all relevant basis functions. These precomputed tables enable rapid assembly of the Hamiltonian and overlap matrices during actual calculations.

The second-order term in Eq. 2.50, which accounts for the density fluctuation of the Columb and XC energies, provides the basis of the DFTB2[127] expansion as

$$\begin{aligned} E^{DFTB2} &= \sum_i \sum_{AB} \sum_{\mu,v} n_i c_\mu c_v \hat{H}^0_{\mu v} + \frac{1}{2}\sum_{AB} V^{rep}_{AB} \\ &+ \frac{1}{2}\int\int \left(\frac{1}{\mathbf{r}_{12}} - \left.\frac{\delta^2 E_{XC}[\rho]}{\delta\rho(\mathbf{r}_1)\delta\rho(\mathbf{r}_2)}\right|_{\rho_0}\right)\delta\rho(\mathbf{r}_1)\delta\rho(\mathbf{r}_2)d\mathbf{r}_1 d\mathbf{r}_2 \end{aligned} \tag{2.57}$$

The second-order term can also be written using the two-electron integral γ_{AB} and the atomic charge fluctuations with respect to the atomic neutral references[127] $\Delta q_A = q_A - q_A^0$ as

$$\begin{aligned} E^2[\rho_1, \delta\rho^2] &= \frac{1}{2}\int\int\left(\frac{1}{\mathbf{r}_{12}} - \frac{\delta^2 E_{XC}[\rho]}{\delta\rho(\mathbf{r}_1)\delta\rho(\mathbf{r}_2)}\bigg|_{\rho_0}\right)\delta\rho(\mathbf{r}_1)\delta\rho(\mathbf{r}_2)d\mathbf{r}_1 d\mathbf{r}_2 \\ &= \frac{1}{2}\sum_{AB}\Delta q_A \Delta q_B \gamma_{AB} \end{aligned} \tag{2.58}$$

and the Eq. 2.57 can be rewritten as follows:

$$E^{DFTB2} = \sum_i \sum_{AB} \sum_{\mu,v} n_i c_\mu c_v \hat{H}^0_{\mu v} + \frac{1}{2}\sum_{AB} V^{rep}_{AB} + \frac{1}{2}\sum_{AB}\Delta q_A \Delta q_B \gamma_{AB}. \tag{2.59}$$

This is the most widely used DFTB scheme, also known as self-consistent charge DFTB or SCC-DFTB.[127] The expansion of DFTB to the third-order term was carried out by Elstner and co-workers.[131] Keeping the two-body contributions, the third-order term (Eq. 2.51) can be expressed as

$$\begin{aligned} E^3[\rho_1, \delta\rho^3] &= \frac{1}{6}\sum_{ABC}\Delta q_A \Delta q_B \Delta q_C \frac{d\gamma_{AB}}{dq_C} \\ &= \frac{1}{6}\sum_{AB}(\Delta q_A^2 \Delta q_B \Gamma_{AB} + \Delta q_A \Delta q_B^2 \Gamma_{BA}), \end{aligned} \tag{2.60}$$

where $\Gamma_{AB} = \left.\frac{d\gamma_{AB}}{dq_B}\right|_{q_A^0}$. The resulting expression of the total DFTB3 energy is then given by

$$\begin{aligned} E^{DFTB3} = \sum_i \sum_{AB} \sum_{\mu,v} n_i c_\mu c_v \hat{H}^0_{\mu v} + \frac{1}{2}\sum_{AB} V^{rep}_{AB} + \frac{1}{2}\sum_{AB}\Delta q_A \Delta q_B \gamma_{AB} \\ + \frac{1}{6}\sum_{AB}(\Delta q_A^2 \Delta q_B \Gamma_{AB} + \Delta q_A \Delta q_B^2 \Gamma_{BA}) \end{aligned} \tag{2.61}$$

In this third-order formulation of DFTB, an explicit dependence on the atomic charges is introduced through an integral that itself depends on the other atomic charges.

The time-dependent extension of DFTB (TD-DFTB) was originally introduced by Niehaus *et al.*[132] within the framework of TD-DFT. In the TD-DFTB formalism, excitation energies are determined by solving the eigenvalue problem given in Eq. 2.43. Within

TD-DFTB, the two-electron integrals $(ia||bj)$ (Eq. 2.44) are evaluated using the DFTB scheme by applying the generalized Mulliken approximation,[132] in which the transition density between different KS orbitals is represented in terms of atomic charges.

2.9 Non-adiabatic dynamics

When a molecule is electronically excited following photoabsorption, its nuclear dynamics can no longer be described within the BO approximation. Following photoexcitation, nuclear motion can lead the system into regions where electronic states are close in energy, enabling electronic transitions mediated by nuclear motion. This phenomenon is known as a non-adiabatic process, in which electronic and nuclear motions are intimately coupled. Such non-adiabatic processes mainly include radiationless pathways, particularly internal conversion (IC) and intersystem crossing (ISC). The theoretical description of these time-dependent non-adiabatic phenomena in molecular systems poses significant challenges. In particular, it requires accurate computations of the energies and couplings of several electronic states, as well as the time propagation of their properties. The full quantum-mechanical treatment of the above processes in large molecular systems is out of the question. To address this issue, several *semiclassical* or *mixed quantum-classical* (MQC) approaches have been developed.[133] In these MQC approaches, the motion of the nuclei is treated classically, while the electronic motion is treated quantum-mechanically. Among the different MQC schemes, the trajectory surface-hopping (TSH)[134] method is the most commonly employed for modeling non-adiabatic dynamics, owing to its simplicity, efficiency, and scalability.[135] The central concept of TSH is that, throughout the non-adiabatic process, the nuclei follow adiabatic motion for the majority of the time and only for a fraction of time, within a relatively small region of configuration space, undergo a non-adiabatic transition. Such non-adiabatic transitions are modeled as instantaneous switches or hops between two adiabatic potential energy surfaces.[134,135] In the TSH approach, the nuclei follow Newton's classical equation of motion:

$$M_A \frac{\delta^2 \vec{R}_A}{\delta t^2} = -\frac{\delta E_{elec}}{\delta \vec{R}_A} \tag{2.62}$$

where M_A and R_A represent the mass and position of the nucleus of A, respectively, and E_{elec} is the electronic energy. The electronic wave-function is expressed as a linear combination of the adiabatic basis states as follows:

$$|\Phi_{elec}(t)\rangle = \sum_{\alpha} c_{\alpha}(t)|\Psi_{\alpha}(t)\rangle \tag{2.63}$$

where α runs over the basis states, $\Psi_{\alpha}(t)$ are adiabatic basis states, and c_{α}(t) are the time-dependent expansion coefficients. The equation of motion for the electrons can be obtained by inserting Eq. 2.63 in the time-dependent SE as follows:[136]

$$\frac{\delta}{\delta t}c_{\beta} = -\sum_{\alpha}\left[\frac{i}{\hbar}H_{\beta\alpha} + K_{\beta\alpha}\right]c_{\alpha} \tag{2.64}$$

where

$$\begin{aligned} H_{\beta\alpha} &= \langle\Psi_{\beta}|H_{elec}|\Psi_{\alpha}\rangle, \\ K_{\beta\alpha} &= \langle\Psi_{\beta}|\frac{\delta}{\delta t}|\Psi_{\alpha}\rangle = \frac{\delta\vec{R}}{\delta t}\cdot\langle\Psi_{\beta}|\frac{\delta}{\delta\vec{R}}|\Psi_{\alpha}\rangle = \vec{v}\cdot\langle\Psi_{\beta}|\nabla|\Psi_{\alpha}\rangle = \vec{v}\cdot F^{c}_{\beta\alpha} \end{aligned} \tag{2.65}$$

In Eq. 2.65, $F_{\beta\alpha}$ represents the non-adiabatic coupling between the states β and α and $\vec{v}$ is the nuclear velocity. During the dynamics process, the hopping probability between the β and α states is given by the following equation according to Tully's fewest-switches surface hopping (FSSH) algorithm[137]

$$P_{\beta\to\alpha} = \frac{\text{Population increment in } \alpha \text{ due to flux from } \beta \text{ during } \Delta t}{\text{Population of } \alpha} \tag{2.66}$$

The population in the α state can then be obtained from the diagonal elements of the following density matrix:

$$\rho_{\alpha\beta}(t) = c_{\alpha}c^{*}_{\beta}. \tag{2.67}$$

The hopping event from β to α state takes place if the following two conditions are fulfilled simultaneously:

1. For a random number, r_t, sampled between 0 and 1, hopping from β to α state happens if

$$\sum_{i=1}^{\alpha-1} P_{\beta\to i}(t) < r_t \leq \sum_{i=1}^{\alpha} P_{\beta\to i}(t) \tag{2.68}$$

2. The energy difference between the final and initial states satisfies the following condition[136]

$$V_\alpha(R(t)) - V_\beta(R(t)) \leq \frac{\left(\sum_m^{N_{at}} v_m \cdot F_{\alpha\beta}^m\right)^2}{2\sum_m^{N_{at}} M_m^{-1}(F_{\alpha\beta}^m)^2}. \tag{2.69}$$

The second condition applies only when the total energy after hopping is larger than before, which satisfies the law of conservation of energy. A situation in which only the first condition is valid is called frustrated hopping.[138]

One shortcoming of Tully's FSSH approach is that the electronic populations are propagated with high coherence.[139–141] A commonly employed strategy to solve this problem is the 'nonlinear decay of mixing' model originally proposed by Truhlar et al.[141] The decoherence effects in the FSSH scheme were implemented by Granucci et al.[142] by correcting the coefficient c_α as

$$\begin{aligned} \bar{c}_\alpha &= c_\alpha \exp\left(\frac{-\Delta t}{\tau_{\alpha\beta}}\right) \forall(\alpha \neq \beta), \\ \bar{c}_\beta &= \frac{c_\beta}{|c_\beta|}\left[1 - \sum_{\alpha\neq\beta} |\bar{c}_\alpha|\right]^{\frac{1}{2}} \end{aligned} \tag{2.70}$$

and the decoherence time is given by the following equation

$$\tau_{\alpha\beta} = \frac{\hbar}{|V_{\alpha\alpha} - V_{\beta\beta}|}\left(1 + \frac{\kappa}{E_{kin}}\right). \tag{2.71}$$

where E_{kin} is the classical nuclear kinetic energy, κ is an empirical decoherence parameter whose recommended value is 0.1 Hartree.

2.10 Excitonic analysis

Analysis of excited-state properties after ab initio calculations is a difficult task. However, in recent times, excitonic analysis based on the one-electron transition density matrix (**1TDM**)[19,143] has been very useful for characterizing excited states. In this analysis, first, the CT numbers denoted as Ω_{AB} are computed from 1TDM. Once the full Ω matrix consisting of all Ω_{AB} is constructed, descriptors such as CT parameter (ω_{CT}),[19,144] exciton size (d_{exc}),[145,146] and the participation ratio of natural transition orbitals (NTOs) (PRNTO)[19,147] are computed to analyze the excited states. The **1TDM** between the ground state and the excited state can be written as

$$\begin{aligned}\gamma^{0I}(r_h, r_e) &= N \int \cdots \int \Psi^0(r_h, r_2, \ldots, r_N)\, \Psi^I(r_e, r_2, \ldots, r_N)\, dr_2 \ldots dr_N \\ &= \chi_{exc}(r_h, r_e),\end{aligned} \tag{2.72}$$

where γ^{0I} is 1TDM between ground (0) and excited (I) states, Ψ^0 and Ψ^I are the many-body ground and excited wave functions, respectively, and r_h and r_e represent the hole and electron co-ordinates, respectively. The **1TDM** is also identified as an exciton wave-function $\chi_{exc}(r_h, r_e)$. The Eq. 2.72 can be rewritten as

$$\gamma^{0I}(r_h, r_e) = \sum_{\mu v} D^{0I}_{\mu v} \chi_\mu(r_h) \chi_v(r_e), \tag{2.73}$$

where χ_μ and χ_v are the atomic orbitals and the element $D^{0I}_{\mu v}$ is defined as

$$D^{0I}_{\mu v} = \langle \Psi^0 | \hat{a}^\dagger_\mu \hat{a}_v | \Psi^I \rangle. \tag{2.74}$$

Here $\hat{a}^+$ and $\hat{a}$ are the one-particle creation and annihilation operators. The descriptors that are obtained by decomposition of **1TDM** are explained below.

2.10.1 Charge transfer number

The charge-transfer number (Ω_{AB}) can be defined as the probability of finding the *hole* and the *electron* on different fragments of a molecular system (Figure 1.1) after electronic

excitation. If we divide a molecular system into two fragments, A and B, the charge transfer number Ω_{AB} is obtained by partial integration over the square of γ^{0I}, restricting the *hole* coordinate to fragment A and the *electron* to fragment B as

$$\Omega_{AB} = \int_A \int_B \gamma^{0I}(r_h, r_e)^2 \, dr_e \, dr_h. \tag{2.75}$$

The Mulliken population analysis[20] of equation 2.75 gives the working equation.

$$\Omega_{AB} = \frac{1}{2} \sum_{\mu \epsilon A} \sum_{v \epsilon B} [(D^{0I}S)_{\mu v}(SD^{0I})_{\mu v} + D^{0I}_{\mu v}(SD^{0I}S)_{\mu v}], \tag{2.76}$$

where S is the overlap matrix between the basis functions.

2.10.2 Charge transfer parameter or total charge transfer

The charge transfer parameter ω_{CT} is defined by summing over the off-diagonal elements of Ω_{AB} matrix,[19], and can be written as

$$\omega_{CT} = \frac{1}{\Omega} \sum_{A, B \neq A} \Omega_{AB}, \tag{2.77}$$

where Ω is the total charge transfer number, and the value of ω_{CT} ranges from 0 to 1, the value close to 0 indicates LE or Frenkel excitonic state, whereas 1 for a fully charge-separated or CT state.

2.10.3 Exciton size

Exciton size d_{exc} is defined as the average distance between the *electron* and the *hole* positions. The exciton size of a system is obtained as an expectation value of root-mean-square (rms) separation between the *electron* and *hole* with respect to the excitonic wave function $\chi_{exc}(r_h, r_e)$ as follows[145,146]

$$\begin{aligned} d^2_{exc} &= < (r_h - r_e)^2 >_{exc} = \frac{< \chi_{exc} | (r_h - r_e)^2 | \chi_{exc} >}{< \chi_{exc} | \chi_{exc} >} \\ &= \frac{1}{\Omega} \iint \gamma^{0I}(r_h, r_e)(r_h - r_e)^2 \gamma^{0I}(r_h, r_e) \, dr_h \, dr_e. \end{aligned} \tag{2.78}$$

Insertion of equation 2.73 into Eq. 2.78 results in the following formula

$$d_{\text{exc}}^2 = \frac{1}{\Omega} \sum_{\xi\epsilon(x,y,z)} (tr(D^{0I} M_\xi^{(2)} D^{0I} S) - 2tr(D^{I0} M_\xi^{(1)} D^{0I} M_\xi^{(1)} + tr(D^{I0} S D^{0I} M_\xi^{(2)})), \quad (2.79)$$

where M_ξ^k refers to the kth-order multipole matrix with respect to the cartesian coordinate ξ. An approximate form of d_{exc} can also be derived from Eq. 2.78 by dividing the double integral into separate regions that correspond to different atoms, M and N, as follows[148]

$$d_{\text{exc}}^2 = \frac{1}{\Omega} \sum_{M,N} \int_A \int_B \gamma^{0I}(r_h, r_e)(r_h - r_e)^2 \gamma^{0I}(r_h, r_e)\, dr_h\, dr_e. \quad (2.80)$$

Approximating $(r_h - r_e)^2$ by the squared distance between the positions of M and N nuclei, denoted as d_{MN}^2, the Eq 2.80 can be written as

$$d_{\text{exc}}^2 = \frac{1}{\Omega} \sum_{M,N} d_{MN}^2 \int_M \int_N \gamma^{0I}(r_h, r_e) \gamma^{0I}(r_h, r_e)\, dr_h\, dr_e. \quad (2.81)$$

This leads to

$$\bar{d}_{\text{exc}} = \sqrt{\frac{1}{\Omega} \sum_{M,N} \Omega_{MN} d_{MN}^2}. \quad (2.82)$$

Therefore, computation of d_{exc} only requires the CT number and coordinates of the two nuclei.

2.10.4 Participation ratio of natural transition orbitals

Natural transition orbitals provide a compact representation of electronic transitions[149]. Those are obtained by the singular value decomposition (SVD)[150] of the 1TDM using unitary matrices **U** and **V** as

$$\tilde{\mathbf{D}}^{0I} = \mathbf{U}\ \ \text{diag}(\sqrt{\lambda_1}, \sqrt{\lambda_2}, \ldots)\mathbf{V}^T \quad (2.83)$$

where unitary matrices **U** and **V** contain the eigenvectors of *hole* (h) and *electron* (e) matrices, respectively, and λ_i denotes the weights of the corresponding electronic transitions. The number of independent pairs of NTOs required to describe an electronic

excitation is given by the values of the participation ratio of natural transition orbitals (PR_{NTO}),[19,20], which can be calculated as

$$PR_{\mathrm{NTO}} = \frac{(\sum_i \lambda_i)^2}{\sum_i \lambda_i^2}. \tag{2.84}$$

A value of one for PR_{NTO} indicates that only one pair of NTOs is required to describe an electronic excitation, while a value > 1 indicates that more than one pair of NTOs is required.

Chapter 3

Conformational effect on the excitonic states of 2-Phenylpyridine oligomers: Ab initio studies and analysis

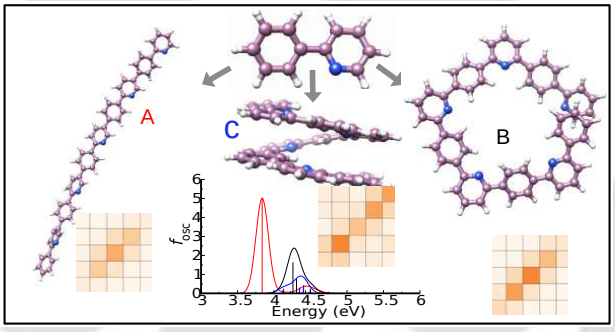

In this chapter, we report the effect of different conformations of 2-Phenylpyridine oligomers ($(\mathbf{PhPy})_{n=1-5}$) on the excited state properties. The computational studies are carried out at the RI-ADC(2)/def2-TZVP level, considering the three conformers namely **A** (linear), **B**(helical), and **C**(helical). The differences in the geometries of the three conformers are reflected in the UV and CD spectra. The UV spectra of conformer **A** show high-intensity peaks compared to the conformers **B** and **C**, for each oligomer. While the helical oligomers of conformers **B** and **C** show high-intensity CD bands, the intensities of CD bands for all of the oligomers of conformer **A** are weaker. Analysis of the properties of the first five excited states in $(\mathbf{PhPy})_5$ reveals that these are partially charge transfer states. Reproduced from "*The Journal of Physical Chemistry A*, **2023**, 127(38), 7898–7907" with permission from the American Chemical Society.

3.1 Introduction

Aromatic heterocyclic-based conjugated oligomers and polymers are among the most extensively studied oligomers in the field of organic electronics.[62–64] Heterocyclic-based conjugated oligomers containing alternate pyridine and pyrrole or thiophene or furan have already been synthesized.[65–68,151,152] Due to the presence of a pyridine ring in these types of conjugated oligomers, they show interesting optical and electronic properties.[69,151,152] One of the important aspects in these conjugated oligomers is that, depending on the linkage pattern between two adjacent monomeric units, whether connected at ortho-, meta-, or para-positions, they form different conformational isomers and show different electronic properties.[13,38,39] Therefore, a simple change of the linkage points leads to a drastic change in the electronic and physical properties, and this in turn affects the overall performance and stability of the corresponding electronic devices.[153–155] In our work, we chose to study the conformational effect on the properties of 2-Phenylpyridine (**PhPy**) oligomers. **PhPy** has been studied both experimentally and theoretically.[156–160] However, the effect of different possible conformers on the optoelectronic properties has not been reported yet. Considering this, in this work, we present the results of a computational study to elucidate the structure-excited state property relationship in **PhPy** oligomers.

In this work, oligomers of **PhPy** are constructed by considering three different conformational isomers **A**, **B**, and **C**. The schematic representations of the three conformers are shown in Figure 3.1. As shown in the figure, the oligomers of conformer **A** are formed by using the meta position of the pyridine ring of one **PhPy** unit and the para position of the phenylene ring in the adjacent **PhPy** unit. In the case of **B**, the oligomers are formed via the ortho position of the pyridine ring of one **PhPy** unit and para position of phenylene ring of the adjacent **PhPy** unit, whereas conformer **C** oligomers resemble the *m*-phenylene oligomer,[13] in which the alternate phenylene ring is replaced by a pyridine ring. Oligomers only up to pentamers are considered in this work. The details of computational methods used in this work are explained in the Computational Details section. In Results and Discussion, we present and compare the UV and CD spectra of

the three different conformers. This is followed by the analysis and characterization of excited states. The final section concludes our work.

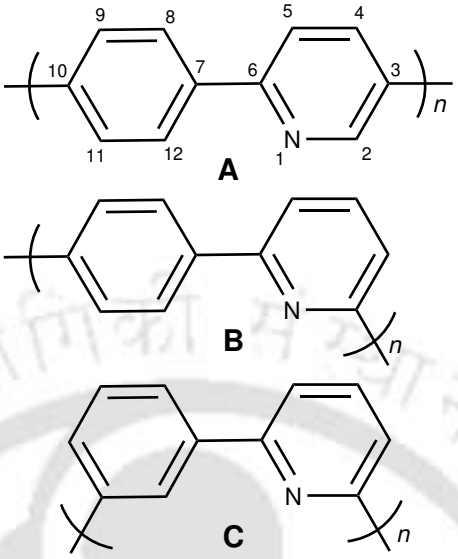

FIGURE 3.1: Schematic representation of the repeating units of three possible conformational isomers of the **PhPy** system, denoted as **A**, **B**, and **C**, where n = 1-5. The dihedral angle between each phenylene and pyridine ring is denoted as ϕ_i, where i = 1-9 in the case of a pentamer, for example.

3.2 Computational Details

Ground state geometry optimizations of the oligomers of **A**, **B**, and **C** were carried out at DFT level using the B3LYP functional[161] and def2-TZVP[162] basis set. The harmonic vibrational frequency calculations were performed at the same level of theory for the optimized geometries to verify that the structures were minima in the potential energy surface. Grimme's D3 empirical dispersion correction was used in all DFT computations.[163–165] The Gaussian 16 program[166] package was used for all the DFT calculations.

For the excited state studies, the ADC(2) method was used. The ADC(2) calculations were carried out at the B3LYP optimized geometries to obtain vertical excitation energies (E_g). The E_g values for monomer were calculated using four different basis sets; def2-SV(P),[167] def2-SVP,[162], def2-TZVP and def2-TZVPP. For the oligomers, the E_gs were

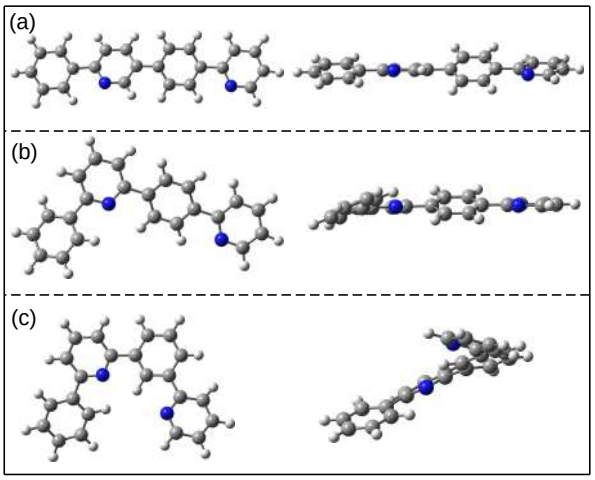

FIGURE 3.2: Ground state optimized geometries of $(\mathbf{PhPy})_2$ for three different conformers, **A**(a), **B**(b), and **C**(c) obtained at the B3LYP-D3/def2-TZVP level. Top and side views are shown in the left and right columns, respectively.

calculated using the def2-TZVP basis set. For the ADC(2) studies, the resolution-of-identity (RI) approximation was used. The ADC(2) calculations were carried out using Turbomole V7.1 software.[168]. Both the optimizations and excitation calculations were performed in the gas phase. The UV and CD spectra of all the oligomers were obtained using Gaussians with a half-width at half maxima of 0.1 eV. The Gabedit software[169] was used to generate the UV and CD spectra. The characterization of the excited states was carried out by considering the excitonic analysis based on the one-electron transition density matrix (1TDM), and for this purpose, the Theodore 3.0 software package[170] was used.

3.3 Results and Discussion

3.3.1 Geometries of Monomers and Oligomers

The geometry of **PhPy** monomer obtained at B3LYP-D3/def2-TZVP level is found to be nonplanar and is in good agreement with the previous results.[157] To discuss the differences in the optimized geometries of the conformers, inter-ring dihedral angles are used. While the monomer has one dihedral angle, the pentamer has nine inter-ring dihedral angles. Optimized structures of $(\mathbf{PhPy})_2$ of conformers **A**, **B**, and **C** are shown in Figure 3.2. From Figure 3.2(a), it is found that the linear conformer **A** has

TABLE 3.1: Calculated Dihedral Angles (ϕ_{1-9}) of $(\mathbf{PhPy})_{n=2-5}$ of Three Conformers **A**, **B**, and **C** at the RI-ADC(2)/def2-TZVP Level

	$(\mathbf{PhPy})_2$			$(\mathbf{PhPy})_3$			$(\mathbf{PhPy})_4$			$(\mathbf{PhPy})_5$		
angle	**A**	**B**	**C**	**A**	**B**	**C**	**A**	**B**	**C**	**A**	**B**	**C**
ϕ_1	-19.53	23.01	-21.16	-19.49	-23.00	12.14	-19.44	22.75	-8.23	-19.62	-22.14	-10.80
ϕ_2	35.86	21.73	-24.27	35.80	-21.68	-25.21	35.95	21.31	-19.16	35.71	-12.32	-11.79
ϕ_3	-19.59	-20.14	23.48	17.17	21.95	-7.02	-16.63	-21.92	5.85	-17.38	25.22	-5.93
ϕ_4				35.86	21.66	-9.81	35.80	-21.75	-25.09	35.58	23.92	-18.30
ϕ_5				-19.46	-20.04	-20.32	-16.68	21.61	-5.46	-17.11	-18.65	-3.98
ϕ_6							35.94	21.40	-11.55	35.82	-21.64	-15.21
ϕ_7							-19.42	-14.73	-15.05	-16.87	21.45	-11.49
ϕ_8										35.91	17.53	-6.70
ϕ_9										-19.58	15.33	-14.25

a nonplanar structure. The values of the dihedral angles are listed in Table 3.1. For **A**, the values of terminal dihedral angles ϕ_1 and ϕ_3 are the same, whereas the dihedral angle in the middle (denoted as ϕ_2) is larger compared to terminal angles. Side view of the conformer **B** reveals that the pyridine rings are nearly in the same plane, on the other hand, the two alternate phenylene rings are in opposite directions to each other. Values of ϕ_1, ϕ_2, and ϕ_3 for this conformer do not differ too much from each other (ϕ_1, ϕ_2, and ϕ_3 are 23.01, 21.73, and -20.14, respectively). In contrast to **A**, and **B**, as the figure shows, the terminal rings of conformer **C** tend to bend away due to steric hindrance between the hydrogen atoms of adjacent rings. Values of ϕ_1, ϕ_2, and ϕ_3 for this oligomer are -21.16, -24.27, and 23.48, respectively. As we move from $(\mathbf{PhPy})_2$ to $(\mathbf{PhPy})_3$, conformer **C** forms a helix-like structure shown in Figure A1. In this helix-like structure, a significant change in dihedral angles is observed which are shown in Table 3.1. However, no significant change in geometry and dihedral angles is observed in the case of **A** and **B** conformers, shown in Figure A1. After addition of another unit to $(\mathbf{PhPy})_3$, conformers **A** and **C** remain in linear and helical forms, respectively, whereas a change in geometry is observed for **B** as shown in Figure A2 and Table 3.1. A different observation is made for pentamers. Figure 3.3(b) shows that a helix is obtained also in the case of conformer **B** for $(\mathbf{PhPy})_5$, and the number of repeating units needed to form a helix-like structure is larger than in conformer **C**. The other two conformers, **A** and **C**, remain in linear and helical forms, respectively shown in Figure 3.3. Geometries of pentamers for conformers **B** and **C** are also characterized by considering parameters such as inner diameter (D_{inner}), outer diameter (D_{outer}), pitch (p_{h}), and the number of repeating units needed to form a helix (u_{h}). D_{inner}, D_{outer} and p_{h} are marked in Figure 3.3 (b). The value of u_{h} for conformer **B** (u_{h}=5) is larger than that for conformer **C** (u_{h}=3). The u_{h}

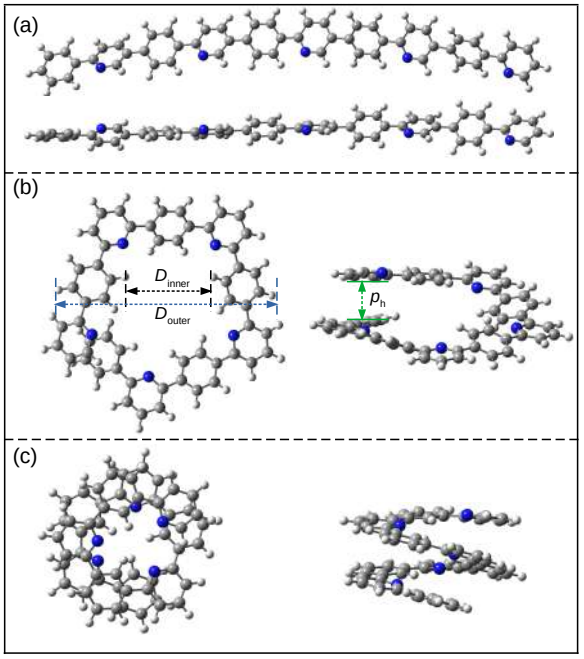

FIGURE 3.3: Optimized structures of $\mathbf{(PhPy)}_5$ of conformer **A**(a), **B**(b), and **C**(c), obtained at B3LYP-D3/def2-TZVP level. Top and side views are shown in the top and bottom panels for **A**, and for **B** and **C**, shown in the left and right columns, respectively. Parameters such as inner diameter (D_{inner}), outer diameter (D_{outer}), and pitch (p_{h}) are marked in (b).

value of a helical system is directly proportional to D_{inner} and D_{outer} values, therefore, the D_{inner} and D_{outer} values for conformer **B** (7.80 and 16.70 Å, respectively) are larger compared to the values for conformer **C** (2.41 and 11.63 Å, respectively). The p_{h} values for conformers **B** and **C** are 3.50 and 3.65 Å, respectively.

Dipole moment (μ) is an important parameter to describe the geometries of oligomers of three different conformers, as the values of μ are different for different conformers.[39,171] The variation of μ with the chain length for each conformer is calculated and plotted in Figure 3.4. As the figure shows, the value of μ increases with an increasing oligomer chain length in the case of conformer **A**. This is due to the increase in the number of heteroatoms (i.e., N atom) with the chain length. In the cases of **B** and **C**, a different trend is observed. For the conformer **B**, the μ value increases from **PhPy** to $\mathbf{(PhPy)}_2$, and then the value decreases and becomes very small as soon as a helix-like structure is formed at n=5. In this conformer, the μ value in $\mathbf{(PhPy)}_2$ is larger than that in the monomer due to the larger number of heteroatoms in $\mathbf{(PhPy)}_2$. Beyond $\mathbf{(PhPy)}_2$, cancellation of the inversely directed bond dipole moments results in a decrease in the

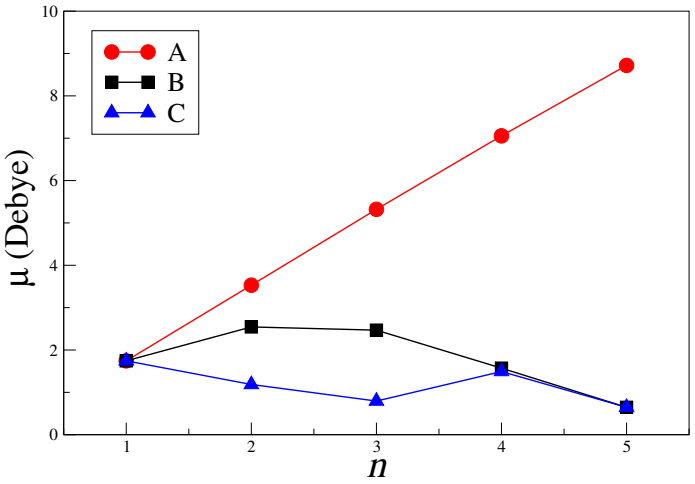

FIGURE 3.4: Dipole moments (μ) of three different conformers **A**, **B**, and **C** plotted against the oligomer chain length n.

μ value. In the case of **C**, the value decreases until it forms a helix (i.e., at n=3). This is again because of the cancellation of the oppositely directed bond dipole moments, which starts at n=2 and then reaches its minimum at n=3. After the completion of the helix, the addition of another unit leads to an increase in the value due to the increasing number of heteroatoms and finally, the value becomes small at n=5, as the second strand starts forming.

3.3.2 Electronic Properties: Absorption and CD Spectra

3.3.2.1 First Vertical Excitation Energies

The vertical excitation energies (E_g) of **PhPy** are calculated using four different basis sets def2-SV(P), def2-SVP, def2-TZVP and def2-TZVPP. The E_gs and oscillator strengths (f_{osc}) obtained using three different basis sets are tabulated in Table 3.2. These E_gs are compared against the available experimental results[156] and also against the results obtained using the symmetry-adapted cluster configuration interaction (SAC-CI) method.[158] As expected, the E_g values decrease with an increase in the size of the basis set. However, differences in the energies obtained using def2-TZVP and def2-TZVPP basis sets are small. The results obtained at the RI-ADC(2)/def2-TZVP level are close

TABLE 3.2: **Vertical Excitation Energies (E_g in eV) and the Corresponding Oscillator Strengths (f_{osc}) of PhPy Using Four Different Basis Sets. Experimental Results (exptl.) Shown in the Last Column**

	E_g/f_{osc}					
State	def2-SV(P)	def2-SVP	def2-TZVP	def2-TZVPP	exptl.[156]	SAC-CI[158]
S_1	4.86/0.004	4.85/0.004	4.75/0.004	4.75/0.004		4.47
S_2	5.04/0.052	5.02/0.047	4.87/0.102	4.85/0.099	4.49	4.49
S_3	5.17/0.185	5.15/0.184	5.01/0.219	5.00/0.221	5.15	4.69
S_4	5.20/0.003	5.18/0.003	5.07/0.001	5.06/0.001		4.85
S_5	5.61/0.480	5.59/0.484	5.38/0.367	5.37/0.369		5.15

to the experimental results, which are also tabulated in Table 3.2. These results also agree well with the SAC-CI results (E_gs obtained using the SAC-CI method corresponding to S_1, S_2, S_3, S_4, and S_5 are 4.47(f_{osc}=0.015), 4.49(f_{osc}=0.110), 4.69(f_{osc}=0.140), 4.85(f_{osc}=0.001), and 5.15 eV(f_{osc}=0.030), respectively). Based on the RI-ADC(2)/def2-TZVP results, excitation at 4.87 eV with an f_{osc} value of 0.102 is assigned as the first absorption maxima which is 0.38 eV blue-shifted from the experimental value. It is to be noted that the excited state at 4.87 eV is the second excited state. The first excited state appears at 4.75 eV with a very small f_{osc} value. The excitation at 5.38 eV with f_{osc}=0.367 is assigned as the second absorption maxima which is 0.23 eV blue-shifted from the experimental value. Keeping the above results in mind, E_g values of all the oligomers for three different conformers **A**, **B**, and **C** are calculated at the RI-ADC(2)/def2-TZVP level of theory.

In Figure 3.5, the first vertical excitation energies (E_g^1 in eV) and the corresponding f_{osc}s of three conformers are plotted against the inverse of the oligomer chain length ($1/n$). As seen in Figure 3.5, the E_g^1 values for each studied conformer decrease with an increasing chain length. However, the decreasing pattern varies from one conformer to another. In the case of conformer **A**, the decrease is more pronounced after **(PhPy)**$_2$, on the other hand, the decreasing pattern against chain length remains consistent in cases of **B** and **C**. The most important feature of this figure is that the f_{osc} values of conformer **A** are much larger compared to those of conformers **B** and **C**. For **A**, the f_{osc} value increases with increasing the chain length. For **B**, on the other hand, the f_{osc} value increases until it starts forming a helix (i.e., until n=3), and once the helix formation starts, the f_{osc} value decreases, and the value becomes very small when it forms a pure

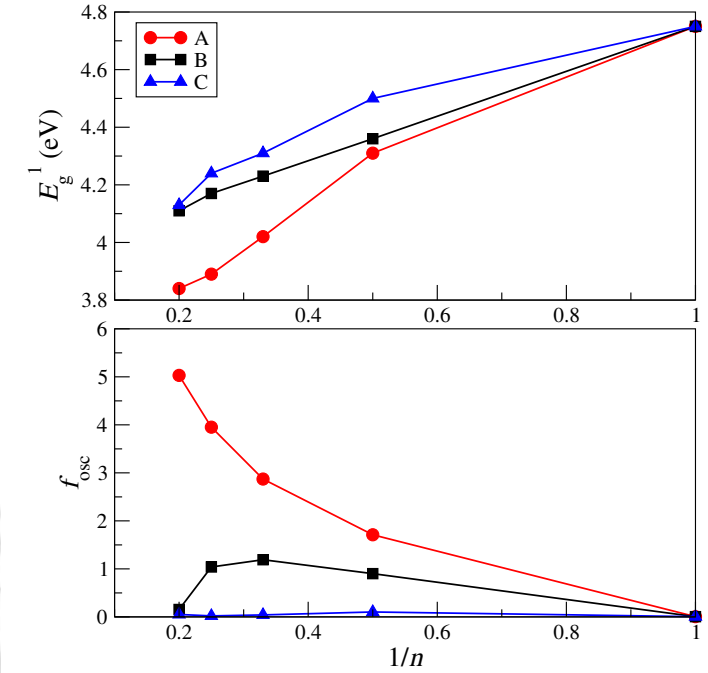

FIGURE 3.5: First excitation energy (E_g^1 in eV) and the corresponding oscillator strength (f_{osc}) of three conformers **A**, **B**, and **C** are plotted against the inverse of chain oligomer length ($1/n$). The results are obtained at the RI-ADC(2)/def2-TZVP level.

helical structure **(PhPy)**$_5$. For conformer **C**, the f_{osc} values remain small; after a small increase from monomer to trimer, the value decreases again, and becomes very small for n=5.

3.3.2.2 UV and CD Spectra of Conformers

Absorption spectra of all of the oligomers up to pentamers of **A**, **B**, and **C** are plotted in Figure 3.6. For each oligomer, ten lowest singlet excitations are considered. Figure 3.6 shows that the simulated absorption spectra of oligomers of conformer **A** are red-shifted compared to those of conformers **B** and **C**. Data corresponding to all ten transitions are tabulated in the Tables A1, A2, A3, and A4, and for a few important transitions, data is shown in Table 3.3. As shown in Fig. 3.6, for all the oligomers of conformers **B** and **C**, more than one significant electronic transition is involved in the absorption spectra, whereas spectra of oligomers of linear conformer **A** show involvement of only one significant electronic transition, i.e., $S_0 \rightarrow S_1$. The absorption

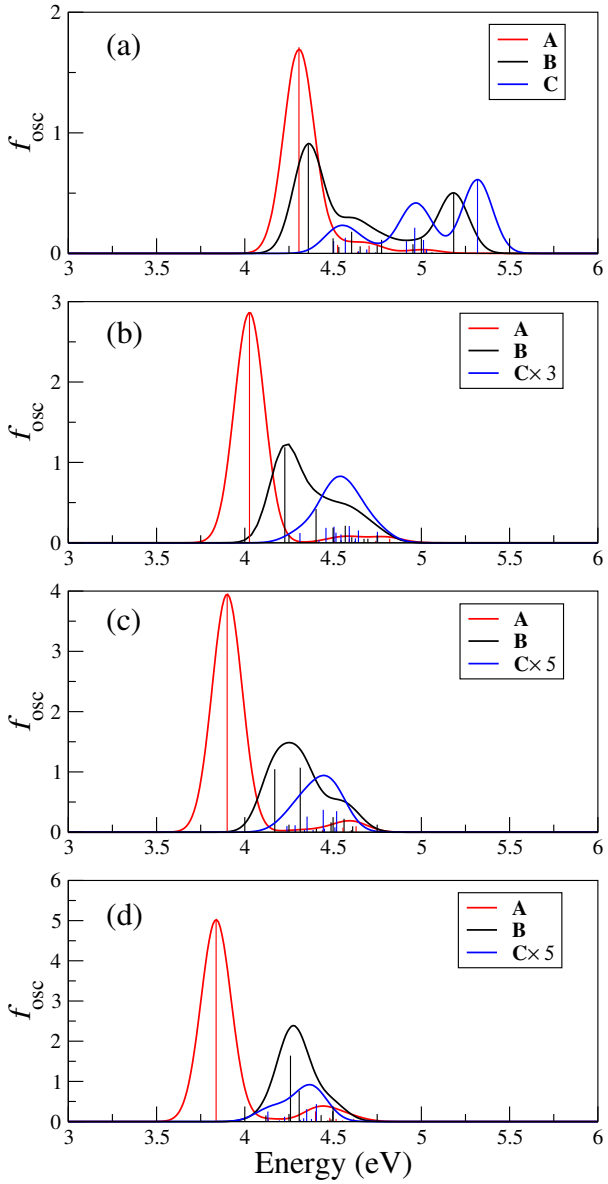

FIGURE 3.6: Absorption spectra of the **A**, **B**, and **C** conformers. Results for **(PhPy)**$_2$, **(PhPy)**$_3$, **(PhPy)**$_4$, and **(PhPy)**$_5$ are shown in parts a-d respectively. These results are obtained at the RI-ADC(2)/def2-TZVP level.

maxima of **A**-**(PhPy)**$_2$, **(PhPy)**$_3$, **(PhPy)**$_4$, and **(PhPy)**$_5$ are at 4.31(f_{osc}=1.710), 4.02(f_{osc}=2.872), 3.89(f_{osc}=3.952), and 3.84(f_{osc}=5.030) eV, respectively. In the above electronic transitions, the orbitals involved are mainly the highest occupied molecular orbital (HOMO) and the lowest unoccupied molecular orbital (LUMO), although the contribution of HOMO→LUMO excitation decreases as n increases.

As mentioned above, the results obtained for conformer **B** are quite different from

that of conformer **A**. For both **B-(PhPy)**$_2$ and **B-(PhPy)**$_3$, $S_0 \rightarrow S_1$ has the largest f_{osc} value. However, for **(PhPy)**$_4$ and **(PhPy)**$_5$, larger f_{osc} values are observed for the $S_0 \rightarrow S_2$ transitions. As seen in Table 3.3, excitation at 4.26 eV(f_{osc}= 1.641) for **(PhPy)**$_5$ corresponds to the transition between S_0 and S_2. The orbitals involved in the electronic transitions of oligomers of conformer **B** are not only the HOMO and LUMO, but also occupied orbitals other than HOMO and unoccupied orbitals other than LUMO are also involved. For example, the electronic transition in **(PhPy)**$_3$ at 4.23 eV(f_{osc}=1.190) involves H$\rightarrow$L+1(66.7%) and H-1$\rightarrow$L(6%) excitations. In the case of **C**, large f_{osc} values are observed for transitions between the S_0 and excited states other than S_1. For **(PhPy)**$_2$, $S_0 \rightarrow S_{10}$ has the highest f_{osc} value, although few other transitions also have considerable f_{osc} values as shown in Table A1. The helical oligomers of **C**, i.e., **(PhPy)**$_3$, **(PhPy)**$_4$, and **(PhPy)**$_5$, show relatively weaker f_{osc}s for all of the transitions, and the highest f_{osc} values for these oligomers correspond to $S_0 \rightarrow S_7$, $S_0 \rightarrow S_6$, and $S_0 \rightarrow S_{10}$, respectively.

TABLE 3.3: Vertical Excitation Energy (E_g), Oscillator Strength (f_{osc}), and Orbitals Involved in Important Electronic Transitions of Oligomers up to **(PhPy)**$_5$ for the Three Conformers Obtained at the RI-ADC(2)/def2-TZVP Level

	A				**B**				**C**			
Oligomer	State	E_g	f_{osc}	Configuration	State	E_g	f_{osc}	Configuration	State	E_g	f_{osc}	Configuration
(PhPy)$_2$	S_1	4.31	1.710	H→L (84 %)	S_1	4.36	0.901	H→L (60.5 %) H→L+1 (20%)	7	4.96	0.213	H-3→L+1 (13.4 %) H-1 →L+3 (9.8%)
					S_{10}	5.18	0.497	H-1→L (34.7%) H→L+1 (12%)	S_{10}	5.32	0.614	H-1→L(28 %) H-2 →L (15.3%)
(PhPy)$_3$	S_1	4.02	2.872	H→L (82%)	S_1	4.23	1.190	H→L+1 (66.7 %) H-1→L (6%)	S_4	4.51	0.067	H-1→L+2 (13.2 %) H-1 →L (8.3%)
					S_2	4.40	0.421	H→L (32%) H-1→L+1 (10%)	S_7	4.59	0.069	H-13→L+2(17.4 %) H-14 →L+1 (11.4%)
(PhPy)$_4$	S_1	3.90	3.952	H→L (73.7%)	S_1	4.17	1.040	H→L+2 (56 %) H-1→L+1 (14.6%)	S_6	4.44	0.074	H-2→L(9.0%) H-17→L(8.8%)
					S_2	4.31	1.070	H→L+1 (40.6%) H-1→L+2 (21.6%)	S_{10}	4.52	0.070	H-2→L+2 (13.2%) H→L(12.0 %)
(PhPy)$_5$	S_1	3.83	5.030	H→L (64.9%)	S_2	4.26	1.641	H→L+2 (36.5 %) H-1→L+3 (18.2%)	S_7	4.35	0.062	H-13→L (10%) H-11→L (6%)
					S_3	4.30	0.765	H→L+1 (28.8%) H-2→L+3 (12.7%)	S_{10}	4.41	0.087	H-3→L+2 (10%) H-2→L (6%)

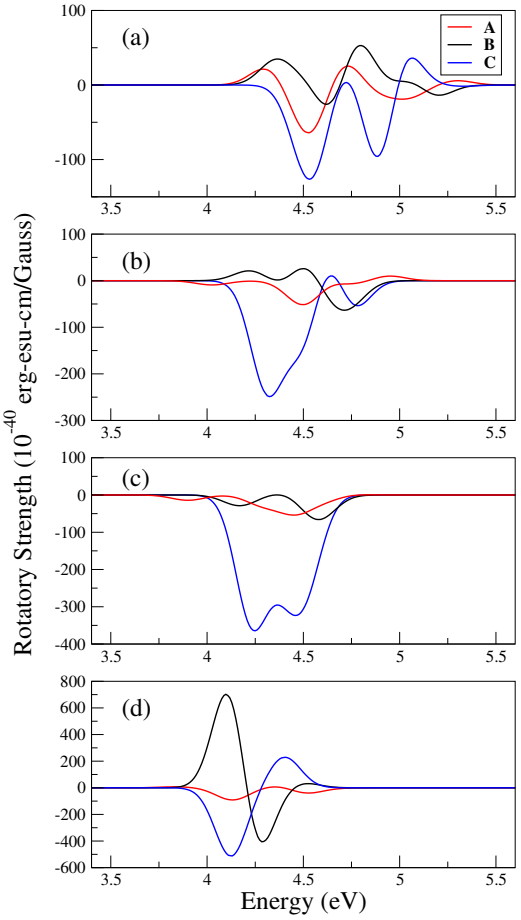

FIGURE 3.7: Simulated CD spectra of conformers **A**, **B**, and **C** for **(PhPy)**$_2$(a), **(PhPy)**$_3$(b), **(PhPy)**$_4$(c), and **(PhPy)**$_5$(d), obtained at the RI-ADC(2)/def2-TZVP level

To understand the chiroptical properties of the studied oligomers, we have simulated the CD spectra at the RI-ADC(2)/def2-TZVP level and the results are shown in Figure 3.7. Although the oligomers of conformer **A** have linear-type structures, their mirror images are nonsuperimposable, and therefore, these oligomers are optically active and show CD spectra with comparatively smaller intensity. Oligomers of conformer **C** have the highest intensity CD bands up to tetramer as compared to those of conformers **A** and **B**. For **(PhPy)**$_5$, the highest intensity CD band is observed for conformer **B**. As shown in Figure 3.7, the spectrum of the dimer of each conformer shows three CD bands. While spectra of conformers **A** and **B** show two positive and one negative bands, the conformer **C** spectrum shows two negative and one positive band. In the case of conformers **A** and **B**, negative bands appear between the two positive bands. In **A**, the highest peaks in the

lower and higher energy positive bands correspond to $S_0 \rightarrow S_1$ and $S_0 \rightarrow S_4$, respectively. However, for **B**, these peaks originate due to $S_0 \rightarrow S_1$ and $S_0 \rightarrow S_6$ transitions. On the other hand, the peaks in negative bands are due to $S_0 \rightarrow S_2$ and $S_0 \rightarrow S_4$ transitions, respectively. For conformer **C**, the two negative bands are lower in energy than the positive band. Intensities of these negative bands are comparatively higher than those of the positive and the negative bands of conformers **A** and **B**. Values of the rotatory strength (R in 10^{-40} erg·esu·cm·gauss^{-1}) of the highest peak of these negative bands lie between -72.64 and -186.40, tabulated in Table A1.

As we move from **(PhPy)**$_2$ to **(PhPy)**$_3$, a significant change is observed in the CD spectra of the conformer **C** which now has a helical structure. In contrast, no major change is seen for **A** and **B**, as shown in Figure A3. In conformer **C**, a high-intensity CD band is observed around 4.3 eV. The highest peak in this band corresponds to an R value of -233.42 at 4.31 eV, and this peak originates due to the $S_0 \rightarrow S_1$ transition. The CD spectra of **C**-**(PhPy)**$_4$ also contain a high-intensity negative band around 4.25 eV along with another peak of a little lower intensity around 4.5 eV. For **A** and **B**-**(PhPy)**$_4$, no noticeable change is observed in CD spectra, shown in Figure A3. In the case of **(PhPy)**$_5$, in addition to conformer **C**, conformer **B** also shows high-intensity CD bands, whereas conformer **A** shows considerably-lower intensity CD bands. In each conformer, two CD bands are observed. For **A**, the two negative CD bands are observed at 4.13 and 4.52 eV, respectively. The highest peak of these two bands arises due to $S_0 \rightarrow S_2$ and $S_0 \rightarrow S_7$, respectively. In the case of **B**, two CD bands, one positive and the other negative, are observed at 4.12 and 4.26 eV, respectively. The highest peaks of these positive and negative CD bands are due to the $S_0 \rightarrow S_1$ and $S_0 \rightarrow S_2$ transitions, respectively. Conformer **C** also shows one positive band and one negative band, but here the negative band is lower in energy than the positive one. The highest peak of the negative band is caused by $S_0 \rightarrow S_1$ transition, whereas for the positive band, it arises due to the $S_0 \rightarrow S_{10}$ transition.

The chirality of a CD active system is quantified in terms of the dissymmetry factor (g_{CD}). The g_{CD} is calculated as[172,173]

$$g_{\mathrm{CD}} = \frac{4 \times R}{D+G} = \frac{4|\boldsymbol{\mu_e}||\boldsymbol{m_e}|\cos\theta}{|\boldsymbol{\mu_e}|^2 + |\boldsymbol{m_e}|^2}. \tag{3.1}$$

where, R, D, and G are the rotatory strength, strength of the electric transition dipole moment (ETDM), and strength of the magnetic transition dipole moment (MTDM), respectively. The ETDM and MTDM vectors are denoted as $\boldsymbol{\mu}$ and $\boldsymbol{m}$ in Eq.3.1, respectively, and θ is the angle between $\boldsymbol{\mu}$ and $\boldsymbol{m}$. In general, in the case of organic molecules, the value of $|\boldsymbol{m}|$ is very small as compared to $|\boldsymbol{\mu}|$, which is responsible for small values of g_{CD}.[174,175] The values of R, $|\boldsymbol{\mu}|$, $|\boldsymbol{m}|$, cos θ, g_{CD}, and $|\boldsymbol{m}|/|\boldsymbol{\mu}|$ corresponding to ten electronic excitations of pentamers for three conformers are tabulated in Table A5. In conformer **A**, the values of $|\boldsymbol{\mu}|$ for the highest peaks of two negative bands are 205.41 and 195.54 esu·cm, respectively, while the $|\boldsymbol{m}|$ values are 0.45 and 0.83 erg·G^{-1}, respectively. In this case, smaller $|\boldsymbol{m}|/|\boldsymbol{\mu}|$ values (0.002 and 0.004, respectively) result in small values of g_{CD} (-0.008 and -0.005, respectively). It is to be noted that while the angle between the two vectors is $\approx 171^\circ$ for the lower energy peak, it is 109° for the second peak. For conformer **B**, the highest peak of the positive band has $|\boldsymbol{\mu}|$ and $|\boldsymbol{m}|$ values of 314.4 and 12.17, respectively. In this case, a large value of 0.039 for $|\boldsymbol{m}|/|\boldsymbol{\mu}|$ results in a large g_{CD} value. However, a small value of $|\boldsymbol{m}|/|\boldsymbol{\mu}|$(0.001) for the highest peak in the negative band is responsible for the small value of g_{CD}(-0.002). In the case of **C**, the $|\boldsymbol{\mu}|$ and $|\boldsymbol{m}|$ values corresponding to the peak at 4.13 eV are 178.61 esu·cm and 4.61 erg·G^{-1}, respectively. Both of these values are comparatively smaller than the corresponding values for the first peak of conformer **B**, and this is responsible for a comparatively lower intensity CD band for conformer **C** than in **B**. In this case, a large g_{CD} value of -0.070 is obtained, which is due to the larger value of $|\boldsymbol{m}|/|\boldsymbol{\mu}|$. The peak at 4.41 eV for conformer **C** has a $|\boldsymbol{\mu}|$ value of 228.32 esu·cm and a $|\boldsymbol{m}|$ value of 0.82 erg·G^{-1}. Although the value of cos θ for this peak is 0.924, a small value of 0.004 for $|\boldsymbol{m}|/|\boldsymbol{\mu}|$ produces a g_{CD} value of 0.013.

TABLE 3.4: Values of ω_{CT}, d_{exc} (in Å), and PR_{NTO} Calculated at the RI-ADC(2)/def2-TZVP Level for **(PhPy)**$_5$ Conformers **A**, **B**, and **C**

	A			**B**			**C**		
State	ω_{CT}	d_{exc}	PR_{NTO}	ω_{CT}	d_{exc}	PR_{NTO}	ω_{CT}	d_{exc}	PR_{NTO}
S_1	0.47	6.22	1.70	0.43	5.17	2.68	0.53	5.12	2.51
S_2	0.44	6.00	2.26	0.48	5.69	2.31	0.59	5.35	3.10
S_3	0.50	7.20	2.70	0.49	5.68	2.60	0.60	5.43	2.90
S_4	0.36	6.67	1.10	0.55	6.26	3.14	0.58	5.20	1.80
S_5	0.37	6.82	2.11	0.56	6.38	2.81	0.52	4.63	2.16

3.3.2.3 Excited State Properties

As mentioned in previous sections, the UV and CD spectra of the oligomers of three conformers of **PhPy** are different from each other. This implies that the excited state properties are also different in the three conformers. For excited-state characterization, we have considered only **(PhPy)**$_5$ of all the studied conformers and their lowest five excited states.

The values of ω_{CT}, d_{exc}, and PR_{NTO} obtained at the RI-ADC(2)/def2-TZVP level are tabulated in Table 3.4. From Table 3.4, it is observed that the ω_{CT} values of the three lowest excited states of the three conformers are close to each other. It is also observed that the d_{exc} values in **A**-**(PhPy)**$_5$ are somewhat larger than those in the other two conformers. It is to be noted that the typical trend of an increase in the d_{exc} value with increasing ω_{CT} value is not maintained for a few cases. The ω_{CT} values of the S_1 state of three conformers **A**, **B**, and **C** are 0.47, 0.43, and 0.53, respectively. These values indicate that S_1 states are partially CT states. The d_{exc} values of this state lie between 5.12 and 6.22 Å, which corresponds well with the ω_{CT} values. The PR_{NTO} values tabulated in Table 3.4 suggest that two sets of NTOs are required to describe the S_1 states of **A** and **C**, whereas three sets of NTOs are required in the case of **B**. The NTOs involved in this state are shown at the top of Figure 3.8. Considering the sets of NTOs with the largest eigenvalues, it is clearly seen that the electron and hole densities in cases of **A** and **B** are spread over the rings in the middle of the chains. On the other hand, in **C**, the electron and hole are spread mainly in the regions of overlap. In these cases, a partial separation of electron and hole is seen, which makes this state a partial CT state. All the transitions shown in Figure 3.8 are identified as $\pi \rightarrow \pi^\star$ transitions.

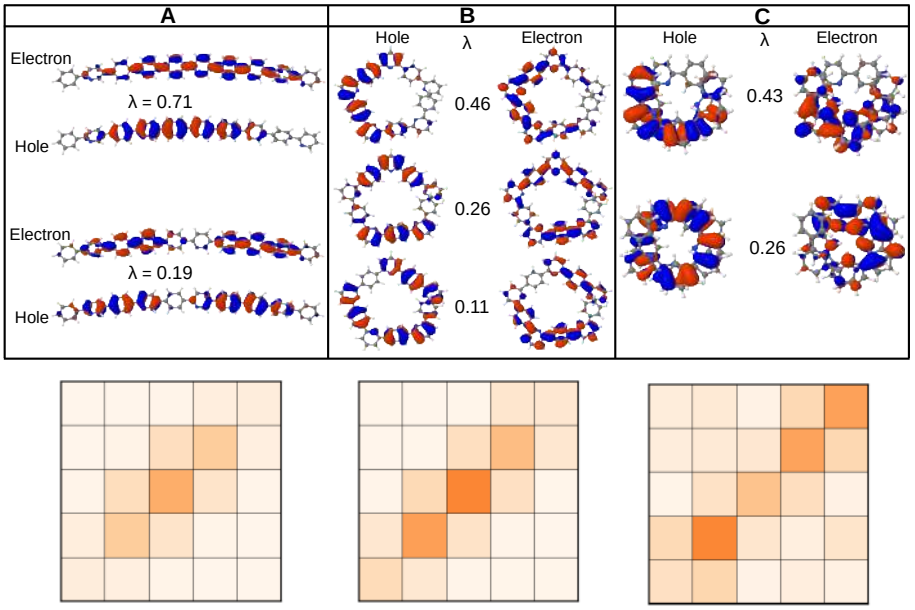

FIGURE 3.8: Natural transition orbitals (top) and electron-hole correlation plots (bottom) correspond to the S_1 state of $(\mathbf{PhPy})_5$ for the three different conformers. The eigenvalue λ indicates the pair's contribution to the excitation.

In addition to the above descriptors, electron-hole (e-h) correlation plots are also considered for analysis of the excited state. Each **PhPy** unit is considered as a fragment; therefore, $(\mathbf{PhPy})_5$ consists of five fragments and the e-h correlation diagram shows a 5×5 matrix. While the position of the electron is along the vertical axis in these e-h correlation plots, the hole position is along the horizontal axis. The diagonal width signifies the extension of the local exciton, whereas the off-diagonal width represents the extent of CT between the fragments. The e-h correlation plots for the S_1 state are shown in the bottom panel of Figure 3.8. These plots confirm the results predicted by the ω_{CT} and d_{exc} values, and NTOs. The plots for **A** and **B** show large diagonal widths spread over the rings in the middle with a small off-diagonal width, responsible for partial CT. The e-h correlation plot in conformer **C** also shows a large diagonal width; however, the terminal rings are involved in this case. Similarly, the off-diagonal squares are comparatively more intense than those in **A** and **B**, in accordance with a slightly larger ω_{CT} value of 0.53.

The ω_{CT} values of S_2 and S_3 states of all of the conformers are close to each other, as was the case for S_1. The ω_{CT} values for these states range from 0.44 to 0.60. The NTOs involved in these states are shown in Figure A4. These NTOs indicate a partial

separation of the electron and hole in **A** and **B**. However, in the case of **C**, a little larger separation of electron and hole is observed which is reflected in ω_{CT} values of 0.59 and 0.60 for S_2 and S_3 states, respectively. The *e-h* plots also support these results by showing slightly intense off-diagonal widths in the case of **C** shown in Figure A5. While the ω_{CT} values for the S_1, S_2, and S_3 states of the three conformers are close to each other, noticeable differences in the ω_{CT} values are observed for the S_4 and S_5 states. The ω_{CT} values of these states in the case of **A** are comparatively smaller (ω_{CT} values for S_4 and S_5 states are 0.36 and 0.37, respectively) than the values in the other two conformers. The *e-h* correlation plots and NTOs also support these results shown in Figures A5 and A6, respectively.

3.4 Conclusion

A comparison of electronic, optical, and excited state properties between three different conformers for 2-Phenylpyridine oligomers is reported in this work. Results are obtained at the RI-ADC(2)/def2-TZVP level of theory. Among the three conformers, conformers **B** and **C** form helical structures at n=5 and n=3, respectively, whereas the conformer **A** has linear geometries for each oligomer. The UV and CD spectra of these three conformers differ. Absorption bands of each oligomer of conformer **A** are red-shifted with respect to those of conformers **B** and **C**. In the case of **A**, the intensity of UV bands is much larger as compared to **B** and **C**, in each oligomer. The helical structures of conformers **B** and **C** exhibit strong CD bands. Excited state characterization of pentamers of the three conformers is also carried out by using three descriptors. From the results, it is found that ω_{CT} values corresponding to the first five excited states of each conformer are in the 0.36-0.60 range, implying partial CT character for each state. However, the ω_{CT} values of most of the excited states of **C** are a little larger as compared to those of **A** and **C**. These results are confirmed by analyzing the NTOs and *e-h* correlation plots. In the future, we aim to report the effect of the inclusion of explicit solvent molecules on the absorption and emission properties of these systems, and such studies are in progress.

Chapter 4

Conformation-driven (de)localization of exciton in 2-Phenylpyridine oligomers: non-adiabatic surface hopping dynamics

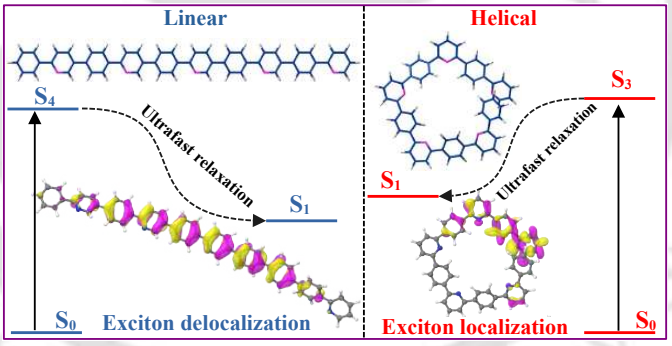

We report on non-adiabatic surface hopping dynamics of exciton localization and delocalization processes in two 2-Phenylpyridine oligomers, one linear ((**PhPy**)$_5$-**A**) and another helical ((**PhPy**)$_5$-**B**). Upon photo-excitation, the two conformers undergo ultrafast internal conversion within 10-100 fs from the high-energy excited state S_4/S_3 to the lowest energy S_1 state. The excited state relaxation results in a delocalization of the exciton over multiple monomeric units in the linear conformer (**PhPy**)$_5$-**A**, while the exciton is localized over a single monomeric unit in the helical conformer (**PhPy**)$_5$-**B**. Reproduced from "*Chem. Commun.*, **2026**, 62, 5447-5451" with permission from ROYAL SOCIETY OF CHEMISTRY.

4.1 Introduction

Modeling the photo-induced processes, such as charge and energy transfer, charge separation and recombination, localization and delocalization of excitons, etc.,[7,176–179] poses significant challenges, as it involves calculating the energies of multiple electronic states and the non-adiabatic couplings between them. In this regard, trajectory-based quantum-classical methods, such as Ehrenfest dynamics and trajectory surface hopping (TSH) dynamics,[134,180] have been useful for addressing the above issue. The TSH is the most widely used method for simulating non-adiabatic dynamics, due to its simplicity, practicality, and scalability.[135] The method requires the calculation of electronic energies, gradients, and couplings between excited states on-the-fly, which is computationally very intensive for larger conjugated systems, even when employing commonly used time-dependent density functional theory (TD-DFT) methods. In recent times, many semiempirical quantum methodologies have been developed to alleviate the problem of resources and time for larger systems.[10,52,181,182] In this context, the semiempirical time-dependent density functional tight binding (TD-DFTB) method, which is analogous to TD-DFT but employs parameterized integrals with smaller basis sets, has also become very useful.[132] In the past few years, photo-induced dynamics employing the TSH with TD-DFTB have been studied for a large number of conjugated systems, including oligomers of phenylenes and acene derivatives.[183–187]

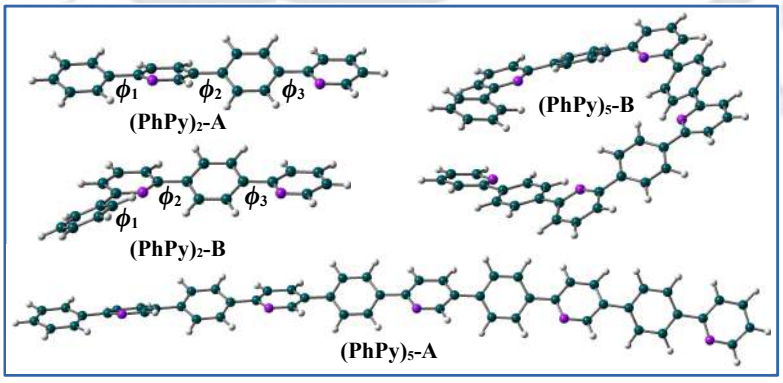

FIGURE 4.1: Ground state optimized geometries of dimers and pentamers of conformers **A** and **B** obtained at the B3LYP-D3BJ/def2-TZVP level.

Oligophenylene and its conformational isomers, such as *ortho*, *meta*, and *para*-oligophenylene, have long been studied due to their interesting optical and electronic properties.[13,43–46]

However, recent studies have shown that the presence of electron-withdrawing pyridine rings in oligomers results in significant alterations in the electrochemical and optical properties compared to the homo-oligomeric forms.[151,188–190] This suggests that the introduction of pyridine rings into oligophenylenes may also lead to significant changes in their electronic and optical properties. In this work, we have considered two different conformers **A** and **B** of oligomers of 2-Phenylpyridine (**PhPy**) shown in Figure 4.1, to investigate how the excited states evolve after photoexcitation. This follows our previous study on the oligomers of **PhPy**[191] which discussed the static excited state properties of three different conformers of oligomers. In conformer **A**, the oligomers are formed by connecting the ***para-*** position of the phenylene ring of one **PhPy** unit with the ***meta-*** position of the pyridine ring of another **PhPy** unit. On the other hand, the oligomers of conformer **B** are formed by connecting the ***para-*** and ***ortho-*** positions of phenylene and pyridine rings of two different **PhPy** units, respectively. Conformer **A** remains linear as we move from **(PhPy)**$_2$ to **(PhPy)**$_5$, while conformer **B** adopts a helical-like structure for **(PhPy)**$_5$ (Figure 4.1). The TSH dynamics were carried out in combination with the TD-DFTB method. In addition to TD-DFTB, the vertical excitation energies (E_g) are also calculated at the long-range corrected (LC) version of TD-DFTB (LC-TD-DFTB),[192,193] and these results are compared with the results obtained at the algebraic diagrammatic construction scheme to the second order (ADC(2)) level.[119–121]

4.2 Computational Details

The TD-DFTB and LC-TD-DFTB calculations are carried out using the ob2 Slater-Koster file[194] utilizing the DFTB+[128] software. The RI-ADC(2) calculations are performed using the def2-SV(P) basis set in conjunction with the resolution of identity (RI) approximation[195]. Turbomole V7.2[196] software is used for the RI-ADC(2) calculations. For the excited-state dynamics simulation, initially, we have generated 500 sets of initial conditions (ICs) using the harmonic-oscillator Wigner distribution.[197] From these initial 500 sets, sets of ICs were selected starting from the bright states by applying a narrow energy window shown in Figures B1 and B2. The following bright excited states are considered for the two conformers while selecting the ICs: S_1, S_3 in **(PhPy)**$_2$-**A**, S_1, S_3,

and S_7 in **(PhPy)**$_2$-**B**, S_1, S_4, and S_6 in **(PhPy)**$_5$-**A**, and S_3, and S_6 states in **(PhPy)**$_5$-**B**. In these figures, the bar plots are for the optimized geometries, and the sticks are for the 500 ICs. In **(PhPy)**$_2$-**A**, the 4.40±0.20 eV energy window produces 89 ICs in the S_3 state, and the 4.25±0.20 eV energy window produces 47 ICs in the S_1 state. In **(PhPy)**$_2$-**B**, the energy window 4.96±0.20 eV produces 39 ICs in the S_7 state, 4.55±0.20 eV produces 65 ICs in the S_3 state, and 4.30±0.20 eV produces 27 ICs. In the case of dimers, we only discuss the dynamics results starting from the S_3 states. Similarly, in the case of pentamers, the dynamics results, which started from the S_4 (**(PhPy)**$_5$-**A**) and S_3(**(PhPy)**$_5$-**B**) states, are discussed. The trajectory surface hopping (TSH) dynamics were carried out utilizing Newton-X[198] software. For the 1TDM analysis, each monomeric unit (**PhPy** unit) is considered as a one fragment; therefore, **(PhPy)**$_2$ and **(PhPy)**$_5$ have two and five fragments, respectively. TheoDORE 3.0 software package[170] was used for carrying out the excitonic analysis.

4.3 Results & Discussion

4.3.1 Excited state dynamics

The E_gs and the corresponding oscillator strengths (f_{osc}) for the first ten excited states calculated on the previously optimized ground state geometries[191] are tabulated in Table B1. In the case of **A**, the TD-DFTB results show a good match with the RI-ADC(2) results in both dimer and pentamer. The E_g values for the dimer obtained at the TD-DFTB level differ by 0.06 to 0.27 eV from the RI-ADC(2) results, while this energy difference is slightly higher in the pentamer (0.47-0.70 eV). Both the TD-DFTB and RI-ADC(2) results predict a bright S_1 state with considerable f_{osc} value in the dimer and pentamer; however, the LC-TD-DFTB predicts a small f_{osc} value for the S_1 state in the dimer (see Table B1). In **B**, though E_g values for the first ten excited states found using TD-DFTB are close to those observed in the RI-ADC(2) results, the values for f_{osc} differ from the RI-ADC(2) results. For example, in the dimer, S_3 is the brightest state in TD-DFTB results, whereas the RI-ADC(2) results indicate S_1 be the brightest state with an f_{osc} value of 0.882. For the pentamer, the RI-ADC(2) results show the highest

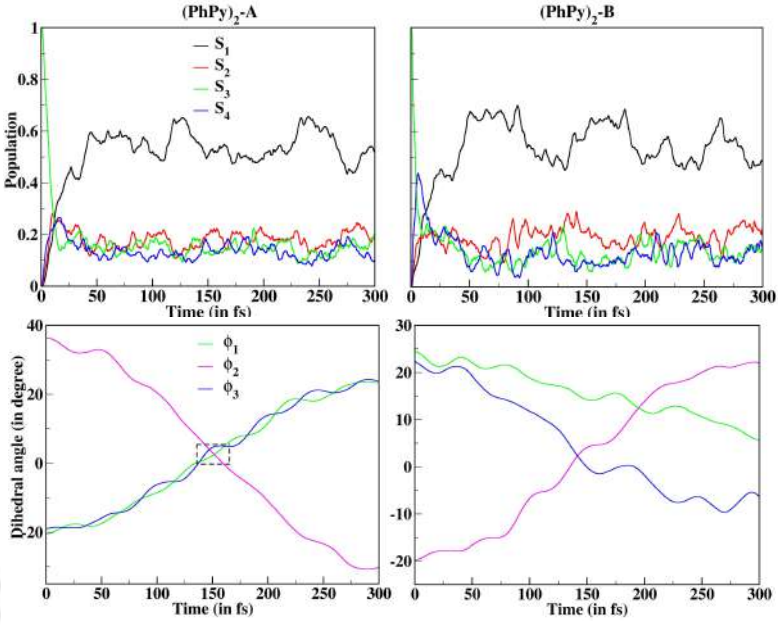

FIGURE 4.2: Average populations of first four excited states (top panel), and average dihedral angles (bottom panel) vs time for dimers.

f_{osc} value of 1.465 for the S_2 state, whereas the TD-DFTB results show small f_{osc} values for all excited states. A similar observation is also noted in the case of LC-TD-DFTB results.

The photo-induced dynamics of the two dimers starting from the S_3 bright states are shown in Figure 4.2(top panel). As the figure shows, conformer **A** undergoes ultrafast internal conversion within 10 fs from initially populated S_3 via the S_2 state to the S_1 state. Conformer **B** shows slightly different behavior as the population of the initially populated excited state (i.e., S_3) gets transferred to a higher excited state (S_4) at first, before relaxing to the S_1 state. This is due to the strong non-adiabatic coupling between the S_3 and S_4 states in that region. For both conformers, after the initial 50 fs, 60% of the total population remains in S_1 and the remaining 40% is shared among the S_2, S_3, and S_4 states, within the considered time frame. The bottom panel of Figure 4.2 shows the evolution of average dihedral angles ϕ_1, ϕ_2, and ϕ_3 (indicated in Figure 4.1) of the two conformers with time. For **A**, at t=0, the molecule has a non-planar backbone with average ϕ_1, ϕ_2, and ϕ_3 values around -20°, 36°, and -19°, respectively. As the time progresses, the ϕ values decrease, and around 150 fs, the values of all three dihedral angles become ≈0°. In the case of **B**, the dynamics is started again with a non-planar geometry (with ϕ_1, ϕ_2, and ϕ_3 values ≈24°, -20°, and 22°, respectively). However, the

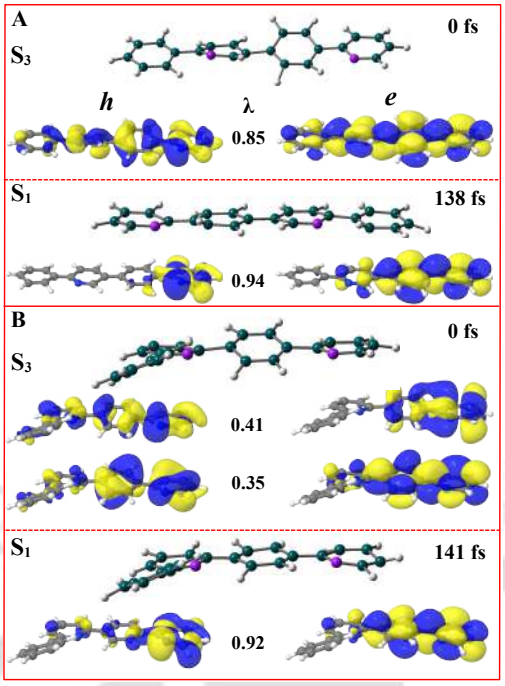

FIGURE 4.3: Geometries and NTOs involved in the current states of a single representative trajectory of **(PhPy)**$_2$-**A** and **B** obtained at the RI-ADC(2) level.

geometry never reaches planarity during the entire time, although the values of ϕ_2 and ϕ_3 become close to 0° around 140 fs.

To gain insight into the nature of excited states during structural evolution, we performed an excitonic analysis of the geometries at various time frames extracted from a single representative trajectory. The ω_{CT} values, *e*-*h* correlation plots, and the NTOs have been considered for describing the characters of the excited states. The values of E_g, f_{osc}, and ω_{CT} corresponding to the current state at two different time frames for the **(PhPy)**$_2$-**A** and **B** are tabulated in Table B2. A closer look at the ω_{CT} values of the first ten excited states, including the current state, indicates that the ω_{CT} values calculated at the TD-DFTB level are somewhat larger compared to those obtained at the RI-ADC(2) level. It is expected as the conventional DFTB is parameterized for the generalized-gradient approximation (GGA) functional, which has a problem in describing the CT character.[199] Considering this, the characterization of the excited state is performed considering the RI-ADC(2) results.

At 0 fs, the RI-ADC(2) results show that the current states (i.e., S_3) of **(PhPy)**$_2$-**A** and **B** have ω_{CT} values of 0.16 and 0.10 (see Table B2), respectively, indicating their LE

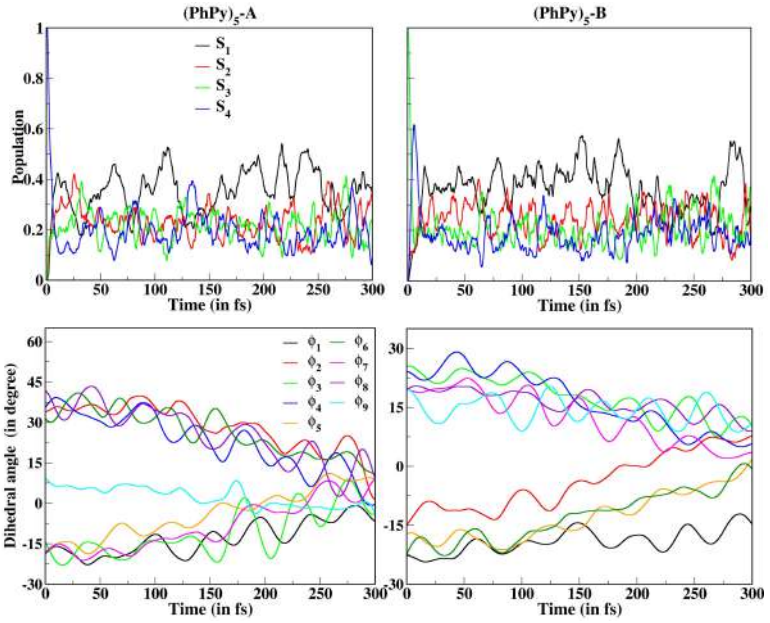

FIGURE 4.4: Average populations of first four excited states (top panel), and average dihedral angles (bottom panel) vs time for pentamers.

characters. The NTOs involved in these states are depicted in Figure 4.3. For **A**, at 0 fs, both the h and the e orbitals are delocalized over the entire dimer backbone, showing the delocalized LE character of this state. When the conformer **A** becomes planar at 138 fs, the current state (S_1) still exhibits a small ω_{CT} value of 0.07. However, the NTOs reveal that the h and e orbitals are now localized on a single monomeric unit, indicating the localization of the exciton during structural relaxation. At 0 fs, the e-h correlation plot (Figure B3) shows contributions from both the diagonal blocks, whereas at 138 fs, only one diagonal block contributes, highlighting the shift from delocalized to localized LE characteristics of the current states. In contrast, for conformer **B**, both at 0 and 141 fs, the h and e orbitals are mostly confined to the same monomeric unit (Figure 4.3), indicating the localized LE characters of the states. The same is observed from the e-h correlation plots (Figure B3), where single intense diagonal blocks are observed at both 0 and 141 fs.

The excited-state dynamics results for the pentamers are shown in Figure 4.4. The photo-induced dynamics of **A** and **B** start from S_4 and S_3 bright states, respectively. As in the dimers, here too, both the conformers undergo ultrafast internal conversion within 10 fs after photo-excitation from the initial excited states (S_4 or S_3) to the S_1

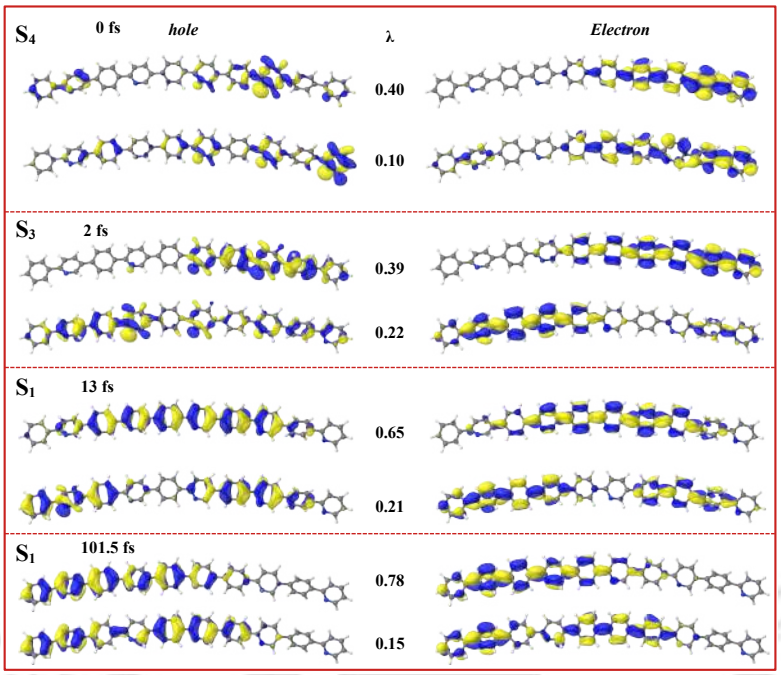

FIGURE 4.5: NTOs involved in the current state of a selected trajectory at different times for **(PhPy)**$_5$-**A** obtained at the RI-ADC(2) level.

states. Beyond this, constant fluctuations in the electronic population are observed for both conformers. This population fluctuation is primarily due to the proximity of the energies of adjacent electronic states in the pentamers. The energies for the first four excited states of a single representative trajectory for **(PhPy)**$_5$-**A** and **B** are presented in Figures B4 and B5, respectively. The figures show that the energy difference between the adjacent excited states is so small that the four states appear to almost coincide. The evolution of the average dihedral angles (ϕ_1-ϕ_9) for the two conformers is also depicted in Figure 4.4 (bottom panel). In conformer **A**, the molecule initially displays a non-planar geometry, with the angles ϕ_1, ϕ_3, ϕ_5, and ϕ_7 ranging from -15° to -20°, while ϕ_2, ϕ_4, ϕ_6, and ϕ_8 are approximately between 30° to 45°. On the other hand, the value of the terminal dihedral angle ϕ_9 is around 8°. As the dynamics progresses, all the dihedral angles tend to converge towards 0°. In **(PhPy)**$_5$-**B**, on the other hand, the value of ϕ_1 remains $\approx$ 20° over the whole 300 fs range, while other angles approach 0°.

The values of ω_{CT} corresponding to the current states at different times during the excited state relaxation process for **(PhPy)**$_5$-**A** and **B** are tabulated in Tables B3 and B4, respectively. As expected, the ω_{CT} values corresponding to the first ten excited states, including the current states, calculated at the TD-DFTB level, are significantly

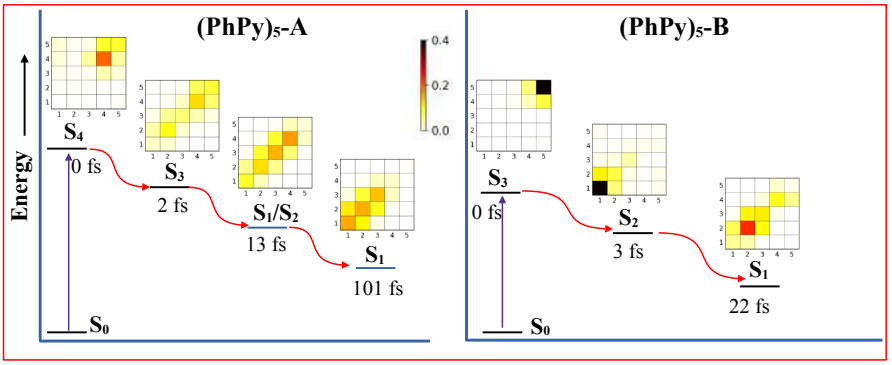

FIGURE 4.6: Schematic representation of the excited states relaxation process in pentamers of conformers **A** and **B**.

larger than those obtained at the RI-ADC(2) level (see Tables B3 and B4). Therefore, we focus solely on the RI-ADC(2) results. For **(PhPy)**$_5$**-A**, as shown in Table B3, the ω_{CT} values for the current states at times 0 fs (S_4), 2 fs (S_3), 13 fs (S_1), and 101.5 fs (S_1) are 0.51, 0.48, 0.44, and 0.51, respectively. Notably, at 13 fs, the f_{osc} values for the S_2 and S_1 states (Table B3) indicate that the energetic order of these states is reversed in the RI-ADC(2) results compared to the TD-DFT results. The NTOs corresponding to the current states during excited state relaxation are presented in Figure 4.5. At 0 fs, the two pairs of NTOs suggest that both the *e* and *h* orbitals are localized on the terminal **PhPy** units, indicating a localized LE state. The *e*-*h* correlation plot shown in Figure B6 supports this observation, showing a single intense diagonal block that signifies the localized LE state. As the dynamics progress, the *h* and *e* orbitals begin to delocalize across multiple **PhPy** units. At 2 fs, the *h* and *e* orbitals are delocalized over one side of the pentamer unit; at 13 fs, those are delocalized over the middle **PhPy** units; and at 101.5 fs, they are delocalized over the left-side **PhPy** units. The *e*-*h* correlation plots further corroborate these findings (see Figure B6). For **(PhPy)**$_5$**-B**, the excited state results are different from the results of **(PhPy)**$_5$**-A**. In this case, the NTOs corresponding to the current states indicate that the *h* and *e* orbitals are confined over a single monomeric unit, but their locations are different at different times, as shown in Figure B7. The *e*-*h* correlation plots also suggest the same, as only a single diagonal block contributes to the electronic excitation shown in Figure B8.

The overall excited state relaxation process in **(PhPy)**$_5$**-A** and **B** is presented in Figure 4.6. In **A**, after photoexcitation, the excited state relaxation process proceeds

via delocalization of the exciton from an initially localized LE state S_4 to the lowest energy excited state S_1. As the figure shows, at 0 fs, the S_4 state is localized on a single **PhPy** unit indicated by an orange block at the top right. When the system relaxes to S_3 from S_4 state at 2 fs, the exciton starts to delocalize over the right-side **PhPy** units, indicated by a large diagonal width from the top right to the middle blocks. At 13 fs, the exciton is delocalized over the middle three blocks, and finally, when the molecule relaxes to the lowest energy S_1 state, the exciton gets delocalized over the bottom left **PhPy** units. In contrast to **A**, the exciton is localized in a single **PhPy** unit during excited state relaxation in **B**. Initially at 0 fs, the exciton is localized over one of the terminal **PhPy** unit, indicated by an intense diagonal block at the top right. Because of its helical structure, the localized exciton is transferred from one terminal **PhPy** unit to another terminal **PhPy** unit during S_3-S_2 relaxation at 3 fs (indicated by a bottom left intense block). Relaxation to the S_1 results in shifting of the localized exciton from the terminal **PhPy** unit to the adjacent **PhPy** unit.

4.4 Conclusion

In this work, we aimed to understand the excited-state dynamics of two different conformers, **A** and **B**, of **PhPy** oligomers. On-the-fly non-adiabatic surface-hopping dynamics were performed using TD-DFTB. In dimers, excited state relaxation leads to a planar structure in conformer **A**, while conformer **B** remains non-planar for up to 300 fs. In **(PhPy)**$_2$-**A**, structural relaxation results in localization of the exciton in the S_1 state from a delocalized LE state S_3. Meanwhile, in conformer **B**, the exciton stays localized throughout the excited relaxation process. As the chain length increases, the linear conformer **(PhPy)**$_5$-**A** shows exciton delocalization across multiple monomeric units during relaxation from the high-energy excited state (S_4) to the lowest energy excited state (S_1). In comparison, the helical conformer **(PhPy)**$_5$-**B** exhibits a movement of the localized exciton from one monomeric unit to another during the relaxation from the S_3 to S_1 states. The delocalization of the exciton in the linear conformer indicates that this conformer may act as a better exciton transport material over the helical form in the field of organic electronics. Our present results could be useful in understanding the exciton

(de)localization processes in similar oligomers and polymers, and in designing devices with improved performances.

Chapter 5

Contrasting the excited state properties of different conformers of *trans-* and *cis-* 2, 2′-Bipyridine oligomers in the gas phase

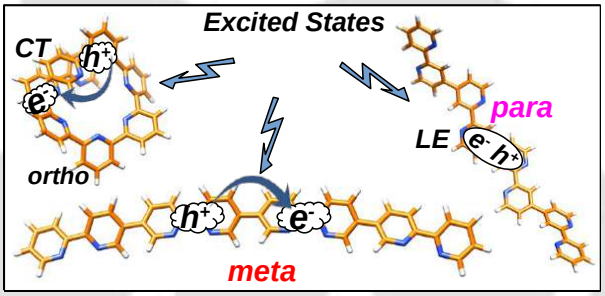

In this chapter, we present conformation-dependent photo-physical and excited state properties of ***trans***- and ***cis***-Bipyridine oligomers at the RI-ADC(2)/def2-TZVPD level. The UV spectra of oligomers of ***m-*** conformer show high-intensity and red-shifted UV bands compared to ***o-*** and ***p-*** oligomers. The CD spectra of ***p-*** oligomers show intense CD bands compared to ***o-*** and ***p-*** oligomers in the case of ***trans***- structures. In contrast, oligomers of each conformer of ***cis***- structures show high-intensity CD bands. The characterization of the first five excited states in $\mathbf{(BPY)}_2$ and $\mathbf{(BPY)}_4$ reveals that these are mainly LE states in dimer (ω_{CT}=0.06-0.32), whereas for tetramer, the ω_{CT} values range from 0.17 to 0.53, indicating the possibility of partial CT characteristics of these states. These observations are also explained using the NTOs and *e-h* correlation plots. Reproduced from "*Physical Chemistry Chemical Physics*, **2024**, 26, 2646-2656" with permission from ROYAL SOCIETY OF CHEMISTRY.

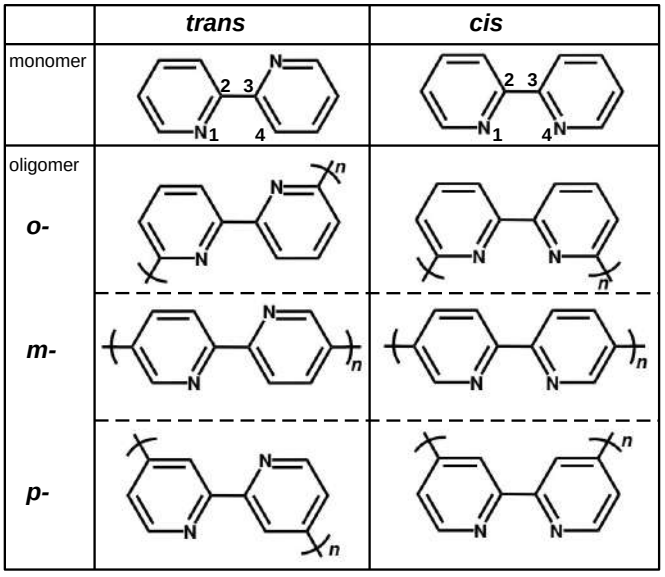

FIGURE 5.1: A schematic representation of the repeating units for three possible conformational isomers of ***trans*** and ***cis*-BPY** systems, denoted as ***o-***, ***m-***, and ***p-***, where n=1-4.

5.1 Introduction

Polypyridine (PPY) is one of the simplest conjugated polymers used in organic electronics,[200–207] in particular, it is used as an efficient electron-transporting material in OLEDs.[203–205] Some of the electrochemical studies reveal that PPY can also act as a suitable anode material in rechargeable batteries.[206,207] The majority of these applications implicitly imply the linear conformer of PPY, and it seems to reason that other possible conformers may function differently in such applications. Recently, Repp and coworkers synthesized *all-trans* and *all-cis* oligomers of pyridine having planar and cyclic geometries, respectively.[208] These results hint that different conformers are possible for PPY. In the case of PPY, many computational studies have also explored the electronic and photo-physical properties of PPY oligomers.[207–212] However, these studies typically focus on the linear conformers of PPY oligomers. In this work, we explore the underlying differences in photophysical and excited state properties between three different conformers of ***trans***- and ***cis***-2,2′-Bipyridine (**BPY**) oligomers. As shown schematically in Figure 3.1, three different conformers are constructed by connecting the repeating units either through *ortho*- (***o-***), *meta*- (***m-***), or *para*- (***p-***) positions. Oligomers up to only tetramers are considered in our study.

5.2 Computational Details

Ground state equilibrium geometries and the corresponding harmonic vibrational frequencies of ***o-***, ***m-***, and ***p-*** conformers of ***trans-*** and ***cis-*****BPY** oligomers were computed at the DFT level. In DFT computations, the B3LYP[88] functional with the def2-SVPD[213] basis set was employed. Grimme's D3 empirical dispersion with Becke and Johnson damping[163–165] was included in all the DFT optimizations. The geometries of all the oligomers were constrained to the C_2 point group.

Excited state studies were performed at ADC(2) level of theory, and two different DFT functionals, B3LYP and CAM-B3LYP.[97] For ADC(2), the resolution-of-identity (RI) approximation was used. At first, vertical excitation energy (E_g) calculations for ***trans-*****BPY** were carried out at RI-ADC(2) level using def2-SVPD and def2-TZVPD[213] basis sets in the gas phase. The excitation energies of ***trans-*****BPY** were also computed using the domain-based local pair natural orbital similarity transformation-based equation of motion coupled cluster singles and doubles (DLPNO-STEOM-CCSD) method. The E_g values for the oligomers were calculated using the def2-TZVPD basis set in the gas phase. While the Turbomole V7.2 software package[196] was used in all the ADC(2) calculations, DLPNO-STEOM-CCSD calculations were carried out using the ORCA software.[214] All DFT computations were performed using the Gaussian 16 computational package.[166]

5.3 Results and Discussion

5.3.1 Geometries

Literature[215] shows that the ***trans-*****BPY** has a planar geometry with a dihedral angle (ϕ) =0° between the two pyridine rings; our ground state result obtained at the B3LYP-D3/def2-SVPD level also predicts the same. For ***cis-*****BPY**, the reported dihedral angle[210,216,217] varies between 34° and 38°, and our result of ϕ=37° agrees well with the reported results. Optimized structures for dimers of ***o-***, ***m-***, and ***p-*** for possible ***trans-*** and ***cis-*** structures are shown in Figure C1. In the case of ***trans-***, among the

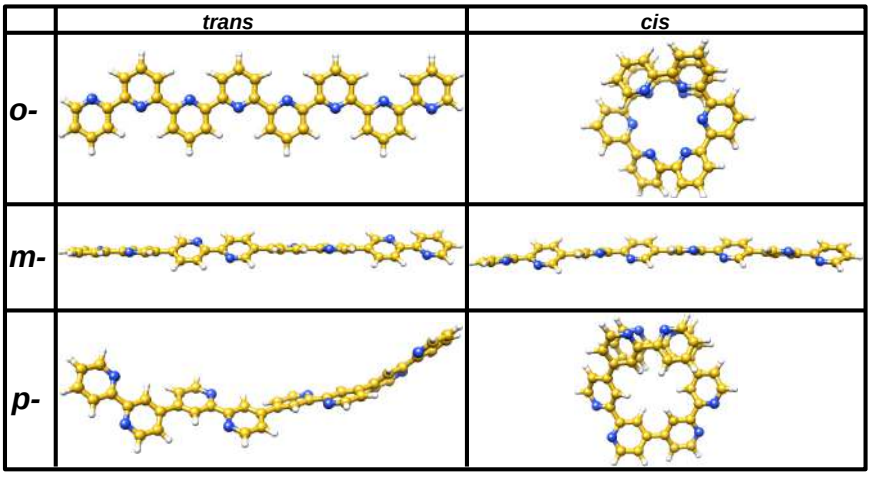

FIGURE 5.2: Optimized geometries of tetramers of ***o-***, ***m-***, and ***p-*** conformers for ***trans***- and ***cis*-BPY** obtained at B3LYP-D3/def2-SVPD level.

three conformers, ***o-*** is the most stable conformer (shown in Table C1) with a planar structure (ϕs are zero, shown in Table C2). In both ***m-*** and ***p-*** isomers, the terminal dihedral angles are almost zero (shown in Table C3). On the other hand, dihedral angles in the middle (ϕ_2) in these two isomers are comparatively large due to the steric hindrance between the nearby hydrogen atoms. In the case of ***cis***, the dimer geometries of ***o-*** and ***p-*** are similar, although the nitrogen atoms are aligned on the inner and outer sides for ***o-*** and ***p-***, respectively. The inter-ring dihedral angles in these two geometries range from 35.7° to 39.6°, as shown in Tables C4-C5. Similar to ***m-trans***- conformer, the ***m-cis***- conformer also shows a linear backbone; however, the dihedral angles are different, as indicated in Table C5.

At n=3, ***cis-o-*** and ***p-*** conformers can form helical and cyclic (cy) structures, whereas only linear- type structures are possible for the ***m-*** conformer. The optimized geometries of these possible structures are shown in Figure C2. For the helical structures, only (P)-type structures are considered. Due to the helical and cyclic geometries, significant changes in dihedral angles are observed compared to their respective dimer geometries, as shown in Tables C4 and C5. In the case of ***trans***-, the geometries of ***o-***, ***m-***, and ***p-*** conformers are similar to their respective dimers, and the dihedral angles also show similar patterns. Figure 5.2 shows the optimized geometries for the tetramers. It is observed that the dihedral angles of ***o-***, ***m-***, and ***p-*** conformers for ***trans***- do not differ much from the corresponding values in dimers and trimers. In contrast, the ***o-*** and ***p-***

conformers for ***cis*** form complete helical structures, while the ***m-*** isomer maintains a linear structure.

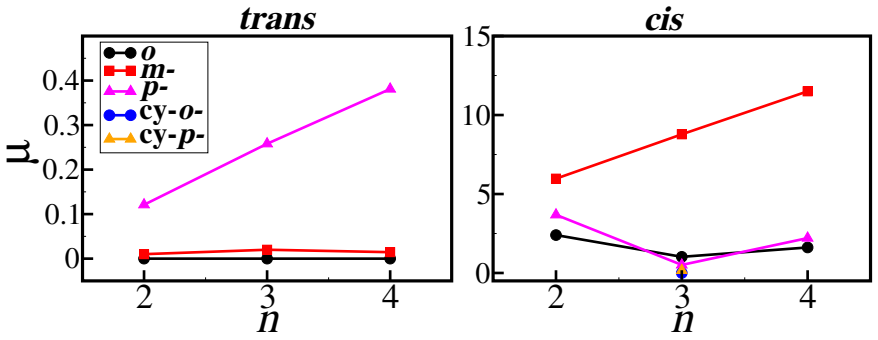

FIGURE 5.3: Variation in ground-state dipole moment ($\boldsymbol{\mu}$) with the oligomer chain length (n) for ***o-***, ***m-***, and ***p-*** conformers of ***trans***- and ***cis*****-BPY** oligomers.

Different conformers of an oligomeric structure also have different dipole moments ($\boldsymbol{\mu}$). Results for our systems are shown in Figure 5.3. In this case, $\boldsymbol{\mu}$ values vary based on the number of nitrogen atoms and orientations of bond dipole moments. As the figure shows, $\boldsymbol{\mu}$ values of all the conformers for ***trans*****-BPY** oligomers are significantly smaller than the ***cis***- counterparts. The $\boldsymbol{\mu}$ values of ***trans***- and ***cis*****-BPY** are 0.00 and 3.10 D, respectively. In the case of ***trans***, flat and planar geometries of ***o-*** oligomers result in the cancellation of oppositely directed bond moments, producing zero $\boldsymbol{\mu}$ value for each. Linear backbone and zero ∠N-C-C-N dihedral angle in each oligomer of ***m-*** conformer leads to zero $\boldsymbol{\mu}$ value. In ***trans***-, only in the case of ***p-*** conformer, $\boldsymbol{\mu}$ value increases with the size of the oligomer, and this is due to the introduction of dihedral angles between the two rings. In ***cis***-, ***o-*** and ***p-*** conformers exhibit a similar pattern; values for dimers are comparatively large, and as soon as a helix (at n=3) is formed, small $\boldsymbol{\mu}$ values are obtained due to the cancellation of oppositely oriented bond moments. Beyond n=3, increase in the number of nitrogen atoms results in an increase in the $\boldsymbol{\mu}$ value. For ***m-***, the $\boldsymbol{\mu}$ value increases linearly with the chain length due to a linear increase in the number of nitrogen atoms.

TABLE 5.1: Vertical excitation energies (E_g in eV) and the corresponding oscillator strengths (f_{osc}) of ***trans*-BPY** using two different basis sets at RI-ADC(2) and at DLPNO-STEOM-CCSD/def2-TZVPD levels. Experimental results (denoted as exptl.) are shown in the last column

	E_g/f_{osc}			
State	def2-SVPD	def2-TZVPD	DLPNO-STEOM-CCSD /def2-TZVPD	exptl.[217]
S_1	4.45/0.002	4.42/0.002	4.47/ 0.003	
S_2	4.84/0.000	4.79/0.000	4.53/ 0.000	
S_3	4.91/0.450	4.83/0.476	4.54/ 0.301	4.44
S_4	4.93/0.000	4.87/0.000	4.78/ 0.000	
S_5	5.04/0.000	5.00/0.000	5.17/ 0.000	
S_6	5.18/0.005	5.15/0.004	5.20/ 0.003	
S_7	5.61/0.277	5.54/0.237	5.42/ 0.334	5.34
S_8	6.32/0.000	6.20/0.000	6.54/0.000	

5.3.2 First vertical excitation energies

The vertical excitation energies (E_g) and corresponding oscillator strengths (f_{osc}) for ***trans*-BPY** obtained at RI-ADC(2) and DLPNO-STEOM-CCSD level are tabulated in Table 5.1. Table 5.1 data shows that the results obtained at RI-ADC(2)/def2-TZVPD level are close to the experimental results and the results obtained at DLPNO-STEOM-CCSD level. The results obtained at both RI-ADC(2) and DLPNO-STEOM-CCSD level indicates that the first and second absorption maxima arise due to $S_0 \rightarrow S_3$ and $S_0 \rightarrow S_7$, respectively. It is worth mentioning here that the mean absolute errors for π-$\pi^\star$ transitions for both DLPNO-STEOM-CCSD and ADC(2) methods are very similar (0.14 and 0.16 eV, respectively) according to the QUEST database.[218] Based on the RI-ADC(2)/def2-TZVPD results, excitation at 4.83 eV(f_{osc}=0.476) is assigned as the first absorption maxima, which is 0.39 eV blue-shifted from the experimental result (4.44 eV). Excitation at 5.54 eV(f_{osc}=0.237) is assigned as the second absorption maxima which is 0.20 eV blue-shifted from the experimental result (5.34 eV). Keeping these results in mind, the E_gs of all the oligomers are calculated at RI-ADC(2)/def2-TZVPD level of theory.

Variation in the optical band gap (i.e., the lowest vertical excitation energy (E_g^1)) and f_{osc} against the oligomer chain length (n) is shown in Figure 5.4. For ***trans*-**, the E_g^1 value shows a small decrease with the chain length for both ***o*-** and ***p*-** conformers. On the other hand, for the ***m*-** isomer, a pronounced decrease in the optical band gap

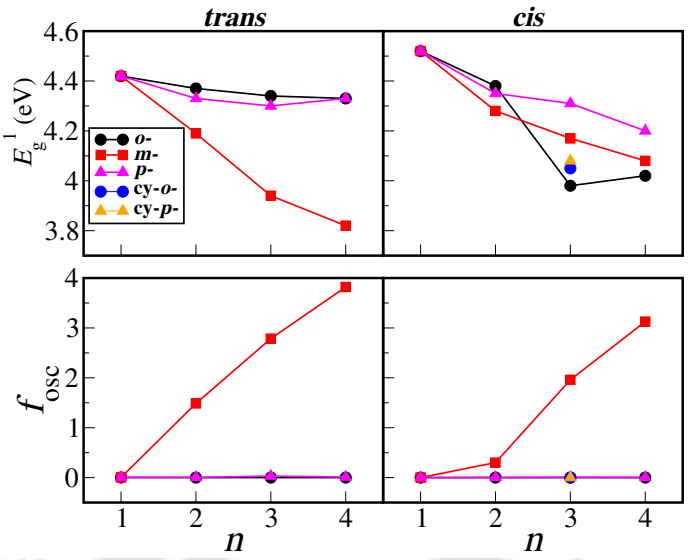

FIGURE 5.4: Variation of the lowest excitation energy (E_g^1 in eV) and the corresponding oscillator strength (f_{osc}) with the oligomer chain length (n) for ***o-***, ***m-***, and ***p-*** conformers for ***trans***- and ***cis*-BPY** oligomers.

is observed. In the case of ***cis***, results are different; a sharp decrease in E_g^1 value is observed for ***m-*** and ***p-*** conformers, whereas in ***o-***, the E_g^1 value decreases till n=3 and then increases for n=4. In both ***trans***- and ***cis***-, f_{osc} values for the $S_0 \rightarrow S_1$ transition are zero for all the oligomer of ***o-*** and ***p-*** conformers. However, for ***m-*** in both cases, the f_{osc} values increase as a function n.

5.3.3 Absorption and CD spectra

Figure 5.5 compares the UV spectra of different conformers. For ***trans***-, UV spectrum of each oligomer of ***m-*** isomer is red-shifted compared to the corresponding oligomers of ***o-*** and ***p-*** structures. In addition, the f_{osc} values for the highest peaks are much larger in the case of ***m-***. Details of the excited states are tabulated in Tables C6-C10. The highest peaks in absorption maxima of all the oligomers of ***m-*** conformer arise due to the $S_0 \rightarrow S_1$ transitions, and these transitions are dominated by H→L excitations, as shown in Table 5.2. In the case of ***o-*** and ***p-***, the absorption spectrum of each oligomer shows more than one significant electronic transition. The dimers of ***o-*** and ***p-*** conformers show three important peaks that arise due to $S_0 \rightarrow S_4$, $S_0 \rightarrow S_7$, and $S_0 \rightarrow S_{15}$ transitions, in each case. For $(\mathbf{BPY})_3$, the absorption spectra of ***o-*** and ***p-*** contain two absorption bands. The highest peak in the lower energy band is due to $S_0 \rightarrow S_8$, whereas for the second

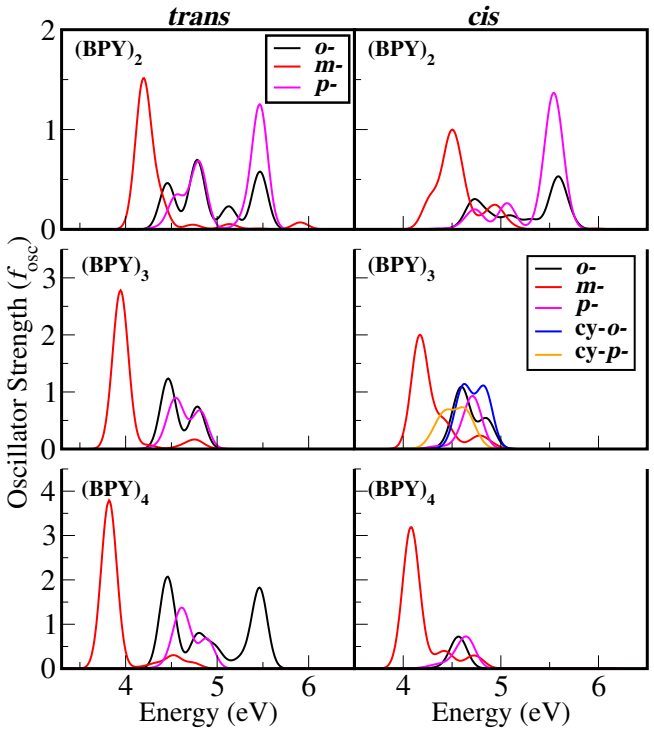

FIGURE 5.5: Simulated UV absorption spectra of ***o-***, ***m-***, and ***p-*** conformers for ***trans*** and ***cis*-BPY** oligomers. The results are obtained at RI-ADC(2)/def2-TZVPD level. In ***cis*-(BPY)$_3$**, f_{osc} values in cases of ***o-***, ***p-***, cy-***o-***, and cy-***p-*** are multiplied by a factor of 3.

bands, the peaks originate due to $S_0 \rightarrow S_{13}$ and $S_0 \rightarrow S_{11}$, for ***o-*** and ***p-***, respectively. At n=4, ***o-*** shows three prominent transitions at 4.46, 4.79, and 5.46 eV with f_{osc} values of 2.060, 0.747, and 1.809, respectively, and these transitions are due to $S_0 \rightarrow S_{8,12,16}$ excitations. Two significant transitions are observed in the case of ***p*-(BPY)$_4$**, one at 4.63 eV (f_{osc}=0.795) and another at 4.89 eV(f_{osc}=0.435). The orbitals involved in the above transitions are not only the HOMO and LUMO; occupied orbitals besides HOMO and unoccupied orbitals besides LUMO are also involved.

TABLE 5.2: Vertical excitation energies (E_g), oscillator strengths (f_{osc}) and orbitals involved in important electronic transitions of three conformers for ***trans***- and ***cis***-**BPY** oligomers up to tetramer. This results are obtained at RI-ADC(2)/def2-TZVPD level

						trans						
		o-				***m-***				***p-***		
oligomer	state	E_g	f_{osc}	configuration	state	E_g	f_{osc}	configuration	state	E_g	f_{osc}	configuration
(BPY)$_2$	$2^1B(S_4)$	4.46	0.460	H→L+6(49%) H→L+2(29%)	$1^1B(S_1)$	4.19	1.487	H→L(74%)	$2^1B(S_4)$	4.55	0.298	H-1→L(44%)
	$4^1B(S_7)$	4.78	0.696	H→L+2(27%) H-1→L(25%)					$4^1B(S_7)$	4.80	0.637	H→L+2(30%) H-1→L+6(26%)
	$8^1B(S_{15})$	5.47	0.580	H-1→L(49%)					$8^1B(S_{15})$	5.47	1.217	H→L+2(29%) H-2→L(15%)
(BPY)$_3$	$4^1B(S_8)$	4.46	1.230	H→L+11(43%) H-1→L+7(19%)	$1^1B(S_1)$	3.94	2.785	H→L(80%)	$4^1B(S_8)$	4.56	0.381	H-12→L+1(13%) H-1→L+1(13%)
	$7^1B(S_{13})$	4.78	0.744	H-1→L+1(21%) H→L+4(13%)					$6^1B(S_{11})$	4.81	0.534	H-1→L+7(23%) H-3→L+4(20%)
(BPY)$_4$	$3^1B(S_8)$	4.46	2.060	H→L+15(39%) H-1→L+11(21%)	$1^1B(S_1)$	3.82	3.795	H→L(72%)	$6^1B(S_{11})$	4.63	0.795	H-3→L(27%)
	$4^1B(S_{12})$	4.79	0.747	H-1→L+3(15%) H-3→L+3(12%)					$8^1B(S_{15})$	4.89	0.435	H-1→L+4(20%) H→L+3(16%)
	$8^1B(S_{16})$	5.46	1.809	H-3→L+1(15%) H-4→L(12%)								
						cis						
(BPY)$_2$	$4^1B(S_7)$	4.72	0.279	H→L+6(55%)	$2^1B(S_3)$	4.48	0.781	H→L(40%) H-8→L(19%)	$3^1A(S_6)$	4.75	0.134	H-1→L+1(45%)
	$7^1A(S_{14})$	5.58	0.476	H-2→L+3(32%) H→L+5(29%)	$6^1B(S_{11})$	4.94	0.217	H→L+5(20%) H→L(14%)	$6^1B(S_{11})$	5.06	0.202	H→L+10(14%) H-1→L+5(13%)
									$8^1B(S_{14})$	5.52	0.944	H→L+4(26%) H-2→L+1(18%)
(BPY)$_3$	$6^1A(S_{12})$	4.60	0.328	H→L+8(28%) H-1→L+7(26%)	$1^1B(S_1)$	4.17	1.960	H→L(60%)	$5^1B(S_9)$	4.71	0.211	H-2→L(38%) H→L+1(16%)
	$8^1B(S_{15})$	4.85	0.176	H→L+12(23%) H-2→L+7(14%)								
cy-**(BPY)**$_3$	$7^1B(S_{14})$	4.62	0.348	H→L+7(35%) H-1→L+8(23%)					$4^1A(S_8)$	4.44	0.161	H-1→L(33%) H→L+1(15%)
	$8^1B(S_{16})$	4.83	0.354	H→L+12(29%) H-2→L+8(16%)					$6^1B(S_{11})$	4.60	0.154	H-2→L(36%)
(BPY)$_4$	$7^1A(S_{13})$	4.56	0.102	H→L+8(22%)	$1^1B(S_1)$	4.08	3.128	H→L(61%) H-1→L+2(12%)	$6^1B(S_{12})$	4.65	0.173	H-3→L(17%) H-2→L(16%)

In the case of ***cis***-, the dimer of each conformer exhibits more than one electronic transition with significant f_{osc} values. For example, the results for ***o***- and ***m***-$(\mathbf{BPY})_2$ show two electronic transitions each (for ***o***-, at 4.72 and 5.58 eV, and for ***m***-, at 4.48 and 4.94 eV), whereas three important transitions are observed for the ***p***- conformer (at 4.75, 5.06, and 5.52 eV). At n=3, the ***o***- and ***p***- conformers start to form helical and cyclic structures, resulting in smaller intensity absorption spectra. The spectra of cyclic conformers of ***o***- and ***p***- $(\mathbf{BPY})_3$ show more than one significant electronic transitions. For example, the spectrum for cy-***o***- exhibits two electronic transitions at 4.62 and 4.83 eV with f_{osc} values of 0.348 and 0.354, respectively. The spectra of helical analogs of ***o***- and ***p***-$(\mathbf{BPY})_3$ show two and one prominent electronic transitions, respectively. The linear ***m***-$(\mathbf{BPY})_3$ also exhibits only one transition ($S_0 \rightarrow S_1$) with an f_{osc} value of 1.960. The absorption maxima for tetramers of ***o***- and ***p***- conformers almost coincide, and the highest peaks corresponding to these absorption maxima are due to $S_0 \rightarrow S_{13}$ (at 4.56 eV) and $S_0 \rightarrow S_{12}$ (at 4.65 eV), respectively. The results for ***m***-$(\mathbf{BPY})_4$ contain a strong absorption peak at 4.08 eV(f_{osc}=3.128) along with small intensity bands in the higher energy region. It is to be noted that, like ***trans***-, here also the absorption spectra of all the oligomers of ***cis***-***m***- are red-shifted compared to the spectra for ***o***- and ***p***- oligomers.

Comparison of the TD-DFT results obtained using B3LYP and CAM-B3LYP functionals against the RI-ADC(2) results for the three conformers of ***trans***- and ***cis***-$(\mathbf{BPY})_4$ is shown in Tables C11 and C12, respectively. The simulated absorption spectra are also compared in Figure C3. From the figure, it is observed that the results obtained using the CAM-B3LYP functional are closer to the RI-ADC(2) results in most of the cases. However, Table C11 shows that while the S_3 state for ***trans***-***o***- is the first bright state in CAM-B3LYP results, both RI-ADC(2) and B3LYP show the S_8 to be the first bright state. In the case of ***cis*** structures, while the absorption maxima in cases of ***o***- and ***p***- obtained using CAM-B3LYP are slightly blue-shifted compared to RI-ADC(2) spectrum, the B3LYP results are red-shifted as compared to the RI-ADC(2) results, although the pattern of UV spectra are similar. In cases of cyclic structures of ***o***-***cis***- and ***p***-***cis***- conformers of $(\mathbf{BPY})_3$, shown in Figure C4, results are similar to their respective tetramer results.

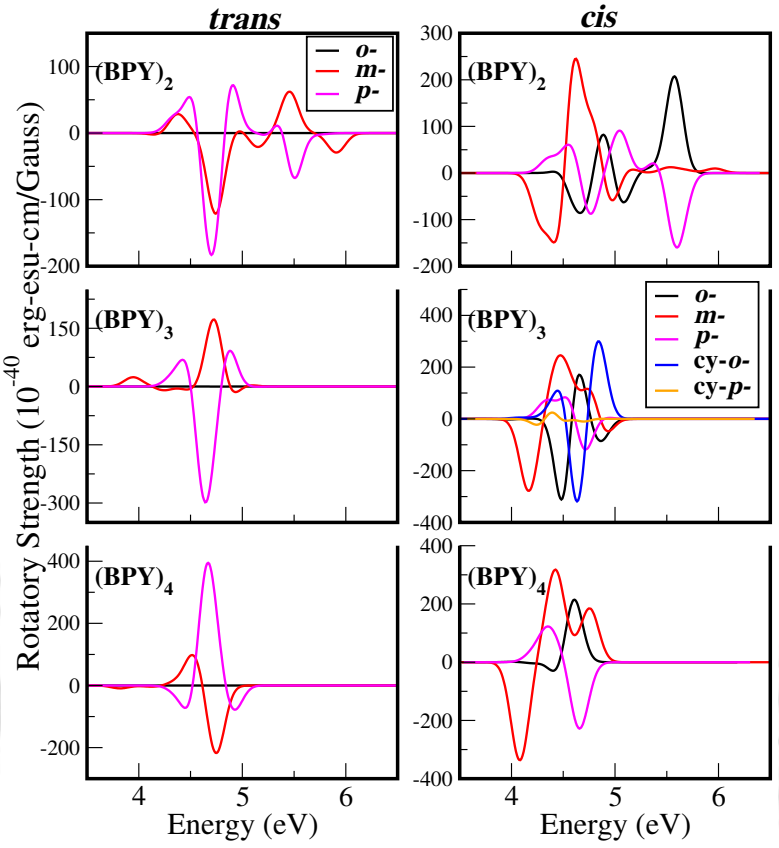

FIGURE 5.6: Simulated CD spectra of ***o-***, ***m-***, and ***p-*** conformers for ***trans***- and ***cis***-**BPY** oligomers. The results are obtained at RI-ADC(2)/def2-TZVPD level.

Similar to UV absorption spectra, the CD spectra are also different for different conformers. The simulated CD spectra of ***o-***, ***m-***, and ***p-*** conformers for both ***trans***- and ***cis***-**BPY** oligomers are shown in Figure 5.6, and the corresponding rotatory strength (R) values are tabulated in Table C6-C10. For ***trans***-, the most intense CD bands are observed in the case of ***p-*** oligomers, and the intensities of CD bands increase as the chain length increases. Along with the intense CD bands, these ***p-*** oligomers also exhibit other peaks with smaller R values. The spectrum of the dimer for the ***p-*** conformer contains one intense negative CD band around 4.66 eV with several small intensity CD bands. The results for **(BPY)**$_3$ show one negative band (at 4.64 eV) with an R value of -244.57 and two small intensity positive CD bands at 4.47 and 4.83 eV. The spectrum for ***p-*****(BPY)**$_4$ displays two weak negative bands around 4.52 and 4.89 eV, and one strong positive CD band at 4.63 eV. The highest peaks in the negative bands arise due to $S_0 \rightarrow S_6$ (at 4.52 eV) and $S_0 \rightarrow S_{16}$ (at 4.89 eV) transition, respectively, and the

positive band is due to the $S_0 \rightarrow S_{11}$ (at 4.63 eV) transition. Because of the flat and planar geometry, all the oligomers of ***o-*** conformer are optically inactive. In ***m-***, although the oligomers have a linear backbone, their mirror images are non-superimposable and therefore, oligomers of ***m-*** show CD bands with comparatively smaller intensity than those for ***p-*** oligomers. The dimer CD spectrum of ***m-*** consists of several small intensity bands, whereas the spectrum **(BPY)**$_3$ shows only one positive CD band around 4.73 eV ($S_0 \rightarrow S_{11}$) with an R value of 199.77. The CD spectrum of ***m-*****(BPY)**$_4$ shows only one positive CD band at 4.52 ($S_0 \rightarrow S_8$) and one negative band at 4.74 eV($S_0 \rightarrow S_{15}$). In the case of ***cis-***, in contrast to ***trans-***, oligomers of each conformer are CD active, and the results show at least one intense CD band for each of those. For **(BPY)**$_2$, the spectra of ***o-*** and ***p-*** conformers show four CD bands. For ***o-***, the bands are appear at 4.72(R=-68.46), 4.89(R=89.00), 5.07(R=-92.64), and 5.58(R=215.72) eV, whereas in ***p-***, bands are observed at 4.56(R=45.18), 4.75(R=-100.47), 5.06(R=132.95), and 5.59(-124.32) eV. The results for ***m-*** isomer display three bands at 4.48(R=-213.58), 4.59(R=310.76), and 4.94(R=-84.32) eV. The CD spectra for trimers of each conformer consist of three bands. The first two intense CD bands of ***o-*** originate due to $S_0 \rightarrow S_{11}$(at 4.51 eV) and $S_0 \rightarrow S_{12}$(at 4.60 eV) transitions, whereas the third band (at 4.85 eV) arises because of S_0 to S_{15} transition. The cyclic analog of ***o-*****(BPY)**$_3$ (cy-***o-***) also shows three CD bands. The three CD bands of ***m-*****(BPY)**$_3$ are obtained at 4.17, 4.55, and 4.78 eV. The intensities of CD bands in the case of ***p-*****(BPY)**$_3$ are comparatively smaller than ***o-*** and ***m-*** isomers. However, the intensities of CD bands are very small in the case of cy-***p-***. For **(BPY)**$_4$, ***o-*** conformer shows only one intense positive CD band (at 4.59 eV). While the ***m-*****(BPY)**$_4$ shows three CD bands at 4.08 eV (with an R= -324.94), 4.42 eV (with an R=284.18) and 4.77 eV (with an R=182.06), respectively. CD spectrum of ***p-*****(BPY)**$_4$ shows one positive and one intense negative band around 4.35 and 4.65 eV, respectively.

The degree of molecular dissymmetry, i.e., the degree of circular polarization, is examined in terms of absorption dissymmetry factors (g_{CD}) defined in Eq. 3.1. The maximum value of $|g_{CD}|$ is 2, according to Eq. 3.1. In the case of typical organic molecules, the values are much smaller (of the order of 10^{-2} to 10^{-4}).[174,175,219,220] This is due to the much smaller value of $\boldsymbol{m_e}$ compared to $\boldsymbol{\mu_e}$ ($\boldsymbol{\mu_e} \gg \boldsymbol{m_e}$). In this scenario, Eq. 3.1 can be

simplified as

$$g_{\mathrm{CD}} \approx \frac{4|\boldsymbol{m_e}|\cos\theta}{|\boldsymbol{\mu_e}|}. \tag{5.1}$$

The values of R, $|\boldsymbol{\mu_e}|$, $|\boldsymbol{m_e}|$, cos θ, and $|\boldsymbol{m_e}|/|\boldsymbol{\mu_e}|$ corresponding to the first sixteen excited states of ***trans***- and ***cis***-**(BPY)**$_4$ for three conformers are tabulated in Tables C9 and C10. In the case of ***trans***-, the g_{CD} values of all the states for ***o***- conformers are zero, as this conformer is optically inactive. For ***m***-, the g_{CD} value corresponding to the highest peak of the positive band (at 4.52 eV) is small (g_{CD}=0.002) due to a small value of $|\boldsymbol{m_e}|/|\boldsymbol{\mu_e}|$(0.001) and a small angle of 62° between the two vectors, whereas for the negative band (at 4.74 eV), an angle of 160° between $\boldsymbol{\mu_e}$ and $\boldsymbol{m_e}$ is responsible for comparatively larger g_{CD} value of -0.015. The g_{CD} values corresponding to the lower energy negative band(at 4.52 eV, R=-138.91) and only positive(at 4.63 eV, R=461.84) band of ***p***- conformer are very small (0.006 and 0.004, respectively) due to small values of $|\boldsymbol{m_e}|/|\boldsymbol{\mu_e}|$. In contrast, a g_{CD} value of -0.020 is obtained for the higher energy negative CD band(at 4.89 eV) due to the large cos θ value of -1.000.

In the case of ***cis***-, the highest peak (at 4.59 eV) of the intense CD band for ***o***- conformer has $|\boldsymbol{\mu_e}|$ and $|\boldsymbol{m_e}|$ values of 171.450 esu·cm and 3.094 erg·G^{-1}, respectively. In this case, a cos θ value of 0.672 and $|\boldsymbol{m_e}|/|\boldsymbol{\mu_e}|$ value of 0.018 results in a large g_{CD} value (g_{CD}=0.049). It is to be noted also that $S_0 \rightarrow S_{14}$ transition is accompanied by an R value of 368.34 erg·esu·cm·G^{-1}. A large value of $|\boldsymbol{m_e}|/|\boldsymbol{\mu_e}|$ (=0.026) and cos θ=0.775 produced a g_{CD} value of 0.082. Similarly, an anti-parallel arrangement of the vectors and a large $|\boldsymbol{m_e}|/|\boldsymbol{\mu_e}|$ results in a $|g_{\mathrm{CD}}|$ value of 0.092 for $S_0 \rightarrow S_{11}$ transition. The first two CD bands (at 4.08 and 4.42 eV) for ***m***- conformer have very small g_{CD} values(-0.001 and 0.006, respectively) due to the small values of $|\boldsymbol{m_e}|/|\boldsymbol{\mu_e}|$. Conversely, for the third CD band($S_0 \rightarrow S_{15}$), cos θ value of 0.906 leads to a g_{CD} value of 0.011. Lastly, for ***p***-, the g_{CD} values corresponding to the positive (at 4.35 eV) and the negative (at 4.65 eV) CD bands are 0.017 and 0.003, respectively.

TABLE 5.3: Values of ω_{CT}, d_{exc}, and PR_{NTO} calculated at RI-ADC(2)/def2-TZVPD level for ***o-***, ***m-***, and ***p-*** isomers of ***trans***- and ***cis***-$(\mathbf{BPY})_2$

trans		***o-***			***m-***			***p-***	
State	ω_{CT}	d_{exc}	PR_{NTO}	ω_{CT}	d_{exc}	PR_{NTO}	ω_{CT}	d_{exc}	PR_{NTO}
S_1	0.27	3.34	1.63	0.31	4.73	1.21	0.13	3.41	1.88
S_2	0.09	3.32	1.87	0.20	3.88	1.45	0.13	3.41	1.97
S_3	0.29	3.98	1.68	0.14	3.82	1.82	0.28	4.03	1.78
S_4	0.32	3.73	1.33	0.24	4.15	2.13	0.25	3.98	2.01
S_5	0.17	3.14	2.51	0.14	3.75	2.05	0.15	3.42	3.13
cis									
S_1	0.29	3.25	1.30	0.23	4.05	1.43	0.25	3.63	1.44
S_2	0.12	3.14	2.15	0.21	3.77	1.51	0.24	3.67	1.44
S_3	0.11	3.14	2.30	0.23	4.28	1.66	0.11	3.63	2.56
S_4	0.26	3.22	1.78	0.10	3.57	2.10	0.12	3.53	2.71
S_5	0.06	3.16	2.41	0.17	3.86	1.88	0.32	3.99	1.78

5.3.4 Excited state properties

UV and CD spectra reveal distinct features in the three conformers indicating differences in the excited state properties. To characterize the excited-state properties, an excitonic analysis based on 1TDM was carried out. In 1TDM analysis, the Ω matrix is calculated considering each **BPY** unit as a fragment. Therefore, $(\mathbf{BPY})_4$ consists of four fragments, and the Ω matrix displays a 4×4 matrix. In the following, we have only considered $(\mathbf{BPY})_2$ and $(\mathbf{BPY})_4$ for ***trans***- and ***cis***- structures and their lowest five excited states to show the differences in the excited state properties between the conformers. The

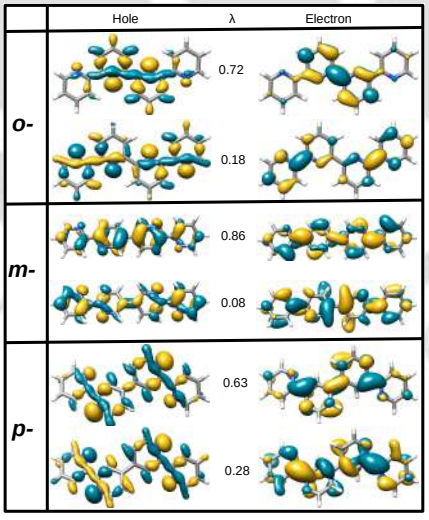

FIGURE 5.7: Natural transition orbitals corresponding to the $S_0 \rightarrow S_1$ transitions of ***trans***-$(\mathbf{BPY})_2$ for the three different conformers considered. Here, the value of λ_{max} indicates the weight of a configuration.

values of ω_{CT}, d_{exc}, and PR_{NTO} of the first five excited states for three conformers of ***trans***- and ***cis***-$(\mathbf{BPY})_2$ are tabulated in Table 5.3. In the case of ***trans***-, the ω_{CT}

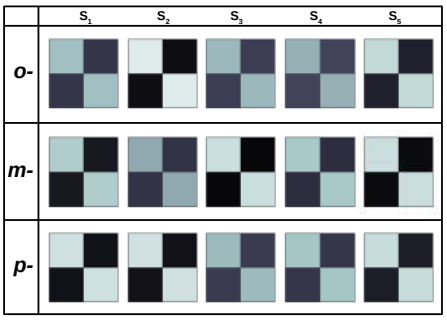

FIGURE 5.8: *e-h* correlation plots for the first five excited states of ***trans*-(BPY)$_2$** for the three different conformers.

TABLE 5.4: Values of ω_{CT}, d_{exc}, and PR_{NTO} calculated at RI-ADC(2)/def2-TZVPD level for ***o-***, ***m-***, and ***p-*** isomers of ***trans***- and ***cis*-(BPY)$_4$**

trans	***o-***			***m-***			***p-***		
State	ω_{CT}	d_{exc}	PR_{NTO}	ω_{CT}	d_{exc}	PR_{NTO}	ω_{CT}	d_{exc}	PR_{NTO}
S_1	0.33	3.89	2.07	0.44	5.91	1.49	0.19	4.09	2.23
S_2	0.44	5.12	2.62	0.30	5.10	1.75	0.19	4.12	2.23
S_3	0.41	5.19	2.02	0.27	4.88	2.61	0.19	4.43	2.22
S_4	0.33	3.94	2.94	0.38	5.53	2.31	0.18	4.57	2.23
S_5	0.42	5.09	3.36	0.29	5.22	2.70	0.47	5.57	2.55
cis									
S_1	0.52	3.93	2.06	0.46	5.81	1.54	0.42	4.17	2.03
S_2	0.53	3.94	2.06	0.33	5.39	1.74	0.40	4.10	2.02
S_3	0.36	4.29	2.53	0.34	5.63	1.82	0.36	4.04	1.46
S_4	0.33	4.10	2.50	0.34	5.96	2.19	0.32	3.93	1.51
S_5	0.51	3.86	2.34	0.32	5.89	2.40	0.42	4.31	2.68

values of S_1 states of ***o-*** and ***m-*** are 0.27 and 0.31, respectively. This indicates that the S_1 states may not considered as pure LE states. For ***p-*** conformer, the ω_{CT} value is 0.13 and is considered a LE state. d_{exc} values of these states lie between 3.34 to 4.73 Å, which is in good agreement with the ω_{CT} values. The values of PR_{NTO} indicate that two states of NTOs are required to describe S_1 states in most cases. NTOs involved in $S_0 \rightarrow S_1$ in each conformer are shown in Figure 5.7, in which no significant separation in the hole and electron densities is observed. However, a slight difference in hole and electron densities is observed in ***o-*** and ***m-*** conformers, which are reflected in ω_{CT} values. The *e-h* correlation plots shown in Figure 5.8 reveal that the S_1 state of ***o-*** and ***m-*** have little off-diagonal width, whereas the ***p-*** shows exciton delocalized into two fragments. The *e-h* correlation plots for S_2 and S_5 of ***o-*** and ***p-***, and S_3 and S_5 states of ***m-*** also show delocalized exciton along the diagonal, which is in accordance with their ω_{CT} values. The other two states of each conformer have slightly larger ω_{CT} values, which is also seen in the *e-h* correlation plots. The d_{exc} values of these states are slightly larger than those of the LE states. In the case of ***cis***-, ω_{CT} of the first excited state (S_1) for the

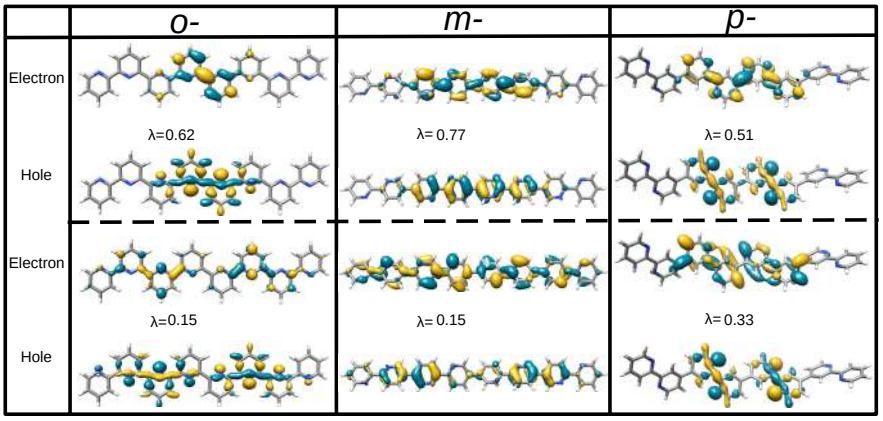

FIGURE 5.9: Natural transition orbitals corresponding to the $S_0 \rightarrow S_1$ transitions of ***trans*-(BPY)$_4$** for the three different conformers considered. Here, the value of λ_{max} indicates the weight of a configuration.

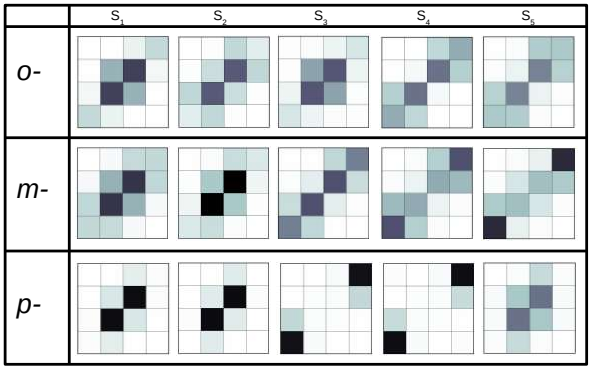

FIGURE 5.10: *e-h* correlation plots for the first five excited states of ***trans*-(BPY)$_4$** for the three different conformers.

three conformers show a magnitude of 0.23-0.29, indicating these may not be considered pure local states. The NTOs involved in the S_1 states are depicted in Figure C5. The second set of NTOs of ***o-*** and ***p-*** show the separation of electron and hole densities at the terminal pyridine rings, which is absent in the case of ***m-*** conformer. Additionally, as shown in Figure C6, the *e-h* correlation plots of S_1 states also predict the same results by showing less intense off-diagonal widths in each case. The S_4 of ***o-***, S_2 and S_3 of ***m-***, and S_2 and S_5 of ***p-***, show similar results as shown by the S_1 state for each conformer. The values of ω_{CT} for other states range from 0.06 to 0.17 and are considered LE states. The *e-h* correlation plots of these states show intense diagonal width, which signifies exciton delocalization in two fragments.

The values of three descriptors for ***trans***- and ***cis*-(BPY)$_4$** are tabulated in Table 5.4. Data tabulated in Table 5.4 shows that in most cases, the ω_{CT} values are larger compared

to the dimer results. The trend of increase in d_{exc} value with increase in ω_{CT} value is maintained except in a few cases. In most cases, the values of PR_{NTO} are greater than two, indicating that a minimum of two sets of NTOs are required to describe an excited state. For ***trans***-, the ω_{CT} value of the S_1 state for ***m***- (0.44) isomer is slightly larger than the values for ***o***- (0.34) and ***p***- (0.19) isomers. The ω_{CT} values for ***o***- and ***m***- indicate partial CT characters of S_1 states. Figure 5.9 shows the NTOs involved in the $S_0 \rightarrow S_1$ transitions. The second set of NTOs of ***o***- and ***m***- conformers shows a partial separation of electron and hole densities in the middle of the chain. It is also to be noted that while S_1 states for ***o***- and ***p***- are of $n \rightarrow \pi^\star$ types, the state is of $\pi \rightarrow \pi^\star$ for ***m***-. The results predicted by ω_{CT} and NTOs are confirmed by the *e*-*h* correlation plots shown in Figure 5.10. For S_1, the ***o***- and ***m***- conformers show slightly intense off-diagonals around the central fragments, indicating charge transfer between the two fragments. On the other hand, the off-diagonal part is almost absent in the case of ***p***- conformer. The *e*-*h* correlation plots for S_2 and S_3 states of ***o***- conformer are similar to the S_1 state with different off-diagonal widths. The S_2 state of ***m***- conformer shows a localized exciton in the middle, while the S_3, S_4, and S_5 states show similar diagonal widths. The results for the S_2 state in the ***p***- isomer are identical to those for S_1, with the exciton located at the middle fragments. On the other hand, the exciton is localized at the terminal fragments for the S_3 and S_4 states. The S_5 state exhibits a small off-diagonal width, which shows up in the ω_{CT} value of 0.47.

In the case of ***cis***-, ω_{CT} values for the S_1 state of ***o***- (0.52), ***m***- (0.46), and ***p***- (0.42) indicate partial CT characters. The NTOs depicted in Figure C7 show that the electron densities are distributed throughout the terminal rings and rings next to the terminal rings. In contrast, the hole densities are located mainly at the terminal rings. On the other hand, a small difference in the locations of densities is observed around the central rings for the ***m***- conformer. The *e*-*h* correlation plot for the S_1 state (shown in Figure C8 shows a small off-diagonal width, indicating CT between two fragments in the middle. In comparison, the CT mainly occurs around the terminal fragments in S_1 state of ***o***- and ***p***- conformers. The S_2 and S_5 states of the ***o***- conformer exhibit *e*-*h* correlation plots similar to the plots for the S_1 state, whereas the S_3 and S_4 states show a different pattern with some CT around the terminal regions. In ***m***-, the *e*-*h* correlation plots for

S_2-S_4 states show some amount of CT either in the middle or terminal regions. The results for the S_2 state of ***p-*** conformer are almost identical to the S_1 state, whereas a little CT around the central regions is observed for the other three states.

The performance of DFT functionals to describe the excited states is also checked by calculating the ω_{CT} values using B3LYP and CAM-B3LYP functional results. The results for the first five excited states are tabulated in Table 5.5. The values of ω_{CT} for the flat and planar structure of ***o-trans*** obtained at CAM-B3LYP are smaller than the results obtained at RI-ADC(2) level, whereas the values at B3LYP are a little larger. In the case of ***m-trans***, the differences in ω_{CT} values between RI-ADC(2) and B3LYP result becomes much larger in some cases; e.g., the ω_{CT} value for the S_3 state at RI-ADC(2), CAM-B3LYP, and B3LYP levels are 0.27, 0.17, and 0.76, respectively. In contrast, for the ***p-*** conformer, the results obtained show a similar variation to the ***o-*** results. The *e*-*h* correlation plots for the first five excited states are compared in Figures C9-C11. For ***o-trans*-(BPY)$_4$**, results for S_1-S_3 and S_5 obtained using CAM-B3LYP match closely with the RI-ADC(2) results. In ***m-trans*-(BPY)$_4$**, while the results for S_1 using CAM-B3LYP match with the RI-ADC(2) results, results for other states differ, e.g., the order of S_2 and S_3 is interchanged. For ***p-***, on the other hand, the *e*-*h* correlation plots for the first four excited states obtained using B3LYP resemble closely the RI-ADC(2) results. In case of CAM-B3LYP, on the other hand, results for S_3 and S_5 differ from the benchmark results. In ***cis-***, the ω_{CT} values of helical ***o-*** conformer obtained using CAM-B3LYP and B3LYP functionals follow a pattern similar to the ***o-trans*** results. In ***m-***, for S_5 state, a difference of 0.45 is observed between the RI-ADC(2) and B3LYP results. For the ***p-*** conformer, ω_{CT} values of the first two states are 0.72 and 0.88 for B3LYP, which are much larger compared to the RI-ADC(2) results. The *e*-*h* plots for the *cis* structures are shown in Figures C12- C14. For ***o-***, results obtained using both B3LYP and CAM-B3LYP for the first four excited states show a very good match with the RI-ADC(2) results. In case of ***m-***, while the first three states obtained using all the three methods are LE states, differences appear for the last two states. In ***p-***, results of CAM-B3LYP are closer to the RI-ADC(2) results. Overall, in most cases, the results obtained using the CAM-B3LYP functional are closer to the RI-ADC(2) results.

TABLE 5.5: Excitation energies (E_g), oscillator strengths(f_{osc}), and ω_{CT} values of first five states of three different conformers of ***trans*-(BPY)$_4$** and ***cis*-(BPY)$_4$** calculated at RI-ADC(2) level and using two different functionals B3LYP and CAM-B3LYP using the def2-TZVPD basis set

trans									
o-									
	RI-ADC(2)			CAM-B3LYP			B3LYP		
State	E_g	f_{osc}	ω_{CT}	E_g	f_{osc}	ω_{CT}	E_g	f_{osc}	ω_{CT}
S_1	4.33	0.000	0.33	4.43	0.000	0.25	3.89	0.000	0.60
S_2	4.35	0.001	0.44	4.43	0.064	0.35	3.89	0.001	0.58
S_3	4.35	0.000	0.41	4.47	1.344	0.25	3.96	0.000	0.56
S_4	4.36	0.000	0.33	4.49	1.060	0.27	3.97	0.015	0.55
S_5	4.38	0.000	0.42	4.49	0.000	0.33	4.07	0.000	0.53
m-									
S_1	3.82	3.795	0.44	3.75	3.723	0.38	3.22	2.928	0.60
S_2	4.09	0.002	0.30	4.16	0.000	0.34	3.65	0.000	0.69
S_3	4.17	0.032	0.27	4.38	0.003	0.17	3.69	0.000	0.76
S_4	4.19	0.000	0.38	4.43	0.011	0.14	3.75	0.001	0.38
S_5	4.28	0.001	0.29	4.50	0.001	0.10	3.82	0.009	0.36
p-									
S_1	4.33	0.010	0.19	4.52	0.024	0.11	4.01	0.017	0.25
S_2	4.33	0.002	0.19	4.52	0.239	0.10	4.02	0.005	0.24
S_3	4.37	0.015	0.19	4.53	0.166	0.09	4.04	0.036	0.20
S_4	4.37	0.000	0.18	4.53	0.003	0.08	4.04	0.001	0.19
S_5	4.52	0.000	0.47	4.56	1.506	0.12	4.11	0.129	0.51
cis									
o-									
S_1	4.02	0.000	0.52	4.36	0.000	0.30	3.90	0.000	0.42
S_2	4.02	0.000	0.53	4.36	0.001	0.30	3.91	0.000	0.42
S_3	4.24	0.000	0.36	4.56	0.000	0.10	4.09	0.001	0.17
S_4	4.25	0.001	0.33	4.57	0.001	0.10	4.09	0.000	0.15
S_5	4.34	0.000	0.51	4.61	0.005	0.19	4.16	0.036	0.49
m-									
S_1	4.08	3.128	0.46	4.03	3.497	0.38	3.50	2.670	0.57
S_2	4.17	0.004	0.33	4.37	0.050	0.30	3.80	0.015	0.48
S_3	4.18	0.128	0.34	4.46	0.022	0.16	3.87	0.015	0.32
S_4	4.28	0.005	0.34	4.47	0.005	0.17	3.91	0.023	0.46
S_5	4.31	0.064	0.32	4.55	0.002	0.11	3.99	0.000	0.77
p-									
S_1	4.20	0.004	0.42	4.56	0.002	0.18	3.92	0.001	0.72
S_2	4.20	0.001	0.40	4.57	0.004	0.18	3.94	0.012	0.88
S_3	4.30	0.002	0.36	4.59	0.003	0.17	4.00	0.000	0.43
S_4	4.31	0.001	0.32	4.60	0.000	0.20	4.03	0.001	0.36
S_5	4.35	0.003	0.42	4.62	0.003	0.28	4.04	0.006	0.41

5.4 Conclusion

In summary, we have compared the photo-physical and excited state properties of three different conformers (***o-***, ***m-***, and ***p-***) for ***trans***- and ***cis*-BPY** oligomers. Analysis of UV spectra reveals that the oligomers of ***m-*** conformer for both ***trans***- and ***cis***-structures show red-shifted UV spectra compared to the ***o-*** and ***p-*** oligomers. On the other hand, the CD spectra show quite different results. For ***trans***, the ***p-*** oligomers show high-intensity CD bands, whereas for ***cis***, the high-intensity CD bands are observed in the case of all the conformers. Furthermore, excited states of $(\mathbf{BPY})_2$ and $(\mathbf{BPY})_4$ are characterized by considering the descriptors ω_{CT}, d_{exc}, and PR_{NTO}. In $(\mathbf{BPY})_2$, results of ω_{CT}, NTOs, and *e-h* suggested that the excited states are mainly LE states in each conformer of ***trans***- and ***cis***- structures. In contrast, the tetramers ω_{CT} values range from 0.19 to 0.53, which indicates some of the states show partial CT character, and this is confirmed by the NTOs and *e-h* correlation plots.

Chapter 6

Insight into the excited states in monomers and π-stacked dimers of azulene-fused acenes: ADC(2) and TD-DFT studies

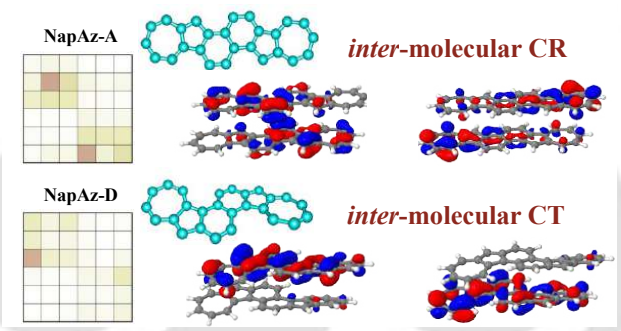

In this chapter, we investigate the nature of the excited states in monomers and π-stacked dimers of azulene-fused naphthalene and anthracene systems, focusing on the interplay between conformational isomers and excited state properties. For the monomers, the states with CT characters are different in naphthalene- and anthracene-based systems. In π-stacked dimers, a few of the excited states are of the charge resonance (CR) type in conformers **NapAz-A**, **NapAz-B**, and **NapAz-C**, and the intermolecular CT type in **NapAz-D**. Overall, among the three DFT functionals considered (CAM-B3LYP, SCS-ωB2GP-PLYP, and SCS-RSX-QIDH), CAM-B3LYP has been found to reproduce well the SCS-ADC(2) excited results in both monomers and π-stacked dimers. Reproduced from "*The Journal of Physical Chemistry A*, **2025**, 129(4), 1085–1098" with permission from American Chemical Society.

6.1 Introduction

Polycyclic aromatic hydrocarbons (PAHs) are widely employed in organic electronic device applications due to their unique optoelectronic properties.[221–223] Among PAHs, acenes have attracted much attention as semiconductor materials.[221,223,224] However, the intrinsic chemical instability of larger acenes (pentacene, hexacene, and so on) toward light and air restricts their use in organic electronics.[225,226] One efficient way to overcome this problem is to replace two benzenoid rings with a non-benzenoid azulene.[75,77,79] Azulene is isoelectronic with naphthalene and has a dipole moment of 1.08 D[227] due to the intermolecular donor-acceptor nature of five and seven-membered rings, and therefore, has unique optoelectronic properties.[227,228] Replacing two benzenoid rings with an azulene unit results in all carbon polyaromatic hydrocarbon with retention of chemical stability and optoelectronic properties.[75–77,79] Azulene-embedded acenes that resemble tetracene were first introduced by Yasunami and co-workers[81] in 1980, considering two isomers. The third isomer of azulene-fused naphthalene was successfully synthesized by Yamamura and co-workers with the aim of providing a facile synthetic route.[82] The azulene-fused anthracene, isoelectronic with pentacene, shows a significantly low optical band gap with high air stability.[75] In addition to the above structures, where only one azulene ring is fused into the acene skeleton, there are also examples where two azulene units are fused on both sides of acene derivatives[77–80] and these have been shown to exhibit better performance in semiconducting materials.

In the case of azulene-fused acenes, studies have mainly focused on their synthesis and their applications in electronic devices. However, molecular-level characterization of the excited states is yet to be done for these types of systems. This sort of studies at the monomeric and aggregate levels provide guidelines at choosing azulene-fused systems better for optoelectronic applications. Considering the above, the present work aims to explore how the excited state properties vary in monomers and π-stacked dimers of azulene-fused naphthalene (**NapAz**) and anthracene (**AntAz**) systems taking into account a few of their isomers. The schematic diagram of four different isomers of **NapAz**, **NapAz-A**, **NapAz-B**, **NapAz-C**, and **NapAz-D**, is shown in Figure 6.1.

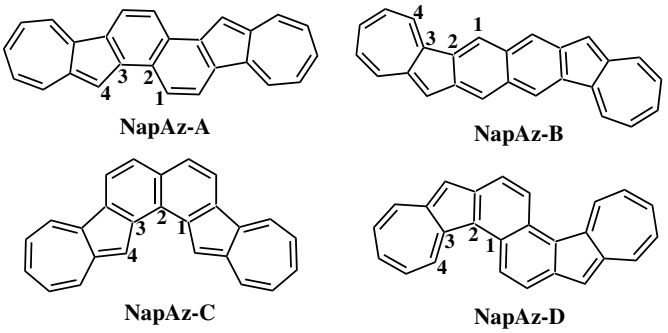

FIGURE 6.1: Schematic diagrams of four isomers of **NapAz**. The dihedral angle (∠C1-C2-C3-C4) between azulene and acene units is denoted as ϕ.

In a similar way, isomers **AntAz-A**, **AntAz-B**, **AntAz-C**, and **AntAz-D** are also constructed for **AntAz**.

In this work, the characterization of excited states in monomers and face-to-face π-stacked dimers for different conformers of diazulene fused naphthalene and anthracene was carried out at the ADC(2) level. Following this, TD-DFT calculations using the most widely used LC hybrid exchange-correlation functional CAM-B3LYP[97] and the spin-component-scaled (SCS)[229] versions of two LC-DH functionals, ωB2GP-PLYP[104] and RSX-QIDH,[230] were performed.[105,231] The two LC-DH functionals are chosen because of their balanced description of intra and intermolecular CT excitations.[105,231] This chapter is organized as follows: In the Computational Details section, we explain the methods used in the computational studies. In the Results and Discussion section, after validating the methodologies by comparing the absorption spectra for monoazulene-fused naphthalene and anthracene systems, the results for the present systems are presented and discussed. Finally, the Conclusions section concludes our findings.

6.2 Computational Details

Ground state (S_0) geometry optimization calculations of all the systems were performed with Møller-Plesset perturbation theory to the second order (MP2).[84] The geometries were constrained to the C_2 symmetry for the isolated monomers, and for π stacked-dimers, the C_1 point group was used. Frequency calculations for the monomers of all isomers and a few π stacked-dimers were carried out at the same level of theory to confirm

that the obtained structures are ground state minima. Excitation energy calculations were performed to compute the vertical excitation energies (E_g) at the ADC(2) level. SCS[229] versions of both the MP2 and ADC(2) methods were used, in addition to the RI approximation[195]. For the E_g value calculations at the SCS-ADC(2) level, sixteen and ten excited states were considered for the monomers and dimers, respectively. In addition, E_g values were also calculated at the TD-DFT level using the CAM-B3LYP and SCS versions of two LC-DH functionals, SCS-ωB2GP-PLYP and SCS-RSX-QIDH. In the method validation section, the E_gs were also computed using ωB97X functional.[99] The Tamm-Dancoff approximation (TDA)[232] and resolution of the identity in combination with the chain of spheres (RIJCOSX)[233] approximation was used in all the TD-DFT calculations. In all cases, the def2-TZVP basis set was used. For the SCS-MP2 and SCS-ADC(2) studies, Turbomole V7.2[196] was utilized and for TD-DFT calculations, the Orca V5.0[234]software package was used. All of the calculations were carried out in the gas phase. UV spectra of isomers were generated using the Gabedit software[169] with Gaussians of half-width at half maxima of 0.1 eV. The characterization of the excited states was carried out by excitonic analysis based on the one-electron transition density matrix (1TDM) and for this purpose, the TheoDORE 3.0 software package[170] was used.

For the **AntAz** dimer, the calculations of E_g values at the SCS-ADC(2)/def2-TZVP level for ten excited states took ≈ 53 hrs on a machine with 144 Intel(R) Xeon(R) Platinum 2.9 GHz processors. On the other hand, TD-DFT calculations for the above system using SCS-ωB2GP-PLYP and CAM-B3LYP functionals required ≈ 19 and 1 h, respectively, on 48 processors.

6.3 Results and Discussion

6.3.1 Validation of Methods

For validating the methodologies used, we started with the monoazulene-fused naphthalene **1a** and monoazulene-fused anthracene **2a** shown in Figure D1. The single crystal X-ray data reveal that both **1a** and **2a** have planar backbones with nearly 0° dihedral angle (ϕ=∠C1-C2-C3-C4) between the azulene and acene moieties.[75] The ground state

TABLE 6.1: Vertical Excitation Energy (E_g in eV) /Oscillator Strength (f_{osc}) for the First Six Excited States of **1a** and **2a** Computed at the SCS-ADC(2) Level and Using Four DFT Functionals. Experimental Results[75] (E_g in eV and ϵ in $M^{-1}cm^{-1}$) are Shown in the Last Column.

	E_g/f_{osc}					$E_g/\epsilon \times 10^{-4}$
			1a			
State	SCS-ADC(2)	CAM-B3LYP	ωB97X	SCS-ωB2GP-PLYP	SCS-RSX-QIDH	exptl.
S_1	2.15 / 0.010	2.28 / 0.013	2.40 / 0.017	2.12 / 0.016	2.03 / 0.016	1.98 /0.036
S_2	3.37 / 0.001	3.35 / 0.006	3.50 / 0.012	3.33 / 0.011	3.31 / 0.011	3.13 /0.760
S_3	4.06 / 0.794	4.33 / 0.320	4.51 / 0.467	4.17 / 0.856	4.11 / 0.886	3.30 /0.750
S_4	4.22 / 0.079	4.42 / 0.336	4.69 / 0.986	4.31 / 0.854	4.22 / 0.897	3.80 /6.300
S_5	4.25 / 1.311	4.56 / 0.652	4.81 / 0.830	4.39 / 0.593	4.34 / 0.586	
S_6	4.57 / 0.021	4.78 / 1.583	5.00 / 0.819	4.70 / 0.655	4.64 / 0.533	
			2a			
S_1	2.04 / 0.010	2.22 / 0.014	2.34 / 0.016	2.02 / 0.015	1.95 / 0.014	1.92 /0.055
S_2	3.20 / 0.011	3.20 / 0.014	3.38 / 0.021	3.20 / 0.019	3.16 / 0.019	2.92 /1.600
S_3	3.64 / 0.430	3.86 / 0.518	4.08 / 0.306	3.83 / 0.477	3.75 / 0.476	3.08 /2.600
S_4	3.84 / 0.749	3.90 / 0.078	4.16 / 0.257	3.79 / 0.017	3.74 / 0.020	3.20 /4.600
S_5	3.93 / 0.258	4.12 / 0.379	4.44 / 1.878	4.06 / 2.447	3.91 / 2.383	3.39 /4.700
S_6	4.05 / 0.979	4.34 / 1.497	4.58 / 0.725	4.14 / 0.175	4.07 / 0.159	3.64 /10.800

geometries shown in Figure D1 obtained at the SCS-MP2/def2-TZVP level also have planar backbones. The frequencies of these two ground-state geometries are positive confirming that the geometries are minima on the potential energy surfaces. Following this, we computed the E_gs at the SCS-ADC(2) level and using four different DFT functionals. The values are given in Table 6.1. Experimental result[75] for **1a** shows four absorption maxima in CH_2Cl_2. Experimental energies and corresponding molar absorption coefficients (ϵ) are also shown in the last column of the table. The reported first absorption maximum centered at 1.98 eV is very weak. The E_g values of the first excited state (S_1) computed at SCS-ADC(2), CAM-B3LYP, SCS-ωB2GP-PLYP, and SCS-RSX-QIDH are 2.15, 2.28, 2.12, and 2.03 eV, respectively, which are in good agreement with the experimental result. However, the energy of the S_1 state obtained using ωB97X is blue-shifted from the experimental result by 0.43 eV. The oscillator strength (f_{osc}) in each case is very small (in the range of 0.010-0.017), in accordance with the experimental result. The second, third, and fourth absorption maxima were reported at 3.13, 3.30, and 3.80 eV, respectively. The fourth absorption maximum has the highest ϵ value of 6.300. The SCS-ADC(2) results indicate S_5 (at 4.25 eV) to be the brightest state with a f_{osc} value of 1.311. In addition, the S_3 state also has an f_{osc} value of 0.794. CAM-B3LYP results show that the S_6 state has the highest f_{osc} value of 1.583, and the S_3-S_5 states also have considerable f_{osc} values. The results for the other three DFT functionals show

that the S_3-S_6 states have significant f_{osc} values, suggesting the involvement of more than one absorption peak, as observed in experimental results.

For **2a**, six absorption maxima were reported, as shown in the last column of Table 6.1. The first absorption maximum appeared at 1.92 eV with a small ϵ value. The first excitation energies obtained using SCS-ADC(2), SCS-ωB2GP-PLYP, and SCS-RSX-QIDH agree well with the experimental result, whereas the CAM-B3LYP and ωB97X excitation energies are 0.30 and 0.42 eV above the experimental result. For the second excitation, except ωB97X, the energies obtained using the other four methods (SCS-ADC(2) and three DFT functionals) are blue-shifted from the experimental result by 0.22-0.28 eV. The energies for the next four states obtained using all of the methods are approximately above 0.4 eV from the reported results. The SCS-ADC(2) and four DFT functionals predict these four states to be bright in accordance with the experimental results. Though the results obtained using ωB97X functionals show a pattern similar to that of the other DFT functionals, the E_g values are far from the experimental results. Considering the above, the E_g calculations and excited state characterization of isomers for the **NapAz** and **AntAz** structures are carried out using the SCS-ADC(2) method and three DFT functionals, CAM-B3LYP, SCS-ωB2GP-PLYP, and SCS-RSX-QIDH.

6.3.2 Geometries of Monomers and Dimers

The ground state geometries of the monomers and π-π stacked dimers of all the isomers for the **NapAz** structure optimized at the SCS-MP2 level are presented in Figure 6.2. The monomers of **NapAz-A** and **NapAz-B** are planar, having almost zero dihedral angles between the azulene and naphthalene units. For **NapAz-C**, the azulene moiety is 2.50° out of the plane from the naphthalene unit due to the steric interaction between the hydrogen atoms attached to the cyclopentene rings. In contrast, the close proximity between the hydrogen atoms of the seven-membered ring and the acene unit lead to a nonplanar structure for **NapAz-D** (the dihedral angle ϕ is $\sim 15°$). The optimized geometries of the monomers for **AntAz-A**, **AntAz-B**, **AntAz-C**, and **AntAz-D** are shown in Figure D2. For **AntAz-A** and **AntAz-B**, results similar to those for **NapAz-A** and **NapAz-B** are observed. In **AntAz-C**, the extra phenylene ring in the acene moiety

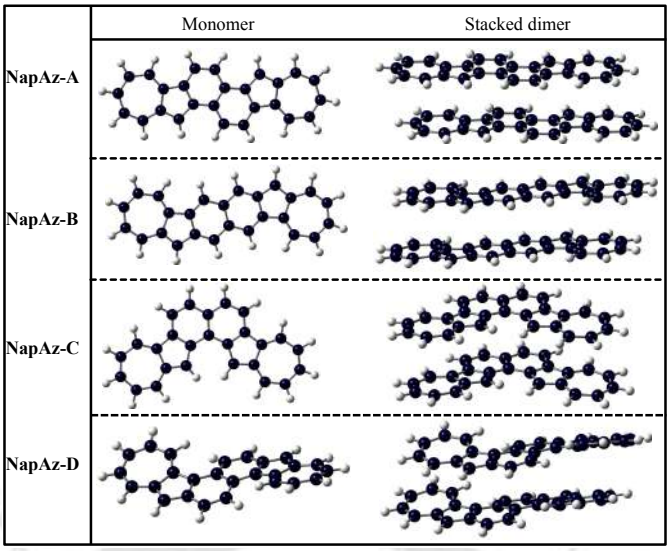

FIGURE 6.2: Ground state optimized geometries of monomers and π-stacked dimers of **NapAz-A**, **NapAz-B**, **NapAz-C**, and **NapAz-D** at the SCS-MP2/def2-TZVP level.

reduces the steric interaction between the hydrogen atoms attached to the cyclopentene rings, leading to a planar geometry. The result for **AntAz-D** is almost similar to that for **NapAz-D**; here, the dihedral angle is slightly smaller than that for **NapAz-D** (12° vs 15°).

In π-stacked dimers, the ϕ values at the two azulene-acene junctions in a monomeric unit are different from each other. In the **NapAz-A** and **NapAz-B** isomers, the differences are small. However, in isomer **NapAz-C**, the ϕ values are ∼8° and 2°. For the isomer **NapAz-D**, the ϕ values at the two ends of one monomeric unit are 14° and 12°, whereas, in another unit, the ϕ values are 13° and 7°. Similar results are observed in the case of π-stacked dimers of **AntAz** isomers. The main geometrical feature of these π-stacked dimers is the stacking distance (R_d). The average R_d values for **NapAz-A**, **NapAz-B**, **NapAz-C**, and **NapAz-D** are 3.24, 3.22, 3.26, and 3.24 Å, respectively. These values are smaller than the corresponding acenes.[235] Accordingly, the binding energies, calculated using the supramolecular approach and shown in Table 6.2, are larger in the azulene-fused naphthalenes than in corresponding acenes.[235] Similarly, in AntAz isomers, the R_d values are 3.28, 3.16, 3.21, and 3.31 Å in **AntAz-A**, **AntAz-B**, **AntAz-C**, and **AntAz-D**, respectively.

TABLE 6.2: Binding energies (in kcal/mol) for the dimers of **NapAz** and **AntAz** isomers

NapAz-A	**NapAz-B**	**NapAz-C**	**NapAz-D**	**AntAz-A**	**AntAz-B**	**AntAz-C**	**AntAz-D**
-35.143	-33.701	-35.106	-35.122	-41.312	-39.972	-40.578	-42.600

TABLE 6.3: Vertical Excitation Energies (E_g) (in eV) and Corresponding Oscillator Strength (f_{osc}) for the First Six Excited States of the Monomers Obtained at the SCS-ADC(2)/def2-TZVP Level

	NapAz-A	**NapAz-B**	**NapAz-C**	**NapAz-D**
State	E_g/f_{osc}			
S_1	2.03 / 0.017	2.08 / 0.047	2.08 / 0.010	1.97 / 0.023
S_2	2.25 / 0.000	2.52 / 0.000	2.19 / 0.022	2.21 / 0.000
S_3	3.15 / 0.052	3.02 / 0.177	2.96 / 0.001	3.07 / 0.004
S_4	3.47 / 0.000	3.64 / 0.000	3.29 / 0.611	3.42 / 0.000
S_5	3.69 / 0.000	3.67 / 0.000	3.52 / 0.972	3.59 / 2.096
S_6	3.69 / 1.241	3.73 / 1.973	3.86 / 0.014	3.66 / 0.000
	AntAz-A	**AntAz-B**	**AntAz-C**	**AntAz-D**
S_1	1.98 / 0.021	2.06 / 0.056	2.03 / 0.011	1.96 / 0.019
S_2	2.10 / 0.000	2.40 / 0.000	2.08 / 0.017	2.09 / 0.000
S_3	3.06 / 0.098	2.87 / 0.327	3.00 / 0.002	2.97 / 0.017
S_4	3.34 / 0.000	3.41 / 0.001	3.21 / 0.769	3.24 / 0.001
S_5	3.44 / 1.225	3.47 / 0.000	3.45 / 1.052	3.41 / 1.912
S_6	3.63 / 2.469	3.49 / 0.000	3.63 / 0.494	3.50 / 0.792

6.3.3 Excitation Energies and Oscillator Strengths

6.3.3.1 Monomers

The E_g values and the corresponding f_{osc}s for the first six excited states of the isomers of **NapAz** and **AntAz** structures are listed in Table 6.3. The E_g values for the S_1 states for the **NapAz** isomers are close to each other (the differences range from 0.00 to 0.11 eV). Among these four, the nonplanar isomer **NapAz-D** has the smallest E_g value of 1.97 eV. As has been reported earlier,[236,237] twisting in polyacenes does not affect the conjugation as the arrangement of π orbitals remains almost undisturbed. The f_{osc} values for all of the isomers are small for the S_1 states, ranging from 0.010 to 0.047. For **NapAz-A**, **NapAz-C** and **NapAz-D**, the E_g values of the S_2 states are close to one another, whereas for **NapAz-B**, the E_g is blue-shifted by around 0.30 eV in comparison to the other three isomers. Except for the **NapAz-C** isomer, the S_2 states of the other three isomers are optically dark. For the next four states, the differences in E_g values are small among the four isomers. Notably, the S_5 and S_6 states of isomer **NapAz-A**

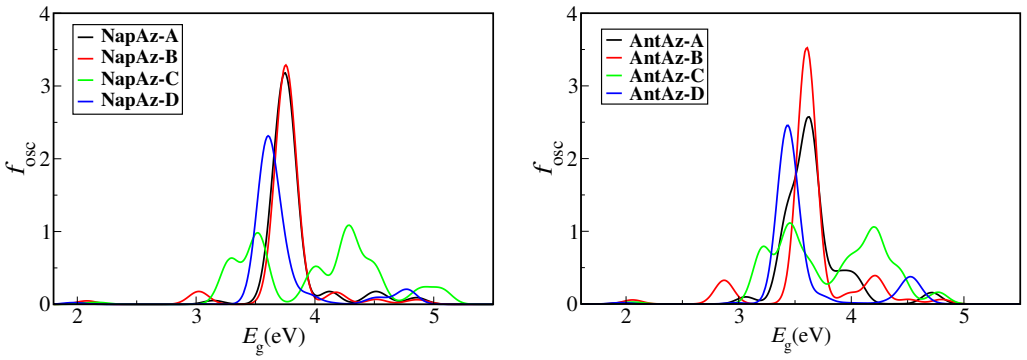

FIGURE 6.3: Comparison of simulated absorption spectra of monomers between four different isomers of **NapAz** (left panel) and **AntAz** (right panel) obtained at the SCS-ADC(2)/def2-TZVP level.

are degenerate, with a value of 3.69 eV. Among the first six excited states, S_6 is the brightest state in **NapAz-A** and **NapAz-B**, whereas for **NapAz-C** and **NapAz-D**, S_5 is the brightest state. In the case of **AntAz** isomers, the first three excited states of the four isomers exhibit results similar to the corresponding isomers of **NapAz** as shown in Table 6.3. The results of the remaining three states differ from those of their corresponding naphthalene counterparts. The S_5 state (observed at 3.44 eV) for **AntAz-A**, which was optically dark in **NapAz-A**, is bright for **AntAz-A** with an f_{osc} value of 1.225. The opposite trend can be seen in the case of **AntAz-B**, where the S_6 state (occurring at 3.49 eV) now has a zero f_{osc} value. Compared to the value for **NapAz-C**, f_{osc} values for S_4, S_5 and S_6 states of **AntAz-C** are found to be larger. The S_4 and S_6 states, which are dark in **NapAz-D**, have considerable f_{osc} values in **AntAz-D**.

The simulated absorption spectra are compared in Figure 6.3. Isomers **NapAz-A**, **NapAz-B**, and **NapAz-D** exhibit strong absorption maxima at around 3.69, 3.73, and 3.59 eV, respectively. These absorption maxima arise mainly due to $S_0 \rightarrow S_6$ transitions for **NapAz-A** and **NapAz-B**, and $S_0 \rightarrow S_5$ for the **NapAz-D** isomer. In addition, these three isomers also show some weak intensity peaks on both sides of the maxima. Notably, the absorption spectra of **NapAz-A** and **NapAz-B** are almost similar. The spectrum for **NapAz-C** is quite different from those for the other three isomers. The absorption spectrum of **NapAz-C** consists of several small intensity peaks between 3.00 and 5.00 eV. In this case, four prominent peaks are observed around 3.29($S_0 \rightarrow S_3$), 3.52($S_0 \rightarrow S_4$), 4.03($S_0 \rightarrow S_9$), and 4.28($S_0 \rightarrow S_{10}$) eV. The results for the anthracene isomers are similar

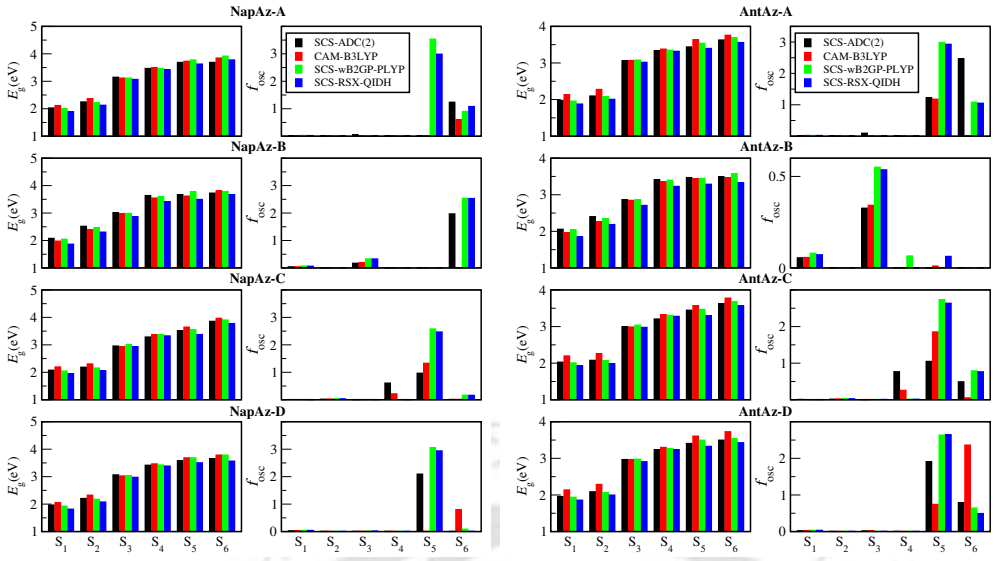

(A) (B)

FIGURE 6.4: Comparison of TD-DFT excitation energies (E_g) and oscillator strengths (f_{osc}) corresponding to the first six excited states with the SCS-ADC(2) results for the monomers of (A) **NapAz** and (B) **AntAz** isomers.

to those of their respective naphthalene derivatives. The absorption spectra of **AntAz-A**, **AntAz-B**, and **AntAz-D** exhibit strong absorption peaks around 3.63($S_0 \rightarrow S_6$), 3.60($S_0 \rightarrow S_7$), and 3.41($S_0 \rightarrow S_5$) eV, respectively. A few weak intensity peaks are also encountered around the higher and lower energy regions. Similar to **NapAz-C**, the absorption spectrum of **AntAz-C** also exhibits several small intensity absorption peaks. It is to be noted that the absorption maxima in isomers of the **AntAz** structure are slightly red-shifted from their respective isomers of the **NapAz** structure.

A comparison of the TD-DFT results with the SCS-ADC(2) results for **NapAz** and **AntAz** isomers is shown in Figure 6.4 and values are tabulated in Table D1 and D2, respectively. From Figure 6.4(A) and Table D1, it is observed that the E_g values for the first six excited states of each isomer of **NapAz** computed using the three DFT functionals generally do not vary much from the SCS-ADC(2) results (differences vary between 0.01 and 0.22 eV). However, differences are observed in the prediction of the f_{osc} values. For the planar isomers **NapAz-A** and **NapAz-B**, and the nonplanar isomer **NapAz-D**, the variation of f_{osc} values for the first four excited states observed in the results of three DFT functionals is almost similar to the SCS-ADC(2) results. For the S_5 and S_6 states of **NapAz-A**, however, the two LC-DH functionals show considerable

f_{osc} values, in contrast to the SCS-ADC(2) results. Table D1 also shows that the most intense transitions in **NapAz-B** and **NapAz-D** are predicted only by the two LC-DH functionals with slightly greater f_{osc} values. It is to be noted that the S_6 and S_7 states are almost degenerate with similar f_{osc} values in the SCS-ADC(2) results. In contrast to the DH functionals, CAM-B3LYP predicts the largest f_{osc} value for the S_7 state. For **NapAz-C**, according to the SCS-ADC(2) results, among the lower excited states, S_5 has the largest f_{osc} value which is reproduced by all the DFT functionals. The results for the **AntAz** isomers (Figure 6.4(B) and Table D2) shows that the E_gs for the first six excited states computed using CAM-B3LYP and SCS-RSX-QIDH functionals differ from the SCS-ADC(2) results by a maximum of 0.2 eV, whereas the SCS-ωB2GP-PLYP results differ by a maximum of 0.1 eV. In SCS-ADC(2) results, the most intense electronic transitions in **AntAz-B** and **AntAz-C** are $S_0 \rightarrow S_7$ and $S_0 \rightarrow S_5$, respectively, and the same is predicted by all of the DFT functionals. For **AntAz-A**, the SCS-ADC(2) results indicate that the S_5 state has an f_{osc} value of 1.225, while the S_6 state has an f_{osc} value of 2.469, almost double that of the S_5 state. This order is reversed in the results of two LC-DH functionals, where the S_5 state has a larger f_{osc} value than the S_6 state. In the CAM-B3LYP results, the S_5 state has an f_{osc} value of 1.183, whereas the order of the S_6 and S_7 states is interchanged as compared to SCS-ADC(2) results. In **AntAz-D**, the order of f_{osc} values between S_5 and S_6 states remains the same in SCS-ωB2GP-PLYP and SCS-RSX-QIDH functional results, whereas the order is reversed in the case of the CAM-B3LYP functional.

6.3.3.2 π-Stacked Dimers

The E_g values for the first six excited states of the π-stacked dimers are tabulated in Table 6.4. Similar to the monomers, here also **NapAz-D** has the smallest E_g value for the S_1 state among four the isomers. Comparing Tables 6.3 and 6.4, it is observed that the E_g values for the first six excited states in stacked dimers of each isomer are smaller than their respective monomer units. The decrease in E_g values is smaller for the S_1 states, whereas it is more prominent as we move from S_1 to S_6. For S_1 states, the E_g values in π-stacked dimers of **NapAz** isomers are 0.17-0.21 eV smaller in comparison

TABLE 6.4: Vertical Excitation Energies (E_g) (in eV) and Corresponding Oscillator Strengths (f_{osc}) for the First Six Excited States of the π-Stacked Dimers

	NapAz-A	**NapAz-B**	**NapAz-C**	**NapAz-D**
State	E_g / f_{osc}			
S_1	1.82 / 0.019	1.91 / 0.054	1.92 / 0.008	1.79 / 0.023
S_2	1.87 / 0.000	1.92 / 0.000	2.00 / 0.012	1.83 / 0.000
S_3	2.10 / 0.000	2.27 / 0.016	2.03 / 0.012	2.06 / 0.002
S_4	2.12 / 0.001	2.39 / 0.000	2.12 / 0.015	2.10 / 0.002
S_5	2.71 / 0.000	2.47 / 0.000	2.64 / 0.009	2.55 / 0.003
S_6	2.75 / 0.008	2.59 / 0.009	2.69 / 0.004	2.61 / 0.007
	AntAz-A	**AntAz-B**	**AntAz-C**	**AntAz-D**
S_1	1.88 / 0.000	1.89 / 0.000	1.91 / 0.002	1.82 / 0.017
S_2	1.88 / 0.028	1.90 / 0.079	1.91 / 0.019	1.85 / 0.001
S_3	2.00 / 0.003	2.13 / 0.015	1.96 / 0.007	1.99 / 0.002
S_4	2.03 / 0.000	2.26 / 0.000	2.01 / 0.015	2.03 / 0.001
S_5	2.68 / 0.000	2.32 / 0.000	2.61 / 0.004	2.56 / 0.003
S_6	2.70 / 0.011	2.45 / 0.009	2.73 / 0.000	2.61 / 0.009

to those of their monomeric units, whereas these values are 0.10-0.14 eV in **AntAz** isomers. For S_2 states, the E_g values for **NapAz-A** and **NapAz-D** are 0.38 eV smaller than their monomeric units, whereas in **NapAz-B** and **NapAz-C**, these values are 0.60 and 0.19 eV, respectively. E_g values for the S_2 states are 0.22, 0.50, 0.17, and 0.24 eV smaller in **AntAz-A**, **AntAz-B**, **AntAz-C**, and **AntAz-D** dimers, respectively, than the corresponding monomer values. On the other hand, in the case of the next four excited states, the E_g values are approximately 1.00 eV smaller than their respective monomer units. It is important to note that the π-stacked dimers of **NapAz-A** and **NapAz-D** have three pairs of closely lying excited states: S_1/S_2, S_3/S_4, and S_5/S_6, and the same observation is also made in the **AntAz** dimers. The f_{osc} values for the S_1 states of **NapAz** and **AntAz** isomers are small, similar to monomer results. The brightest states in the monomers become almost dark in the corresponding dimers, for example, S_6 states of **NapAz-A** and **NapAz-B**, S_4-S_5 states of **NapAz-C**, and the S_5 state of **NapAz-D** have negligible f_{osc}s. Similar results are also observed in the case of **AntAz** isomers, in which S_5-S_6 states of **AntAz-A** and **AntAz-D**, and S_4-S_6 states of **AntAz-C** have very small f_{osc} values in dimeric forms compared to their monomeric forms. The f_{osc} values of S_5 and S_6 states in stacked dimers are small due to the CT characters of these states, which are shown in the later section.

The simulated absorption spectra of all four isomers for **NapAz** and **AntAz** are shown

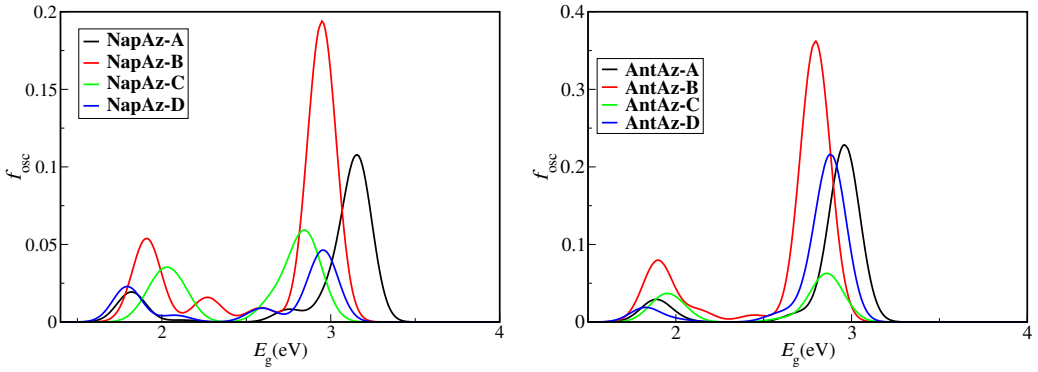

FIGURE 6.5: Comparison of simulated absorption spectra for π-stacked dimers of four different isomers of **NapAz** (left panel) and **AntAz** (right panel) obtained at the SCS-ADC(2)/def2-TZVP level.

in Figure 6.5. The figure shows that each isomer of **NapAz** and **AntAz** structures exhibits more than one absorption peak. It is also observed that both **NapAz-B** and **AntAz-B** dimers show the highest intensity absorption peaks. The highest peaks in these absorption spectra arise due to $S_0 \rightarrow S_8$(at 2.95 eV) and $S_0 \rightarrow S_9$(at 2.79 eV) for **NapAz-B** and **AntAz-B**, respectively. In addition, the **NapAz-B** isomer has two small intensity peaks in the lower energy region (at 1.92 and 2.27 eV), whereas **AntAz-B** shows one peak in the lower energy region (at 1.90 eV). The high-intensity peaks in the absorption maxima of **NapAz-A**, **NapAz-C**, and **NapAz-D** are obtained at 3.16 ($S_0 \rightarrow S_{10}$), 3.82($S_0 \rightarrow S_8$), and 2.97 eV($S_0 \rightarrow S_{10}$), respectively. For **AntAz-A**, **AntAz-C**, and **AntAz-D**, the pattern of absorption spectra is similar to the absorption spectra of the **AntAz-B** isomer. The high-intensity absorption peaks of **AntAz-A**, **AntAz-C**, and **AntAz-D** isomers arise due to $S_0 \rightarrow S_9$(at 2.98 eV), $S_0 \rightarrow S_{10}$(at 2.82 eV), and $S_0 \rightarrow S_{10}$(at 2.89 eV), respectively.

Figure D3 and Table D3 show a comparison of the TD-DFT energies and f_{osc} values with the SCS-ADC(2) results. From Table D3, it is observed that the E_g values for **NapAz** isomers calculated using the DFT functionals deviate from the SCS-ADC(2) results by a maximum of 0.36 eV, which happens in the case of S_{10} of **NapAz-B** for SCS-RSX-QIDH. From f_{osc} values, it is observed that the orders of f_{osc}s for S_5 and S_6 states in **NapAz-A**, and S_1 and S_2 states in **NapAz-B** are interchanged in CAM-B3LYP results, whereas the trend of f_{osc}s for the S_1-S_6 states in **NapAz-C** and **NapAz-D** remains the same, as compared to the SCS-ADC(2) results. For SCS-ωB2GP-PLYP, the

S_1 states are the brightest in **NapAz-A** and **NapAz-D**, while S_4 has the largest f_{osc} value for **NapAz-C**. However, in **NapAz-B**, the largest f_{osc} (0.292) value is observed for the S_8 state which matches with the SCS-ADC(2) value. Results for **AntAz** isomers are shown in Figure D4 and tabulated in Table D4. Among the first six states, the prominent electronic transitions in each isomer are predicted by all the DFT functionals; for example, the S_2 states of **AntAz-A** and **AntAz-B**, the S_2 and S_4 states of **AntAz-C**, and the S_1 and S_6 states of **AntAz-D** isomers. For S_7-S_{10} in **AntAz-A**, CAM-B3LYP predicts the f_{osc} value for S_8, while the DH functionals show zero f_{osc}s. In **AntAz-B**, the f_{osc} values indicate a possible swapping of the S_9 and S_{10} states. Similarly, both the DH functionals show swappings of S_8 and S_9 states. In case of the **AntAz-C** and **AntAz-D**, trends in f_{osc} values for S_7-S_{10} states in CAM-B3LYP are similar to SCS-ADC(2) results.

6.3.4 Excited State Characterization

For the computation of the Ω matrix containing all Ω_{AB} values, each monomer is divided into three fragments, and each stacked dimer is divided into six fragments. The fragmentation schemes for a monomer and a stacked dimer are shown in Figure D5 considering one of the isomers of **NapAz**. Therefore, plotting of Ω gives 3×3 and 6×6 matrices for monomers and dimers, respectively.

6.3.4.1 Monomers

The values of the three descriptors ω_{CT}, d_{exc}, and PR_{NTO} computed for the four isomers of **NapAz** and **AntAz** are tabulated in Table D5, and a comparison of the first two descriptors is shown in Figure 6.6. The ω_{CT} values of the first four excited states in **NapAz-A** are in the range of 0.26-0.47, in which the S_2 state has the smallest ω_{CT} value of 0.26. In addition, the S_6 and S_8 states also have ω_{CT} values of 0.55 and 0.50, respectively. However, the value is 0.93 for the S_5 state, indicating the CT nature of this state. The d_{exc} value for the S_5 state (d_{exc}=7.93) is comparatively larger than the other states, in accordance with the ω_{CT} values. The *e*-*h* correlation plots for the first four excited states shown in Figure 6.7 are similar to each other, in which the diagonal shows that the *e*-*h* pair or exciton is delocalized between fragments 1 and 2. The Ω_{AB}

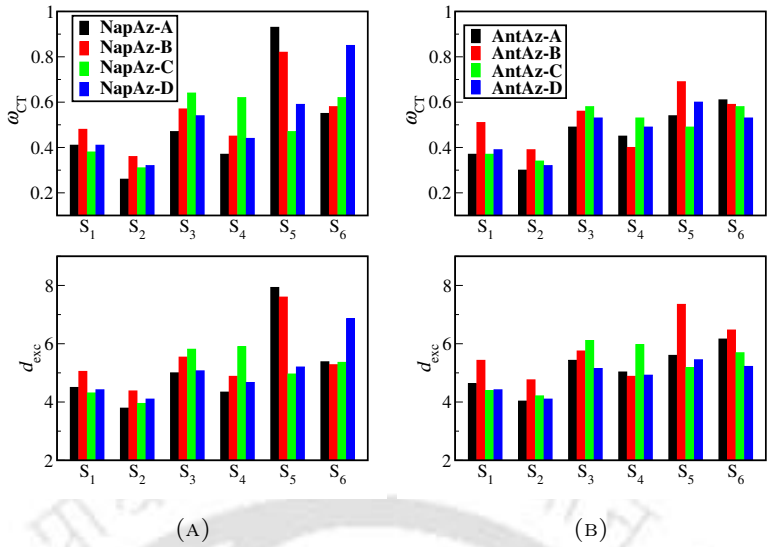

FIGURE 6.6: CT parameter (ω_{CT}) and exciton size (d_{exc}) for the first six excited states for monomers of (a) **NapAz** and (b) **AntAz** isomers at the SCS-ADC(2)/def2-TZVP level.

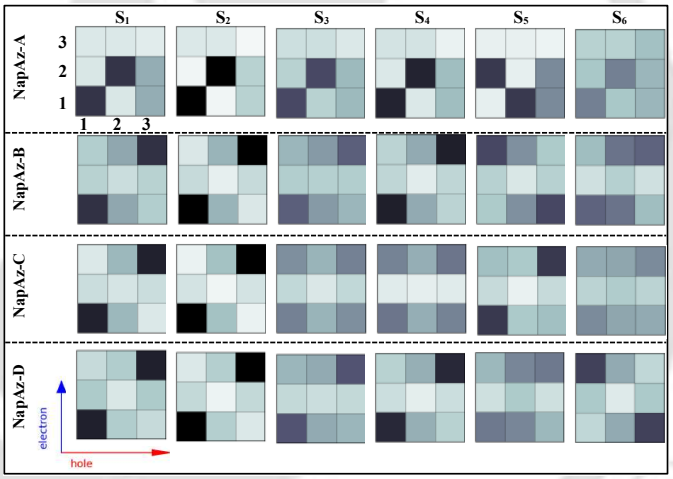

FIGURE 6.7: Electron-hole correlation plots for the first six excited states of the monomers of **NapAz-A**, **NapAz-B**, **NapAz-C**, and **NapAz-D** obtained at the SCS-ADC(2)/def2-TZVP level.

matrix for the S_5 state shows comparatively intense off-diagonal widths along both the e and h directions, indicating the movement of e from fragment 1 to fragment 2, and vice versa. As a result, this state is considered a charge resonance (CR) state. Similar to **NapAz-A**, the S_5 and S_9 states of **NapAz-B** also have large ω_{CT} (0.82) values and the d_{exc} values are also larger for these than the other excited states. The S_3, S_6, S_8 and S_{10} states also have slightly large ω_{CT} values (≈ 0.6) and may be considered as partially CT states. The e-h correlation plot for the S_5 state in **NapAz-B** shown in Figure 6.7 has off-diagonal contributions at the two terminals, indicating a CR state. The S_3 and S_6

states also show off-diagonal elements, indicating their partial CT nature. In the case of **NapAz-C**, the values of ω_{CT} for the S_1, S_2 and S_5 states are in the range of 0.31-0.47, whereas the remaining states have values larger than 0.6, indicating partial CT natures. The d_{exc} values shown in the same table follow the order of the ω_{CT} values. The small intense off-diagonal contribution to the *e*-*h* correlation plots of S_3, S_4 and S_6 states is in accordance with the ω_{CT} values. The other three states have diagonal contributions at the two terminals, which signifies exciton localization at the terminal fragments. The excited state results of **NapAz-D** shown in Table D5 differ from those of the other three isomers. Here, S_6 has a large ω_{CT} value of 0.85 with a d_{exc} value of 6.86 Å, indicating its CT character. While the first two states are LE states, the ω_{CT} values are ≥ 0.54 for the others. The *e*-*h* correlation plot of the S_6 state has off-diagonal contributions at the two terminals, indicating a CR state. However, comparatively less intense off-diagonal width can be seen in S_3 and S_5 states, indicating a partial CT state.

The PR_{NTO} values in Table D5 show that two pairs of NTOs are required to describe the S_5 states of all **NapAz** isomers. On the other hand, while only one set of NTOs is required for the $S_0 \rightarrow S_1$ transition in **NapAz-B**, two pairs of NTOs take part in describing the same state for the others. The NTOs involved in the S_1 and S_5 states for the **NapAz** isomers are shown in Figure D6. The figure shows that, in each isomer, the *e* and *h* orbitals of the first pairs of NTOs corresponding to the S_0-S_1 transitions are evenly distributed over the whole monomeric units. For the second pairs of NTOs in **NapAz-A** and **NapAz-C**, the *e* orbitals are situated over the two terminal azulene units, whereas the *h* orbitals are distributed over the whole monomeric units. The weight of the second pair of NTOs is smaller than that of the first pair, and this leads to a small ω_{CT} value. A significant difference is observed in the case of the S_5 states. In **NapAz-A**, the first pair of NTOs show that the *h* orbitals are localized on the central fragment, whereas the *e* orbitals are situated at the terminal fragments. Similarly, in **NapAz-B**, the *h* and *e* orbitals for the second set of NTOs are located on different fragments. However, in **NapAz-C** and **NapAz-D** isomers, no clear difference between the positions of the *e* and *h* orbitals is observed in either pair of the NTOs.

Among the states of the **AntAz** isomers, two states in **AntAz-B** and only the S_7 states

in **AntAz-A** and **AntAz-D** have ω_{CT} values larger than 0.7, indicating their pure CT nature. Some of the other excited states in each isomer have ω_{CT} values of 0.45-0.69 and may be considered as partial CT states. The d_{exc} values shown in the same table follow the trend of the ω_{CT} values. The *e*-*h* correlation plots for the ten excited states are shown in Figure D7. These correlation plots reiterate that S_7 states in **AntAz-A** and **AntAz-D**, for example, are CT states. The PR_{NTO} values tabulated in Table D5 indicate that two pairs of NTOs are required to describe the S_1 and S_5 states in most of the cases. The NTOs involved in the S_1 and S_5 states are plotted in Figure D8. In each isomer, the NTOs of S_1 state show that the *e* and *h* densities are distributed over the same fragments. For the S_5 state of **AntAz-A**, small changes in the positions of *h* and *e* orbitals are observed for the first pair of NTOs, whereas in **AntAz-B** and **AntAz-D**, the changes are observed for the second pair of NTOs. This leads to comparatively larger ω_{CT} values for the S_5 states. No major differences in the positions of *e* and *h* orbitals are observed in the NTOs of the states for the **AntAz-C** isomer.

The values of the descriptors are also calculated at the TD-DFT level using the three DFT functionals, and the results are compared with the SCS-ADC(2) results. In the following, we only discuss the ω_{CT} values and the *e*-*h* correlation plots. The results for the **NapAz** isomers are shown in Figure 6.8. In **NapAz-A**, all of the DFT functionals reliably predict the ω_{CT} values of the first four and S_6 excited states. However, among the three DFT functionals, only the CAM-B3LYP correctly estimates the CT character of the S_5 state. The *e*-*h* correlation plots for the S_1-S_4 and S_6 states (shown in Figure D9) obtained using the DFT functionals align with the ω_{CT} values. For **NapAz-B**, only the SCS-ωB2GP-PLYP functional correctly predicts the CT character of the S_5 state. The other two functionals suggest the CT characters for the S_4 states, in contrast with the SCS-ADC(2) results. The *e*-*h* correlation plots presented in Figure D10 corroborate the above results. A closer look at these correlation plots makes it clear that the state ordering for S_4 and S_5 states is changed in CAM-B3LYP and SCS-RSX-QIDH functionals. In **NapAz-C**, the CAM-B3LYP functional reproduces the partial CT character of the S_3 and S_6 states predicted by SCS-ADC(2). However, the order of ω_{CT} values for the S_4 and S_5 states is reversed in CAM-B3LYP results, indicating state swapping. The ω_{CT} values for the S_1-S_2 and S_5-S_6 states obtained using the two LC-DH functionals are

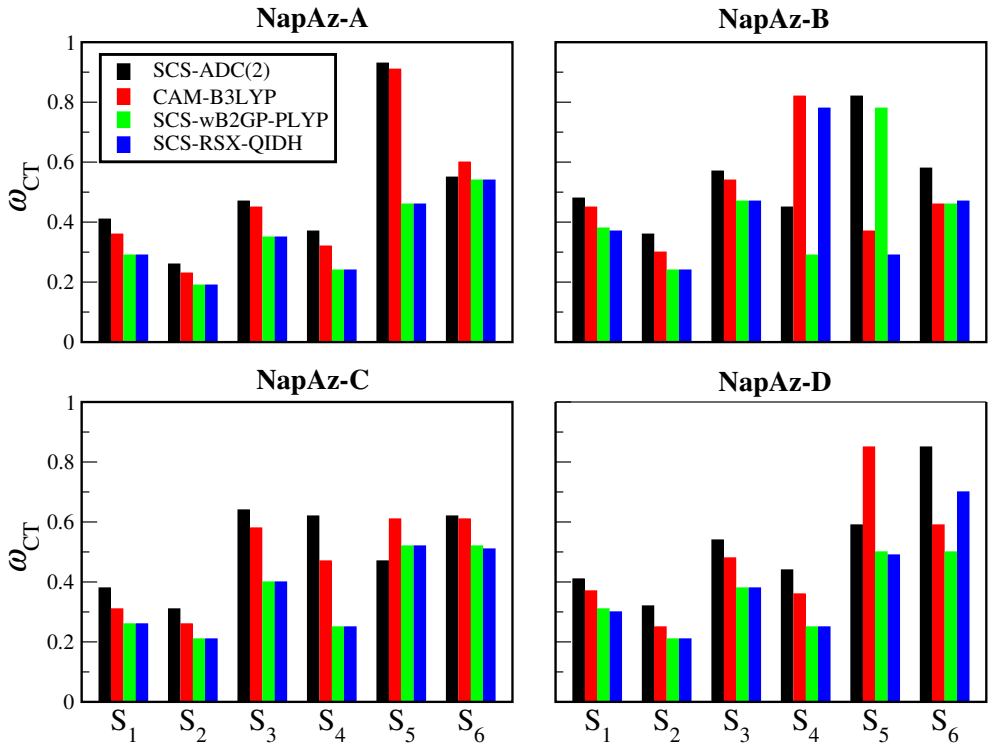

FIGURE 6.8: Comparison of TD-DFT ω_{CT} values for the first six excited states with the SCS-ADC(2) results for the monomers of **NapAz-A**, **NapAz-B**, **NapAz-C**, and **NapAz-D**.

close to SCS-ADC(2) values, however, for the S_3-S_4 states, the results are away from SCS-ADC(2) results. The *e-h* correlation plots for **NapAz-C** shown in Figure D11 align with the ω_{CT} results. In **NapAz-D**, the SCS-ADC(2) results predict the partial CT and CT characters of the S_5 and S_6 states, respectively. Similar results are observed in the SCS-RSX-QIDH functional, while the results are reversed in CAM-B3LYP. On the other hand, the SCS-ωB2GP-PLYP results predict partial CT character for both states. The *e-h* correlation plots also predict the same as shown in Figure D12.

The TD-DFT results for the **AntAz** isomers are tabulated in Table D7 and shown in Figure D13. In **AntAz-A**, the ω_{CT} values for the first five excited states computed using the three DFT functionals closely match the SCS-ADC(2) results. However, while the SCS-ADC(2) results indicate partial CT and full CT characters for the S_6 and S_7 states, respectively, the order interchanges in CAM-B3LYP results, as shown in Table D7. The two DH functionals predict partial CT for both states. The CT characters of S_9 and S_{10} states in **AntAz-B** are only predicted by CAM-B3LYP, while the other

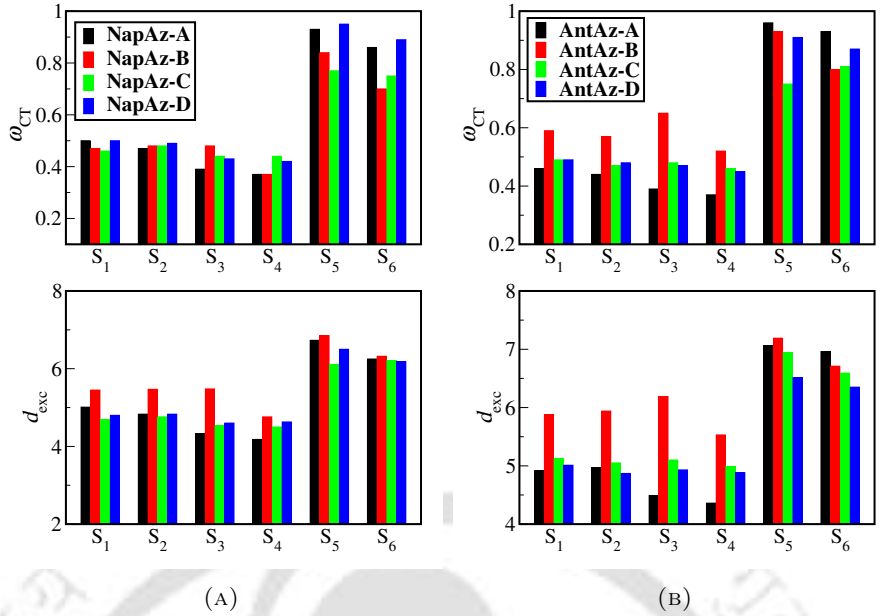

FIGURE 6.9: Values of CT parameter (ω_{CT}) and exciton size (d_{exc}) for the first six excited states of dimers of (a)**NapAz** and (b)**AntAz** isomers at the SCS-ADC(2)/def2-TZVP level.

two functionals predict partial CT characters of these states. The partial CT states in **AntAz-C** are explained well by CAM-B3LYP. In **AntAz-D**, the CT character of the S_7 state is explained by CAM-B3LYP and SCS-RSX-QIDH functionals.

6.3.4.2 π-Stacked Dimers

For the π-stacked dimers, the values of the three descriptors are listed in Table D8. Figure 6.9 shows plots of values of ω_{CT} and d_{exc} for the six states. The ω_{CT} values for the S_1-S_4 states of each **NapAz** isomer range from 0.37 to 0.50. Values of 0.70-0.95 are observed for a few other higher excited states. For example, the S_5 and S_6 states in all of the isomers are CT states. Accordingly, in each isomer, the d_{exc} values for the S_5 and S_6 states are comparatively larger (6.11-6.85) than the values for the first four excited states (4.18-5.45). The *e*-*h* correlation plots presented in Figure 6.10 also suggest the same for the excited state characters. The *e*-*h* correlation plots corresponding to the first four excited states in **NapAz-A** exhibit a pattern dominated by diagonal contributions, whereas in the case of S_5 and S_6 states, the off-diagonal contributions over fragments 4, 5, and 6 along both *e* and *h* axes indicate mutual CT between the two monomeric units, leading to CR states. Similar results are observed in the case of the **NapAz-B** isomer;

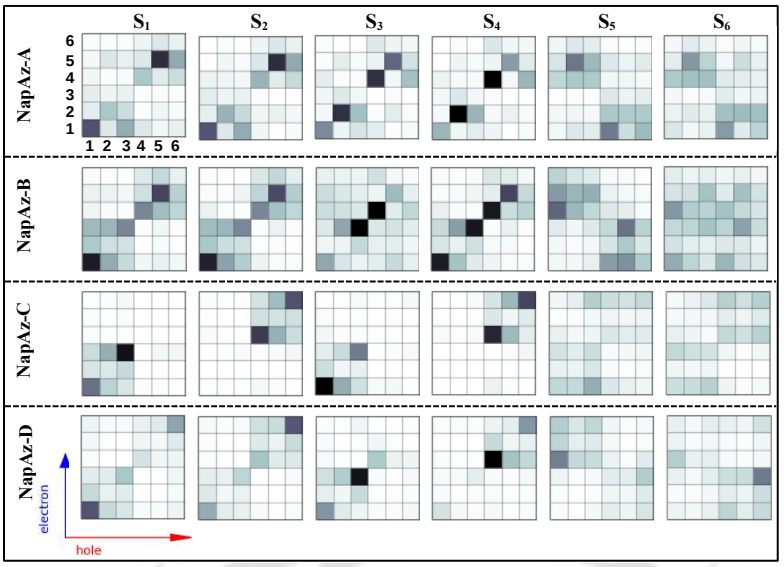

FIGURE 6.10: Electron-hole correlation plots for first six excited states of the π-stacked dimers of **NapAz-A**, **NapAz-B**, **NapAz-C**, and **NapAz-D** at the SCS-ADC(2)/def2-TZVP level.

while dominant diagonal contributions are observed in cases of the first four excited states, off-diagonal contributions are dominant in S_5. However, the S_6 state shows a quite different pattern involving both diagonal and off-diagonal contributions. In the *e*-*h* correlation plots for the first four excited in **NapAz-C**, the contributions are from one of the monomeric units (i.e., either fragments 1, 2, and 3 or fragments 4, 5, and 6), indicating that the exciton is confined to a single monomeric unit. It is to be noted that there are some off-diagonal contributions in each case, representing intramolecular CT. The S_5 and S_6 states exhibit both diagonal and off-diagonal widths, which is consistent with their relatively smaller ω_{CT} values than those of the other three isomers. For the S_5 and S_6 in **NapAz-D**, the off-diagonal contributions are mainly present on one of the monomeric units, indicating CT from one monomeric unit to another and these are considered as intermolecular CT states.

The NTOs involved in the $S_0 \rightarrow S_1$ and $S_0 \rightarrow S_5$ transitions for the four isomers of the **NapAz** structures are shown in Figure 6.11. In **NapAz-A**, **NapAz-B**, and **NapAz-D**, the *h* and *e* orbitals of the S_1 state are distributed over both the monomeric units, and there is no significant difference in the positions of *e* and *h* orbitals. On the other hand, in **NapAz-C**, the *e* and *h* densities are localized over single monomeric units with no change in positions. In S_5 states of **NapAz-A**, **NapAz-B**, and **NapAz-C**, the *e* and

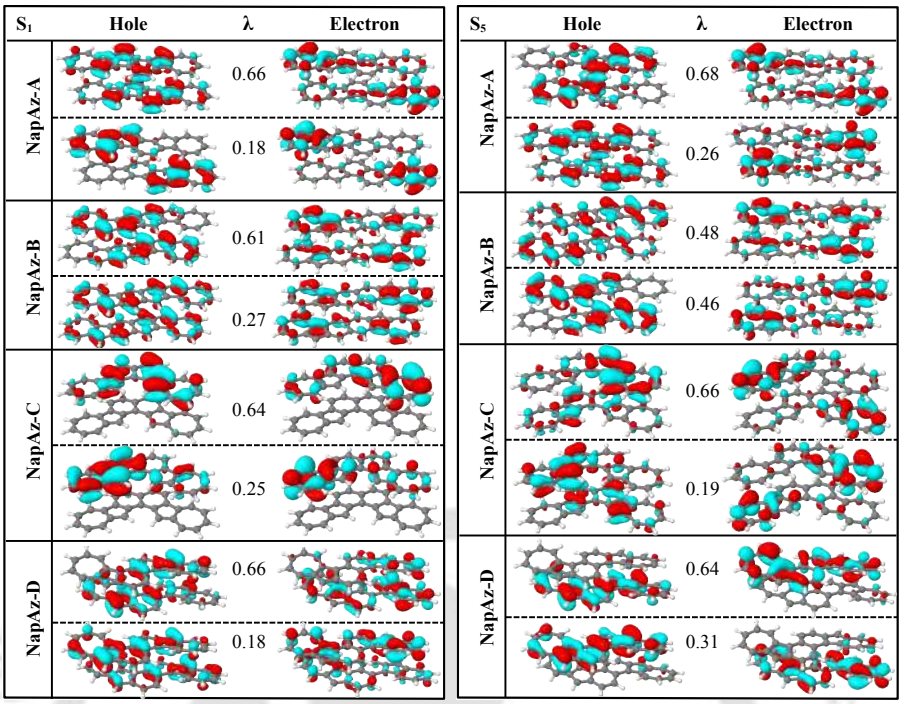

(A) (B)

FIGURE 6.11: NTOs involved in (a) S_1 and (b) S_5 states for the π-stacked dimers of **NapAz-A**, **NapAz-B**, **NapAz-C**, and **NapAz-D**, obtained at the SCS-ADC(2)/def2-TZVP level. The eigenvalue λ indicates the weight of the pair's contribution.

h densities are found in both the monomeric units at different locations, representing CR states. However, for S_5 in **NapAz-D**, *h* and *e* orbitals are over different monomeric units, indicating unidirectional CT from one monomeric unit to another.

Excited-state characterization of **AntAz** shows results similar to those of the corresponding **NapAz** isomers. Table D8 shows that, for **AntAz** isomers, the ω_{CT} values for the S_5 and S_6 states in each isomer are larger (ranging from 0.75 to 0.96) compared to the first four excited states. As expected, the d_{exc} values (6.35-7.19) are also large in the cases of S_5 and S_6 states in each isomer. The ω_{CT} values for the other four higher excited states are also comparatively large. Comparing the values for the first four states, it is found that the values for the first four excited states of the **AntAz-B** isomer are slightly larger (0.52-0.68) compared to the S_1-S_4 results of the other three isomers. The *e*-*h* correlation plots for six excited states and NTOs corresponding to S_1 and S_5 states are shown in Figures D14- D16, respectively. In **AntAz-A**, the *e*-*h* correlation plots for the S_1-S_4 states show that the exciton is spread mostly along the diagonal width. Figure D15 containing the NTOs for S_1 shows that the *h* and *e* densities

are distributed across all of the fragments, confirming the delocalization of the exciton. For the S_5 and S_6 states, in accordance with the ω_{CT} values, the *e*-*h* correlation plots show their CR characters. The NTOs for the S_5 state (Figure D16) confirm these results by displaying *h* and *e* densities over both monomeric units, albeit in different fragments. In **AntAz-B**, large diagonal contributions are observed for the S_1-S_4 states with small contributions from the off-diagonals in the monomeric units, and this is responsible for slightly larger ω_{CT} values for these four states than the S_1-S_4 states of the other three isomers. Differences in the positions of *h* and *e* densities are observed in the NTOs of the S_1 state (Figure D15), indicating its partial CT character. The *e*-*h* correlation plot and NTOs indicate the CR character of the S_5 state. In contrast, a different pattern in the *e*-*h* correlation plots is observed for the S_6 state, where both diagonal and off-diagonal contributions are present. For the S_1-S_4 states of **AntAz-C** and **AntAz-D**, Figure D14 shows that the densities of Ω_{AB} are concentrated either along the diagonals or around the diagonals of one monomeric unit, signifying the localization of the exciton in single monomeric units. The NTOs involved in $S_0 \rightarrow S_1$ transitions (Figure D15) also predict the same by showing *h* and *e* densities over the same monomeric unit. In **AntAz-C**, both diagonal and off-diagonal contributions are observed for the S_5 and S_6 states. The NTOs for the S_5 state show that the *h* orbitals are mainly distributed over the central fragments of both monomeric units, whereas the *e* densities are on the terminal azulene units, indicating intramolecular CT. In the **AntAz-D**, the *e*-*h* correlation plots and NTOs indicate the CR character of the S_5 and S_6 states.

A comparison of ω_{CT} values obtained using the three DFT functionals with the SCS-ADC(2) results is shown in Figure 6.12, and the values are listed in Table D9. As the figure shows, in most cases, the LE characters of the first four excited states are well explained by all of the DFT functionals. However, the distinction occurs when describing the CT characters of S_5 and S_6 states. The CT character of the S_6 state in **NapAz-A** is correctly estimated by all the DFT functionals, whereas the CT character of S_5 is explained by only CAM-B3LYP and SCS-RSX-QIDH functionals. The *e*-*h* correlation plots shown in Figure D17 confirm the TD-DFT results. In the case of **NapAz-B**, the CT character of the S_5 state is only explained by the SCS-ωB2GP-PLYP functional, while the other two functionals show the CT character for the S_4 state. The *e*-*h* correlation

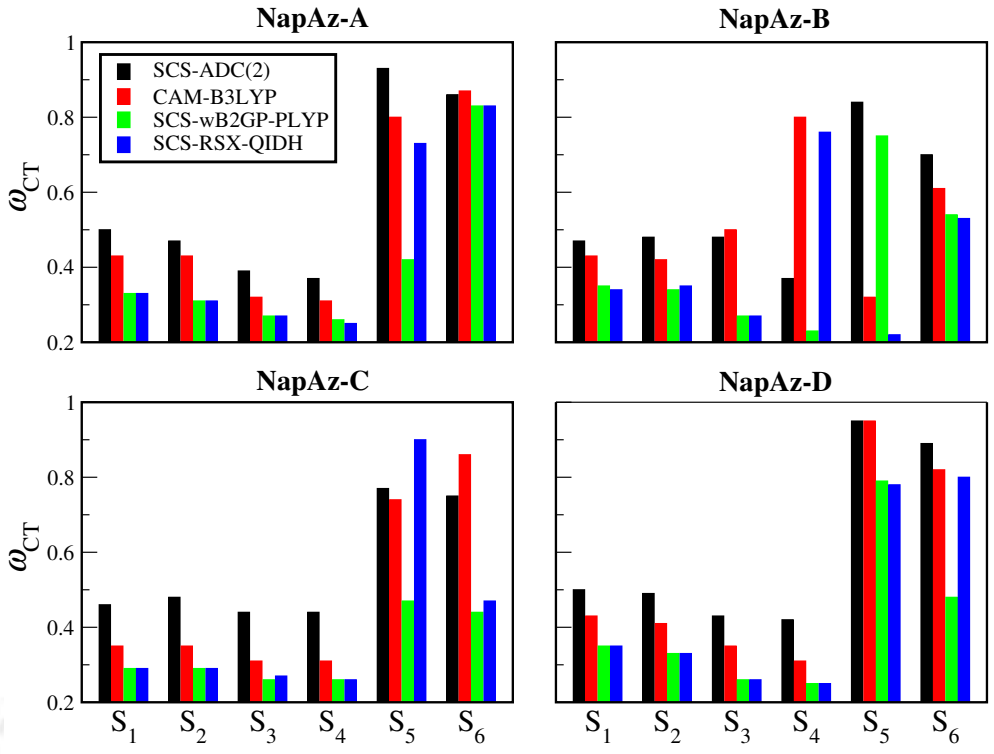

FIGURE 6.12: Comparison of ω_{CT} values obtained using three DFT functionals with the SCS-ADC(2) results for the π-stacked dimers of **NapAz** isomers.

plots of S_4 and S_5 states presented in Figure D18 confirm that the state order of S_4 and S_5 is reversed in the CAM-B3LYP and SCS-RSX-QIDH results. For the S_6 state, the ω_{CT} values computed using all DFT functionals are small compared with the SCS-ADC(2) values. For **NapAz-C**, the ω_{CT} values obtained using CAM-B3LYP and SCS-RSX-QIDH functionals indicate the CT character of the S_5 state, whereas for the S_6 state, only CAM-B3LYP reproduced the SCS-ADC(2) results. The *e*-*h* correlation plots shown in Figure D19 corroborate the above results. It is interesting to note that the S_7-S_8 states have CT characters according to SCS-ADC(2) results, and these are also explained by the CAM-B3LYP functional. In isomer **NapAz-D**, ω_{CT} values and the *e*-*h* correlation plots (shown in Figure D20) for the S_5 state obtained using all of the DFT functionals are similar to the SCS-ADC(2) results. For the S_6 state, only the SCS-ωB2GP-PLYP functional is not able to describe the CT character. Like **NapAz-C**, here also the CT characters of S_7-S_{10} are reproduced by the CAM-B3LYP functional.

The TD-DFT results for the **AntAz** isomers are plotted in Figure D21 and the data are tabulated in Table D10. Similar to the **NapAz** isomers, the LE characters of the

first four excited states, in **AntAz-A**, **AntAz-C** and **AntAz-D**, are explained by all of the DFT functionals. In **AntAz-A**, all of the DFT functionals correctly estimate the CT character of the S_5 and S_6 states. For **AntAz-B**, the state order of S_4 and S_5 states is swapped in CAM-B3LYP results compared to the SCS-ADC(2) results. The SCS-ωB2GP-PLYP results predicted the partial CT characters for the S_5 and S_6 states, while the SCS-RSX-QIDH functional predicted the CT and partial CT characters of S_5 and S_6 states, respectively. For **AntAz-C**, the ω_{CT} values for the S_5 and S_6 states obtained using the CAM-B3LYP and SCS-RSX-QIDH functionals are close to the SCS-ADC(2) results, whereas these values are smaller in the SCS-ωB2GP-PLYP results. In isomer **AntAz-D**, the CAM-B3LYP functional correctly estimates the CT characters of both S_5 and S_6, whereas SCS-ωB2GP-PLYP and SCS-RSX-QIDH functionals predicted the CT characters of S_6 and S_5 states, respectively. A detailed examination of ω_{CT} values in Table D10 reveals that the CAM-B3LYP can also describe the CT characters of S_7-S_{10} states in most cases (**AntAz-A**, **AntAz-C**, and **AntAz-D**).

6.4 Conclusions

In this work, we report the results of an investigation on the excited properties of monomers and π-stacked dimers corresponding to four different isomers of azulene-fused naphthalene and anthracene. The results obtained at the TD-DFT level are compared against the SCS-ADC(2) results. In the case of monomers, the SCS-ADC(2) analysis revealed that low-lying excited states are mostly of local excitation types. A few higher-lying excited states exhibit either partial or full CT characteristics. In the case of stacked dimers, the excited state results are different from those of their monomeric forms. For **NapAz-A**, **NapAz-B**, and **NapAz-C**, S_5 and S_6 states are mainly CR type states where there are mutual CTs between the two monomeric units, whereas a unidirectional intermolecular CT is observed in isomer **NapAz-D**. Similar results are observed for the **AntAz** isomers, where a few higher excited states have large ω_{CT} values. The S_5 and S_6 states of **AntAz-A** and **AntAz-D** and the S_5 state of **AntAz-B** have CR characters, whereas the S_5 and S_6 states in **AntAz-C** are intramolecular CT type. The CT characters of many excited states in most cases of monomers and π-stacked dimers are

explained well by the CAM-B3LYP functional. However, among the two LC-DH functionals, the SCS-RSX-QIDH shows promising results for describing the CT character in π-stacked dimers, whereas in most cases, the results of the SCS-ωB2GP-PLYP functional underestimate the SCS-ADC(2) results.

Chapter 7

Conformation-induced excimer formation in covalently-linked dimer of azulene-fused anthracene

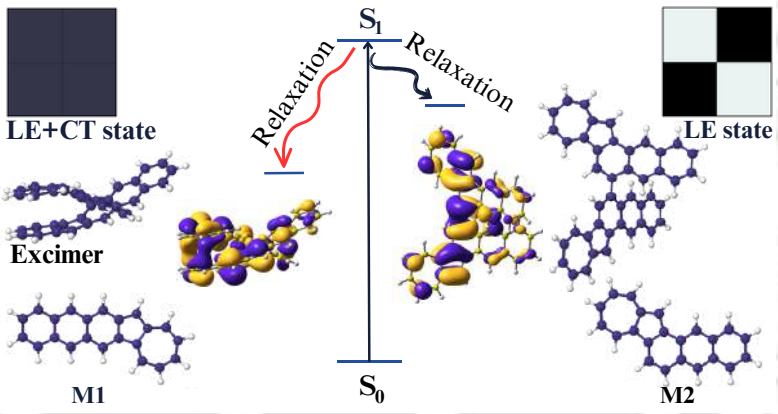

In this chapter, we explore excimer formation in a specific conformer of covalently linked azulene-fused anthracenes, out of two conformers, **M1** and **M2**, using the MP2 and ADC(2) methods. In conformer **M1**, the azulene units are oriented towards each other, leading to excimer formation in the S_1 state. This is confirmed by the orbital overlap of the azulene units and the charge transfer (CT) character of the S_1 state. In contrast, in conformer **M2**, the azulene rings are oriented away from each other, and this results in minimal geometric changes in the excited state geometry, keeping the CT features intact. Reproduced from "*The Journal of Physical Chemistry A*, **2025**, 129(4), 1085–1098" with permission from American Chemical Society.

7.1 Introduction

Excimer formation is observed in various multichromophoric systems, such as in covalently-linked dimers,[27,32,33,238,239] and co-facial,[25,34,240] and slip-stacked[25,241] arrangements of conjugated molecular systems. Among these, covalently-linked dimers are structurally more susceptible to showing dynamic electronic interaction in the excited state.[32,33,242] This flexibility in terms of interchromophoric torsional motion can enable transitions from LE states to symmetry-breaking charge separation (SB-CS).[243–245] In addition, structural relaxation accompanying this torsional motion often results in excimer formation.[32,33] For instance, an experimental and theoretical investigation by Hariharan and coworkers[32] showed the mechanism of structural relaxation in an excited state leading to an excimer formation in a covalently-linked orthogonal perylenediimide dimer, noting its inhibitory effect on the SB-CS. In these orthogonal dimers, such relaxation induces a π-stacked foldamer geometry, promoting strong interactions between the two chromophores in the excited state and resulting in stabilization. Similarly, Xia and coworkers studied the excimer formation in a covalently linked aminonaphthalimide dimer using spectroscopic tools. They also computed exciton and CT coupling between NI units during structural relaxation at the TD-DFT level to explain excimer formation.[33]

Recent studies have highlighted the potential of covalently linked orthogonal tetracene[246,247] and pentacene[248,249] dimers as promising materials for efficient SF processes. In these systems, the CT states play a crucial role in mediating the formation of correlated triplet pairs ^{1}(TT) and facilitating the SF fission process. It is known that the chemical stability of acenes decreases with an increase in the size of acenes.[225,226] To address this issue, one promising approach is to substitute the two benzenoid rings with a non-benzenoid azulene moiety. This substitution results again in an all-carbon polyaromatic hydrocarbon that maintains chemical stability while exhibiting desirable optoelectronic properties.[75–77,79] In our study, we explore how replacing two benzenoid rings with azulene moieties in both pentacene units of the directly linked pentacene dimer can lead to the formation of an excimer. For this, we have considered two different conformers, **M1** and **M2**, as shown in Figure 7.1. The two monomers differ in their locations of fusion of azulene units with

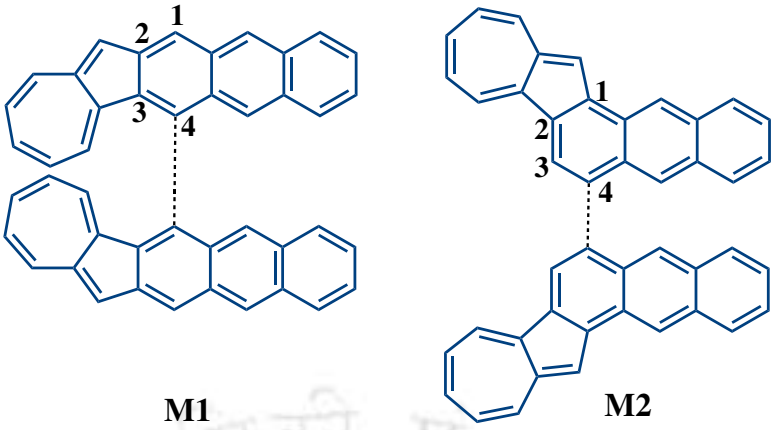

FIGURE 7.1: Schematic representation of two conformers **M1** and **M2** of covalently-linked dimer of azulene-fused anthracene.

the anthracenes; while in conformer **M1**, the five-membered rings of the azulene units are fused at the 2, 3 positions of the anthracene, in **M2**, the five-membered rings are fused at the 1, 2 positions. As shown in Figure 7.1, the monomers are covalently linked via the C4 carbon atoms of the anthracene units. Computational and theoretical studies are very important tools to underpin excimer formation. Theoretical and computational studies are usually performed at the TD-DFT level to explain excimer formation.[32,241,250] In our study, we employ the Møller-Plesset perturbation theory to the second order(MP2)[84] and ADC(2) methods to study the excimer formation. We discuss the excimer formation by computing the CT characters, observing molecular orbital (MO) interactions, and the structural changes occurring during the excimer formation.

7.2 Computational Details

Geometry optimizations in the ground state are performed using the MP2 method. The vertical excitation energies (E_g) calculations and excited-state optimizations are carried out using the ADC(2) method in conjunction with the def2-SVP basis set. Resolution of identity (RI)[195] approximation is used in all the calculations. In all the calculations, the geometries of molecular systems are constrained to the C_2 point group. For the computation of the Ω matrix containing all Ω_{AB} values, each system is divided into two fragments, **A** and **B**. The fragmentation scheme considering conformer **M2** is shown in Figure E1. Therefore, plotting of Ω gives 2x2 matrices shown in Figure 7.3. The

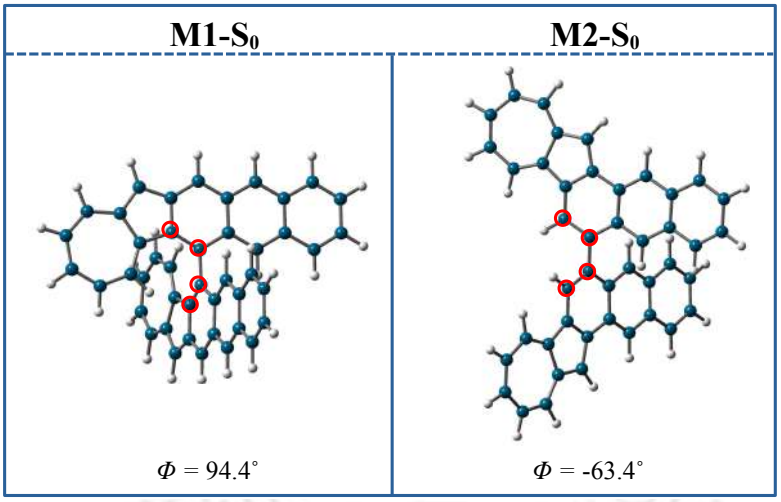

FIGURE 7.2: Ground state (S_0) optimized geometries of the two conformers **M1** and **M2** obtained at the RI-MP2/def2-SVP level. The dihedral angles between the four carbon atoms, denoted as ϕ in text, are marked by the red circles.

Turbomole V7.2[196] software is used for the RI-MP2 and RI-ADC(2) calculations. The CT analysis is carried out using the TheoDORE 3.0 software package[170].

7.3 Results

7.3.1 Ground State and Vertical Excitation

At first, the validity of the methods is checked by performing additional calculations for the experimentally studied 3,13′-bis(mesityl)-6,6′-dipentacenyl (DP-Mes).[248,249] The S_0 optimized geometry of DP-Mes, shown in Figure E2, obtained at the RI-MP2 level shows a near-orthogonal geometry, similar to the X-ray crystallography results.[248] The calculated vertical excitation energy of the S_1 state at RI-ADC(2)/ def2-SVP level is 2.14 eV, which is also close to the experimentally observed energy value of 2.02 eV.[248]

The ground state optimized geometries of the conformers **M1** and **M2**, denoted as **M1-S$_0$** and **M2-S$_0$**, respectively, obtained at the RI-MP2/def2-SVP level are shown in Figure 7.2. **M2-S$_0$** is energetically more stable than the **M1-S$_0$** with an interchromophoric dihedral angle (ϕ) of -63.4°. On the other hand, **M1-S$_0$** has a nearly orthogonal geometry with a ϕ value of 93.7°. The two conformers have almost the same interchromophoric C-C bond distance, ≈1.47 Å.

TABLE 7.1: Vertical excitation energy/oscillator strength (E_g/f_{osc}) and the corresponding ω_{CT} values for the first six excited states computed at the RI-ADC(2)/def2-SVP level for the S_0 optimized geometries.

	M1-S_0			**M2-S_0**		
State		E_g/f_{osc}	ω_{CT}		E_g/f_{osc}	ω_{CT}
S_1	1^1B	1.93 / 0.044	0.02	1^1A	1.90 / 0.007	0.04
S_2	1^1A	1.95 / 0.017	0.02	1^1B	1.90 / 0.015	0.04
S_3	2^1A	2.49 / 0.001	0.96	2^1B	3.07 / 0.119	0.08
S_4	2^1B	2.49 / 0.002	0.97	2^1A	3.12 / 0.011	0.04
S_5	3^1B	2.92 / 0.219	0.02	3^1B	3.26 / 0.016	0.89
S_6	3^1A	2.92 / 0.074	0.03	3^1A	3.28 / 0.006	0.93

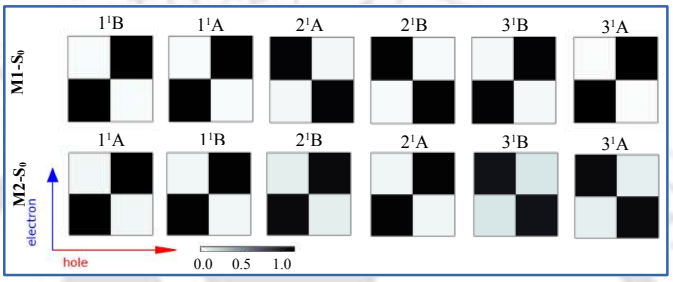

FIGURE 7.3: Electron-hole correlation plots for the first six excited states for **M1-S_0** and **M2-S_0** geometries at the RI-ADC(2)/def2-SVP level.

M1-S_0 and **M2-S_0** exhibit distinct electronic excitation pictures, as shown in Table 7.1. For each conformer, Table 7.1 shows three pairs of energetically degenerate excited states, $1^1A/1^1B$, $2^1A/2^1B$, and $3^1A/3^1B$, each with different oscillator strength (f_{osc}) values. The excitation energy (E_g) values for the first pair of excited states in both conformers are close. However, for the subsequent two pairs of excited states, the E_g values in **M1-S_0** are smaller than those in **M2-S_0**. Additionally, the f_{osc} values for the $1^1A/1^1B$ pair are slightly larger in **M1-S_0** compared to the values in **M2-S_0**. The values of ω_{CT} for the 1^1A and 1^1B states shown in the same table suggest that these are LE states. An examination of the corresponding *e*-*h* correlation plots, shown in Figure 7.3, reveals the delocalization of the exciton over both the fragments. The NTOs involved in these transitions are depicted in Figure E3. As the figure shows, the *h* and *e* orbital densities are distributed over both the monomeric units (mainly on the azulene moieties), and their locations are the same, indicating their delocalized LE characters. For **M2-S_0**, the *h* and *e* densities are localized on the azulene units of each monomeric fragment, suggesting the involvement of only azulene units for these delocalized LE states. For the $2^1A/2^1B$ states of **M1-S_0**, the ω_{CT} values are close to one, which implies the CT

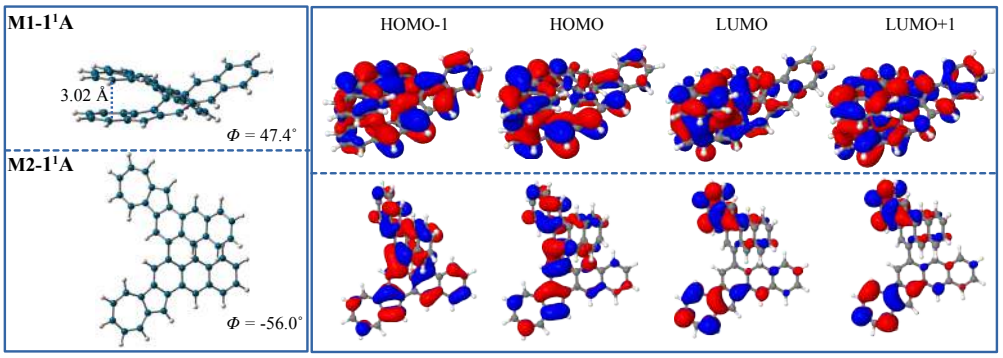

FIGURE 7.4: 1^1A state optimized geometries of **M1** and **M2** (left panel) and MOs involved in $S_0 \rightarrow 1^1$A and $S_0 \rightarrow 1^1$B transitions on 1^1A optimized geometries (right panel).

nature of these states. As observed in Figure 7.3, the *e*-*h* correlation plots for these two states exhibit off-diagonal elements along both axes. This sort of a CT state in which two opposite CT transitions come into resonance is termed a charge resonance (CR) state.[19,170] In **M2-S$_0$**, in contrast, CR characteristics are noted for the 3^1A/3^1B states (Figure 7.3). This shows that while the CR states in **M1-S$_0$** occur immediately after the 1^1A/1^1B states, in **M2-S$_0$**, the CR states are energetically distant from the 1^1A/1^1B states. In the following section, we explore how the energetic proximity of CR and LE states in **M1-S$_0$** can facilitate the mixing of these states during structural relaxation in the excited states, leading to the formation of excimer states.

7.3.2 Excited State Structure and Excimer Formation

Optimization of the conformer **M1** in the 1^1A state leads to a π-stacked foldamer structure **M1-1^{1}A**, depicted in Figure 7.4. In this π-stacked **M1-1^{1}A** structure, the ϕ value is about 47.4°, which is 46.3° smaller than for the **M1-S$_0$** geometry, and the π-π stacking distance between the two azulene moieties is 3.02 Å, indicating strong intramolecular interaction. The MOs (HOMO-1, HOMO, LUMO, and LUMO+1) of the **M1-1^{1}A** geometry are shown in Figure 7.4 (right panel). Upon formation of π-stacked foldamer structure, the molecular orbitals in **M1-1^{1}A** are delocalized over the azulene moieties of two monomeric units, hinting at the excimer formation. In contrast, for **M2** in the 1^1A state, optimization does not produce a foldamer structure. As shown in Figure 7.4, in **M2-1^{1}A**, the two azulene moieties are away from each other, restricting the excimer formation.

TABLE 7.2: Vertical excitation energy/oscillator strength (E_g/f_{osc}) and the corresponding ω_{CT} values for the first six excited states computed for 1^1A optimized geometries at RI-ADC(2)/def2-SVP level

	M1-1^{1}A			**M2-1^{1}A**		
State		E_g/f_{osc}	ω_{CT}		E_g/f_{osc}	ω_{CT}
S_1	1^1A	0.53 / 0.002	0.50	1^1A	1.50 / 0.006	0.06
S_2	1^1B	0.95 / 0.001	0.33	1^1B	1.51 / 0.007	0.06
S_3	2^1B	1.52 / 0.051	0.66	2^1B	2.82 / 0.124	0.18
S_4	2^1A	1.85 / 0.007	0.51	2^1A	2.86 / 0.010	0.46
S_5	3^1A	2.18 / 0.018	0.45	3^1B	2.91 / 0.060	0.88
S_6	3^1B	2.24 / 0.108	0.46	3^1A	2.95 / 0.010	0.49

The E_g values for the first six excited states of **M1-1^{1}A** and **M2-1^{1}A** geometries are tabulated in Table 7.2. The energetic order of the first six excited states for **M1-1^{1}A** geometry differs from those for the **M1-S$_0$**. In addition, the degeneracies of the three pairs of excited states observed for **M1-S$_0$** are lost for **M1-1^{1}A** geometry. A closer look at the E_g values of 1^1A and 2^1A states for **M1-S$_0$** and **M1-1^{1}A** geometries (in Tables 7.1 and 7.2) reveals that while 2^1A is the third excited state appearing close to 1^1A for **M1-S$_0$**(the energy difference is 0.54 eV), 1^1A and 2^1A states for **M1-1^{1}A** structure are first and the fourth excited states, respectively, and the energy difference between the two is larger (the energy difference is 1.32 eV) in this case. This indicates that the same symmetry 1^1A and 2^1A states may interact during structural relaxation in the 1^1A state. The interaction between these two states results in a distribution of CT character, resulting in an ω_{CT} value of 0.50 each for 1^1A and 2^1A states which ultimately stabilizes the excimer. This sort of interaction between the 1^1A-LE and the CR state is not possible for the **M2-S$_0$** geometry, as these states are away from each other. This is clear from the state ordering and the energy difference between the 1^1A-LE and 3^1A-CR state for **M2-1^{1}A** (Table 7.2) which remains the same as in **M2-S$_0$** (Table 7.1). The *e-h* correlation plots corresponding to the first six excited states starting from **M1-1^{1}A** and **M2-1^{1}A** geometries depicted in Figure 7.5 confirm the above results. The *e-h* correlation plots for the 1^1A and 2^1A states for **M1-1^{1}A** show a similar pattern where the same amount of diagonal and off-diagonal contributions are present, indicating the mixed characters of these states. In **M2-1^{1}A**, the 1^1A state remains a pure LE state, having diagonal contributions from each fragment. However, the *e-h* correlation plots for the 2^1A and 3^1A states have diagonal and off-diagonal contributions, indicating their

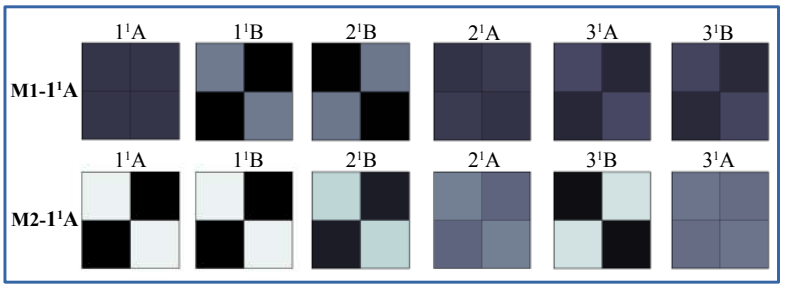

FIGURE 7.5: Electron-hole correlation plots of the first six excited states for **M1-1^{1}A** and **M2-1^{1}A** geometries.

partial CT nature. The NTOs involved in $S_0 \rightarrow 1^1A$ for **M1-1^{1}A** and **M2-1^{1}A** are shown in Figure E4. As observed in the figure, there is a small difference in the locations of the hole and electron in the anthracene units for **M1-1^{1}A**, and this leads to an ω_{CT} value of 0.50. No significant difference in the locations of the hole and electron is observed for **M2-1^{1}A**, which indicates the LE character of the 1^1A state.

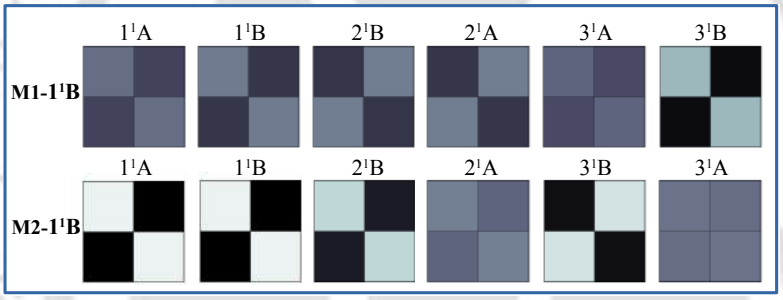

FIGURE 7.6: Electron-hole correlation plots of the first six excited states for **M1-1^{1}B** and **M2-1^{1}B** geometries.

In **M1**, π-stacked foldamer structures, similar to **M1-1^{1}A**, are also observed in the 1^1B, 2^1A, and 2^1B states, as shown in Figures E5 and E6. The energy of the foldamer structure in the 1^1B state is slightly higher (by 0.23 eV) than that of the 1^1A state. In contrast, the energies of the structures in the 2^1B and 2^1A states are 0.75 eV and 0.90 eV higher than that of the 1^1A state, respectively. In the case of conformer **M2**, no such π-stacked foldamer structures are observed in these three excited states as shown in Figures 7.4, E5, and E7. The results for the first six excited states on the 1^1B optimized geometries (**M1-1^{1}B** and **M2-1^{1}B**) are tabulated in Table 7.3. In **M1-1^{1}B**, the first two states (1^1A and 1^1B) are almost degenerate, as observed for the **M1-S$_0$** geometry. Notably, the E_g value for the 1^1A state of **M1-1^{1}B** is 0.27 eV larger than that of the 1^1A state of **M1-1^{1}A** (Table 7.2). Further, in **M1-1^{1}B**, the 2^1A and 2^1B states are

TABLE 7.3: Vertical excitation energy/oscillator strength (E_g/f_{osc}) and corresponding ω_{CT} values for the first six excited states computed for 1^1B optimized geometries at RI-ADC(2)/def2-SVP level

	M1-1^{1}B			**M2-1^{1}B**		
State		E_g/ f_{osc}	ω_{CT}		E_g/ f_{osc}	ω_{CT}
S_1	1^1A	0.80 / 0.008	0.44	1^1A	1.50 / 0.006	0.06
S_2	1^1B	0.85 / 0.002	0.40	1^1B	1.51 / 0.007	0.06
S_3	2^1B	1.67 / 0.044	0.61	2^1B	2.83 / 0.119	0.17
S_4	2^1A	1.73 / 0.001	0.60	2^1A	2.86 / 0.010	0.46
S_5	3^1A	2.20 / 0.026	0.46	3^1B	2.91 / 0.057	0.88
S_6	3^1B	2.34 / 0.043	0.24	3^1A	2.95 / 0.011	0.49

energetically close, which is not observed for the **M1-1^{1}A** geometry. The 50/50 mixture of LE and CT characters for the 1^1A and 2^1A states of **M1-1^{1}A** (shown in Table 7.2 and Figure 7.5) is absent for the 1^1A and 2^1A states of **M1-1^{1}B** (Table 7.3 and Figure 7.6). An ω_{CT} value of 0.44 for 1^1A state of **M1-1^{1}B** geometry indicates a partial CT state. The 1^1B and 2^1B states of **M1-1^{1}B** have similar *e-h* correlation plots like those observed for the **M1-1^{1}A** geometry. In the case of **M2-1^{1}B**, the E_g and ω_{CT} values for the first six excited states (shown in Table 7.3) are almost similar to those observed for **M2-1^{1}A** geometry (Table 7.2). The *e-h* correlation plots are also the same for the first six excited states (Figures 7.5 and 7.6). Therefore, unlike for **M1**, the excited state optimizations of **M2** in the 1^1A and 1^1B states result in similar changes in geometries and in electronic excitations.

The E_g and ω_{CT} values corresponding to the first six excited states for the 2^1A and 2^1B optimized geometries of **M1** and **M2** are presented in Table E1. The ω_{CT} values of 2^1A and 2^1B states for these geometries are 0.80 and 0.89, respectively, which are not very different than the values of those states for the ground state optimized structures (see Table 7.1). This indicates that although the optimizations in these states result in foldamer structures, character of the excited states remain unchanged. Therefore, these states are not excimer-type states.[31] For **M2**, while optimization in 2^1A results in no significant change in the character of 2^1A, when compared to the ground state optimized results, optimization in 2^1B shows an increase in the ω_{CT} value for the 2^1B state.

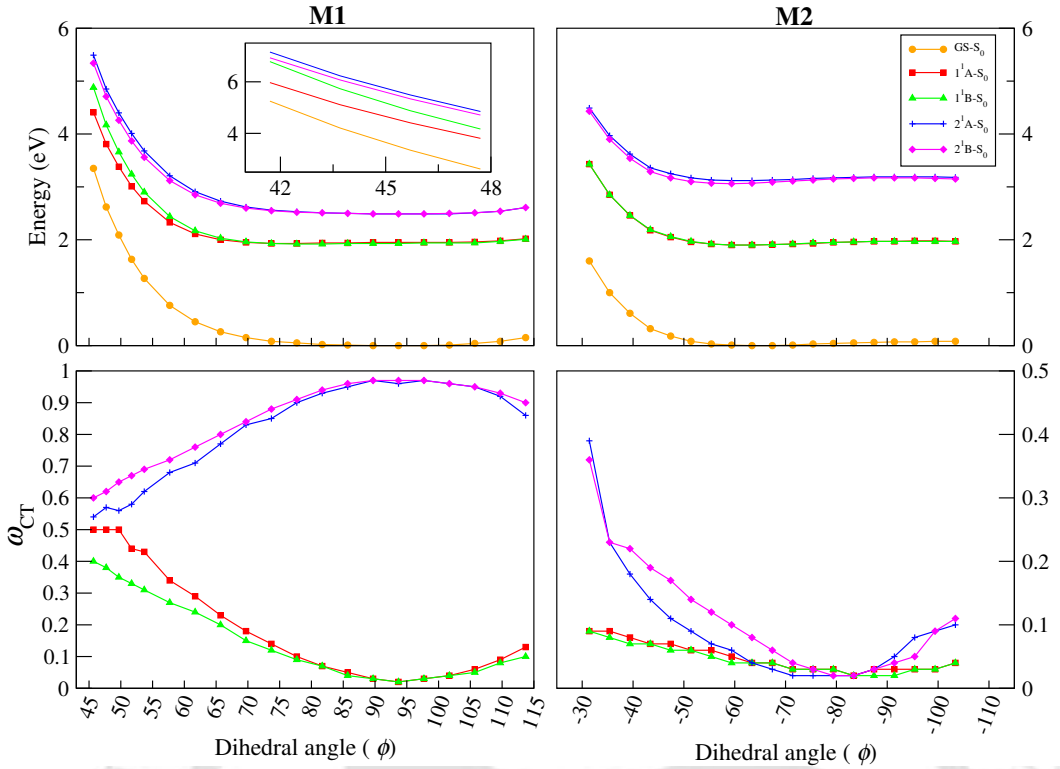

FIGURE 7.7: PECs for the ground state and first four excited states along the inter-chromophoric dihedral angle (Top panel) and the ω_{CT} values for the first four excited states (Bottom panel).

7.3.3 Potential Energy Scan

To understand the structural relaxation along the torsional motion, rigid scans were performed along this torsional mode for **M1-S$_0$** and **M2-S$_0$** structures. Potential energy curves (PECs) for the ground and first four excited states along the torsional angle are shown in Figure 7.7. The energies are tabulated in Tables E2 and E3, for **M1-S$_0$** and **M2-S$_0$**, respectively. In **M1**, the ground state energy and E_g values of the first four excited states increase with a decrease in the torsional angle below 73.7°. In **M2**, the increase in energy values of the ground state and first four excited states is observed below -51.4°. In **M1**, the azulene units come close during the torsional motion, resulting in large energies for all the states. In contrast, in **M2**, the azulene units are oriented in opposite directions, which accounts for less steep curves than in **M1**. In addition, PECs for all the states show flat behavior beyond 70° and -55°, for **M1** and **M2**, respectively. Interestingly, the two pairs of excited states remain energetically close in **M2** throughout the scanning region. However, in the case of **M1**, the degeneracy is

lost below 65°. Looking at the values in Table E2 and Figure 7.7 (inset plot) for **M1**, it is observed that the energy difference between the 1^1A and 1^1B states increase with decrease in the ϕ value, while the S_0-1^1A energy gap decreases. As shown in Table 7.2, a similar energetic order for the first four excited states is also observed for the **M1-1^{1}A** geometry, whereas the 1^1A/1^1B and 2^1A/2^1B pairs remain almost degenerate for the **M1-1^{1}B** geometry (Table 7.3). This indicates that the conformer **M1** is more likely to form an excimer in the 1^1A state. Figure 7.7 also shows the evolution of the CT character of these four excited states as a function of the torsional angle. In **M1**, the CT character for the 1^1A state (an LE state) increases with a decrease in the torsional angle, while the CT character for the 2^1A (a CR state) decreases. A similar pattern is observed for the 1^1B-LE and 2^1B-CR states. The ω_{CT} values tabulated in Table E2 reveal that 1^1A and 1^1B are the counterparts of 2^1A and 2^1B states, respectively. In the 50 to 46° region (near **M1-1^{1}A** geometry), the curves for the 1^1A and 2^1A states become very close, indicating weak interaction among these two states and resulting in an ω_{CT} value of approximately 0.50 for each of them. In contrast, the CT curves for the 1^1B and 2^1B states are away from each other, consistent with the results obtained for **M1-1^{1}A** geometry. This suggests a greater probability of excimer formation in the 1^1A state. In **M2**, the CT characters for the 1^1A or 1^1B states remain very small in the entire region. The *e*-*h* correlation plots for the 1^1A states for different values of torsional angles for **M1** and **M2** are shown in Figures E8 and E9, respectively. For **M1**, the off-diagonal blocks become darker as we move towards smaller torsional angles. Finally, the off-diagonal and diagonal blocks have the same amount of Ω for the 49.7-45.7° region(excimeric region). On the other hand, in **M2**, the *e*-*h* correlation plot for the 1^1A state at each PEC step shows intense diagonal elements, indicating LE characters throughout the PEC.

Rigid scans along the torsional angles are also performed for the **M1-1^{1}A** and **M2-1^{1}A** geometries. The results are shown in Figure 7.8 and the values are tabulated in Tables E4 and E5. The PEC for the 1^1A state in **M1-1^{1}A** shows a minimum at 47.5°, signifying the excimer stabilization. For **M2-1^{1}A**, the PECs for all the states show patterns similar to the results for the **M2-S$_0$** geometry. As the figure shows, the CT curves for the first four excited states of **M1-1^{1}A** geometry have a similar pattern to that observed in the case of S_0 optimized geometries (Figure 7.7). The CT curves for

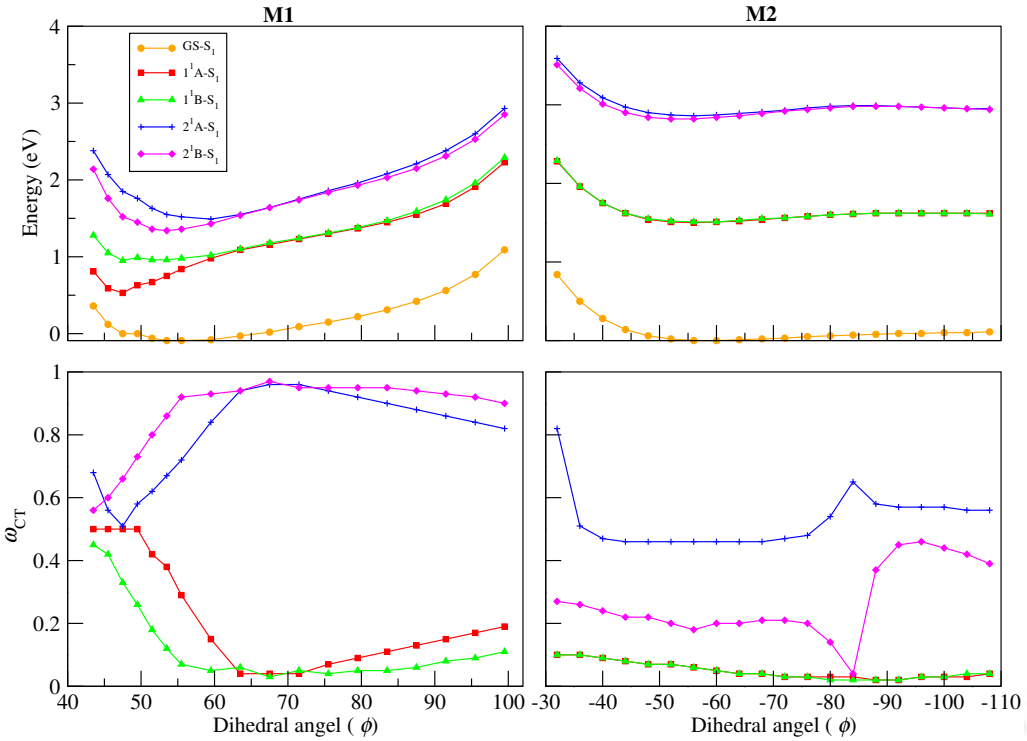

FIGURE 7.8: Potential energy curves for the ground and first four excited states along the inter-chromophoric dihedral angle (Top panel) and the ω_{CT} values for the first four excited states (Bottom panel) for the 1^1A optimized geometries.

the 1^1A and 2^1A states maintain their symbiotic relationship till 47.5°. At 47.5°, the 1^1A state has a 50/50 mixture of LE and CT characters, and as the ϕ value increases, the CT character for this state falls off rapidly. For **M2-1^{1}A** geometry, in contrast, the ω_{CT} values remain very small in the entire scanning region.

7.4 Discussion

The overall structural relaxation process in the excited states of the two conformers, **M1** and **M2**, is presented in Figure 7.9. In the ground state (GS-S_0), **M1** features an interchromophoric dihedral angle of 93.7°, whereas **M2** exhibits an angle of -63.4°. In GS-S_0, both conformers exhibit three pairs of energetically degenerate excited states: 1^1A/1^1B, 2^1A/2^1B, and 3^1A/3^1B. For **M1**, the first pair of excited states (1^1A-S_0/1^1B-S_0) is characterized as an LE state, with E_g values ranging from 1.93 to 1.95 eV, while the second pair(2^1A/2^1B) possesses CT characters. In **M2**, the first two pairs of excited states are also LE states, whereas the third pair (3^1A/3^1B) displays CT characteristics.

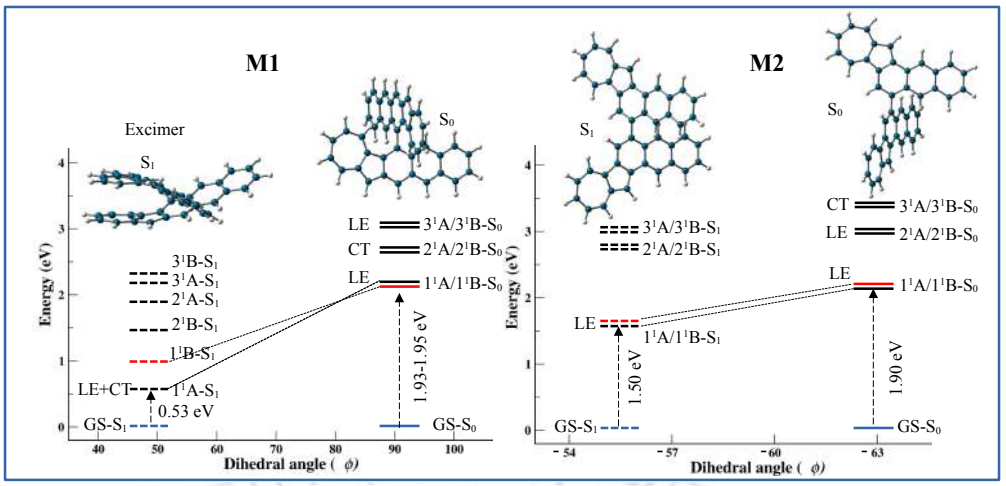

FIGURE 7.9: Schematic energy diagram of excimer formation. GS-S_0 and GS-S_1 are the reference ground states of S_0 and 1^1A optimized geometries, respectively.

During excited state optimization in the 1^1A state, conformer **M1** relaxes into a π-stacked foldamer geometry, significantly altering its dihedral angle from 93.7° (GS-S_0) to 47.4° (GS-S_1). This structural adjustment results in a strong interaction between the 1^1A-LE and 2^1A-CT states. The interaction between 1^1A-LE and 2^1A-CT leads to the distribution of CT characters to the 1^1A state and makes this state a mixed (LE+CT) state, indicating the potential formation of an excimer. In contrast, the optimization of **M2** in the 1^1A state leads to only a slight change in the dihedral angle, shifting from -63.4° (GS-S_0) to -56.0° (GS-S_1), with no significant alteration in the CT character of the 1^1A state. In short, the excited state properties and structural relaxation processes are dependent on the locations where the azulene units are fused with anthracene.

7.5 Conclusion

This study focused on the understanding of the complex relationship between molecular structure and excited state properties using high-level quantum chemistry methods like RI-MP2 and RI-ADC(2). The positioning of azulene units attached to covalently-linked anthracene units plays a crucial role in influencing the energy levels of LE and CT states, eventually affecting excited-state relaxation processes. In one of the conformers, where the azulene units are aligned in the same direction (**M1**), both LE and CT states are close to each other, with the latter being slightly higher in energy. Due to the

favorable structural configuration and the energetic arrangement of LE and CT states, this conformer easily adopts a π-stacked foldamer structure upon relaxation in the S_1 state. This foldamer configuration exhibits distinctive electronic properties related to orbital overlap and has significant CT character, indicating the excimer formation. In contrast, the conformer in which the azulene units are oriented in opposite directions (**M2**), the CT state is found to be energetically distant from the LE state. Here, the conformer shows minor geometric distortion in its first excited state, and this state is devoid of any CT character.

Chapter 8

Summary and conclusions

In designing suitable organic electronic devices, conformational isomers of an organic molecule play an important role in determining device performance and efficiency. At the molecular level, the energetics of excited states and their properties, which are key factors influencing device performance, are significantly affected by different molecular conformations. Experimental studies have reported on the dependence of device performance on different molecular isomers; these studies are mainly focused on synthesis and applications and lack a molecular-level understanding. In this context, computational tools are invaluable for exploring excited-state properties for various molecular conformations. In this thesis, we have shown how the excited-state properties of a conjugated system differ across conformers using advanced computational methods.

In chapter 3, we considered the three conformers, namely **A** (linear), **B** (helical), and **C** (helical), and showed conformation-dependent excited-state properties of 2-Phenylpyridine oligomers ($(\mathbf{PhPy})_{n=1-5}$). The UV spectra of conformer **A** show higher intensity peaks compared to the results for conformers **B** and **C**, for each oligomer. While the helical oligomers of conformers **B** and **C** show high-intensity CD bands, all the oligomer conformers **A** show weaker CD bands. Analysis of the properties of the first five excited states in $(\mathbf{PhPy})_5$ reveals that these are partially charge-transfer states.

In chapter 4, we report on how molecular conformations can impact exciton (de)localization processes, using the non-adiabatic surface-hopping dynamics approach, considering 2-Phenylpyridine oligomers and their two different conformers: a linear and a helical one. In the linear pentamer, excited-state relaxation involves the delocalization of the exciton across multiple monomer units. In contrast, the relaxation in the helical pentamer proceeds with the localization of the exciton on a single monomeric unit.

In chapter 5, we present conformation-dependent photo-physical and excited state properties of ***trans***- and ***cis***-Bipyridine oligomers at the RI-ADC(2)/def2-TZVPD level. The meta conformers of ***trans***- and ***cis***-structures exhibit high-intensity and red-shifted UV bands compared to both **ortho** and **para** conformers. In the case of ***trans***-structures, **para** oligomers exhibit stronger CD bands than **ortho**- and **meta**-conformers. In contrast, each ***cis***-conformer shows high-intensity CD bands. The first five excited states in dimers have LE characters with ω_{CT} values of 0.06-0.32 in each conformer. However, in tetramers, the excited states exhibit slightly larger ω_{CT} values, ranging from 0.17 to 0.53, indicating their partial CT characters.

In chapter 6, the interplay between *intra* and *inter*-molecular CT is presented considering four different conformers of monomers and π-stacked dimers of azulene-fused naphthalene and anthracene systems at the RI-ADC(2) and TD-DFT levels. For the monomers, the states with CT characters are different in naphthalene- and anthracene-based systems. In π-stacked dimers, a few of the excited states are of charge resonance (CR) type in conformers **NapAz-A**, **NapAz-B**, and **NapAz-C**, and intermolecular CT type in **NapAz-D**.

In chapter 7, the possibility of excimer formation in covalently linked azulene-fused anthracene dimers is reported at the RI-ADC(2) level, considering two different conformational isomers, **M1** and **M2**. The azulene units are oriented towards each other in conformer **M1**, which leads to excimer formation in the first excited state. This is confirmed by the orbital overlap of the azulene units and the CT character of the S_1 state. In contrast, conformer **M2**, in which the azulene rings are oriented away from each other, shows minimal changes in the excited-state geometry relative to the ground state, preserving the CT features.

In this thesis, we explored how excited-state properties and dynamics can differ significantly depending on a molecule's conformation. Photo-induced exciton (de)localization, intra- and intermolecular CT, and excimer formation are all dependent on molecular conformation. In the future, we would like to extend our studies to molecular clusters and explore their behavior. Additionally, we would also like to incorporate the solvent

environment into our studies, as it has been shown to significantly influence the formation of excimer and CT states.

References

[1] Kuik, M.; Wetzelaer, G.-J. A.; Nicolai, H. T.; Craciun, N. I.; De Leeuw, D. M.; Blom, P. W. 25th anniversary article: charge transport and recombination in polymer light-emitting diodes. *Adv. Mater.* **2014**, *26*, 512–531.

[2] Zampetti, A.; Minotto, A.; Cacialli, F. Near-infrared (NIR) organic light-emitting diodes (OLEDs): challenges and opportunities. *Adv. Funct. Mater.* **2019**, *29*, 1807623.

[3] Zou, S.-J.; Shen, Y.; Xie, F.-M.; Chen, J.-D.; Li, Y.-Q.; Tang, J.-X. Recent advances in organic light-emitting diodes: toward smart lighting and displays. *Mate. Chem. Front.* **2020**, *4*, 788–820.

[4] Ding, L.; Yu, Z.-D.; Wang, X.-Y.; Yao, Z.-F.; Lu, Y.; Yang, C.-Y.; Wang, J.-Y.; Pei, J. Polymer Semiconductors: Synthesis, Processing, and Applications. *Chem. Res.* **2023**, *123*, 7421–7497.

[5] Zhang, G.; Lin, F. R.; Qi, F.; Heumüller, T.; Distler, A.; Egelhaaf, H.-J.; Li, N.; Chow, P. C.; Brabec, C. J.; Jen, A. K.-Y.; others Renewed prospects for organic photovoltaics. *Chem. Rev.* **2022**, *122*, 14180–14274.

[6] Xu, X.; Yu, L.; Meng, H.; Dai, L.; Yan, H.; Li, R.; Peng, Q. Polymer solar cells with 18.74% efficiency: from bulk heterojunction to interdigitated bulk heterojunction. *Adv. Funct. Mater.* **2022**, *32*, 2108797.

[7] Fratini, S.; Nikolka, M.; Salleo, A.; Schweicher, G.; Sirringhaus, H. Charge transport in high-mobility conjugated polymers and molecular semiconductors. *Nat. Mater.* **2020**, *19*, 491–502.

[8] Yao, Z.-F.; Wang, J.-Y.; Pei, J. High-performance polymer field-effect transistors: from the perspective of multi-level microstructures. *Chem. Sci.* **2021**, *12*, 1193–1205.

[9] Repp, J.; Liljeroth, P.; Meyer, G. Coherent electron–nuclear coupling in oligothiophene molecular wires. *Nat. Phys.* **2010**, *6*, 975–979.

[10] Nelson, T.; Fernandez-Alberti, S.; Roitberg, A. E.; Tretiak, S. Electronic Delocalization, Vibrational Dynamics, and Energy Transfer in Organic Chromophores. *J. Phys. Chem. Lett.* **2017**, *8*, 3020–3031.

[11] Dimitriev, O. P. Dynamics of Excitons in Conjugated Molecules and Organic Semiconductor Systems. *Chem. Rev.* **2022**, *122*, 8487–8593.

[12] Iwamoto, T.; Watanabe, Y.; Sakamoto, Y.; Suzuki, T.; Yamago, S. Selective and Random Syntheses of [n]Cycloparaphenylenes (n = 8–13) and Size Dependence of Their Electronic Properties. *J. Am. Chem. Soc.* **2011**, *133*, 8354–8361.

[13] Guiglion, P.; Zwijnenburg, M. A. Contrasting the optical properties of the different isomers of oligophenylene. *Phys. Chem. Chem. Phys.* **2015**, *17*, 17854–17863.

[14] Park, K. H.; Kim, W.; Yang, J.; Kim, D. Excited-state structural relaxation and exciton delocalization dynamics in linear and cyclic π-conjugated oligothiophenes. *Chem. Soc. Rev.* **2018**, *47*, 4279–4294.

[15] Floß, G.; Saalfrank, P. The Photoinduced E $\rightarrow$ Z Isomerization of Bisazobenzenes: A Surface Hopping Molecular Dynamics Study. *J. Phys. Chem. A* **2015**, *119*, 5026–5037.

[16] Lukeš, V.; Aquino, A. J. A.; Lischka, H.; Kauffmann, H.-F. Dependence of optical properties of oligo-para-phenylenes on torsional modes and chain length. *J. Phys. Chem. B* **2007**, *111*, 7954–7962.

[17] Panda, A. N.; Plasser, F.; Aquino, A. J.; Burghardt, I.; Lischka, H. Electronically excited states in poly (p-phenylenevinylene): vertical excitations and torsional potentials from high-level ab initio calculations. *J. Phys. Chem. A* **2013**, *117*, 2181–2189.

[18] Mewes, S. A.; Dreuw, A. Density-based descriptors and exciton analyses for visualizing and understanding the electronic structure of excited states. *Phys. Chem. Chem. Phys.* **2019**, *21*, 2843–2856.

[19] Plasser, F.; Lischka, H. Analysis of excitonic and charge transfer interactions from quantum chemical calculations. *J. Chem. Theory Comput.* **2012**, *8*, 2777–2789.

[20] Plasser, F.; Wormit, M.; Dreuw, A. New tools for the systematic analysis and visualization of electronic excitations. I. Formalism. *J. Chem. Phys.* **2014**, *141*, 024106.

[21] Menke, S. M.; Ran, N. A.; Bazan, G. C.; Friend, R. H. Understanding energy loss in organic solar cells: toward a new efficiency regime. *Joule* **2018**, *2*, 25–35.

[22] Yost, S. R.; Lee, J.; Wilson, M. W.; Wu, T.; McMahon, D. P.; Parkhurst, R. R.; Thompson, N. J.; Congreve, D. N.; Rao, A.; Johnson, K.; others A transferable model for singlet-fission kinetics. *Nat. Chem.* **2014**, *6*, 492–497.

[23] Smith, M. B.; Michl, J. Singlet Fission. *Chem. Rev.* **2010**, *110*, 6891–6936.

[24] Casanova, D. Theoretical Modeling of Singlet Fission. *Chem. Rev.* **2018**, *118*, 7164–7207.

[25] Margulies, E. A.; Shoer, L. E.; Eaton, S. W.; Wasielewski, M. R. Excimer formation in cofacial and slip-stacked perylene-3, 4: 9, 10-bis (dicarboximide) dimers on a redox-inactive triptycene scaffold. *Phys. Chem. Chem. Phys.* **2014**, *16*, 23735–23742.

[26] Bae, Y. J.; Shimizu, D.; Schultz, J. D.; Kang, G.; Zhou, J.; Schatz, G. C.; Osuka, A.; Wasielewski, M. R. Balancing charge transfer and Frenkel exciton coupling leads to excimer formation in molecular dimers: Implications for singlet fission. *J. Phys. Chem. A* **2020**, *124*, 8478–8487.

[27] Singh, R.; Kim, M.; Lee, J.-J.; Ye, T.; Keivanidis, P. E.; Cho, K. Excimer formation effects and trap-assisted charge recombination loss channels in organic solar cells of perylene diimide dimer acceptors. *J. Mate. Chem. C* **2020**, *8*, 1686–1696.

[28] Birks, J. Excimers and exciplexes. *Nature* **1967**, *214*, 1187–1190.

[29] Förster, T. Excimers. *Angew. Chem. Int. Ed.* **1969**, *8*, 333–343.

[30] Birks, J. Excimers. *Rep. Prog. Phys.* **1975**, *38*, 903.

[31] Young, R. M.; Wasielewski, M. R. Mixed electronic states in molecular dimers: Connecting singlet fission, excimer formation, and symmetry-breaking charge transfer. *Acc. Chem. Res.* **2020**, *53*, 1957–1968.

[32] Sebastian, E.; Sunny, J.; Hariharan, M. Excimer evolution hampers symmetry-broken charge-separated states. *Chem. Sci.* **2022**, *13*, 10824–10835.

[33] Jing, R.; Li, Y.; Tajima, K.; Wan, Y.; Fukui, N.; Shinokubo, H.; Kuang, Z.; Xia, A. Excimer Formation Driven by Excited-State Structural Relaxation in a Covalent Aminonaphthalimide Dimer. *J. Phys. Chem. Lett.* **2024**, *15*, 1469–1476.

[34] Sung, J.; Nowak-Król, A.; Schlosser, F.; Fimmel, B.; Kim, W.; Kim, D.; W, F. Direct observation of excimer-mediated intramolecular electron transfer in a cofacially-stacked perylene bisimide pair. *J. Am. Chem. Soc.* **2016**, *138*, 9029–9032.

[35] Yu, Y.; Chien, S.-C.; Sun, J.; Hettiaratchy, E. C.; Myers, R. C.; Lin, L.-C.; Wu, Y. Excimer-mediated intermolecular charge transfer in self-assembled donor–acceptor dyes on metal oxides. *J. Am. Chem. Soc.* **2019**, *141*, 8727–8731.

[36] Margulies, E. A.; Logsdon, J. L.; Miller, C. E.; Ma, L.; Simonoff, E.; Young, R. M.; Schatz, G. C.; Wasielewski, M. R. Direct observation of a charge-transfer state preceding high-yield singlet fission in terrylenediimide thin films. *J. Am. Chem. Soc.* **2017**, *139*, 663–671.

[37] Mauck, C. M.; Hartnett, P. E.; Margulies, E. A.; Ma, L.; Miller, C. E.; Schatz, G. C.; Marks, T. J.; Wasielewski, M. R. Singlet fission via an excimer-like intermediate in 3, 6-bis (thiophen-2-yl) diketopyrrolopyrrole derivatives. *J. Am. Chem. Soc.* **2016**, *138*, 11749–11761.

[38] Sahu, H.; Panda, A. N. Helical and Nonhelical Structures of Vinylene- and Azomethine-Linked Heterocyclic Oligomers: A Computational Study of Conformation-Dependent Optoelectronic Properties. *J. Phys. Chem. A* **2015**, *119*, 22855–22865.

[39] Chen, R.-F.; Liu, L.-Y.; Fu, H.; Zheng, C.; Xu, H.; Fan, Q.-L.; Huang, W. The influence of the linkage pattern on the optoelectronic properties of polysilafluorenes: a theoretical study. *J. Phys. Chem. B* **2011**, *115*, 242–248.

[40] You, X.; Hu, J.; Wu, M.; Huang, H.; Shao, G.; Zhang, J.; Wu, D.; Xia, J. Isomeric Effect on Optoelectronic Properties and Photovoltaic Performance of Anthraquinone-Core Perylene Diimide (PDI) and Helical PDI dimers. *Chem. - Eur. J.* **2019**, *25*, 12137–12144.

[41] Ma, Z.; Fu, H.; Meng, D.; Jiang, W.; Sun, Y.; Wang, Z. Isomeric N-Annulated Perylene Diimide Dimers for Organic Solar Cells. *Chem. - Asian. J.* **2018**, *13*, 918–923.

[42] Guo, Y.; Ma, Z.; Niu, X.; Zhang, W.; Tao, M.; Guo, Q.; Wang, Z.; Xia, A. Bridge-Mediated Charge Separation in Isomeric N-Annulated Perylene Diimide Dimers. *J. Am. Chem. Soc.* **2019**, *141*, 12789–12796.

[43] Mathew, S. M.; Engle, J. T.; Ziegler, C. J.; Hartley, C. S. The Role of Arene–Arene Interactions in the Folding of ortho-Phenylenes. *J. Am. Chem. Soc.* **2013**, *135*, 6714–6722.

[44] Liao, Y.; Devkota, G. P.; Batra, V.; Franklin, J. R.; Ginn, S. B.; Browner-Smith, D. D. E.; Tierney, D. L.; Hartley, C. S. Distinct Folding Behavior of ortho-Phenylenes and 2,3-Pyrazinylenes. *J. Org. Chem.* **2025**, *90*, 16025–16031.

[45] Ben, T.; Goto, H.; Miwa, K.; Goto, H.; Morino, K.; Furusho, Y.; Yashima, E. Synthesis and Helix Formation of Poly(m-phenylene)s Bearing Optically Active Oligo(ethylene oxide) Side Chains in Protic Media. *Macromolecules* **2008**, *41*, 4506–4509.

[46] Banerjee, M.; Shukla, R.; Rathore, R. Synthesis, optical, and electronic properties of soluble poly-p-phenylene oligomers as models for molecular wires. *J. Am. Chem. Soc.* **2009**, *131*, 1780–1786.

[47] He, J.; Crase, J. L.; Wadumethrige, S. H.; Thakur, K.; Dai, L.; Zou, S.; Rathore, R.; Hartley, C. S. ortho-Phenylenes: Unusual conjugated oligomers with a surprisingly long effective conjugation length. *J. Am. Chem. Soc.* **2010**, *132*, 13848–13857.

[48] Hartley, C. S. Excited-State Behavior of ortho-Phenylenes. *J. Org. Chem.* **2011**, *76*, 9188–9191.

[49] Nijegorodov, N.; Downey, W.; Danailov, M. Systematic investigation of absorption, fluorescence and laser properties of some p- and m-oligophenylenes. *Spectrochim. Acta A Mol. Biomol. Spectrosc.* **2000**, *56*, 783–795.

[50] Jasti, R.; Bhattacharjee, J.; Neaton, J. B.; Bertozzi, C. R. Synthesis, Characterization, and Theory of [9]-, [12]-, and [18]Cycloparaphenylene: Carbon Nanohoop Structures. *J. Am. Chem. Soc.* **2008**, *130*, 17646–17647.

[51] Darzi, E. R.; Jasti, R. The dynamic, size-dependent properties of [5]–[12]cycloparaphenylenes. *Chem. Soc. Rev.* **2015**, *44*, 6401–6410.

[52] Nelson, T. R.; Ondarse-Alvarez, D.; Oldani, N.; Rodriguez-Hernandez, B.; Alfonso-Hernandez, L.; Galindo, J. F.; Kleiman, V. D.; Fernandez-Alberti, S.; Roitberg, A. E.; Tretiak, S. Coherent exciton-vibrational dynamics and energy transfer in conjugated organics. *Nat. Commun.* **2018**, *9*, 2316.

[53] Krömer, J.; Rios-Carreras, I.; Fuhrmann, G.; Musch, C.; Wunderlin, M.; Debaerdemaeker, T.; Mena-Osteritz, E.; Bäuerle, P. Synthesis of the First Fully α-Conjugated Macrocyclic Oligothiophenes: Cyclo[n]thiophenes with Tunable Cavities in the Nanometer Regime. *Angew. Chem. Int. Ed.* **2000**, *39*, 3481–3486.

[54] Bednarz, M.; Reineker, P.; Mena-Osteritz, E.; Bäuerle, P. Optical absorption spectra of linear and cyclic thiophenes—selection rules manifestation. *J. Lumin.* **2004**, *110*, 225–231.

[55] Glenis, S.; Benz, M.; LeGoff, E.; Schindler, J. L.; Kannewurf, C. R.; Kanatzidis, M. G. Polyfuran: a new synthetic approach and electronic properties. *J. Am. Chem. Soc.* **1993**, *115*, 12519–12525.

[56] Politis, J. K.; Nemes, J. C. a. Synthesis and Characterization of Regiorandom and Regioregular Poly(3-octylfuran). *J. Am. Chem. Soc.* **2001**, *123*, 2537–2547.

[57] Varni, A. J.; Fortney, A.; Baker, M. A.; Worch, J. C.; Qiu, Y.; Yaron, D.; Bernhard, S.; Noonan, K. J. T.; Kowalewski, T. Photostable Helical Polyfurans. *J. Am. Chem. Soc.* **2019**, *141*, 8858–8867.

[58] Wasielewski, M. R. Photoinduced electron transfer in supramolecular systems for artificial photosynthesis. *Chem. Rev.* **1992**, *92*, 435–461.

[59] Vauthey, E. Photoinduced Symmetry-Breaking Charge Separation. *Chem. Phys. Chem.* **2012**, *13*, 2001–2011.

[60] Roy, R.; Chawla, S.; Sharma, V.; Pal, A. K.; Silori, Y.; Datta, A.; De, A. K.; Koner, A. L. Ultrafast symmetry-breaking charge separation in Perylenemonoimide-embedded multichromophores: impact of regioisomerism. *Chem. Sci.* **2024**, *15*, 6363–6377.

[61] Mazumder, A.; Vinod, K.; Thomas, A. C.; Hariharan, M. Accelerating Symmetry-Breaking Charge Separation in an Angular versus Linear Perylenediimide Dimer through the Modulation of Coulombic Coupling. *J. Phys. Chem. Lett.* **2025**, *16*, 4819–4827.

[62] Ye, S.; Lotocki, V.; Xu, H.; Seferos, D. S. Group 16 conjugated polymers based on furan, thiophene, selenophene, and tellurophene. *Chem. Soc. Rev.* **2022**,

[63] Huang, J.; Yu, G. Structural engineering in polymer semiconductors with aromatic N-heterocycles. *Chem. Mater.* **2021**, *33*, 1513–1539.

[64] Gidron, O.; Bendikov, M. α-oligofurans: an emerging class of conjugated oligomers for organic electronics. *Angew. Chem. Int. Ed.* **2014**, *53*, 2546–2555.

[65] Tabatchnik-Rebillon, A.; Aubé, C.; Bakkali, H.; Delaunay, T.; Manh, G. T.; Blot, V.; Thobie-Gautier, C.; Renault, E.; Soulard, M.; Planchat, A.; others Electrochemical Synthesis and Characterisation of Alternating Tripyridyl–Dipyrrole Molecular Strands with Multiple Nitrogen-Based Donor–Acceptor Binding Sites. *Chem. - Eur. J.* **2010**, *16*, 11876–11889.

[66] Meth-Cohn, O.; Jiang, H. Ligands containing alternating 2, 6-linked pyridine and 2, 5-linked thiophene units 1. *J. Chem. Soc. Perkin Trans. 2* **1998**, 3737–3746.

[67] Jones, R. A.; Civcir, P. U. Extended heterocyclic systems 2. The synthesis and characterisation of (2-furyl) pyridines,(2-thienyl) pyridines, and furan-pyridine and thiophene-pyridine oligomers. *Tetrahedron* **1997**, *53*, 11529–11540.

[68] Yamamoto, T.; Zhou, Z.-h.; Kanbara, T.; Shimura, M.; Kizu, K.; Maruyama, T.; Nakamura, Y.; Fukuda, T.; Lee, B.-L.; Ooba, N.; others π-conjugated donor- acceptor copolymers constituted of π-excessive and π-deficient arylene units. Optical and electrochemical properties in relation to CT structure of the polymer. *J. Am. Chem. Soc.* **1996**, *118*, 10389–10399.

[69] Welch, G. C.; Coffin, R.; Peet, J.; Bazan, G. C. Band gap control in conjugated oligomers via Lewis acids. *J. Am. Chem. Soc.* **2009**, *131*, 10802–10803.

[70] Kjelstrup-Hansen, J.; Norton, J. E.; da Silva Filho, D. A.; Brédas, J.-L.; Rubahn, H.-G. Charge transport in oligo phenylene and phenylene–thiophene nanofibers. *Org. Elec.* **2009**, *10*, 1228–1234.

[71] Varene, E.; Bogner, L.; Bronner, C.; Tegeder, P. Ultrafast Exciton Population, Relaxation, and Decay Dynamics in Thin Oligothiophene Films. *Phys. Rev. Lett.* **2012**, *109*, 207601.

[72] Bronsch, W.; Wagner, T.; Baum, S.; Wansleben, M.; Zielke, K.; Ghanbari, E.; Györök, M.; Navarro-Quezada, A.; Zeppenfeld, P.; Weinelt, M.; Gahl, C. Interplay between Morphology and Electronic Structure in α-Sexithiophene Films on Au(111). *J. Phys. Chem. C* **2019**, *123*, 7931–7939.

[73] Ghosh, S.; Jana, B.; Ghosh, A.; Guldi, D. M.; Patra, A. The Impact of Aggregation of Quaterthiophenes on the Excited State Dynamics. *J. Phys. Chem. Lett.* **2021**, *12*, 3424–3430.

[74] Perkins, M. A.; Cline, L. M.; Tschumper, G. S. Torsional Profiles of Thiophene and Furan Oligomers: Probing the Effects of Heterogeneity and Chain Length. *J. Phys. Chem. A* **2021**, *125*, 6228–6237.

[75] Murai, M.; Iba, S.; Ota, H.; Takai, K. Azulene-Fused Linear Polycyclic Aromatic Hydrocarbons with Small Bandgap, High Stability, and Reversible Stimuli Responsiveness. *Org. Lett.* **2017**, *19*, 5585–5588.

[76] Xin, H.; Li, J.; Yang, X.; Gao, X. Azulene-based BN-heteroaromatics. *J. Org. Chem.* **2019**, *85*, 70–78.

[77] Xin, H.; Li, J.; Lu, R.-Q.; Gao, X.; Swager, T. M. Azulene–pyridine-fused heteroaromatics. *J. Am. Chem. Soc.* **2020**, *142*, 13598–13605.

[78] Xin, H.; Hou, B.; Gao, X. Azulene-based π-functional materials: design, synthesis, and applications. *Acc. Chem. Res.* **2021**, *54*, 1737–1753.

[79] Ong, A.; Tao, T.; Jiang, Q.; Han, Y.; Ou, Y.; Huang, K.-W.; Chi, C. Azulene-Fused Acenes. *Angew. Chem.* **2022**, *134*, e202209286.

[80] Yu, B.; Du, P.; Guo, J.; Xin, H.; Zhang, J. Nonalternant isomer of pentacene fusing two azulene units. *Chin. Chem. Lett.* **2024**, *35*, 109321.

[81] Yasunami, M.; Yang, P.; Kondo, Y.; Noro, Y.; Takase, K. The synthesis of naphth [2, 1-a]-and naphth [2, 3-a] azulenes. *Chem. Lett.* **1980**, *9*, 167–170.

[82] Yamamura, K.; Kawabata, S.; Kimura, T.; Eda, K.; Hashimoto, M. Novel synthesis of benzalacetone analogues of naphth [a] azulenes by intramolecular tropylium ion-mediated furan ring-opening reaction and X-ray investigation of a naphth [1, 2-a] azulene derivative. *J. Org. Chem.* **2005**, *70*, 8902–8906.

[83] Szabo, A.; Ostlund, N. S. *Modern quantum chemistry: introduction to advanced electronic structure theory*; Courier Corporation, 2012.

[84] Møller, C.; Plesset, M. S. Note on an approximation treatment for many-electron systems. *Phys. Rev.* **1934**, *46*, 618.

[85] Brillouin, L. Les problèmes de perturbations et les champs self-consistents. *J. Phys. Radium* **1932**, *3*, 373–389.

[86] Hohenberg, P.; Kohn, W. Inhomogeneous Electron Gas. *Phys. Rev.* **1964**, *136*, B864–B871.

[87] Kohn, W.; Sham, L. J. Self-Consistent Equations Including Exchange and Correlation Effects. *Phys. Rev.* **1965**, *140*, A1133–A1138.

[88] Becke, A. Density-functional thermochemistry. III. The role of exact exchange (1993) J. *Chem. Phys.* **1993**, *98*, 5648.

[89] Stephens, P. J.; Devlin, F. J.; Chabalowski, C. F.; Frisch, M. J. Ab Initio Calculation of Vibrational Absorption and Circular Dichroism Spectra Using Density Functional Force Fields. *J. Phys. Chem.* **1994**, *98*, 11623–11627.

[90] Becke, A. D. Density-functional exchange-energy approximation with correct asymptotic behavior. *Phys. Rev. A* **1988**, *38*, 3098–3100.

[91] Lee, C.; Yang, W.; Parr, R. G. Development of the Colle-Salvetti correlation-energy formula into a functional of the electron density. *Phys. Rev. B* **1988**, *37*, 785–789.

[92] Dreuw, A.; Weisman, J. L.; Head-Gordon, M. Long-range charge-transfer excited states in time-dependent density functional theory require non-local exchange. *J. Chem. Phys.* **2003**, *119*, 2943–2946.

[93] Dreuw, A.; Head-Gordon, M. Failure of time-dependent density functional theory for long-range charge-transfer excited states: the zincbacteriochlorin- bacteriochlorin and bacteriochlorophyll- spheroidene complexes. *J. Am. Chem. Soc.* **2004**, *126*, 4007–4016.

[94] Magyar, R.; Tretiak, S. Dependence of spurious charge-transfer excited states on orbital exchange in TDDFT: large molecules and clusters. *J. Chem. Theory Comput.* **2007**, *3*, 976–987.

[95] Kümmel, S. Charge-Transfer Excitations: a challenge for time-dependent density functional theory that has been met. *Adv. Energy Mater.* **2017**, *7*, 1700440.

[96] Iikura, H.; Tsuneda, T.; Yanai, T.; Hirao, K. A long-range correction scheme for generalized-gradient-approximation exchange functionals. *J. Chem. Phys.* **2001**, *115*, 3540–3544.

[97] Yanai, T.; Tew, D. P.; Handy, N. C. A new hybrid exchange–correlation functional using the Coulomb-attenuating method (CAM-B3LYP). *Chem. Phys. Lett.* **2004**, *393*, 51–57.

[98] Vydrov, O. A.; Scuseria, G. E. Assessment of a long-range corrected hybrid functional. *J. Chem. Phys.* **2006**, *125*, 234109.

[99] Chai, J.-D.; Head-Gordon, M. Systematic optimization of long-range corrected hybrid density functionals. *J. Chem. Phys.* **2008**, *128*, 084106.

[100] Chai, J.-D.; Head-Gordon, M. Long-range corrected hybrid density functionals with damped atom–atom dispersion corrections. *Phys. Chem. Chem. Phys.* **2008**, *10*, 6615–6620.

[101] Peverati, R.; Truhlar, D. G. Improving the accuracy of hybrid meta-GGA density functionals by range separation. *J. Phys. Chem. Lett.* **2011**, *2*, 2810–2817.

[102] Grimme, S.; Neese, F. Double-hybrid density functional theory for excited electronic states of molecules. *J. Chem. Phys.* **2007**, *127*, 154116.

[103] Goerigk, L.; Grimme, S. Double-hybrid density functionals. *Wiley Interdiscip. Rev.: Comput. Mol. Sci.* **2014**, *4*, 576–600.

[104] Casanova-Páez, M.; Dardis, M. B.; Goerigk, L. ωB2PLYP and ωB2GPPLYP: the first two double-hybrid density functionals with long-range correction optimized for excitation energies. *J. Chem. Theory Comput.* **2019**, *15*, 4735–4744.

[105] Casanova-Páez, M.; Goerigk, L. Time-dependent long-range-corrected double-hybrid density functionals with spin-component and spin-opposite scaling: A comprehensive analysis of singlet–singlet and singlet–triplet excitation energies. *J. Chem. Theory Comput.* **2021**, *17*, 5165–5186.

[106] Brémond, É.; Ottochian, A.; Pérez-Jiménez, Á. J.; Ciofini, I.; Scalmani, G.; Frisch, M. J.; Sancho-García, J. C.; Adamo, C. Assessing challenging intra-and inter-molecular charge-transfer excitations energies with double-hybrid density functionals. *J. Comput. Chem.* **2021**, *42*, 970–981.

[107] Casanova-Páez, M.; Goerigk, L. Assessing the Tamm–Dancoff approximation, singlet–singlet, and singlet–triplet excitations with the latest long-range corrected double-hybrid density functionals. *J. Chem. Phys.* **2020**, *153*, 064106.

[108] Mester, D.; Kállay, M. Accurate spectral properties within double-hybrid density functional theory: a spin-scaled range-separated second-order algebraic-diagrammatic construction-based approach. *J. Chem. Theory Comput.* **2022**, *18*, 865–882.

[109] Mester, D.; Kállay, M. A simple range-separated double-hybrid density functional theory for excited states. *J. Chem. Theory Comput.* **2021**, *17*, 927–942.

[110] Sandoval-Salinas, M. E.; Brémond, E.; Pérez-Jiménez, A. J.; Adamo, C.; Sancho-García, J. C. Excitation energies of polycylic aromatic hydrocarbons by double-hybrid functionals: Assessing the PBE0-DH and PBE-QIDH models and their range-separated versions. *J. Chem. Phys.* **2023**, *158*, 044105.

[111] Sancho-García, J. C.; Brémond, E.; Ricci, G.; Pérez-Jiménez, A. J.; Olivier, Y.; Adamo, C. Violation of Hund's rule in molecules: Predicting the excited-state energy inversion by TD-DFT with double-hybrid methods. *J. Chem. Phys.* **2022**, *156*, 034105.

[112] Runge, E.; Gross, E. K. Density-functional theory for time-dependent systems. *Phys. Rev. Lett.* **1984**, *52*, 997.

[113] Ullrich, C. *Time-dependent density-functional theory: concepts and applications*; Oxford University Press, 2012.

[114] Ullrich, C. A. A snapshot of time-dependent density-functional theory. *APL Comput. Phys.* **2025**, *1*, 020901.

[115] Yabana, K.; Bertsch, G. F. Time-dependent local-density approximation in real time. *Phys. Rev. B* **1996**, *54*, 4484–4487.

[116] CASIDA, M. E. *Recent Advances in Density Functional Methods*; 1995; pp 155–192.

[117] Marques, M. A.; Gross, E. K. Time-dependent density functional theory. *Ann. Rev. Phys. Chem.* **2004**, *55*, 427–455.

[118] Huix-Rotllant, M.; Ferré, N.; Barbatti, M. *Quantum Chemistry and Dynamics of Excited States*; John Wiley & Sons, Ltd, 2020; Chapter 2, pp 13–46.

[119] Schirmer, J. Beyond the random-phase approximation: A new approximation scheme for the polarization propagator. *Phys. Rev. A* **1982**, *26*, 2395.

[120] Trofimov, A.; Schirmer, J. An efficient polarization propagator approach to valence electron excitation spectra. *J. Phys. B: At., Mol. Opt. Phys.* **1995**, *28*, 2299.

[121] Trofimov, A.; Stelter, G.; Schirmer, J. A consistent third-order propagator method for electronic excitation. *J. Chem. Phys.* **1999**, *111*, 9982–9999.

[122] Schirmer, J. Closed-form intermediate representations of many-body propagators and resolvent matrices. *Phys. Rev. A* **1991**, *43*, 4647–4659.

[123] Mertins, F.; Schirmer, J. Algebraic propagator approaches and intermediate-state representations. I. The biorthogonal and unitary coupled-cluster methods. *Phys. Rev. A* **1996**, *53*, 2140–2152.

[124] Dreuw, A.; Papapostolou, A.; Dempwolff, A. L. Algebraic Diagrammatic Construction Schemes Employing the Intermediate State Formalism: Theory, Capabilities, and Interpretation. *J. Phys. Chem. A* **2023**, *127*, 6635–6646.

[125] Porezag, D.; Frauenheim, T.; Köhler, T.; Seifert, G.; Kaschner, R. Construction of tight-binding-like potentials on the basis of density-functional theory: Application to carbon. *Phys. Rev. B* **1995**, *51*, 12947–12957.

[126] Seifert, G.; Porezag, D.; Frauenheim, T. Calculations of molecules, clusters, and solids with a simplified LCAO-DFT-LDA scheme. *Int. J. Quantum Chem.* **1996**, *58*, 185–192.

[127] Elstner, M.; Porezag, D.; Jungnickel, G.; Elsner, J.; Haugk, M.; Frauenheim, T.; Suhai, S.; Seifert, G. Self-consistent-charge density-functional tight-binding method for simulations of complex materials properties. *Phys. Rev. B* **1998**, *58*, 7260–7268.

[128] Hourahine, B.; Aradi, B.; Blum, V.; Bonafe, F.; Buccheri, A.; Camacho, C.; Cevallos, C.; Deshaye, M.; Dumitrică, T.; Dominguez, A.; others DFTB+, a software package for efficient approximate density functional theory based atomistic simulations. *J. Chem. Phys.* **2020**, *152*, 124101.

[129] Seifert, G.; Joswig, J.-O. Density-functional tight binding—an approximate density-functional theory method. *WIREs Comput. Mol. Sci.* **2012**, *2*, 456–465.

[130] Eschrig, H.; Bergert, I. An optimized LCAO version for band structure calculations application to copper. *phys. stat. sol. (b)* **1978**, *90*, 621–628.

[131] Gaus, M.; Cui, Q.; Elstner, M. DFTB3: Extension of the Self-Consistent-Charge Density-Functional Tight-Binding Method (SCC-DFTB). *J. Chem. Theory Comput.* **2011**, *7*, 931–948.

[132] Niehaus, T. A.; Suhai, S.; Della Sala, F.; Lugli, P.; Elstner, M.; Seifert, G.; Frauenheim, T. Tight-binding approach to time-dependent density-functional response theory. *Phys. Rev. B* **2001**, *63*, 085108.

[133] C. Tully, J. Mixed quantum–classical dynamics. *Faraday Discuss.* **1998**, *110*, 407–419.

[134] Tully, J. C.; Preston, R. K. Trajectory surface hopping approach to nonadiabatic molecular collisions: the reaction of H+ with D2. *J. Chem. Phys.* **1971**, *55*, 562–572.

[135] Mai, S.; Marquetand, P.; González, L. *Quantum Chemistry and Dynamics of Excited States*; John Wiley & Sons, Ltd, 2020; Chapter 16, pp 499–530.

[136] Barbatti, M. Nonadiabatic dynamics with trajectory surface hopping method. *WIREs Comput. Mol. Sci.* **2011**, *1*, 620–633.

[137] Tully, J. C. Molecular dynamics with electronic transitions. *J. Chem. Phys.* **1990**, *93*, 1061–1071.

[138] Jasper, A. W.; Stechmann, S. N.; Truhlar, D. G. Fewest-switches with time uncertainty: A modified trajectory surface-hopping algorithm with better accuracy for classically forbidden electronic transitions. *J. Chem. Phys.* **2002**, *116*, 5424–5431.

[139] Schwartz, B. J.; Bittner, E. R.; Prezhdo, O. V.; Rossky, P. J. Quantum decoherence and the isotope effect in condensed phase nonadiabatic molecular dynamics simulations. *J. Chem. Phys.* **1996**, *104*, 5942–5955.

[140] Thachuk, M.; Ivanov, M. Y.; Wardlaw, D. M. A semiclassical approach to intense-field above-threshold dissociation in the long wavelength limit. II. Conservation principles and coherence in surface hopping. *J. Chem. Phys.* **1998**, *109*, 5747–5760.

[141] Zhu, C.; Jasper, A. W.; Truhlar, D. G. Non-Born-Oppenheimer Liouville-von Neumann Dynamics. Evolution of a Subsystem Controlled by Linear and Population-Driven Decay of Mixing with Decoherent and Coherent Switching. *J. Chem. Theory Comput.* **2005**, *1*, 527–540.

[142] Granucci, G.; Persico, M.; Zoccante, A. Including quantum decoherence in surface hopping. *J. Chem. Phys.* **2010**, *133*, 134111.

[143] Plasser, F.; Wormit, M.; Dreuw, A. New tools for the systematic analysis and visualization of electronic excitations. I. Formalism. *J. Chem. Phys.* **2014**, *141*.

[144] Le Bahers, T.; Adamo, C.; Ciofini, I. A qualitative index of spatial extent in charge-transfer excitations. *J. Chem. Theory Comput.* **2011**, *7*, 2498–2506.

[145] Bäppler, S. A.; Plasser, F.; Wormit, M.; Dreuw, A. Exciton analysis of many-body wave functions: Bridging the gap between the quasiparticle and molecular orbital pictures. *Phys. Rev. A* **2014**, *90*, 052521.

[146] Mewes, S. A.; Plasser, F.; Dreuw, A. Universal exciton size in organic polymers is determined by nonlocal orbital exchange in time-dependent density functional theory. *J. Phys. Chem. Lett.* **2017**, *8*, 1205–1210.

[147] Czader, A.; Bittner, E. R. Calculations of the exciton coupling elements between the DNA bases using the transition density cube method. *J. Chem. Phys.* **2008**, *128*, 01B613.

[148] Mewes, S. A.; Mewes, J.-M.; Dreuw, A.; Plasser, F. Excitons in poly (para phenylene vinylene): a quantum-chemical perspective based on high-level ab initio calculations. *Phys. Chem. Chem. Phys.* **2016**, *18*, 2548–2563.

[149] Martin, R. L. Natural transition orbitals. *J. Chem. Phys.* **2003**, *118*, 4775–4777.

[150] Mayer, I. Using singular value decomposition for a compact presentation and improved interpretation of the CIS wave functions. *Chem. Phys. Lett.* **2007**, *437*, 284–286.

[151] Rocha, S. V.; Finney, N. S. Synthesis and Evaluation of 2, 5-Linked Alternating Pyridine- Thiophene Oligomers. *Org. Lett.* **2010**, *12*, 2598–2601.

[152] Rocha, S. V.; Finney, N. S. Systematic evaluation of 2, 6-linked pyridine–thiophene oligomers. *J. Org. Chem.* **2013**, *78*, 11255–11261.

[153] Cai, G.; Chen, Z.; Li, M.; Li, Y.; Xue, P.; Cao, Q.; Chi, W.; Liu, H.; Xia, X.; An, Q.; others Revealing the Sole Impact of Acceptor's Molecular Conformation to Energy Loss and Device Performance of Organic Solar Cells through Positional Isomers. *Adv. Sci.* **2022**, *9*, 2103428.

[154] Lu, B.; Zhang, Z.; Jia, B.; Cai, G.; Zhu, J.; Lu, X.; Zhan, X.; Yao, Y. Precise Synthesis of Fused Decacyclic Electron Acceptor Isomers for Organic Solar Cells. *Sol. RRR* **2021**, *5*, 2100163.

[155] Loser, S.; Miyauchi, H.; Hennek, J. W.; Smith, J.; Huang, C.; Facchetti, A.; Marks, T. J. A "zig-zag" naphthodithiophene core for increased efficiency in solution-processed small molecule solar cells. *Chem. Commun.* **2012**, *48*, 8511–8513.

[156] Krumholz, P. Structural studies on polynuclear pyridine compounds. *J. Am. Chem. Soc.* **1951**, *73*, 3487–3492.

[157] Dobbs, K. D.; Sohlberg, K. 2-Phenylpyridine: to twist or not to twist? *J. Chem. Theory Comput.* **2006**, *2*, 1530–1537.

[158] Lu, Y.-P.; Ehara, M. Electronic structure and optical properties of chelating heteroatomic conjugated molecules: a SAC-CI study. *Theor. Chem. Acc.* **2009**, *124*, 395–408.

[159] Göller, A.; Grummt, U.-W. Torsional barriers in biphenyl, 2, 2'-bipyridine and 2-phenylpyridine. *Chem. Phys. Lett.* **2000**, *321*, 399–405.

[160] Ribeiro da Silva, M.; Matos, M.; Rio, C.; Morais, V.; Wang, J.; Nichols, G.; Chickos, J. A thermochemical and theoretical study of the phenylpyridine isomers. *J. Phys. Chem. A* **2000**, *104*, 1774–1778.

[161] Becke, A. Density-functional thermochemistry. III. The role of exact exchange (1993) J. *Chem. Phys. 98*, 5648.

[162] Weigend, F.; Ahlrichs, R. Balanced basis sets of split valence, triple zeta valence and quadruple zeta valence quality for H to Rn: Design and assessment of accuracy. *Phys. Chem. Chem. Phys.* **2005**, *7*, 3297–3305.

[163] Grimme, S.; Antony, J.; Ehrlich, S.; Krieg, H. A consistent and accurate ab initio parametrization of density functional dispersion correction (DFT-D) for the 94 elements H-Pu. *J. Chem. Phys.* **2010**, *132*, 154104.

[164] Grimme, S. Density functional theory with London dispersion corrections. *Wiley Interdiscip. Rev.: Comput. Mol. Sci.* **2011**, *1*, 211–228.

[165] Grimme, S.; Ehrlich, S.; Goerigk, L. Effect of the damping function in dispersion corrected density functional theory. *J. Comput. Chem.* **2011**, *32*, 1456–1465.

[166] Frisch, M. e.; Trucks, G.; Schlegel, H.; Scuseria, G.; Robb, M.; Cheeseman, J.; Scalmani, G.; Barone, V.; Petersson, G.; Nakatsuji, H.; others Gaussian 16. 2016.

[167] Schäfer, A.; Horn, H.; Ahlrichs, R. Fully optimized contracted Gaussian basis sets for atoms Li to Kr. *J. Chem. Phys.* **1992**, *97*, 2571–2577.

[168] TURBOMOLE V7.1 2016, a development of University of Karlsruhe and Forschungszentrum Karlsruhe GmbH, 1989-2007, TURBOMOLE GmbH, since 2007; available from `https://www.turbomole.org`.

[169] Allouche, A.-R. Gabedit A graphical user interface for computational chemistry softwares. *J. Comput. Chem.* **2011**, *32*, 174–182.

[170] Plasser, F. TheoDORE: A toolbox for a detailed and automated analysis of electronic excited state computations. *J. Chem. Phys.* **2020**, *152*, 084108.

[171] Liu, Y.-L.; Feng, J.-K.; Ren, A.-M. Theoretical study on photophysical properties of bis-dipolar diphenylamino-endcapped oligoarylfluorenes as light-emitting materials. *J. Phys. Chem. A* **2008**, *112*, 3157–3164.

[172] Richardson, F. S.; Riehl, J. P. Circularly polarized luminescence spectroscopy. *Chem. Rev.* **1977**, *77*, 773–792.

[173] Berova, N.; Nakanishi, K.; Woody, R. W. *Circular dichroism: principles and applications, 2nd ed.*; Wiley-VCH: New York, 2000; pp 185–215.

[174] Mori, T. Chiroptical properties of symmetric double, triple, and multiple helicenes. *Chem. Rev.* **2021**, *121*, 2373–2412.

[175] Zhou, F.; Huang, Z.; Huang, Z.; Cheng, R.; Yang, Y.; You, J. Triple Oxa [7] helicene with circularly polarized luminescence: Enhancing the dissymmetry factors via helicene subunit multiplication. *Org. Lett.* **2021**, *23*, 4559–4563.

[176] Brédas, J.-L.; Beljonne, D.; Coropceanu, V.; Cornil, J. Charge-Transfer and Energy-Transfer Processes in π-Conjugated Oligomers and Polymers: A Molecular Picture. *Chem. Rev.* **2004**, *104*, 4971–5004.

[177] Nelson, T. R.; White, A. J.; Bjorgaard, J. A.; Sifain, A. E.; Zhang, Y.; Nebgen, B.; Fernandez-Alberti, S.; Mozyrsky, D.; Roitberg, A. E.; Tretiak, S. Non-adiabatic Excited-State Molecular Dynamics: Theory and Applications for Modeling Photophysics in Extended Molecular Materials. *Chem. Rev.* **2020**, *120*, 2215–2287.

[178] Titov, E.; Humeniuk, A.; Mitrić, R. Exciton localization in excited-state dynamics of a tetracene trimer: a surface hopping LC-TDDFTB study. *Phys. Chem. Chem. Phys.* **2018**, *20*, 25995–26007.

[179] Di Maiolo, F.; Brey, D.; Binder, R.; Burghardt, I. Quantum dynamical simulations of intra-chain exciton diffusion in an oligo (para-phenylene vinylene) chain at finite temperature. *J. Chem. Phys.* **2020**, *153*, 184107.

[180] Hammes-Schiffer, S.; Tully, J. C. Proton transfer in solution: Molecular dynamics with quantum transitions. *J. Chem. Phys.* **1994**, *101*, 4657–4667.

[181] Phun, G. S.; Kern, D. B.; Sfeir, M. Y.; Azoulay, J. D.; Wong, B. M. Energy Transfer Mechanisms in Large Low-Bandgap Polymers from Time-Resolved Experiments and Nonadiabatic Molecular Dynamics Calculations. *Chem. Mater.* **2025**, *37*, 3769–3775.

[182] Vogt, J.-R.; Schulz, M.; Souza Mattos, R.; Barbatti, M.; Persico, M.; Granucci, G.; Hutter, J.; Hehn, A. A Density Functional Theory and Semiempirical Framework for Trajectory Surface Hopping on Extended Systems. *J. Chem. Theory Comput.* **2025**, *21*, 10474–10488.

[183] Stojanovic, L.; Aziz, S. G.; Hilal, R. H.; Plasser, F.; Niehaus, T. A.; Barbatti, M. Nonadiabatic dynamics of cycloparaphenylenes with TD-DFTB surface hopping. *J. Chem. Theory Comput.* **2017**, *13*, 5846–5860.

[184] Wu, X.; Wen, S.; Song, H.; Frauenheim, T.; Tretiak, S.; Yam, C.; Zhang, Y. Nonadiabatic molecular dynamics simulations based on time-dependent density functional tight-binding method. *J. Chem. Phys.* **2022**, *157*, 084114.

[185] Posenitskiy, E.; Rapacioli, M.; Lepetit, B.; Lemoine, D.; Spiegelman, F. Nonadiabatic molecular dynamics investigation of the size dependence of the electronic relaxation in polyacenes. *Phys. Chem. Chem. Phys.* **2019**, *21*, 12139–12149.

[186] Posenitskiy, E.; Rapacioli, M.; Lemoine, D.; Spiegelman, F. Theoretical investigation of the electronic relaxation in highly excited chrysene and tetracene: The effect of armchair vs zigzag edge. *J. Chem. Phys.* **2020**, *152*, 074306.

[187] Rapacioli, M.; Buey, M. Y.; Spiegelman, F. Addressing electronic and dynamical evolution of molecules and molecular clusters: DFTB simulations of energy relaxation in polycyclic aromatic hydrocarbons. *Phys. Chem. Chem. Phys.* **2024**, *26*, 1499–1515.

[188] Kumagai, A.; Fukumoto, H.; Yamamoto, T. Chemical and Electrochemical Oxidation of Thiophene-Pyridine and Thiophene-Pyrimidine Co-Oligomers in Solutions. *J. Phys. Chem. B* **2007**, *111*, 8020–8026.

[189] Rocha, S. V.; Finney, N. S. Systematic Evaluation of 2,6-Linked Pyridine–Thiophene Oligomers. *J. Org. Chem.* **2013**, *78*, 11255–11261.

[190] Steen, A. E.; Ellington, T. L.; Nguyen, S. T.; Balasubramaniam, S.; Chandrasiri, I.; Delcamp, J. H.; Tschumper, G. S.; Hammer, N. I.; Watkins, D. L. Characterization of Furan- and Thiophene-Containing Bispyridyl Oligomers via Spectroscopic, Electrochemical, and TD-DFT Methods. *J. Phys. Chem. C* **2019**, *123*, 15176–15185.

[191] Mandal, P.; Panda, A. N. Conformational Effect on the Excitonic States of 2-Phenylpyridine Oligomers: Ab Initio Studies and Analysis. *J. Phys. Chem. A* **2023**, *127*, 7898–7907.

[192] Lutsker, V.; Aradi, B.; Niehaus, T. A. Implementation and benchmark of a long-range corrected functional in the density functional based tight-binding method. *J. Chem. Phys.* **2015**, *143*, 184107.

[193] Kranz, J. J.; Elstner, M.; Aradi, B.; Frauenheim, T.; Lutsker, V.; Garcia, A. D.; Niehaus, T. A. Time-Dependent Extension of the Long-Range Corrected Density Functional Based Tight-Binding Method. *J. Chem. Theory Comput.* **2017**, *13*, 1737–1747.

[194] Vuong, V. Q.; Akkarapattiakal Kuriappan, J.; Kubillus, M.; Kranz, J. J.; Mast, T.; Niehaus, T. A.; Irle, S.; Elstner, M. Parametrization and Benchmark of Long-Range Corrected DFTB2 for Organic Molecules. *J. Chem. Theory Comput.* **2018**, *14*, 115–125.

[195] Hättig, C.; Weigend, F. CC2 excitation energy calculations on large molecules using the resolution of the identity approximation. *J. Chem. Phys.* **2000**, *113*, 5154–5161.

[196] TURBOMOLE V7.2 2016, a development of University of Karlsruhe and Forschungszentrum Karlsruhe GmbH, 1989-2007, TURBOMOLE GmbH, since 2007; available from `https://www.turbomole.org`.

[197] Wigner, E. On the Quantum Correction For Thermodynamic Equilibrium. *Phys. Rev.* **1932**, *40*, 749–759.

[198] Barbatti, M. et al. Newton-X Platform: New Software Developments for Surface Hopping and Nuclear Ensembles. *J. Chem. Theory Comput.* **2022**, *18*, 6851–6865.

[199] Dreuw, A.; Head-Gordon, M. Single-reference ab initio methods for the calculation of excited states of large molecules. *Chem. Rev.* **2005**, *105*, 4009–4037.

[200] Gebler, D.; Wang, Y.; Blatchford, J.; Jessen, S.; Lin, L.-B.; Gustafson, T.; Wang, H.; Swager, T.; MacDiarmid, A.; Epstein, A. Blue electroluminescent devices based on soluble poly (p-pyridine). *J. App. Phys.* **1995**, *78*, 4264–4266.

[201] Blatchford, J.; Jessen, S.; Lin, L.-B.; Gustafson, T.; Fu, D.-K.; Wang, H.-L.; Swager, T.; MacDiarmid, A.; Epstein, A. Photoluminescence in pyridine-based polymers: Role of aggregates. *Phys. Rev. B* **1996**, *54*, 9180.

[202] Halim, M.; Samuel, I.; Rebourt, E.; Monkman, A. Measurement of time dependent quantum yield of poly(p-pyridine) and poly(p-phenylenevinylene). *Synth. Met.* **1997**, *84*, 951–952.

[203] Dailey, S.; Halim, M.; Rebourt, E.; Horsburgh, L.; Samuel, I.; Monkman, A. An efficient electron-transporting polymer for light-emitting diodes. *J. Phys. Condens. Matter.* **1998**, *10*, 5171.

[204] Hwang, M.-Y.; Hua, M.-Y.; Chen, S.-A. Poly (pyridine-2, 5-diyl) as electron-transport/hole blocking layer in poly (phenylene vinylene) light-emitting diode. *Polymer* **1999**, *40*, 3233–3235.

[205] Halim, M.; Samuel, I.; Pillow, J.; Monkman, A.; Burn, P. Control of colour and charge injection in conjugated dendrimer/polypyridine bilayer LEDs. *Synth. Met.* **1999**, *102*, 1571–1574.

[206] Yang, L.; Mihali, V.-A.; Brandell, D.; Strømme, M.; Sjodin, M. Conjugated pyridine-based polymers characterized as conductivity carrying components in anode materials. *J. Phys. Chem. C* **2014**, *118*, 25956–25963.

[207] Araujo, R. B.; Banerjee, A.; Panigrahi, P.; Yang, L.; Sjödin, M.; Strømme, M.; Araujo, C. M.; Ahuja, R. Assessing the electrochemical properties of polypyridine and polythiophene for prospective applications in sustainable organic batteries. *Phys. Chem. Chem. Phys.* **2017**, *19*, 3307–3314.

[208] Patera, L. L.; Amler, J.; Repp, J. On-Surface Synthesis of Polypyridine: Strain Enforces Extended Linear Chains. *Chemistry* **2022**, *4*, 112–117.

[209] Blatchford, J.; Gustafson, T.; Epstein, A. Electronic structure of pyridine-based polymers. *J. Chem. Phys.* **1996**, *105*, 9214–9226.

[210] Vaschetto, M. E.; Retamal, B. A.; Monkman, A. P.; Springborg, M. First-principles calculations of pyridines: From monomer to polymer. *J. Phys. Chem. A* **1999**, *103*, 11096–11103.

[211] Greczynski, G.; Johansson, N.; Lögdlund, M.; Pettersson, L.; Salaneck, W. R.; Horsburgh, L.; Monkman, A.; dos Santos, D.; Brédas, J. Electronic structure of pristine and sodium doped poly (p-pyridine). *J. Chem. Phys.* **2001**, *114*, 4243–4252.

[212] Tammer, M.; Horsburgh, L.; Monkman, A. P.; Brown, W.; Burrows, H. D. Effect of Chain Rigidity and Effective Conjugation Length on the Structural and Photophysical Properties of Pyridine-Based Luminescent Polymers. *Adv. Funct. Mater.* **2002**, *12*, 447–454.

[213] Rappoport, D.; Furche, F. Property-optimized Gaussian basis sets for molecular response calculations. *J. Chem. Phys.* **2010**, *133*.

[214] Neese, F.; Wennmohs, F.; Becker, U.; Riplinger, C. The ORCA quantum chemistry program package. *J. Chem. Phys.* **2020**, *152*, 224108.

[215] Merritt, L.; Schroeder, E. The crystal structure of 2, 2′-bipyridine. *Acta Crystallogr.* **1956**, *9*, 801–804.

[216] Zahn, S.; Reckien, W.; Kirchner, B.; Staats, H.; Matthey, J.; Lützen, A. Towards Allosteric Receptors: Adjustment of the Rotation Barrier of 2, 2′-Bipyridine Derivatives. *Chem. - Eur. J.* **2009**, *15*, 2572–2580.

[217] De Bruecker, L.; Everaert, J.; Van Der Voort, P.; Stevens, C. V.; Waroquier, M.; Van Speybroeck, V. Structural and Photophysical Properties of Various Polypyridyl Ligands: A Combined Experimental and Computational Study. *Chem. Phys. Chem.* **2020**, *21*, 2489–2505.

[218] Véril, M.; Scemama, A.; Caffarel, M.; Lipparini, F.; Boggio-Pasqua, M.; Jacquemin, D.; Loos, P.-F. QUESTDB: A database of highly accurate excitation energies for the electronic structure community. *Wiley Interdiscip. Rev.: Comput. Mol. Sci.* **2021**, *11*, e1517.

[219] Izquierdo-García, P.; Fernández-García, J. M.; Medina Rivero, S.; Šámal, M.; Rybáček, J.; Bednárová, L.; Ramírez-Barroso, S.; Ramírez, F. J.; Rodríguez, R.; Perles, J.; García-Fresnadillo, D.; Crassous, J.; Casado, J.; Stará, I. G.; Martín, N. Helical Bilayer Nanographenes: Impact of the Helicene Length on the Structural, Electrochemical, Photophysical, and Chiroptical Properties. *J. Am. Chem. Soc.* **2023**, *145*, 11599–11610.

[220] Zhou, Q.; Hou, X.; Wang, J.; Ni, Y.; Fan, W.; Li, Z.; Wei, X.; Li, K.; Yuan, W.; Xu, Z.; others A Fused [5] Helicene Dimer with a Figure-Eight Topology: Synthesis, Chiral Resolution, and Electronic Properties. *Angew. Chem. Int. Ed.* **2023**, *62*, e202302266.

[221] Anthony, J. E. Functionalized acenes and heteroacenes for organic electronics. *Chem. Rev.* **2006**, *106*, 5028–5048.

[222] Wu, J.; Pisula, W.; Müllen, K. Graphenes as potential material for electronics. *Chem. Rev.* **2007**, *107*, 718–747.

[223] Anthony, J. E. The larger acenes: versatile organic semiconductors. *Angew. Chem. Int. Ed.* **2008**, *47*, 452–483.

[224] Tönshoff, C.; Bettinger, H. F. Pushing the limits of acene chemistry: The recent surge of large acenes. *Chem. - Eur. J.* **2021**, *27*, 3193–3212.

[225] Payne, M. M.; Parkin, S. R.; Anthony, J. E. Functionalized higher acenes: hexacene and heptacene. *J. Am. Chem. Soc.* **2005**, *127*, 8028–8029.

[226] Kaur, I.; Jia, W.; Kopreski, R. P.; Selvarasah, S.; Dokmeci, M. R.; Pramanik, C.; McGruer, N. E.; Miller, G. P. Substituent effects in pentacenes: gaining control over HOMO- LUMO gaps and photooxidative resistances. *J. Am. Chem. Soc.* **2008**, *130*, 16274–16286.

[227] Anderson Jr, A. G.; Steckler, B. M. Azulene. VIII. A study of the visible absorption spectra and dipole moments of some 1-and 1, 3-substituted azulenes1, 2. *J. Am. Chem. Soc.* **1959**, *81*, 4941–4946.

[228] Michl, J.; Thulstrup, E. W. Why is azulene blue and anthracene white? A simple MO picture. *Tetrahedron* **1976**, *32*, 205–209.

[229] Grimme, S. Improved second-order Møller–Plesset perturbation theory by separate scaling of parallel-and antiparallel-spin pair correlation energies. *J. Chem. Phys.* **2003**, *118*, 9095–9102.

[230] Bremond, E.; Savarese, M.; Pérez-Jiménez, Á. J.; Sancho-García, J. C.; Adamo, C. Range-separated double-hybrid functional from nonempirical constraints. *J. Chem. Theory Comput.* **2018**, *14*, 4052–4062.

[231] Mester, D.; Kállay, M. Charge-transfer excitations within density functional theory: How accurate are the most recommended approaches? *J. Chem. Theory Comput.* **2022**, *18*, 1646–1662.

[232] Hirata, S.; Head-Gordon, M. Time-dependent density functional theory within the Tamm–Dancoff approximation. *Chem. Phys. Lett.* **1999**, *314*, 291–299.

[233] Neese, F.; Wennmohs, F.; Hansen, A.; Becker, U. Efficient, approximate and parallel Hartree–Fock and hybrid DFT calculations. A 'chain-of-spheres' algorithm for the Hartree–Fock exchange. *Chem. Phys.* **2009**, *356*, 98–109.

[234] Neese, F. Software update: The ORCA program system - Version 5.0. *Wiley Interdiscip. Rev.: Comput. Mol. Sci.* **2022**, *12*, e1606.

[235] Silva, N. J.; Machado, F. B.; Lischka, H.; Aquino, A. J. π–π stacking between polyaromatic hydrocarbon sheets beyond dispersion interactions. *Phys. Chem. Chem. Phys.* **2016**, *18*, 22300–22310.

[236] Norton, J. E.; Houk, K. Electronic structures and properties of twisted polyacenes. *J. Am. Chem. Soc.* **2005**, *127*, 4162–4163.

[237] Bedi, A.; Gidron, O. Chiroptical properties of twisted acenes: Experimental and computational study. *Chemistry–A European Journal* **2019**, *25*, 3279–3285.

[238] Feng, X.; Krylov, A. I. On couplings and excimers: lessons from studies of singlet fission in covalently linked tetracene dimers. *Phys. Chem. Chem. Phys.* **2016**, *18*, 7751–7761.

[239] Qin, C.; Zhang, Z.; Xu, Q.; Song, J.; Jiao, Z.; Ma, S.; Qin, R.; Jiang, Y. Direct Observation of Ultrafast Relaxation Dynamics of a Mixed Excimer State in Perylene Monoimide Dimer by Femtosecond Transient Absorption. *J. Phys. Chem. Lett.* **2023**, *14*, 2455–2462.

[240] Cook, R. E.; Phelan, B. T.; Kamire, R. J.; Majewski, M. B.; Young, R. M.; Wasielewski, M. R. Excimer formation and symmetry-breaking charge transfer in cofacial perylene dimers. *J. Phys. Chem. A* **2017**, *121*, 1607–1615.

[241] Hoche, J.; Schmitt, H.-C.; Humeniuk, A.; Fischer, I.; Mitrić, R.; Röhr, M. I. The mechanism of excimer formation: An experimental and theoretical study on the pyrene dimer. *Phys. Chem. Chem. Phys.* **2017**, *19*, 25002–25015.

[242] Estergreen, L.; Mencke, A. R.; Cotton, D. E.; Korovina, N. V.; Michl, J.; Roberts, S. T.; Thompson, M. E.; Bradforth, S. E. Controlling symmetry breaking charge transfer in BODIPY pairs. *Acc. Chem. Res.* **2022**, *55*, 1561–1572.

[243] Ma, L.; Kuang, Z.; Wang, Z.; Zhao, H.; Wan, Y.; Zhang, X.-F.; Li, Y.; Xia, A. Ultrafast charge separation driven by torsional motion in orthogonal boron dipyrromethene dimer. *J. Phys. Chem. Lett.* **2023**, *14*, 702–708.

[244] Piet, J. J.; Schuddeboom, W.; Wegewijs, B. R.; Grozema, F. C.; Warman, J. M. Symmetry breaking in the relaxed S1 excited state of bianthryl derivatives in weakly polar solvents. *J. Am. Chem. Soc.* **2001**, *123*, 5337–5347.

[245] Hashimoto, S.; Yabushita, A.; Kobayashi, T.; Okamura, K.; Iwakura, I. Direct observation of the change in transient molecular structure of 9, 9′-bianthryl using a 10 fs pulse UV laser. *Chem. Phys.* **2018**, *512*, 128–134.

[246] Alvertis, A. M.; Lukman, S.; Hele, T. J.; Fuemmeler, E. G.; Feng, J.; Wu, J.; Greenham, N. C.; Chin, A. W.; Musser, A. J. Switching between coherent and incoherent singlet fission via solvent-induced symmetry breaking. *J. Am. Chem. Soc.* **2019**, *141*, 17558–17570.

[247] Mattos, R. S.; Burghardt, I.; Aquino, A. J.; Cardozo, T. M.; Lischka, H. On the cooperative origin of solvent-enhanced symmetry-breaking charge transfer in a covalently bound tetracene dimer leading to singlet fission. *J. Am. Chem. Soc.* **2022**, *144*, 23492–23504.

[248] Lukman, S.; Musser, A. J.; Chen, K.; Athanasopoulos, S.; Yong, C. K.; Zeng, Z.; Ye, Q.; Chi, C.; Hodgkiss, J. M.; Wu, J.; others Tuneable singlet exciton fission and triplet–triplet annihilation in an orthogonal pentacene dimer. *Adv. Funct. Mater.* **2015**, *25*, 5452–5461.

[249] Lukman, S.; Chen, K.; Hodgkiss, J. M.; Turban, D. H.; Hine, N. D.; Dong, S.; Wu, J.; Greenham, N. C.; Musser, A. J. Tuning the role of charge-transfer states in intramolecular singlet exciton fission through side-group engineering. *Nat. Commun.* **2016**, *7*, 13622.

[250] Gao, Y.; Liu, H.; Zhang, S.; Gu, Q.; Shen, Y.; Ge, Y.; Yang, B. Excimer formation and evolution of excited state properties in discrete dimeric stacking of an anthracene derivative: a computational investigation. *Phys. Chem. Chem. Phys.* **2018**, *20*, 12129–12137.

Appendices

Appendix A

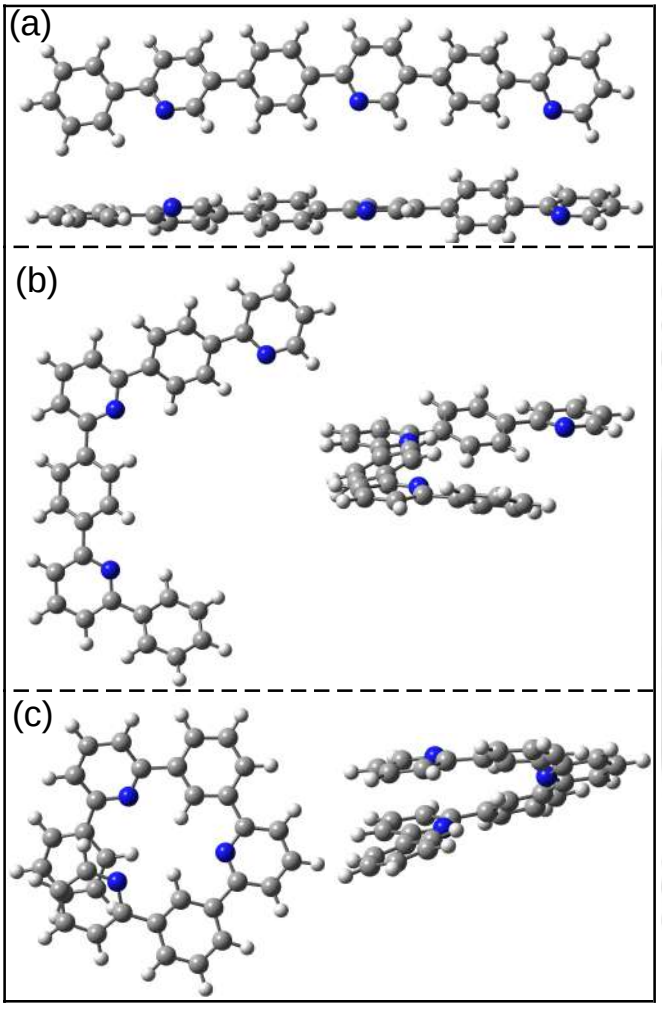

FIGURE A1: Optimized ground state structures of $(\mathbf{PhPy})_3$ for conformers **A**(a), **B**(b), and **C**(c) obtained at B3LYP-D3/def2-TZVP level. Top and side views are shown at the top and bottom, respectively, for **A**. For **B** and **C**, top and side views are shown in the left and right columns, respectively.

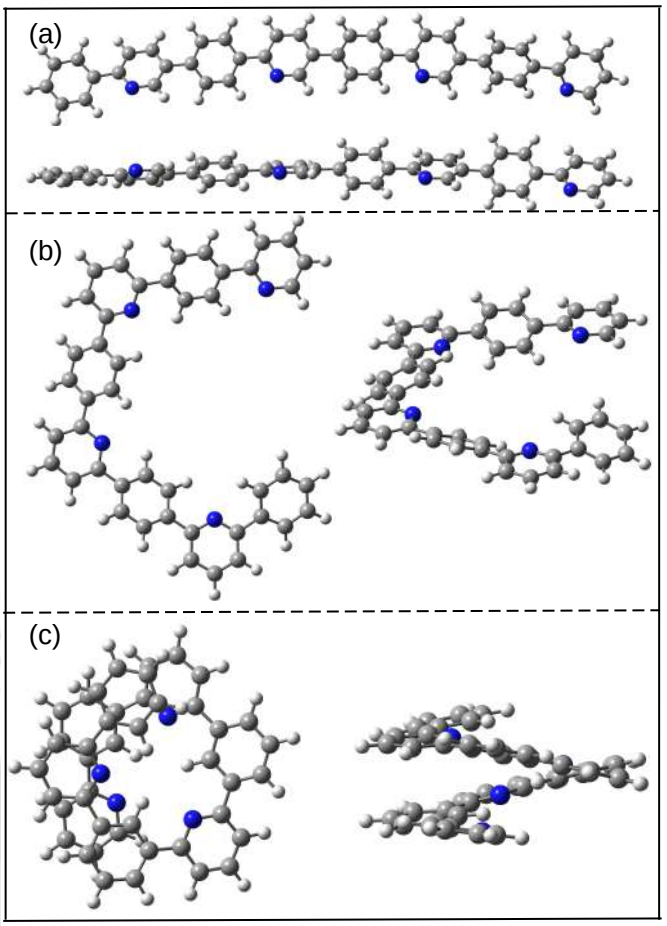

FIGURE A2: Optimized geometries of $(\mathbf{PhPy})_4$ for conformers **A**(a), **B**(b), and **C**(c) obtained at B3LYP-D3/def2-TZVP level. For **A**, top and side views are shown at the top and bottom, respectively. For **B** and **C**, these are shown in the left and right columns, respectively.

TABLE A1: E_g, f_{osc}, and the Rotatory Strengths (R in 10^{-40} erg·esu·cm/Gauss) of the First Ten Excited States of **(PhPy)**$_2$ for three Conformers Obtained at RI-ADC(2)/def2-TZVP Level

Oligomer		**A**			**B**			**C**		
	State	E_g	f_{osc}	R	E_g	f_{osc}	R	E_g	f_{osc}	R
(PhPy)$_2$	S_1	4.31	1.711	23.22	4.36	0.901	33.76	4.50	0.102	-72.64
	S_2	4.53	0.071	-64.79	4.53	0.054	9.30	4.57	0.130	-60.62
	S_3	4.64	0.014	-11.51	4.61	0.179	4.03	4.64	0.018	-30.22
	S_4	4.70	0.065	43.55	4.65	0.059	-64.51	4.69	0.033	56.42
	S_5	4.72	0.004	-4.97	4.68	0.002	15.15	4.74	0.009	-2.76
	S_6	4.92	0.007	-13.49	4.77	0.113	64.51	4.92	0.101	-186.40
	S_7	4.97	0.002	6.20	4.95	0.076	-0.58	4.96	0.213	110.40
	S_8	5.02	0.024	-10.05	5.01	0.009	-4.22	5.01	0.112	-25.57
	S_9	5.06	0.003	-8.99	5.06	0.008	12.38	5.03	0.033	47.71
	S_{10}	5.29	0.001	6.00	5.18	0.497	-16.77	5.32	0.614	-1.68

TABLE A2: E_g, f_{osc}, and the Rotatory Strengths (R in 10^{-40} erg·esu·cm/Gauss) of the First Ten Excited States of **(PhPy)**$_3$ for three Conformers Obtained at RI-ADC(2)/def2-TZVP Level

Oligomer		**A**			**B**			**C**		
	State	E_g	f_{osc}	R	E_g	f_{osc}	R	E_g	f_{osc}	R
(PhPy)$_3$	S_1	4.02	2.872	-9.15	4.23	1.188	22.45	4.31	0.041	-233.42
	S_2	4.43	0.006	-7.38	4.40	0.421	-14.76	4.42	0.011	-10.41
	S_3	4.45	0.024	-45.36	4.50	0.064	24.47	4.46	0.062	17.65
	S_4	4.55	0.010	-2.30	4.54	0.033	6.37	4.51	0.067	-164.72
	S_5	4.59	0.046	-2.96	4.57	0.213	51.98	4.52	0.042	-5.72
	S_6	4.64	0.003	16.13	4.61	0.070	-77.65	4.54	0.035	-9.54
	S_7	4.7	0.007	-16.68	4.62	0.019	7.59	4.59	0.069	67.69
	S_8	4.74	0.025	2.93	4.68	0.050	17.37	4.63	0.018	-0.92
	S_9	4.82	0.051	-3.07	4.70	0.051	-34.31	4.64	0.051	37.13
	S_{10}	4.93	0.001	10.96	4.75	0.089	-32.45	4.75	0.046	-72.64

TABLE A3: E_g, f_{osc}, and the Rotatory Strengths (R in 10^{-40} erg·esu·cm/Gauss) of the First Ten Excited States of **(PhPy)**$_4$ for three Conformers Obtained at RI-ADC(2)/def2-TZVP Level

Oligomer	**A**				**B**			**C**		
	State	E_g	f_{osc}	R	E_g	f_{osc}	R	E_g	f_{osc}	R
(PhPy)$_4$	S_1	3.89	3.952	-14.22	4.17	1.045	-28.96	4.36	0.021	-398.33
	S_2	4.28	0.030	-26.24	4.31	1.070	0.06	4.37	0.023	82.40
	S_3	4.43	0.032	-15.09	4.41	0.055	6.07	4.50	0.007	51.33
	S_4	4.45	0.006	-25.81	4.49	0.164	-0.82	4.57	0.052	-104.02
	S_5	4.51	0.003	-7.75	4.52	0.032	4.07	4.66	0.007	-62.51
	S_6	4.55	0.075	-3.82	4.54	0.008	3.07	4.69	0.074	-50.33
	S_7	4.6	0.015	-4.04	4.56	0.223	-55.07	4.70	0.012	-54.19
	S_8	4.63	0.099	5.62	4.59	0.004	-2.71	4.70	0.001	-6.34
	S_9	4.64	0.007	-15.60	4.60	0.033	-0.37	4.78	0.016	-0.16
	S_{10}	4.7	0.001	5.07	4.61	0.098	-16.60	4.84	0.070	-178.46

TABLE A4: E_g, f_{osc}, and the Rotatory Strengths (R in 10^{-40} erg·esu·cm/Gauss) of the First Ten Excited States of **(PhPy)**$_5$ for three Conformers Obtained at RI-ADC(2)/def2-TZVP Level

Oligomer	**A**				**B**			**C**		
	State	E_g	f_{osc}	R	E_g	f_{osc}	R	E_g	f_{osc}	R
(PhPy)$_5$	S_1	3.84	5.029	7.55	4.12	0.154	831.93	4.13	0.050	-564.97
	S_2	4.13	0.066	-91.72	4.26	1.641	-635.89	4.20	0.006	28.37
	S_3	4.40	0.253	36.93	4.31	0.765	81.61	4.23	0.024	79.20
	S_4	4.44	0.004	-13.89	4.39	0.001	-5.77	4.27	0.001	-23.56
	S_5	4.44	0.008	-27.61	4.43	0.160	-16.99	4.31	0.001	-25.53
	S_6	4.48	0.095	31.76	4.45	0.008	-2.13	4.31	0.009	-59.95
	S_7	4.52	0.065	-53.83	4.47	0.033	12.77	4.33	0.017	-17.40
	S_8	4.55	0.027	-15.31	4.49	0.055	4.28	4.35	0.062	106.74
	S_9	4.58	0.005	23.54	4.50	0.255	40.56	4.38	0.013	30.66
	S_{10}	4.62	0.068	-9.02	4.53	0.013	-7.58	4.41	0.087	172.96

TABLE A5: E_g, f_{osc}, Rotatory Strengths (R in erg·esu·cm/Gauss), $|\mu|$ (in esu-cm), $|m|$ (in erg-G^{-1}), cos θ, g_{CD}, and $|m|/|\mu|$ Values of the First Ten Excited States of **(PhPy)**$_5$ for Three Conformers Obtained at RI-ADC(2)/def2-TZVP Level

State	E_g	$R/10^{-40}$	$\|\mu\|/10^{-20}$	$\|m\|/10^{-20}$	cos θ	g_{CD}	$\|m\|/\|\mu\|$
A-(PhPy)$_5$							
S_1	3.84	7.54	1859.12	2.59	0.002	0.000	0.001
S_2	4.13	-91.71	205.41	0.45	-0.989	-0.008	0.002
S_3	4.40	36.92	389.75	1.30	0.073	0.001	0.003
S_4	4.44	-13.89	47.16	0.33	-0.887	-0.025	0.007
S_5	4.44	-27.61	70.44	0.52	-0.755	-0.022	0.007
S_6	4.48	31.75	236.2	0.54	0.251	0.002	0.002
S_7	4.52	-53.83	195.54	0.83	-0.330	-0.005	0.004
S_8	4.55	-15.31	125.91	0.36	-0.338	-0.003	0.003
S_9	4.58	23.53	51.83	0.71	0.643	0.035	0.014
S_{10}	4.62	-9.01	196.43	0.84	-0.055	-0.000	0.004
B-(PhPy)$_5$							
S_1	4.12	831.93	314.4	12.17	0.217	0.033	0.039
S_2	4.26	-635.89	1007.96	1.27	-0.497	-0.002	0.001
S_3	4.31	81.60	684.39	0.87	0.137	0.000	0.001
S_4	4.39	-5.76	28.2	0.49	-0.414	-0.029	0.018
S_5	4.43	-16.99	308.36	1.11	-0.050	-0.000	0.004
S_6	4.45	-2.13	68.51	0.47	-0.066	-0.001	0.007
S_7	4.47	12.76	138.78	0.90	0.102	0.002	0.006
S_8	4.49	4.27	180.57	0.26	0.092	0.000	0.001
S_9	4.50	40.55	386.84	2.10	0.050	0.001	0.005
S_{10}	4.53	-7.57	88.03	0.09	-0.916	-0.003	0.001
C-(PhPy)$_5$							
S_1	4.13	-564.96	178.61	4.61	-0.686	-0.070	0.026
S_2	4.20	28.37	61.37	0.60	0.764	0.030	0.010
S_3	4.23	79.19	122.68	0.96	0.675	0.021	0.008
S_4	4.27	-23.55	28.14	1.20	-0.697	-0.118	0.043
S_5	4.31	-25.53	23.12	1.11	-0.996	-0.190	0.048
S_6	4.31	-59.95	74.18	1.44	-0.562	-0.043	0.019
S_7	4.33	-17.40	100.82	0.86	-0.201	-0.006	0.009
S_8	4.35	106.73	193.15	1.02	0.54	0.011	0.005
S_9	4.38	30.66	88.74	0.67	0.514	0.015	0.008
S_{10}	4.41	172.96	228.32	0.82	0.924	0.013	0.004

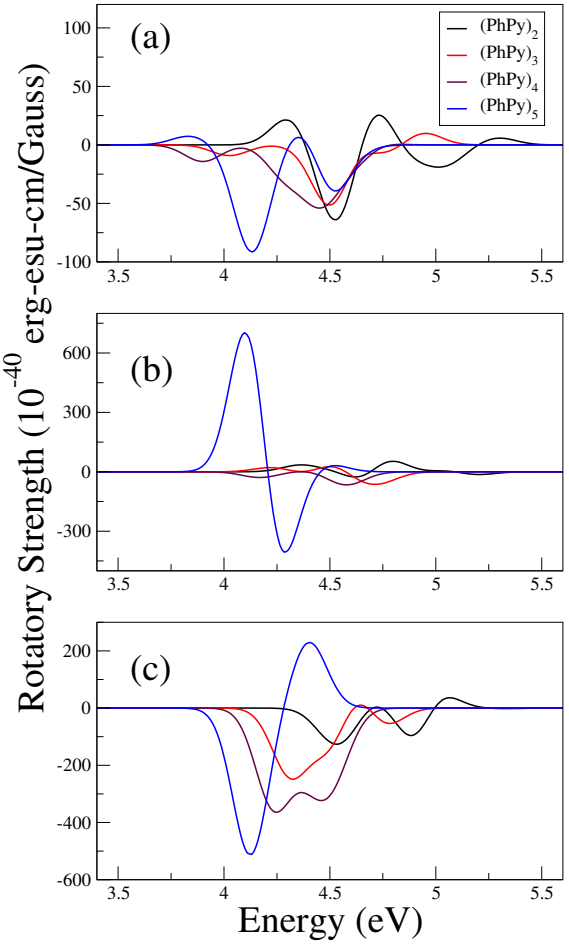

FIGURE A3: CD spectra of oligomers of three different conformers; **A** (a), **B** (b), and **C** (c). The results are obtained at RI-ADC(2)/def2-TZVP level.

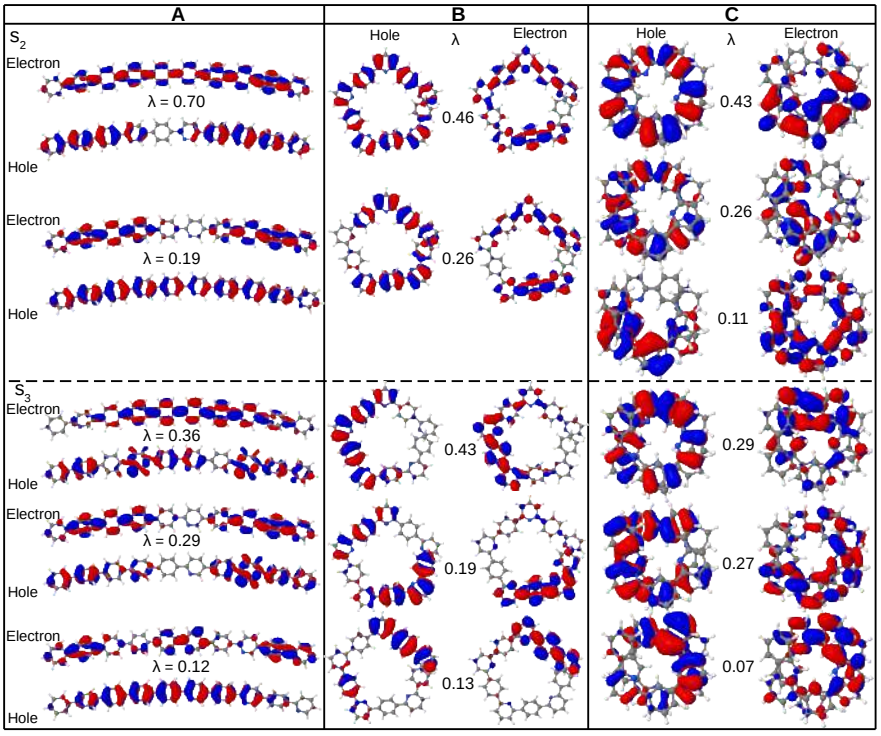

FIGURE A4: Natural transition orbitals involved in S_2 and S_3 states of $(\mathbf{PhPy})_5$ for the three conformers, obtained at RI-ADC(2)/def2-TZVP level. The eigenvalue λ indicates the pair's contribution to the excitation.

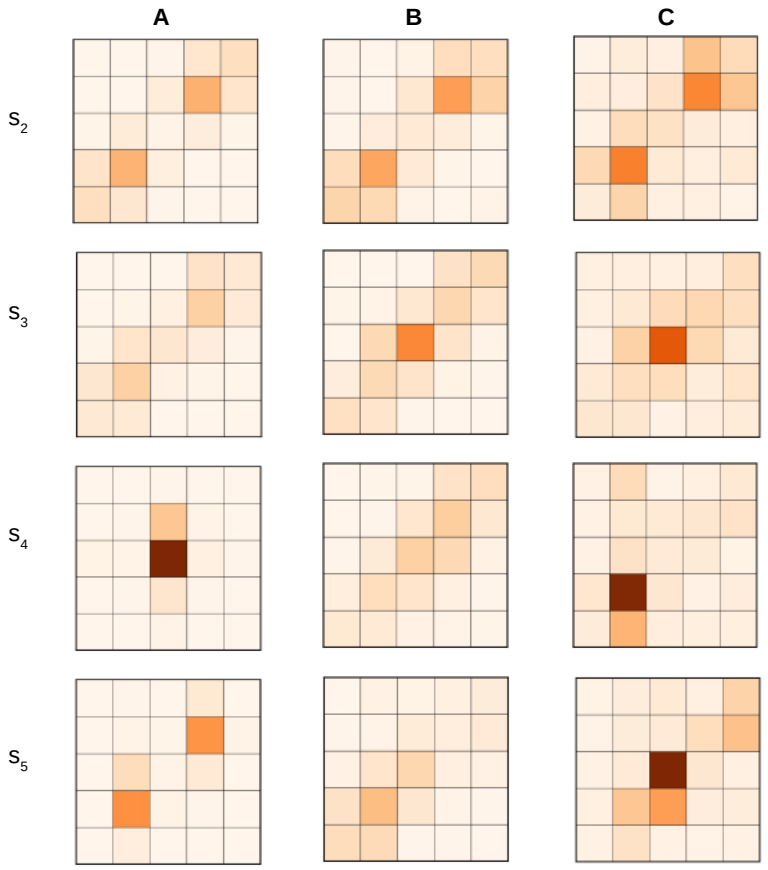

FIGURE A5: Electron-hole correlation plots for the S_2, S_3, S_4, and S_5 states of **(PhPy)**$_5$ of all the three conformers.

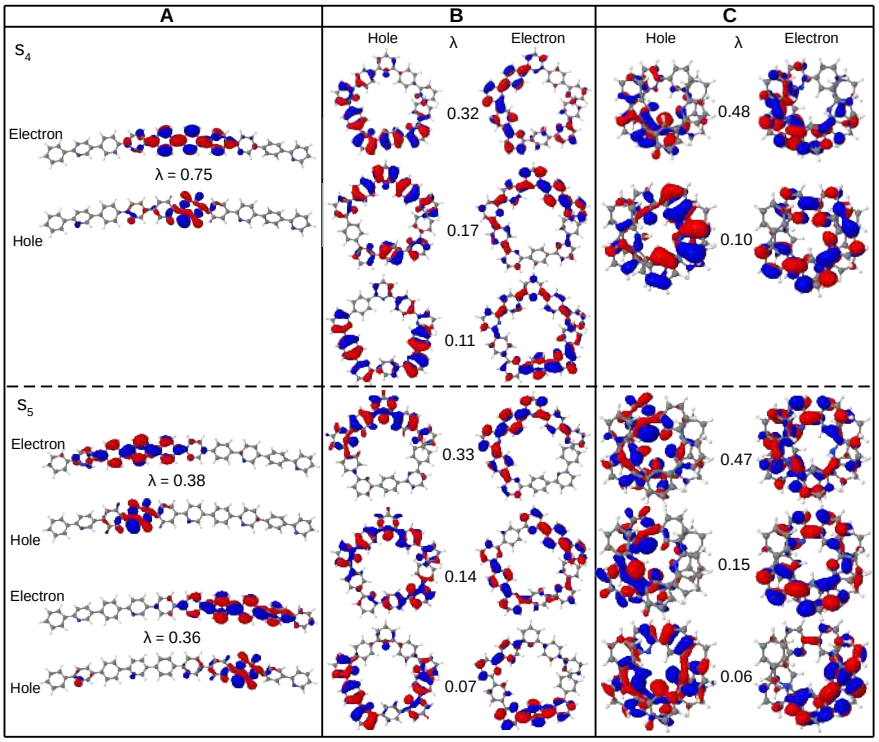

FIGURE A6: Natural transition orbitals involved in S_4 and S_5 states of $\mathbf{(PhPy)_5}$ for the three conformers, obtained at RI-ADC(2)/def2-TZVP level. The eigenvalue λ indicates the pair's contribution to the excitation.

Appendix B

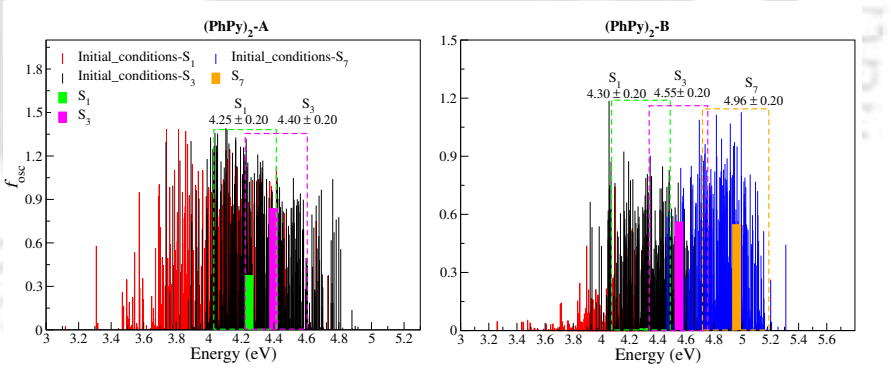

FIGURE B1: Energy window for the initial condition sampling of $(\mathbf{PhPy})_2$.

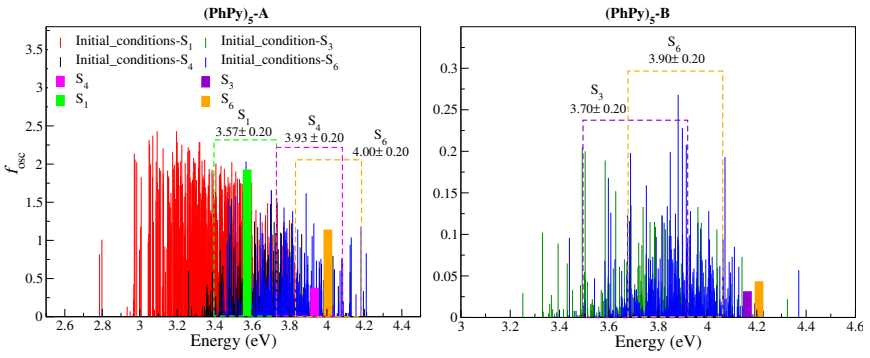

FIGURE B2: Energy window for the initial condition sampling of $(\mathbf{PhPy})_2$.

TABLE B1: Excitation energy (E_g) and the corresponding oscillator strengths (f_{osc}) values for the first ten excited states of **(PhPy)**$_2$ and **(PhPy)**$_5$

			A			
	(PhPy)$_2$			**(PhPy)**$_5$		
State	TD-DFTB	LC-TD-DFTB	RI-ADC(2)	TD-DFTB	LC-TD-DFTB	RI-ADC(2)
S_1	4.25 / 0.374	4.23 / 0.046	4.51 / 1.539	3.57 / 1.922	4.11 / 2.065	4.04 / 5.185
S_2	4.36 / 0.102	4.40 / 0.000	4.63 / 0.268	3.71 / 0.037	4.17 / 0.019	4.34 / 0.066
S_3	4.40 / 0.838	4.66 / 1.555	4.77 / 0.003	3.90 / 0.022	4.19 / 0.036	4.53 / 0.084
S_4	4.79 / 0.003	4.98 / 0.000	4.85 / 0.055	3.93 / 0.374	4.22 / 0.650	4.54 / 0.001
S_5	5.08 / 0.027	5.05 / 0.000	4.90 / 0.046	3.99 / 0.001	4.26 / 2.083	4.54 / 0.011
S_6	5.16 / 0.001	5.41 / 0.003	5.06 / 0.010	4.01 / 1.135	4.40 / 0.000	4.60 / 0.004
S_7	5.27 / 0.006	5.55 / 0.001	5.11 / 0.003	4.03 / 0.051	4.51 / 0.060	4.67 / 0.320
S_8	5.32 / 0.024	5.65 / 0.011	5.17 / 0.033	4.04 / 0.077	4.83 / 0.352	4.74 / 0.024
S_9	5.41 / 0.006	5.73 / 0.004	5.21 / 0.014	4.08 / 0.003	4.98 / 0.000	4.75 / 0.006
S_{10}	5.43 / 0.007	5.77 / 0.000	5.53 / 0.002	4.11 / 0.006	4.98 / 0.000	4.79 / 0.059
			B			
S_1	4.30 / 0.010	4.34 / 0.004	4.57 / 0.822	4.06 / 0.002	4.27 / 0.001	4.34 / 0.167
S_2	4.43 / 0.002	4.39 / 0.001	4.68 / 0.015	4.13 / 0.004	4.28 / 0.000	4.47 / 1.465
S_3	4.55 / 0.560	4.46 / 0.001	4.75 / 0.073	4.16 / 0.031	4.29 / 0.001	4.51 / 0.538
S_4	4.75 / 0.009	4.84 / 1.133	4.81 / 0.189	4.18 / 0.001	4.32 / 0.004	4.56 / 0.066
S_5	4.83 / 0.090	5.04 / 0.000	4.83 / 0.008	4.19 / 0.001	4.33 / 0.004	4.59 / 0.073
S_6	4.89 / 0.013	5.32 / 0.199	4.94 / 0.227	4.21 / 0.043	4.35 / 0.000	4.61 / 0.013
S_7	4.96 / 0.547	5.48 / 0.254	5.10 / 0.035	4.22 / 0.014	4.36 / 0.002	4.61 / 0.089
S_8	5.28 / 0.001	5.51 / 0.003	5.17 / 0.016	4.23 / 0.007	4.38 / 0.003	4.63 / 0.140
S_9	5.40 / 0.003	5.78 / 0.000	5.22 / 0.030	4.24 / 0.006	4.44 / 0.000	4.66 / 0.018
S_{10}	5.47 / 0.005	5.79 / 0.003	5.42 / 0.599	4.25 / 0.005	4.64 / 0.173	4.69 / 0.105

TABLE B2: Excitation energy (E_g), oscillator strengths (f_{osc}), and ω_{CT} values for the first ten excited states at different times of single representative trajectories for **(PhPy)**$_2$-**A** and **B**

TD-DFTB								
	(PhPy)$_2$-**A**				**(PhPy)**$_2$-**B**			
	0 fs (S_3)		138 fs (S_1)		0 fs (S_3)		141 fs (S_1)	
State	E_g/ f_{osc}	ω_{CT}	E_g/ f_{osc}	ω_{CT}	E_g/ f_{osc}	ω_{CT}	E_g/ f_{osc}	ω_{CT}
S_1	4.04 / 0.585	0.58	2.27 / 0.018	0.47	4.25 / 0.013	0.77	2.99 / 0.037	0.30
S_2	4.08 / 0.002	0.37	3.19 / 0.070	0.54	4.45 / 0.015	0.23	3.36 / 0.145	0.69
S_3	4.34 / 0.643	0.63	3.30 / 0.000	0.53	4.71 / 0.566	0.57	3.48 / 0.010	0.97
S_4	4.60 / 0.001	0.82	3.48 / 1.572	0.55	4.90 / 0.261	0.65	3.67 / 0.621	0.61
S_5	4.90 / 0.007	0.60	3.63 / 0.004	0.04	4.96 / 0.009	0.71	3.79 / 0.077	0.48
S_6	4.94 / 0.024	0.39	3.89 / 0.002	0.78	5.11 / 0.012	0.24	3.93 / 0.208	0.65
S_7	5.04 / 0.007	0.68	4.02 / 0.002	0.90	5.16 / 0.015	0.45	4.02 / 0.007	0.43
S_8	5.10 / 0.006	0.51	4.24 / 0.000	0.90	5.22 / 0.018	0.49	4.10 / 0.111	0.55
S_9	5.13 / 0.006	0.47	4.24 / 0.001	0.56	5.26 / 0.033	0.74	4.30 / 0.048	0.59
S_{10}	5.21 / 0.005	0.54	4.26 / 0.024	0.53	5.29 / 0.012	0.71	4.47 / 0.002	0.25
RI-ADC(2)								
S_1	4.26 / 0.729	0.29	2.87 / 0.006	0.07	4.51 / 0.232	0.32	3.44 / 0.080	0.08
S_2	4.46 / 0.209	0.11	3.63 / 0.665	0.32	4.59 / 0.004	0.05	3.77 / 0.567	0.37
S_3	4.54 / 0.633	0.16	3.76 / 1.488	0.36	4.77 / 0.101	0.10	3.89 / 0.320	0.32
S_4	4.64 / 0.175	0.21	3.92 / 0.004	0.23	4.84 / 0.351	0.14	4.09 / 0.401	0.22
S_5	4.71 / 0.012	0.19	4.12 / 0.002	0.01	4.90 / 0.260	0.26	4.21 / 0.046	0.26
S_6	4.90 / 0.003	0.11	4.36 / 0.002	0.09	5.01 / 0.067	0.16	4.35 / 0.032	0.22
S_7	4.94 / 0.026	0.11	4.57 / 0.005	0.24	5.09 / 0.182	0.19	4.55 / 0.027	0.14
S_8	4.99 / 0.003	0.03	4.70 / 0.007	0.29	5.23 / 0.112	0.16	4.57 / 0.015	0.06
S_9	5.04 / 0.052	0.17	4.74 / 0.001	0.38	5.36 / 0.035	0.14	4.75 / 0.142	0.16
S_{10}	5.38 / 0.017	0.14	4.78 / 0.005	0.25	5.86 / 0.306	0.22	4.83 / 0.357	0.17

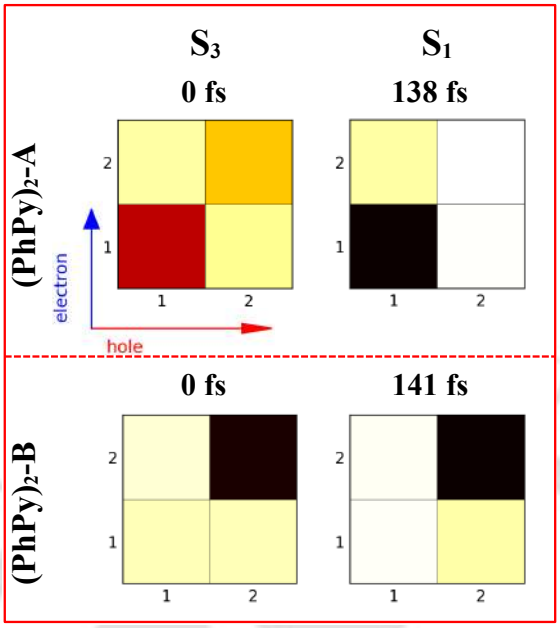

FIGURE B3: Electron-hole correlation plots involved in the current states of a selected trajectory at different times for **(PhPy)**$_2$**-A** and **B** obtained at the RI-ADC(2) level.

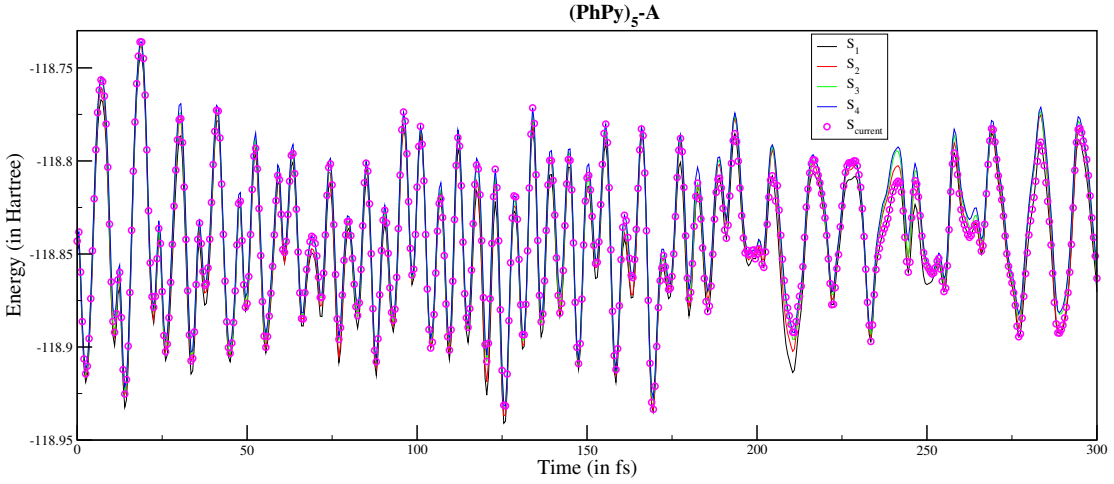

FIGURE B4: Energies of the first four excited states S_1-S_4 of a single representative trajectory as a function of time of **(PhPy)**$_5$**-A**. Magenta circles indicate the current state of the system.

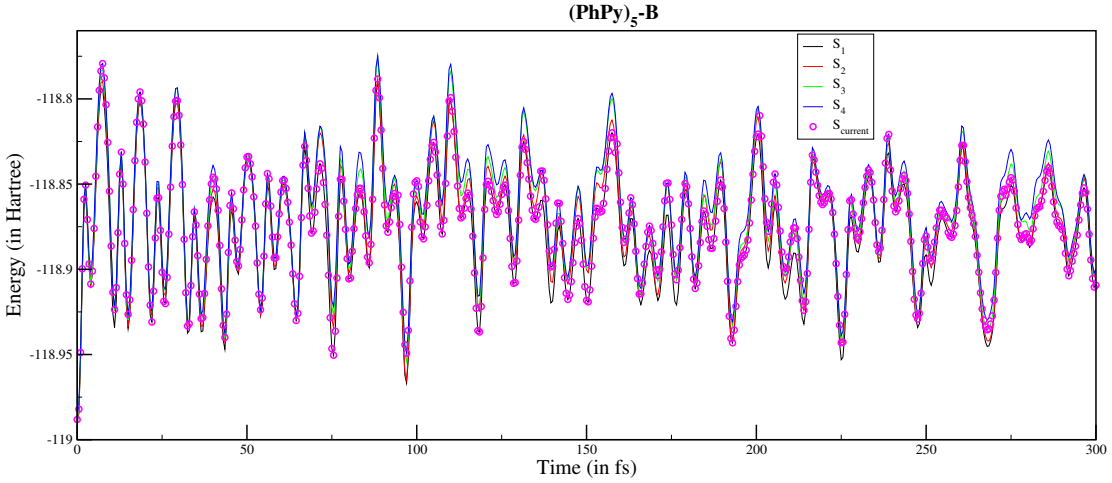

FIGURE B5: Energies of the first four excited states S_1-S_4 of a single representative trajectory as a function of time of $(\mathbf{PhPy})_5$-**B**. Magenta circles indicate the current state of the system.

TABLE B3: Excitation energy (E_g), oscillator strengths (f_{osc}), and ω_{CT} values for the first ten excited states at different times of single representative trajectories for **(PhPy)$_5$-A**

TD-DFTB								
	0 fs (S_4)		2 fs (S_3)		13 fs (S_2)		101.5 fs (S_1)	
State	E_g / f_{osc}	ω_{CT}	E_g / f_{osc}	ω_{CT}	E_g / f_{osc}	ω_{CT}	E_g / f_{osc}	ω_{CT}
S_1	3.69 / 1.049	0.87	3.46 / 1.669	0.83	2.79 / 0.729	0.93	2.64 / 1.393	0.78
S_2	3.75 / 0.001	0.93	3.56 / 0.010	0.94	3.00 / 1.365	0.87	2.72 / 0.420	0.64
S_3	3.88 / 0.079	0.86	3.65 / 0.155	0.93	3.06 / 0.153	0.90	2.79 / 0.029	0.97
S_4	3.89 / 0.142	0.87	3.70 / 0.363	0.89	3.19 / 0.156	0.76	2.81 / 0.182	0.92
S_5	3.96 / 0.027	0.85	3.76 / 0.015	0.87	3.30 / 0.462	0.86	3.03 / 0.096	0.92
S_6	3.96 / 0.725	0.85	3.77 / 0.003	0.95	3.39 / 0.075	0.89	3.07 / 0.113	0.86
S_7	3.97 / 0.157	0.91	3.84 / 0.001	0.71	3.41 / 0.771	0.76	3.13 / 0.094	0.93
S_8	4.02 / 0.037	0.87	3.88 / 0.293	0.87	3.53 / 0.066	0.68	3.16 / 0.011	0.98
S_9	4.07 / 0.002	0.53	3.91 / 0.074	0.67	3.55 / 0.085	0.73	3.17 / 0.013	0.75
S_{10}	4.08 / 0.012	0.91	3.94 / 0.280	0.84	3.56 / 0.042	0.75	3.25 / 1.225	0.83
RI-ADC(2)								
S_1	4.17 / 4.471	0.44	3.92 / 4.381	0.46	3.49 / 4.415	0.44	3.30 / 4.133	0.51
S_2	4.28 / 0.061	0.13	4.27 / 0.025	0.37	3.61 / 0.341	0.29	3.44 / 0.029	0.50
S_3	4.33 / 0.006	0.15	4.32 / 0.248	0.48	3.85 / 0.197	0.44	3.69 / 0.225	0.49
S_4	4.35 / 0.022	0.51	4.34 / 0.024	0.26	4.11 / 0.023	0.35	3.73 / 0.082	0.38
S_5	4.46 / 0.094	0.42	4.36 / 0.022	0.43	4.17 / 0.040	0.30	3.97 / 0.104	0.37
S_6	4.50 / 0.072	0.47	4.37 / 0.003	0.09	4.24 / 0.378	0.45	4.07 / 0.013	0.13
S_7	4.59 / 0.190	0.39	4.40 / 0.022	0.41	4.31 / 0.006	0.11	4.11 / 0.638	0.50
S_8	4.63 / 0.419	0.43	4.45 / 0.094	0.50	4.36 / 0.020	0.38	4.19 / 0.005	0.15
S_9	4.68 / 0.012	0.45	4.48 / 0.007	0.47	4.39 / 0.060	0.51	4.22 / 0.016	0.66
S_{10}	4.71 / 0.017	0.43	4.55 / 0.515	0.43	4.46 / 0.014	0.45	4.23 / 0.022	0.50

TABLE B4: Excitation energy (E_g), oscillator strengths (f_{osc}), and ω_{CT} values for the first ten excited states at different times of single representative trajectories for **(PhPy)$_5$-B**

	TD-DFTB					
	0 fs (S_3)		3 fs (S_2)		22 fs (S_1)	
State	E_g / f_{osc}	ω_{CT}	E_g / f_{osc}	ω_{CT}	E_g / f_{osc}	ω_{CT}
S_1	3.54 / 0.000	1.00	3.43 / 0.021	0.48	3.46 / 0.002	0.99
S_2	3.62 / 0.007	0.99	3.51 / 0.000	1.00	3.60 / 0.012	0.97
S_3	3.67 / 0.067	0.57	3.53 / 0.000	1.00	3.69 / 0.153	0.80
S_4	3.68 / 0.001	0.65	3.58 / 0.000	1.00	3.70 / 0.006	0.91
S_5	3.80 / 0.030	0.95	3.65 / 0.005	0.97	3.72 / 0.002	0.75
S_6	3.83 / 0.005	0.99	3.66 / 0.013	0.89	3.75 / 0.005	0.97
S_7	3.92 / 0.001	0.96	3.70 / 0.000	1.00	3.76 / 0.026	0.86
S_8	3.92 / 0.008	0.98	3.75 / 0.009	0.95	3.84 / 0.003	0.93
S_9	3.93 / 0.021	0.96	3.79 / 0.004	0.72	3.85 / 0.004	0.82
S_{10}	3.99 / 0.010	0.61	3.79 / 0.018	0.92	3.88 / 0.072	0.87
	RI-ADC(2)					
S_1	4.05 / 0.511	0.31	3.98 / 0.290	0.38	4.02 / 0.209	0.46
S_2	4.16 / 0.301	0.35	4.08 / 0.016	0.33	4.12 / 1.556	0.44
S_3	4.29 / 0.001	0.17	4.14 / 0.812	0.42	4.16 / 0.083	0.49
S_4	4.32 / 0.019	0.27	4.17 / 0.022	0.23	4.24 / 0.102	0.44
S_5	4.43 / 0.622	0.47	4.25 / 0.115	0.37	4.30 / 0.285	0.55
S_6	4.44 / 0.469	0.49	4.27 / 0.071	0.43	4.43 / 0.000	0.49
S_7	4.48 / 0.022	0.45	4.28 / 0.492	0.49	4.47 / 0.164	0.47
S_8	4.51 / 0.222	0.64	4.36 / 0.501	0.39	4.47 / 0.129	0.45
S_9	4.54 / 0.188	0.60	4.41 / 0.114	0.49	4.52 / 0.067	0.43
S_{10}	4.55 / 0.432	0.54	4.42 / 0.148	0.33	4.55 / 0.958	0.48

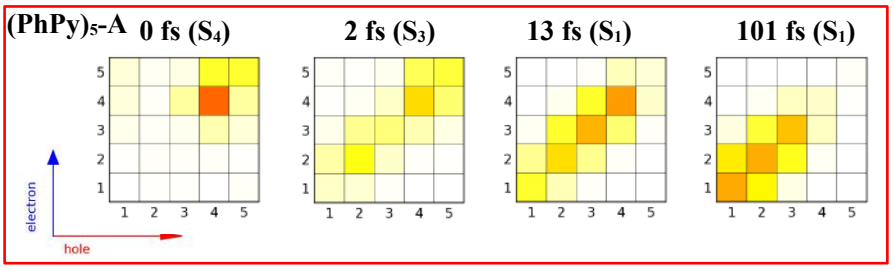

FIGURE B6: Electron-hole correlation plots involved in the current state of a selected trajectory at different times for **(PhPy)$_5$-A** obtained at the RI-ADC(2) level.

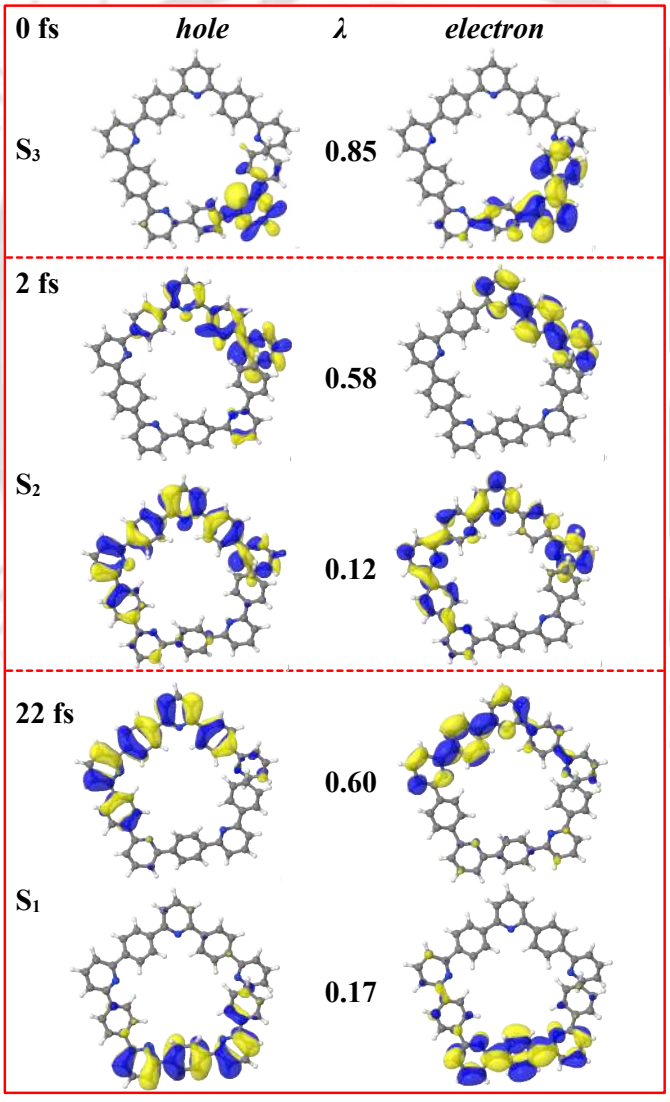

FIGURE B7: NTOs involved in the current state of a selected trajectory at different times for **(PhPy)$_5$-B** obtained at the RI-ADC(2) level.

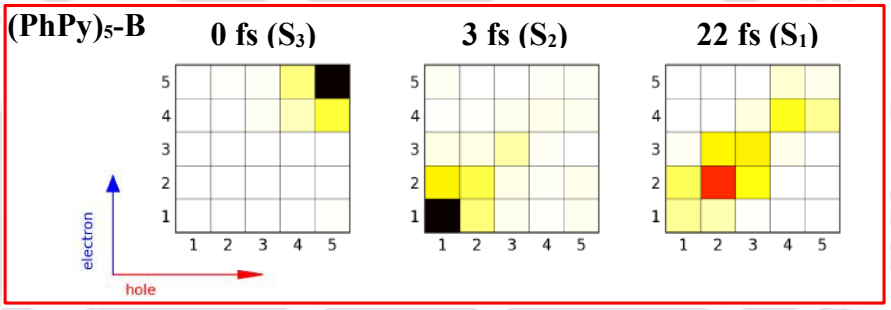

FIGURE B8: Electron-hole correlation plots involved in the current state of a selected trajectory at different times for **(PhPy)$_5$-B** obtained at the RI-ADC(2) level.

Appendix C

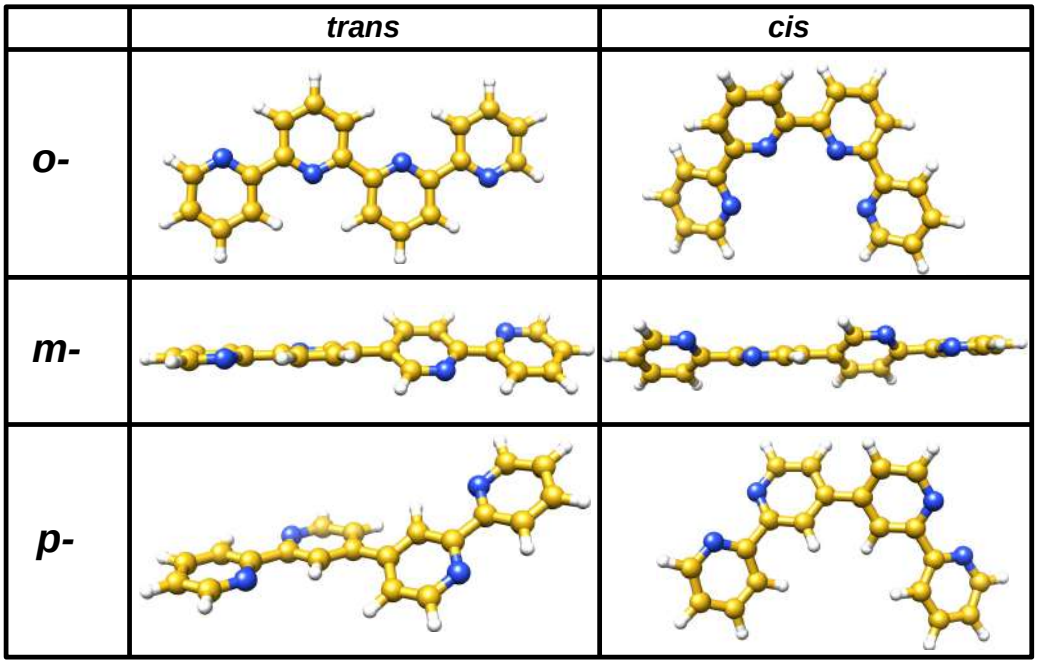

FIGURE C1: Ground state optimized structures of ***trans***- and ***cis***-$(\mathbf{BPY})_2$ for ***o***-, ***m***-, and ***p***- conformers obtained at B3LYP-D3/def2-SVPD level.

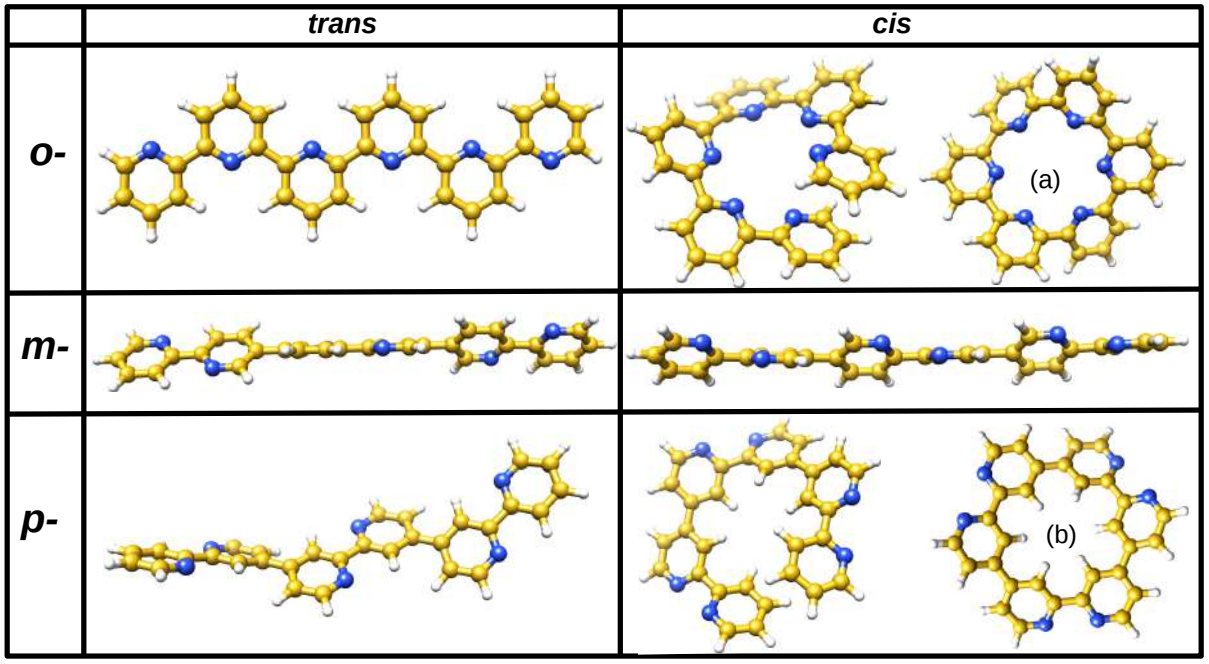

FIGURE C2: Optimized geometries of ***trans***- and ***cis***-$(\mathbf{BPY})_3$ for ***o***-, ***m***-, and ***p***- conformers. In this figure, (a) and (b) are the cyclic (cy) analogs of ***o***- and ***p***- conformers, respectively.

TABLE C1: Energies (in eV) of ground state optimized structures of all the oligomers at B3LYP-D3/def2-SVPD level

trans	$(\mathbf{BPY})_2$	$(\mathbf{BPY})_3$	$(\mathbf{BPY})_4$
o-	0.00	0.00	0.00
m-	0.19	0.38	0.57
p-	0.17	0.33	0.50
cis			
o-	0.91	1.38	0.50
cy-***o-***		33.91	
m-	0.88	1.28	1.77
p-	0.86	1.12	1.04
cy-***p-***		33.67	

TABLE C2: Calculated dihedral angles (ϕ_{1-7}) of $(\mathbf{BPY})_2$-$(\mathbf{BPY})_4$ for ***trans***- structures of ***o-*** conformer at B3LYP-D3/def2-SVPD level

Angle	$(\mathbf{BPY})_2$	$(\mathbf{BPY})_3$	$(\mathbf{BPY})_4$
ϕ_1	0	0	0
ϕ_2	0	0	0
ϕ_3	0	0	0
ϕ_4		0	0
ϕ_5		0	0
ϕ_6			0
ϕ_7			0

TABLE C3: Calculated dihedral angles (ϕ_{1-7}) of $(\mathbf{BPY})_2$-$(\mathbf{BPY})_4$ for ***trans***- structures of ***m-*** and ***p-*** conformers at B3LYP-D3/def2-SVPD level

	m-			***p-***		
Angle	$(\mathbf{BPY})_2$	$(\mathbf{BPY})_3$	$(\mathbf{BPY})_4$	$(\mathbf{BPY})_2$	$(\mathbf{BPY})_3$	$(\mathbf{BPY})_4$
ϕ_1	0	0	0	-0.8	-0.8	0.6
ϕ_2	37.2	-37	37.1	33.7	33.6	-33.3
ϕ_3	0	0	0	-0.5	-1.6	1.6
ϕ_4		37	37.2		33.6	-33.5
ϕ_5		0	0		0.5	1.6
ϕ_6			37.1			-33.3
ϕ_7			0			0.8

In the case of ***trans*** oligomers for ***o-*** conformer, only one type of the dihedral angle ϕ_i, defined as ∠N-C-C-C, is used. In ***m-*** and ***p-***, two types of dihedral angles, ϕ_j and ϕ_k, are used which are defined as ∠N-C-C-C and ∠C-C-C-C, respectively. Similarly, in the case of ***cis-o-*** conformer, only one type of dihedral angle ϕ_i=∠N-C-C-N is used, whereas for ***m-*** and ***p-*** two types of dihedral angles ϕ_j=∠N-C-C-N and ϕ_k=∠C-C-C-C are used. In the case of tetramers, for example, i=1-7, j=1, 3, 5, 7, and k=2, 4, 6.

TABLE C4: Calculated dihedral angles (ϕ_{1-7}) of **(BPY)**$_2$-**(BPY)**$_4$ for ***cis***- structures of ***o***- conformer at B3LYP-D3/def2-SVPD level

	o-			
Angle	**(BPY)**$_2$	**(BPY)**$_3$	cy-**(BPY)**$_3$	**(BPY)**$_4$
ϕ_1	39.6	-30.3	-26.5	38.7
ϕ_2	-38.4	20.8	-26.5	-26.0
ϕ_3	39.6	-44.6	51.7	53.3
ϕ_4		20.8	-26.5	-38.6
ϕ_5		-30.3	-26.5	53.3
ϕ_6			51.7	-26.0
ϕ_7				38.7

TABLE C5: Calculated dihedral angles (ϕ_{1-7}) of **(BPY)**$_2$-**(BPY)**$_4$ for ***cis***- structures of ***m***- and ***p***- conformers at B3LYP-D3/def2-SVPD level

	m-			***p***-			
Angle	**(BPY)**$_2$	**(BPY)**$_3$	**(BPY)**$_4$	**(BPY)**$_2$	**(BPY)**$_3$	cy-**(BPY)**$_3$	**(BPY)**$_4$
ϕ_1	35.2	35.3	35.2	-37.3	-40.0	-17.5	-42.5
ϕ_2	-37.9	-37.7	-37.8	35.7	26.8	-23.9	29.0
ϕ_3	35.2	33.2	33.0	-37.3	-42.2	41.6	-42
ϕ_4		-37.8	-37.8		26.8	-23.9	22.3
ϕ_5		35.3	33.1		-40.0	-17.5	-42.0
ϕ_6			-37.8			39.0	29.0
ϕ_7			35.2				-42.5

TABLE C6: Vertical excitation energies (E_g), oscillator strengths (f_{osc}) and the rotatory strengths (R in 10^{-40} erg-esu-cm/Gauss) of first sixteen excited states for three conformers of ***trans***- and ***cis***-**(BPY)**$_2$ obtained at RI-ADC(2)/def2-TZVPD level

trans		***o-***				***m-***				***p-***		
State	irrep	E_g	f_{osc}	R	irrep	E_g	f_{osc}	R	irrep	E_g	f_{osc}	R
S_1	A	4.37	0.000	0.00	B	4.19	1.487	-1.68	A	4.33	0.005	-6.41
S_2	B	4.37	0.000	0.00	A	4.20	0.002	-1.80	B	4.34	0.013	29.95
S_3	A	4.39	0.000	0.00	B	4.38	0.292	28.89	A	4.51	0.014	-11.13
S_4	B	4.46	0.460	0.00	A	4.62	0.000	1.84	B	4.55	0.298	102.66
S_5	A	4.48	0.004	0.00	A	4.64	0.001	2.40	A	4.64	0.000	2.56
S_6	B	4.70	0.000	0.00	B	4.73	0.036	-56.86	B	4.66	0.060	-160.54
S_7	B	4.78	0.696	0.00	B	4.75	0.010	-62.68	B	4.80	0.637	-235.95
S_8	B	4.79	0.000	0.00	A	4.82	0.001	-8.71	A	4.84	0.034	237.77
S_9	A	4.80	0.000	0.00	B	4.92	0.001	13.02	B	4.91	0.001	0.86
S_{10}	A	4.82	0.000	0.00	A	4.94	0.000	-2.53	A	4.91	0.000	-0.11
S_{11}	A	5.05	0.004	0.00	B	5.10	0.006	12.17	A	5.08	0.005	3.28
S_{12}	B	5.06	0.000	0.00	A	5.12	0.006	-10.70	B	5.08	0.000	-1.66
S_{13}	B	5.13	0.228	0.00	B	5.14	0.041	-21.79	B	5.30	0.113	-13.22
S_{14}	A	5.35	0.000	0.00	A	5.39	0.000	2.66	A	5.41	0.027	90.78
S_{15}	B	5.47	0.580	0.00	A	5.46	0.008	60.34	B	5.47	1.217	-127.51
S_{16}	A	5.74	0.000	0.00	B	5.91	0.070	-29.31	A	5.75	0.000	-1.82
cis												
S_1	A	4.38	0.000	0.55	B	4.28	0.301	-99.18	B	4.35	0.003	-7.50
S_2	B	4.44	0.001	-2.91	A	4.31	0.000	-4.22	A	4.36	0.005	37.99
S_3	A	4.47	0.000	0.67	B	4.48	0.781	-213.58	A	4.56	0.008	45.18
S_4	B	4.52	0.003	25.56	A	4.55	0.000	0.42	B	4.57	0.007	13.80
S_5	A	4.58	0.001	-14.94	B	4.59	0.383	310.76	B	4.68	0.065	22.93
S_6	B	4.59	0.010	-46.51	A	4.78	0.000	-2.55	A	4.75	0.134	-100.47
S_7	B	4.72	0.279	-68.46	B	4.79	0.076	108.99	B	4.77	0.001	-4.37
S_8	A	4.86	0.002	17.60	A	4.86	0.000	-4.24	A	4.77	0.012	-4.69
S_9	B	4.86	0.003	-6.70	A	4.90	0.000	0.01	B	4.91	0.003	0.00
S_{10}	A	4.89	0.121	89.00	B	4.90	0.005	17.34	A	4.91	0.001	8.11
S_{11}	B	5.07	0.015	-92.64	B	4.94	0.217	-84.32	B	5.06	0.202	132.95
S_{12}	A	5.10	0.118	23.02	A	5.06	0.015	-14.32	A	5.08	0.062	-46.53
S_{13}	B	5.31	0.095	9.21	B	5.10	0.022	23.01	B	5.42	0.101	35.92
S_{14}	A	5.58	0.476	215.72	A	5.52	0.002	11.30	B	5.52	0.944	-24.65
S_{15}	B	5.68	0.078	-19.81	A	5.68	0.003	5.81	A	5.59	0.457	-124.32
S_{16}	A	5.70	0.028	5.03	B	5.96	0.008	9.70	A	5.66	0.064	-29.72

TABLE C7: Vertical excitation energies (E_g), oscillator strengths (f_{osc}) and the rotatory strengths (R in 10^{-40} erg-esu-cm/Gauss) of first sixteen excited states for three conformers of ***trans***- and ***cis***-**(BPY)**$_3$ obtained at RI-ADC(2)/def2-TZVPD level

trans			***o-***				***m-***				***p-***	
State		E_g	f_{osc}	R	irrep	E_g	f_{osc}	R	irrep	E_g	f_{osc}	R
S_1	A	4.34	0.000	0.00	B	3.94	2.785	23.69	A	4.30	0.007	0.03
S_2	B	4.35	0.000	0.00	A	4.12	0.001	2.61	A	4.33	0.001	-10.91
S_3	A	4.36	0.000	0.00	B	4.25	0.065	-12.97	B	4.33	0.019	34.58
S_4	B	4.37	0.001	0.00	A	4.30	0.001	3.20	B	4.47	0.137	87.82
S_5	A	4.37	0.000	0.00	A	4.49	0.002	-9.67	A	4.48	0.015	-43.96
S_6	B	4.42	0.000	0.00	B	4.55	0.009	-1.30	B	4.53	0.317	71.28
S_7	A	4.43	0.000	0.00	A	4.56	0.000	4.76	A	4.55	0.044	133.02
S_8	B	4.46	1.230	-0.01	B	4.63	0.039	-11.91	B	4.56	0.381	-217.32
S_9	A	4.50	0.007	0.00	A	4.69	0.001	-1.23	A	4.64	0.001	-4.82
S_{10}	B	4.65	0.000	0.00	A	4.71	0.000	4.50	B	4.64	0.120	-244.57
S_{11}	A	4.75	0.000	0.00	B	4.73	0.056	199.77	B	4.81	0.534	-494.18
S_{12}	B	4.75	0.000	0.00	B	4.78	0.100	-22.73	A	4.83	0.123	565.32
S_{13}	B	4.78	0.744	-0.02	B	4.89	0.007	-35.00	A	4.90	0.000	-0.65
S_{14}	A	4.79	0.000	0.00	A	4.92	0.000	3.59	A	4.91	0.000	0.51
S_{15}	B	4.83	0.000	0.00	B	4.93	0.001	3.66	B	4.91	0.000	0.97
S_{16}	A	4.84	0.000	0.00	A	5.05	0.002	4.08	B	5.07	0.001	-1.19
cis												
S_1	B	3.98	0.000	-1.77	B	4.17	1.960	-274.92	B	4.31	0.007	24.89
S_2	A	3.98	0.000	-0.76	A	4.18	0.001	-5.16	A	4.31	0.000	5.00
S_3	B	4.15	0.000	-0.41	A	4.30	0.000	1.27	A	4.34	0.001	8.13
S_4	A	4.16	0.000	2.10	B	4.33	0.235	-5.04	B	4.37	0.008	35.70
S_5	A	4.31	0.000	-0.10	B	4.43	0.365	184.29	B	4.55	0.001	-21.27
S_6	B	4.34	0.002	-2.24	A	4.54	0.002	5.25	A	4.56	0.012	65.44
S_7	B	4.38	0.000	4.91	B	4.55	0.044	121.95	B	4.58	0.019	82.03
S_8	A	4.38	0.000	-1.56	A	4.67	0.011	-4.77	A	4.63	0.025	-42.42
S_9	A	4.44	0.001	15.75	B	4.76	0.115	27.44	B	4.71	0.211	-139.30
S_{10}	B	4.44	0.002	31.47	A	4.77	0.000	-1.28	A	4.73	0.034	5.35
S_{11}	B	4.51	0.049	-514.84	B	4.78	0.074	136.53	B	4.76	0.000	0.03
S_{12}	A	4.60	0.328	345.84	A	4.81	0.006	-22.97	A	4.76	0.000	-1.80
S_{13}	B	4.67	0.004	-0.06	B	4.84	0.015	-24.76	A	4.77	0.049	8.71
S_{14}	A	4.68	0.004	15.53	B	4.89	0.066	-61.39	B	4.79	0.004	4.83
S_{15}	B	4.85	0.176	-93.22	A	4.90	0.000	0.04	B	4.89	0.002	-3.79
S_{16}	A	4.88	0.001	2.05	A	4.91	0.000	0.01	A	4.89	0.000	9.38

TABLE C8: Vertical excitation energies (E_g), oscillator strengths (f_{osc}) and the rotatory strengths (R in 10^{-40} erg-esu-cm/Gauss) of first sixteen excited states for cy-***o-*** and cy-***p-*** conformers of ***cis*-(BPY)$_3$** obtained at RI-ADC(2)/def2-TZVPD level

	cy- ***o-***				cy- ***p-***			
State	irrep	E_g	f_{osc}	R	irrep	E_g	f_{osc}	R
S_1	A	4.05	0.000	0.00	B	4.08	0.000	0.10
S_2	B	4.05	0.001	4.06	A	4.08	0.001	-0.37
S_3	B	4.18	0.000	1.96	A	4.30	0.020	3.20
S_4	A	4.18	0.000	0.56	B	4.33	0.026	-113.55
S_5	A	4.39	0.001	23.68	B	4.33	0.010	-46.02
S_6	B	4.40	0.000	7.25	A	4.34	0.012	90.82
S_7	B	4.40	0.000	7.42	B	4.39	0.017	121.59
S_8	A	4.40	0.000	0.00	A	4.44	0.161	-63.88
S_9	B	4.49	0.001	-16.16	B	4.49	0.003	-1.49
S_{10}	A	4.51	0.000	4.62	A	4.49	0.000	-4.52
S_{11}	A	4.52	0.012	200.15	B	4.60	0.154	24.71
S_{12}	A	4.54	0.000	0.00	A	4.67	0.061	-44.97
S_{13}	B	4.55	0.014	31.24	B	4.69	0.013	12.29
S_{14}	B	4.62	0.348	-452.78	A	4.69	0.004	6.79
S_{15}	A	4.82	0.000	0.00	A	4.72	0.006	-1.60
S_{16}	B	4.83	0.354	317.22	B	4.76	0.023	3.83

TABLE C9: E_g, f_{osc}, Rotatory Strengths (R in erg·esu·cm/Gauss), $|\mu|$ (in esu-cm), $|m|$ (in erg-G^{-1}), cos θ, g_{CD}, and $|m|/|\mu|$ values of the first sixteen excited states of ***trans*-(BPY)$_4$** for three conformers obtained at RI-ADC(2)/def2-TZVPD level

State	irrep	E_g	f_{osc}	$R/10^{-40}$	$\|\mu\|/10^{-20}$	$\|m\|/10^{-20}$	cos θ	g_{CD}	$\|m\|/\|\mu\|$
					***o*-**				
S_1	A	4.33	0.000	0.00	3.537	0.000	0.000	0.000	0.000
S_2	A	4.35	0.000	0.00	0.000	0.752	0.000	0.000	Inf
S_3	B	4.35	0.001	0.00	28.699	0.000	0.000	0.000	0.000
S_4	A	4.36	0.000	0.00	2.665	0.000	0.992	0.000	0.000
S_5	A	4.38	0.000	0.00	0.000	2.578	0.000	0.000	Inf
S_6	A	4.39	0.000	0.00	14.058	0.000	0.000	0.000	0.000
S_7	B	4.41	0.013	0.00	87.001	0.000	0.000	0.000	0.000
S_8	B	4.46	2.060	0.00	1104.190	0.000	0.000	0.000	0.000
S_9	A	4.46	0.000	0.00	0.000	0.881	0.000	0.000	Inf
S_{10}	A	4.51	0.009	-0.01	73.286	0.000	-0.763	0.000	0.000
S_{11}	A	4.70	0.000	0.00	10.560	0.000	0.000	0.000	0.000
S_{12}	B	4.79	0.747	0.00	641.601	0.000	0.000	0.000	0.000
S_{13}	B	4.97	0.465	0.00	497.053	0.000	0.000	0.000	0.000
S_{14}	B	5.12	0.067	0.00	186.130	0.000	0.000	0.000	0.000
S_{15}	B	5.27	0.216	0.00	328.783	0.000	0.000	0.000	0.000
S_{16}	B	5.46	1.809	0.00	934.459	0.000	0.000	0.000	0.000
					***m*-**				
S_1	B	3.82	3.796	-9.29	1619.100	0.038	-0.151	0.000	0.000
S_2	A	4.09	0.002	-1.47	34.167	0.043	-1.000	-0.005	0.001
S_3	B	4.17	0.032	-4.72	141.604	0.346	-0.096	-0.001	0.002
S_4	A	4.19	0.000	2.67	13.522	0.198	1.000	0.059	0.015
S_5	A	4.28	0.001	-4.97	18.814	0.264	-1.000	-0.056	0.014
S_6	B	4.33	0.110	13.53	258.454	0.295	0.178	0.001	0.001
S_7	A	4.50	0.000	-2.76	11.727	0.236	-1.000	-0.080	0.020
S_8	B	4.52	0.288	98.00	409.653	0.513	0.466	0.002	0.001
S_9	A	4.54	0.000	3.47	6.923	0.502	1.000	0.288	0.072
S_{10}	B	4.57	0.000	-0.14	1.240	0.372	-0.303	-0.334	0.300
S_{11}	A	4.64	0.000	4.94	14.121	0.350	1.000	0.099	0.025
S_{12}	B	4.64	0.007	11.30	60.993	0.237	0.781	0.012	0.004
S_{13}	A	4.71	0.001	-0.65	18.426	0.035	-1.000	-0.008	0.002
S_{14}	B	4.72	0.004	30.48	46.522	0.659	0.995	0.056	0.014
S_{15}	B	4.74	0.120	-252.97	258.214	1.039	-0.943	-0.015	0.004
S_{16}	A	4.76	0.001	-4.68	16.917	0.277	-1.000	-0.065	0.016
					***p*-**				
S_1	A	4.33	0.010	8.75	76.791	0.114	1.000	0.006	0.001
S_2	B	4.33	0.002	-8.61	34.083	0.340	-0.744	-0.030	0.010
S_3	A	4.37	0.000	6.06	7.753	0.782	1.000	0.399	0.101
S_4	B	4.37	0.015	-26.28	95.222	0.367	-0.752	-0.012	0.004
S_5	A	4.52	0.000	-6.77	8.720	0.777	-1.000	-0.354	0.089
S_6	B	4.52	0.152	-138.91	297.647	0.808	-0.578	-0.006	0.003
S_7	A	4.54	0.032	49.94	136.574	0.366	1.000	0.011	0.003
S_8	B	4.56	0.282	-36.31	403.326	0.735	-0.122	-0.001	0.002
S_9	A	4.61	0.008	6.04	68.041	0.089	1.000	0.005	0.001
S_{10}	B	4.61	0.013	22.63	84.615	1.256	0.213	0.013	0.015
S_{11}	B	4.63	0.795	461.84	673.165	2.235	0.307	0.004	0.003
S_{12}	A	4.63	0.094	-305.63	231.629	1.320	-1.000	-0.023	0.006
S_{13}	B	4.68	0.152	286.69	292.923	1.710	0.572	0.013	0.006
S_{14}	A	4.69	0.029	-14.02	127.547	0.110	-1.000	-0.003	0.001
S_{15}	B	4.89	0.435	549.80	484.638	4.221	0.269	0.009	0.009
S_{16}	A	4.89	0.230	-628.03	352.488	1.782	-1.000	-0.020	0.005

TABLE C10: E_g, f_{osc}, Rotatory Strengths (R in erg·esu·cm/Gauss), $|\mu|$ (in esu-cm), $|m|$ (in erg-G^{-1}), cos θ, g_{CD}, and $|m|/|\mu|$ values of the first sixteen excited states of ***cis*-(BPY)$_4$** for three conformers obtained at RI-ADC(2)/def2-TZVPD level

State	irrep	E_g	f_{osc}	$R/10^{-40}$	$\|\mu\|/10^{-20}$	$\|m\|/10^{-20}$	cos θ	g_{CD}	$\|m\|/\|\mu\|$
					o-				
S_1	A	4.02	0.000	0.74	13.041	0.057	1.000	0.017	0.004
S_2	B	4.02	0.000	0.63	6.979	0.228	0.395	0.052	0.033
S_3	A	4.24	0.001	-1.45	22.833	0.063	-1.000	-0.011	0.003
S_4	B	4.24	0.000	-4.69	16.672	0.327	-0.861	-0.068	0.020
S_5	A	4.34	0.000	4.41	17.004	0.260	1.000	0.061	0.015
S_6	B	4.35	0.003	9.36	39.451	0.478	0.496	0.024	0.012
S_7	A	4.38	0.000	0.75	14.946	0.050	1.000	0.013	0.003
S_8	A	4.40	0.001	2.95	19.019	0.155	1.000	0.033	0.008
S_9	B	4.40	0.002	-25.55	35.812	0.729	-0.979	-0.080	0.020
S_{10}	B	4.46	0.000	-10.39	16.733	0.643	-0.966	-0.148	0.038
S_{11}	A	4.48	0.002	-25.68	33.354	0.770	-1.000	-0.092	0.023
S_{12}	B	4.49	0.005	-5.41	53.307	0.250	-0.406	-0.008	0.005
S_{13}	A	4.56	0.102	-316.42	243.441	1.300	-1.000	-0.021	0.005
S_{14}	B	4.56	0.031	368.34	134.373	3.538	0.775	0.082	0.026
S_{15}	A	4.57	0.054	-187.12	175.980	1.063	-1.000	-0.024	0.006
S_{16}	B	4.59	0.051	356.53	171.450	3.094	0.672	0.049	0.018
					m-				
S_1	B	4.08	3.128	-324.94	1422.290	1.683	-0.136	-0.001	0.001
S_2	A	4.17	0.004	-13.595	51.910	0.262	-1.000	-0.020	0.005
S_3	B	4.18	0.128	-12.36	284.552	0.449	-0.097	-0.001	0.002
S_4	A	4.28	0.005	22.26	55.848	0.399	1.000	0.029	0.007
S_5	B	4.31	0.064	19.32	198.506	0.364	0.267	0.002	0.002
S_6	A	4.37	0.007	4.46	66.594	0.067	1.000	0.004	0.001
S_7	B	4.42	0.330	284.18	443.343	0.986	0.650	0.006	0.002
S_8	A	4.48	0.038	11.45	148.589	0.077	1.000	0.002	0.001
S_9	B	4.54	0.009	38.60	70.826	0.746	0.731	0.031	0.011
S_{10}	A	4.56	0.008	-18.68	66.878	0.279	-1.000	-0.017	0.004
S_{11}	B	4.70	0.185	38.01	322.158	0.880	0.134	0.002	0.003
S_{12}	A	4.75	0.003	2.79	43.385	0.064	1.000	0.006	0.001
S_{13}	A	4.77	0.000	-0.81	2.366	0.344	-1.000	-0.569	0.145
S_{14}	B	4.77	0.000	0.81	6.045	0.345	0.387	0.088	0.057
S_{15}	B	4.77	0.124	182.06	262.179	0.766	0.906	0.011	0.003
S_{16}	A	4.79	0.011	-30.67	76.059	0.403	-1.000	-0.021	0.005
					p-				
S_1	A	4.20	0.001	4.11	29.829	0.138	1.000	0.019	0.005
S_2	B	4.20	0.004	21.21	49.720	0.802	0.532	0.034	0.016
S_3	B	4.30	0.002	0.40	34.899	0.024	0.487	0.001	0.001
S_4	A	4.31	0.001	18.05	27.545	0.655	1.000	0.095	0.024
S_5	A	4.35	0.003	28.13	43.081	0.653	1.000	0.061	0.015
S_6	B	4.35	0.017	41.20	100.048	0.816	0.505	0.017	0.008
S_7	B	4.37	0.005	19.42	53.638	0.698	0.519	0.027	0.013
S_8	A	4.42	0.001	17.96	23.023	0.780	1.000	0.135	0.034
S_9	A	4.45	0.001	-14.58	18.690	0.780	-1.000	-0.167	0.042
S_{10}	B	4.50	0.021	46.00	110.008	1.290	0.324	0.015	0.012
S_{11}	B	4.55	0.041	-18.81	153.927	1.250	-0.098	-0.003	0.008
S_{12}	A	4.65	0.173	-190.09	313.104	0.607	-1.000	-0.008	0.002
S_{13}	B	4.67	0.011	4.94	79.276	0.772	0.081	0.003	0.010
S_{14}	A	4.69	0.003	-9.37	41.180	0.227	-1.000	-0.022	0.006
S_{15}	B	4.69	0.033	-33.20	135.208	0.716	-0.343	-0.007	0.005
S_{16}	A	4.71	0.002	-6.18	30.604	0.202	-1.000	-0.026	0.007

TABLE C11: Excitation energies (E_g) and oscillator strengths(f_{osc}) of three different conformers for ***trans*-(BPY)$_4$** calculated at RI-ADC(2) level and using two different functionals B3LYP and CAM-B3LYP using the def2-TZVPD basis set

					o-				
	RI-ADC(2)			CAM-B3LYP			B3LYP		
State	Irrep	E_g	f_{osc}	Irrep	E_g	f_{osc}	Irrep	E_g	f_{osc}
S_1	A	4.33	0.000	A	4.43	0.000	A	3.89	0.000
S_2	B	4.35	0.001	B	4.43	0.064	B	3.89	0.001
S_3	A	4.35	0.000	B	4.47	1.344	A	3.96	0.000
S_4	A	4.36	0.000	B	4.49	1.060	B	3.97	0.015
S_5	A	4.38	0.000	A	4.49	0.000	A	4.07	0.000
S_6	A	4.39	0.000	A	4.55	0.000	B	4.09	0.000
S_7	B	4.41	0.013	B	4.59	0.000	A	4.10	0.000
S_8	B	4.46	2.060	A	4.59	0.002	B	4.11	1.741
S_9	A	4.46	0.000	B	4.61	0.000	B	4.11	0.026
S_{10}	A	4.51	0.009	A	4.61	0.001	A	4.12	0.000
S_{11}	A	4.70	0.000	A	4.63	0.007	B	4.13	0.000
S_{12}	B	4.79	0.747	B	4.65	0.000	A	4.13	0.000
S_{13}	B	4.97	0.465	A	4.71	0.000	A	4.17	0.000
S_{14}	B	5.12	0.067	B	4.76	0.784	B	4.17	0.000
S_{15}	B	5.27	0.216	A	4.82	0.000	A	4.23	0.006
S_{16}	B	5.46	1.809	B	4.84	0.000	A	4.25	0.000
					m-				
S_1	B	3.82	3.795	B	3.75	3.723	B	3.22	2.928
S_2	A	4.09	0.002	A	4.16	0.000	A	3.65	0.000
S_3	B	4.17	0.032	A	4.38	0.003	A	3.69	0.000
S_4	A	4.19	0.000	B	4.43	0.011	A	3.75	0.001
S_5	A	4.28	0.001	A	4.50	0.001	B	3.82	0.009
S_6	B	4.33	0.110	B	4.53	0.026	A	3.94	0.000
S_7	A	4.50	0.000	B	4.55	0.273	B	4.00	0.157
S_8	B	4.52	0.288	A	4.70	0.000	B	4.01	0.527
S_9	A	4.54	0.000	A	4.74	0.001	B	4.03	0.021
S_{10}	B	4.57	0.000	B	4.75	0.001	B	4.14	0.001
S_{11}	A	4.64	0.000	A	4.79	0.000	A	4.19	0.000
S_{12}	B	4.64	0.007	B	4.84	0.004	A	4.21	0.000
S_{13}	A	4.71	0.001	A	4.87	0.001	B	4.26	0.000
S_{14}	B	4.72	0.004	B	4.88	0.014	B	4.33	0.001
S_{15}	B	4.74	0.120	B	4.90	0.005	A	4.33	0.001
S_{16}	A	4.76	0.001	A	4.91	0.000	A	4.36	0.001
					p-				
S_1	A	4.33	0.010	A	4.52	0.024	A	4.01	0.017
S_2	B	4.33	0.002	B	4.52	0.239	B	4.02	0.005
S_3	B	4.37	0.015	B	4.53	0.166	B	4.04	0.036
S_4	A	4.37	0.000	A	4.53	0.003	A	4.04	0.001
S_5	A	4.52	0.000	B	4.56	1.506	B	4.11	0.129
S_6	B	4.52	0.152	A	4.63	0.161	A	4.11	0.014
S_7	A	4.54	0.032	A	4.64	0.121	A	4.12	0.026
S_8	B	4.57	0.282	B	4.64	0.041	B	4.15	0.798
S_9	B	4.61	0.013	A	4.71	0.011	B	4.17	0.011
S_{10}	A	4.61	0.008	B	4.73	0.012	A	4.20	0.048
S_{11}	B	4.63	0.795	A	4.78	0.013	A	4.25	0.001
S_{12}	A	4.63	0.094	B	4.80	0.065	B	4.28	0.042
S_{13}	B	4.68	0.152	B	4.84	0.027	B	4.31	0.088
S_{14}	A	4.69	0.029	A	4.84	0.009	A	4.31	0.030
S_{15}	B	4.89	0.435	B	4.91	0.171	B	4.37	0.112
S_{16}	A	4.89	0.230	A	4.91	0.099	A	4.38	0.000

TABLE C12: Excitation energies (E_g) and oscillator strengths(f_{osc}) for three different conformers of ***cis*-(BPY)$_4$** calculated at RI-ADC(2) level and using two different functionals B3LYP and CAM-B3LYP using the def2-TZVPD basis set

					o-				
	RI-ADC(2)			CAM-B3LYP			B3LYP		
State	Irrep	E_g	f_{osc}	Irrep	E_g	f_{osc}	Irrep	E_g	f_{osc}
S_1	B	4.02	0.000	B	4.36	0.000	B	3.90	0.000
S_2	A	4.02	0.000	A	4.36	0.001	A	3.91	0.000
S_3	B	4.24	0.000	A	4.56	0.000	A	4.09	0.001
S_4	A	4.25	0.001	B	4.57	0.001	B	4.09	0.000
S_5	A	4.34	0.000	B	4.61	0.005	B	4.16	0.036
S_6	B	4.35	0.003	A	4.62	0.000	A	4.17	0.003
S_7	A	4.38	0.000	A	4.62	0.001	A	4.18	0.006
S_8	B	4.40	0.002	B	4.65	0.013	B	4.18	0.009
S_9	A	4.40	0.001	A	4.66	0.020	A	4.19	0.017
S_{10}	B	4.46	0.000	B	4.67	0.002	B	4.20	0.017
S_{11}	A	4.48	0.002	B	4.70	0.065	B	4.23	0.028
S_{12}	B	4.49	0.005	A	4.71	0.172	A	4.27	0.002
S_{13}	A	4.56	0.102	A	4.78	0.003	A	4.27	0.001
S_{14}	B	4.56	0.031	B	4.78	0.013	B	4.29	0.004
S_{15}	A	4.57	0.054	A	4.88	0.026	A	4.29	0.000
S_{16}	B	4.59	0.051	B	4.89	0.011	B	4.34	0.025
					m-				
S_1	B	4.08	3.128	B	4.03	3.497	B	3.50	2.670
S_2	A	4.17	0.004	A	4.37	0.050	A	3.80	0.015
S_3	B	4.18	0.128	B	4.46	0.022	B	3.87	0.015
S_4	A	4.28	0.005	A	4.47	0.005	A	3.91	0.023
S_5	B	4.31	0.064	B	4.55	0.002	A	3.99	0.000
S_6	A	4.37	0.007	A	4.57	0.007	B	3.99	0.000
S_7	B	4.42	0.330	A	4.66	0.003	A	4.01	0.007
S_8	A	4.48	0.038	B	4.67	0.077	A	4.09	0.002
S_9	B	4.54	0.009	B	4.72	0.010	B	4.11	0.005
S_{10}	A	4.56	0.008	A	4.73	0.001	B	4.19	0.094
S_{11}	B	4.70	0.185	B	4.79	0.200	A	4.20	0.000
S_{12}	A	4.75	0.003	A	4.91	0.004	B	4.23	0.546
S_{13}	B	4.77	0.000	B	4.94	0.008	B	4.28	0.009
S_{14}	A	4.77	0.000	A	4.96	0.000	B	4.37	0.005
S_{15}	B	4.77	0.124	B	4.96	0.008	A	4.48	0.005
S_{16}	A	4.80	0.011	A	4.98	0.006	B	4.48	0.028
					p-				
S_1	B	4.20	0.004	A	4.56	0.002	A	3.92	0.001
S_2	A	4.20	0.001	B	4.57	0.004	B	3.94	0.012
S_3	B	4.30	0.002	B	4.59	0.003	B	4.00	0.000
S_4	A	4.31	0.001	A	4.60	0.000	A	4.03	0.001
S_5	A	4.35	0.003	A	4.62	0.003	B	4.04	0.006
S_6	B	4.35	0.017	B	4.63	0.009	A	4.08	0.002
S_7	B	4.37	0.005	B	4.64	0.024	B	4.08	0.002
S_8	A	4.42	0.001	A	4.66	0.007	B	4.13	0.013
S_9	A	4.45	0.001	A	4.69	0.001	A	4.13	0.003
S_{10}	B	4.50	0.021	B	4.72	0.003	B	4.15	0.006
S_{11}	B	4.55	0.041	B	4.78	0.085	A	4.15	0.001
S_{12}	A	4.65	0.173	A	4.86	0.264	A	4.17	0.001
S_{13}	B	4.67	0.011	B	4.92	0.041	B	4.25	0.005
S_{14}	A	4.69	0.003	A	4.97	0.029	B	4.29	0.002
S_{15}	B	4.70	0.033	B	5.01	0.004	A	4.32	0.103
S_{16}	A	4.71	0.002	A	5.01	0.008	A	4.34	0.000

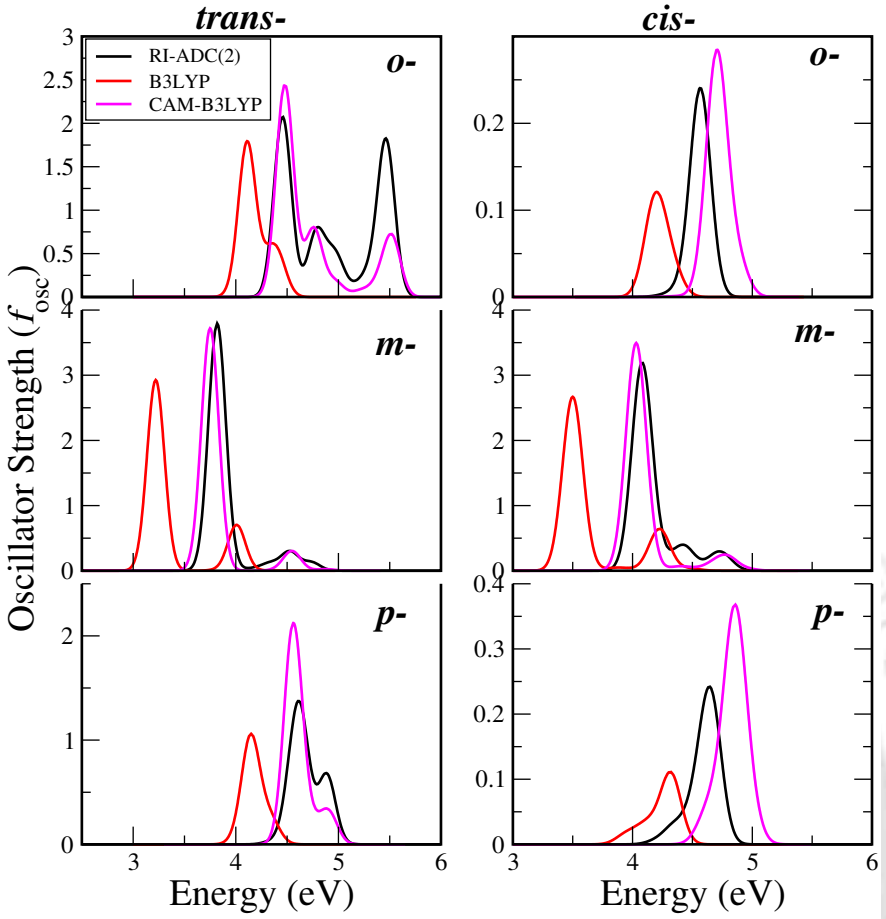

FIGURE C3: Absorption spectra of ***o-***, ***m-***, and ***p-*** conformers for ***trans-*** and ***cis-*** $(\mathbf{BPY})_4$ obtained at RI-ADC(2) level and using two different functionals B3LYP and CAM-B3LYP using the def2-TZVPD basis set

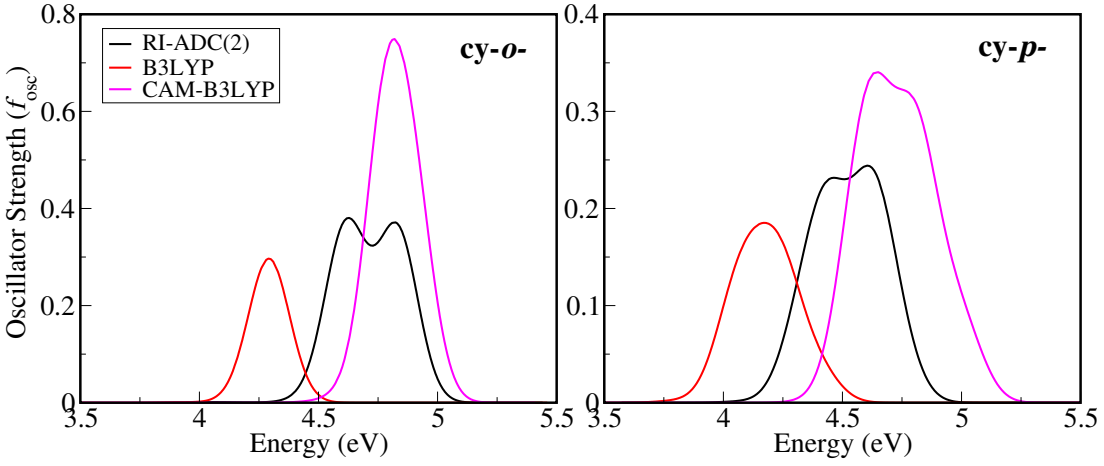

FIGURE C4: Absorption spectra of cy-***o-*** and cy-***p-*** obtained at RI-ADC(2) level and using two different functionals B3LYP and CAM-B3LYP using the def2-TZVPD basis set

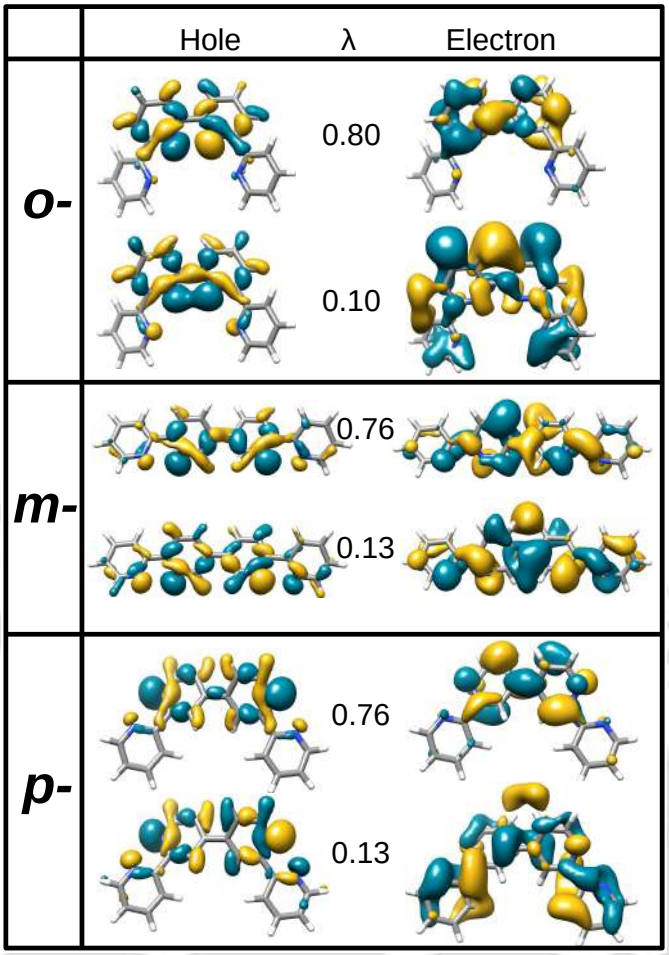

FIGURE C5: Natural transition orbitals corresponding to the S_1 states of three different conformers of ***cis*-(BPY)$_2$**. Here, λ_{max} value represents the weight of a configuration.

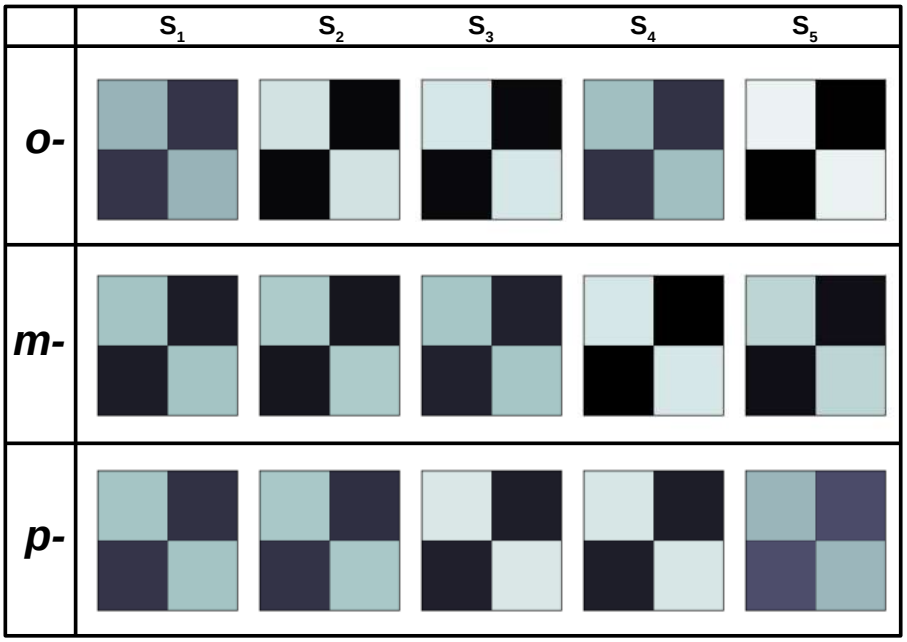

FIGURE C6: *e-h* correlation plots corresponding to the first five excited states of ***cis*-(BPY)$_2$** for three different conformers.

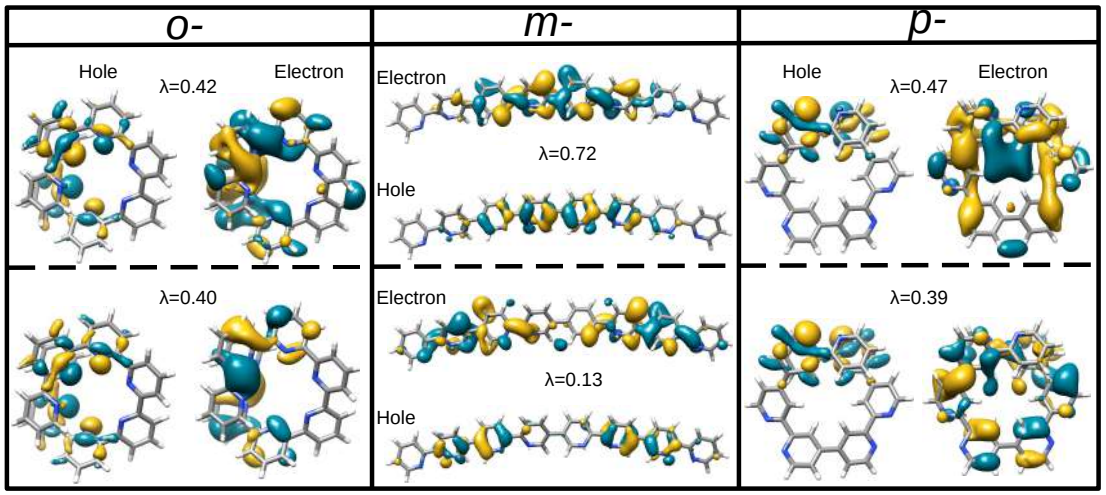

FIGURE C7: Natural transition orbitals corresponding to the S_1 states of three different conformers of ***cis*-(BPY)$_4$**. Here, λ_{max} value represents the weight of a configuration.

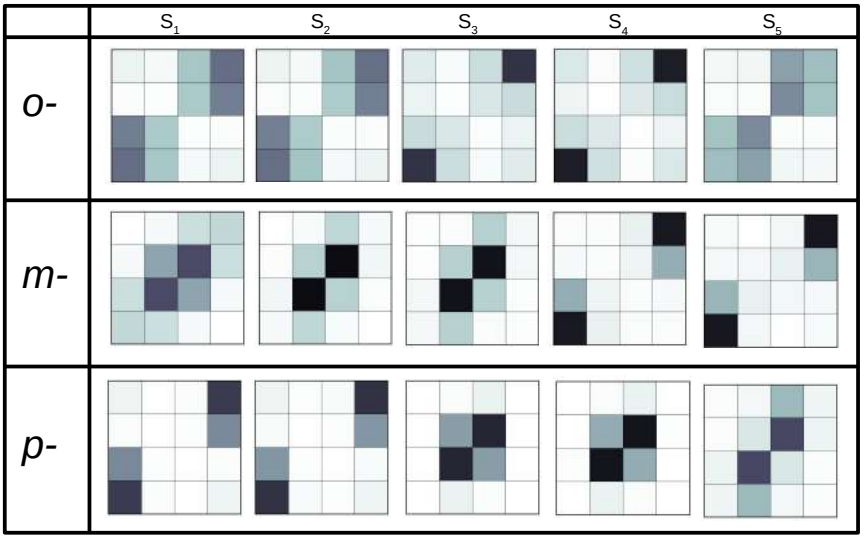

FIGURE C8: *e-h* correlation plots corresponding to the first five excited states of ***cis*-(BPY)$_4$** for three different conformers.

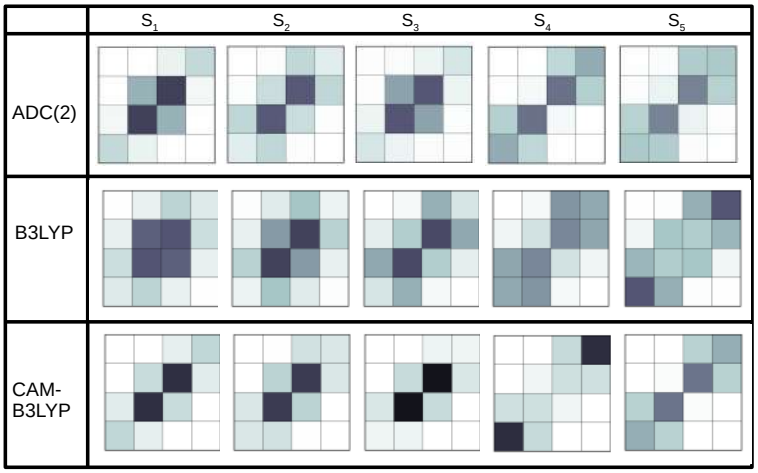

FIGURE C9: *e-h* correlation plots obtained using the RI-ADC(2) method, and B3LYP and CAM-B3LYP functionals for the first five excited states of ***o-trans*-(BPY)$_4$**

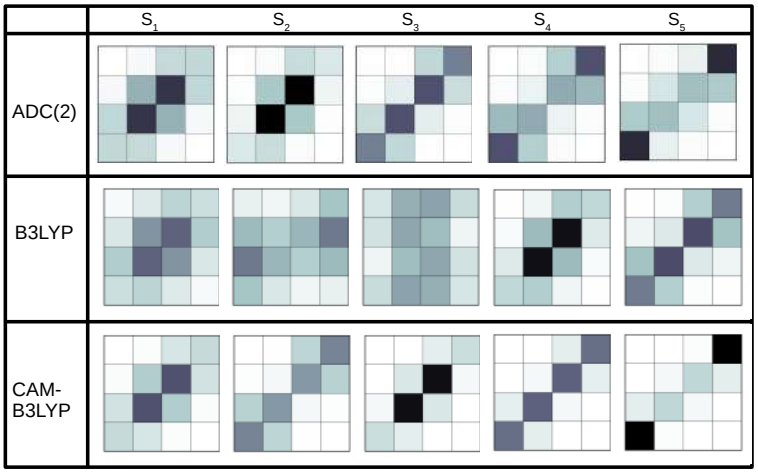

FIGURE C10: *e-h* correlation plots obtained using the RI-ADC(2) method, and B3LYP and CAM-B3LYP functionals for the first five excited states of ***m-trans*-(BPY)$_4$**

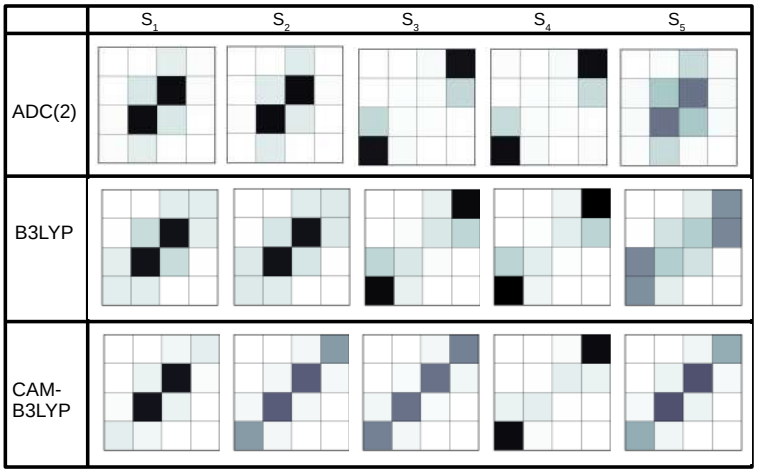

FIGURE C11: *e-h* correlation plots obtained using the RI-ADC(2) method, and B3LYP and CAM-B3LYP functionals for the first five excited states of ***p-trans*-(BPY)$_4$**

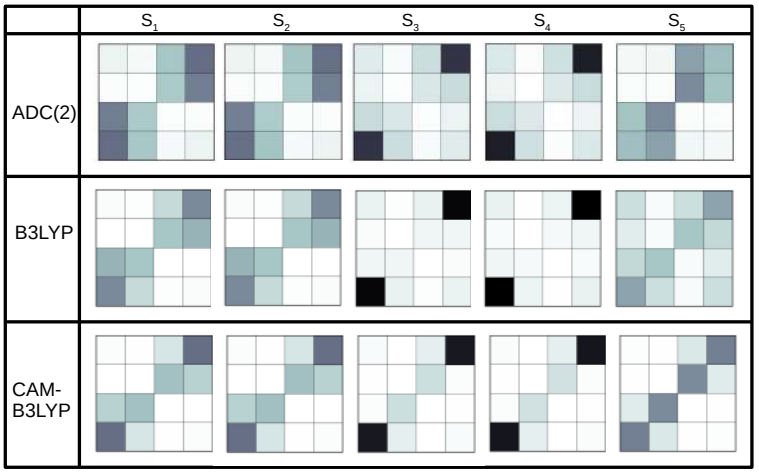

FIGURE C12: *e-h* correlation plots obtained using the RI-ADC(2) method, and B3LYP and CAM-B3LYP functionals for the first five excited states of ***o-cis*-(BPY)$_4$**

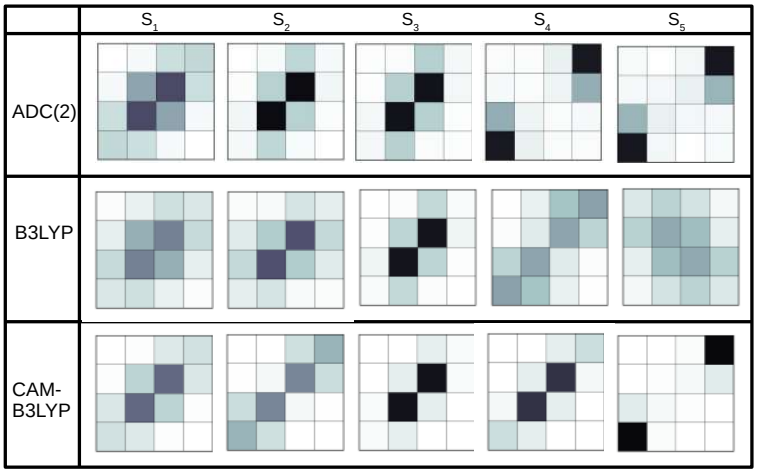

FIGURE C13: *e-h* correlation plots obtained using the RI-ADC(2) method, and B3LYP and CAM-B3LYP functionals for the first five excited states of ***m-cis*-(BPY)$_4$**

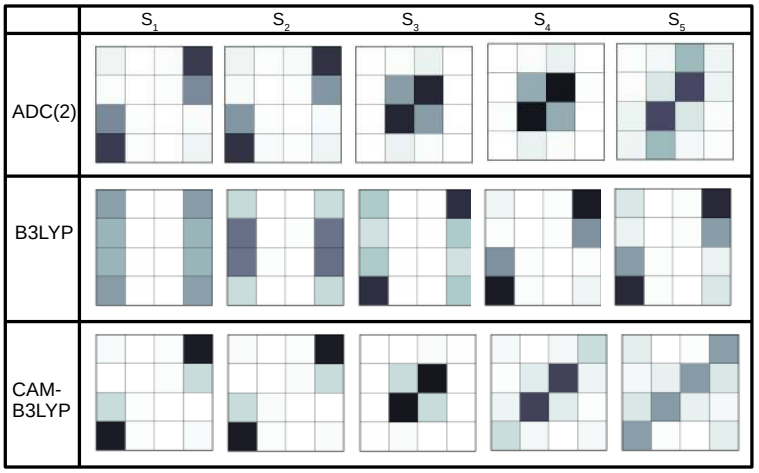

FIGURE C14: *e-h* correlation plots obtained using the RI-ADC(2) method, and B3LYP and CAM-B3LYP functionals for the first five excited states of ***p-cis*-(BPY)$_4$**

Appendix D

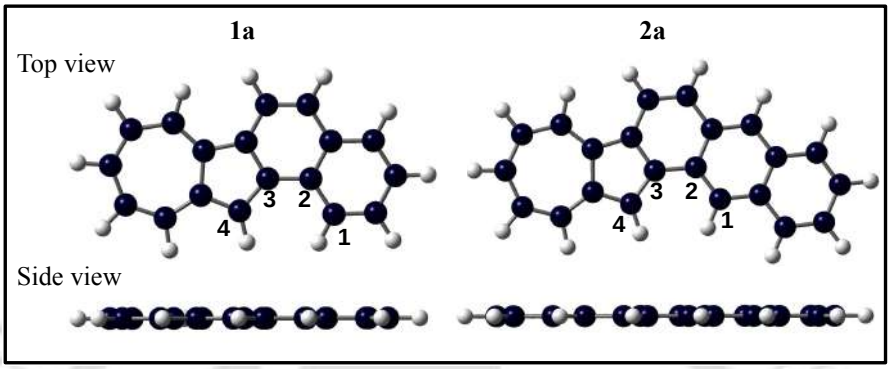

FIGURE D1: Ground state optimized geometries of **1a** and **2a** obtained at the SCS-MP2/def2-TZVP level. The dihedral angle (∠C1-C2-C3-C4) between azulene and acene units is denoted as ϕ.

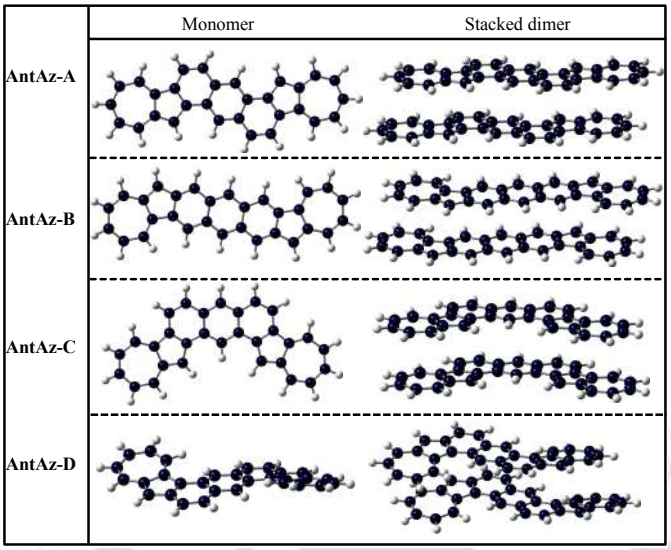

FIGURE D2: Ground state optimized geometries of monomer and π-stacked dimers of **AntAz-A**, **AntAz-B**, **AntAz-C**, and **AntAz-D** at the SCS-MP2/def2-TZVP level.

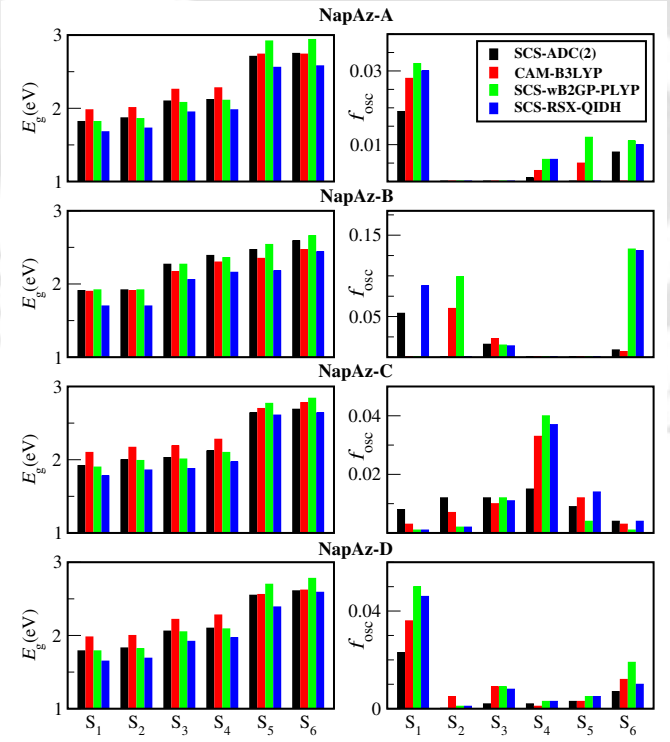

FIGURE D3: Comparison of TD-DFT excitation energies (E_g) and oscillator strengths (f_{osc}) corresponding to the first six excited states with the SCS-ADC(2) results for the π-stacked dimers of **NapAz** isomers.

TABLE D1: Comparison of TD-DFT excitation energies (E_g) and oscillator strengths (f_{osc}) against the SCS-ADC(2) results for the monomers of **NapAz** isomers

State	SCS-ADC(2)	CAM-B3LYP	SCS-ωB2GP-PLYP	SCS-RSX-QIDH
NapAz-A				
S_1	2.03 / 0.017	2.12 / 0.024	2.01 / 0.032	1.89 / 0.031
S_2	2.25 / 0.000	2.37 / 0.000	2.22 / 0.000	2.13 / 0.000
S_3	3.15 / 0.052	3.12 / 0.002	3.12 / 0.004	3.07 / 0.004
S_4	3.47 / 0.000	3.50 / 0.000	3.46 / 0.000	3.42 / 0.000
S_5	3.69 / 0.000	3.73 / 0.000	3.78 / 3.538	3.63 / 3.449
S_6	3.69 / 1.241	3.85 / 0.602	3.92 / 0.906	3.78 / 0.835
S_7	3.77 / 2.329	4.00 / 3.114	4.00 / 0.000	3.80 / 0.000
S_8	4.12 / 0.176	4.22 / 0.000	4.16 / 0.000	3.92 / 0.000
S_9	4.14 / 0.000	4.33 / 0.160	4.17 / 0.194	4.04 / 0.191
S_{10}	4.34 / 0.000	4.56 / 0.000	4.40 / 0.000	4.17 / 0.000
NapAz-B				
S_1	2.08 / 0.047	1.98 / 0.048	2.05 / 0.075	1.87 / 0.068
S_2	2.52 / 0.000	2.40 / 0.000	2.46 / 0.000	2.31 / 0.000
S_3	3.02 / 0.177	2.97 / 0.201	2.99 / 0.336	2.87 / 0.334
S_4	3.64 / 0.000	3.55 / 0.000	3.60 / 0.000	3.42 / 0.000
S_5	3.67 / 0.000	3.62 / 0.000	3.78 / 0.000	3.50 / 0.000
S_6	3.73 / 1.973	3.81 / 0.004	3.79 / 2.540	3.67 / 2.534
S_7	3.78 / 1.462	3.96 / 4.188	3.83 / 1.494	3.67 / 1.350
S_8	4.18 / 0.166	4.26 / 0.000	4.20 / 0.057	4.05 / 0.053
S_9	4.24 / 0.000	4.30 / 0.296	4.43 / 0.000	4.23 / 0.000
S_{10}	4.50 / 0.000	4.56 / 0.100	4.65 / 0.000	4.45 / 0.000
NapAz-C				
S_1	2.08 / 0.010	2.20 / 0.009	2.05 / 0.001	1.95 / 0.001
S_2	2.19 / 0.022	2.31 / 0.029	2.16 / 0.037	2.06 / 0.036
S_3	2.96 / 0.001	2.94 / 0.000	3.01 / 0.000	2.94 / 0.000
S_4	3.29 / 0.611	3.37 / 0.221	3.37 / 0.001	3.33 / 0.001
S_5	3.52 / 0.972	3.65 / 1.334	3.56 / 2.584	3.38 / 2.473
S_6	3.86 / 0.014	3.97 / 0.017	3.91 / 0.168	3.78 / 0.166
S_7	3.87 / 0.002	4.01 / 0.001	4.06 / 0.055	3.85 / 0.052
S_8	3.98 / 0.227	4.12 / 0.142	4.08 / 0.198	3.95 / 0.198
S_9	4.03 / 0.307	4.28 / 0.019	4.21 / 0.338	4.11 / 0.478
S_{10}	4.28 / 1.040	4.45 / 0.016	4.38 / 0.536	4.11 / 0.336
NapAz-D				
S_1	1.97 / 0.023	2.06 / 0.035	1.93 / 0.047	1.82 / 0.045
S_2	2.21 / 0.000	2.33 / 0.000	2.18 / 0.000	2.08 / 0.000
S_3	3.07 / 0.004	3.03 / 0.008	3.04 / 0.017	2.98 / 0.017
S_4	3.42 / 0.000	3.47 / 0.000	3.43 / 0.000	3.39 / 0.000
S_5	3.59 / 2.096	3.69 / 0.000	3.69 / 3.057	3.51 / 2.942
S_6	3.66 / 0.000	3.79 / 0.804	3.79 / 0.093	3.57 / 0.005
S_7	3.72 / 0.593	3.94 / 2.294	3.83 / 0.005	3.68 / 0.059
S_8	3.94 / 0.129	4.13 / 0.153	4.04 / 0.262	3.89 / 0.253
S_9	4.13 / 0.018	4.35 / 0.006	4.27 / 0.024	4.10 / 0.024
S_{10}	4.24 / 0.000	4.45 / 0.001	4.53 / 0.043	4.38 / 0.042

TABLE D2: Comparision of SCS-ADC(2) and TD-DFT excitation energies (E_gs) and corresponding oscillator strength (f_{osc}) for the first six excited states of **AntAz** monomers

State	SCS-ADC(2)	CAM-B3LYP	SCS-wB2GP-PLYP	SCS-RSX-QIDH
AntAz-A				
S_1	1.98 / 0.021	2.14 / 0.026	1.96 / 0.027	1.88 / 0.026
S_2	2.10 / 0.000	2.28 / 0.000	2.08 / 0.000	2.01 / 0.000
S_3	3.06 / 0.098	3.07 / 0.002	3.08 / 0.004	3.02 / 0.004
S_4	3.34 / 0.000	3.38 / 0.000	3.35 / 0.000	3.32 / 0.000
S_5	3.44 / 1.225	3.64 / 1.183	3.54 / 2.990	3.40 / 2.931
S_6	3.63 / 2.469	3.76 / 0.000	3.69 / 1.085	3.56 / 1.054
S_7	3.70 / 0.000	3.80 / 2.364	3.97 / 0.000	3.81 / 0.000
S_8	3.88 / 0.355	4.07 / 0.501	4.04 / 1.260	3.92 / 1.153
S_9	4.03 / 0.000	4.14 / 0.000	4.10 / 0.243	3.97 / 0.000
S_{10}	4.03 / 0.354	4.23 / 1.196	4.19 / 0.000	4.00 / 0.245
AntAz-B				
S_1	2.06 / 0.056	1.96 / 0.058	2.04 / 0.081	1.85 / 0.073
S_2	2.40 / 0.000	2.27 / 0.000	2.35 / 0.000	2.19 / 0.000
S_3	2.87 / 0.327	2.85 / 0.343	2.86 / 0.551	2.71 / 0.537
S_4	3.41 / 0.001	3.35 / 0.000	3.40 / 0.066	3.23 / 0.000
S_5	3.47 / 0.000	3.44 / 0.011	3.45 / 0.000	3.29 / 0.064
S_6	3.49 / 0.000	3.46 / 0.000	3.58 / 0.000	3.33 / 0.000
S_7	3.60 / 3.536	3.74 / 4.050	3.69 / 4.260	3.53 / 4.061
S_8	3.99 / 0.145	4.05 / 0.312	3.95 / 0.143	3.79 / 0.152
S_9	4.02 / 0.000	4.06 / 0.000	4.26 / 0.000	4.07 / 0.000
S_{10}	4.21 / 0.387	4.22 / 0.575	4.38 / 0.056	4.17 / 0.058
AntAz-C				
S_1	2.03 / 0.011	2.20 / 0.009	2.01 / 0.002	1.93 / 0.001
S_2	2.08 / 0.017	2.26 / 0.025	2.07 / 0.030	1.99 / 0.029
S_3	3.00 / 0.002	2.99 / 0.005	3.04 / 0.011	2.98 / 0.011
S_4	3.21 / 0.769	3.33 / 0.261	3.31 / 0.018	3.28 / 0.016
S_5	3.45 / 1.052	3.57 / 1.856	3.47 / 2.739	3.30 / 2.639
S_6	3.63 / 0.494	3.78 / 0.056	3.68 / 0.793	3.57 / 0.768
S_7	3.82 / 0.056	3.93 / 0.001	3.97 / 0.098	3.85 / 0.102
S_8	3.85 / 0.085	4.03 / 0.176	4.01 / 0.196	3.89 / 0.186
S_9	3.95 / 0.390	4.17 / 0.318	4.10 / 0.031	4.01 / 0.029
S_{10}	4.07 / 0.385	4.25 / 0.074	4.35 / 0.777	4.16 / 0.782
AntAz-D				
S_1	1.96 / 0.019	2.14 / 0.031	1.94 / 0.038	1.86 / 0.037
S_2	2.09 / 0.000	2.29 / 0.000	2.07 / 0.000	2.00 / 0.000
S_3	2.97 / 0.017	2.97 / 0.028	2.98 / 0.003	2.91 / 0.003
S_4	3.24 / 0.001	3.30 / 0.000	3.27 / 0.000	3.24 / 0.000
S_5	3.41 / 1.912	3.61 / 0.746	3.50 / 2.638	3.33 / 2.646
S_6	3.50 / 0.792	3.73 / 2.365	3.54 / 0.647	3.43 / 0.497
S_7	3.71 / 0.003	3.80 / 0.001	3.87 / 0.119	3.73 / 0.003
S_8	3.73 / 0.107	3.91 / 0.148	3.97 / 0.022	3.76 / 0.113
S_9	3.95 / 0.014	4.10 / 0.005	4.06 / 0.003	3.84 / 0.023
S_{10}	4.11 / 0.000	4.26 / 0.051	4.27 / 0.029	4.12 / 0.029

TABLE D3: Comparison of TD-DFT excitation energies (E_g) and oscillator strengths (f_{osc}) against the SCS-ADC(2) results for the π-stacked dimers of **NapAz** isomers

State	SCS-ADC(2)	CAM-B3LYP	SCS-ωB2GP-PLYP	SCS-RSX-QIDH
NapAz-A				
S_1	1.82 / 0.019	1.98 / 0.028	1.82 / 0.032	1.68 / 0.030
S_2	1.87 / 0.000	2.01 / 0.000	1.86 / 0.000	1.73 / 0.000
S_3	2.10 / 0.000	2.26 / 0.000	2.08 / 0.000	1.95 / 0.000
S_4	2.12 / 0.001	2.28 / 0.003	2.11 / 0.006	1.98 / 0.006
S_5	2.71 / 0.000	2.74 / 0.005	2.92 / 0.012	2.56 / 0.000
S_6	2.75 / 0.008	2.74 / 0.000	2.94 / 0.011	2.58 / 0.010
S_7	2.96 / 0.000	3.00 / 0.000	2.97 / 0.001	2.81 / 0.012
S_8	3.01 / 0.019	3.04 / 0.035	3.01 / 0.000	2.84 / 0.103
S_9	3.06 / 0.000	3.10 / 0.000	3.13 / 0.000	2.84 / 0.000
S_{10}	3.16 / 0.104	3.10 / 0.016	3.14 / 0.002	2.93 / 0.000
NapAz-B				
S_1	1.91 / 0.054	1.90 / 0.000	1.92 / 0.000	1.70 / 0.088
S_2	1.92 / 0.000	1.91 / 0.060	1.92 / 0.099	1.70 / 0.000
S_3	2.27 / 0.016	2.17 / 0.023	2.27 / 0.015	2.06 / 0.014
S_4	2.39 / 0.000	2.30 / 0.000	2.36 / 0.000	2.16 / 0.000
S_5	2.47 / 0.000	2.35 / 0.000	2.54 / 0.000	2.18 / 0.000
S_6	2.59 / 0.009	2.47 / 0.007	2.66 / 0.133	2.44 / 0.131
S_7	2.85 / 0.000	2.83 / 0.000	2.79 / 0.000	2.53 / 0.258
S_8	2.95 / 0.194	2.85 / 0.000	2.89 / 0.292	2.61 / 0.000
S_9	3.00 / 0.000	2.92 / 0.070	3.05 / 0.000	2.73 / 0.010
S_{10}	3.11 / 0.000	2.93 / 0.158	3.13 / 0.011	2.75 / 0.000
NapAz-C				
S_1	1.92 / 0.008	2.10 / 0.003	1.90 / 0.001	1.78 / 0.001
S_2	2.00 / 0.012	2.17 / 0.007	1.99 / 0.002	1.86 / 0.002
S_3	2.03 / 0.012	2.19 / 0.010	2.01 / 0.012	1.88 / 0.011
S_4	2.12 / 0.015	2.28 / 0.033	2.10 / 0.040	1.97 / 0.037
S_5	2.64 / 0.009	2.70 / 0.012	2.77 / 0.004	2.61 / 0.014
S_6	2.69 / 0.004	2.78 / 0.003	2.84 / 0.001	2.64 / 0.004
S_7	2.74 / 0.006	2.79 / 0.003	2.94 / 0.004	2.68 / 0.007
S_8	2.82 / 0.032	2.85 / 0.001	2.97 / 0.015	2.69 / 0.015
S_9	2.87 / 0.020	2.94 / 0.011	2.99 / 0.003	2.72 / 0.001
S_{10}	2.93 / 0.010	3.03 / 0.001	3.00 / 0.002	2.77 / 0.003
NapAz-D				
S_1	1.79 / 0.023	1.98 / 0.036	1.79 / 0.050	1.65 / 0.046
S_2	1.83 / 0.000	2.00 / 0.005	1.82 / 0.001	1.69 / 0.001
S_3	2.06 / 0.002	2.22 / 0.009	2.05 / 0.009	1.92 / 0.008
S_4	2.10 / 0.002	2.28 / 0.001	2.09 / 0.003	1.97 / 0.003
S_5	2.55 / 0.003	2.56 / 0.003	2.70 / 0.005	2.39 / 0.005
S_6	2.61 / 0.007	2.62 / 0.012	2.78 / 0.019	2.59 / 0.010
S_7	2.85 / 0.002	2.89 / 0.001	2.88 / 0.000	2.65 / 0.018
S_8	2.86 / 0.001	2.93 / 0.000	2.92 / 0.009	2.77 / 0.000
S_9	2.92 / 0.013	2.97 / 0.016	3.06 / 0.005	2.80 / 0.009
S_{10}	2.97 / 0.034	3.00 / 0.021	3.09 / 0.044	2.90 / 0.006

TABLE D4: Comparision of SCS-ADC(2) and TD-DFT excitation energies (E_gs) and corresponding oscillator strength (f_{osc}) for the first ten excited states of **AntAz** dimers

State	SCS-ADC(2)	CAM-B3LYP	SCS-wB2GP-PLYP	SCS-RSX-QIDH
AntAz-A				
S_1	1.88 / 0.000	2.09 / 0.000	1.88 / 0.000	1.77 / 0.000
S_2	1.88 / 0.028	2.11 / 0.036	1.89 / 0.033	1.78 / 0.031
S_3	2.00 / 0.003	2.20 / 0.001	1.99 / 0.002	1.88 / 0.002
S_4	2.03 / 0.000	2.26 / 0.000	2.03 / 0.000	1.93 / 0.000
S_5	2.68 / 0.000	2.73 / 0.000	2.86 / 0.001	2.49 / 0.001
S_6	2.70 / 0.011	2.74 / 0.000	2.89 / 0.000	2.50 / 0.000
S_7	2.78 / 0.000	2.86 / 0.000	2.93 / 0.003	2.76 / 0.000
S_8	2.94 / 0.103	2.99 / 0.048	2.96 / 0.000	2.78 / 0.000
S_9	2.98 / 0.130	3.03 / 0.000	2.96 / 0.000	2.83 / 0.003
S_{10}	2.98 / 0.002	3.05 / 0.001	3.05 / 0.000	2.87 / 0.000
AntAz-B				
S_1	1.89 / 0.000	1.87 / 0.000	1.91 / 0.000	1.68 / 0.000
S_2	1.90 / 0.079	1.91 / 0.081	1.94 / 0.120	1.70 / 0.105
S_3	2.13 / 0.015	2.04 / 0.029	2.15 / 0.020	1.92 / 0.017
S_4	2.26 / 0.000	2.15 / 0.000	2.26 / 0.000	2.06 / 0.000
S_5	2.32 / 0.000	2.23 / 0.000	2.50 / 0.000	2.18 / 0.000
S_6	2.45 / 0.009	2.34 / 0.004	2.51 / 0.148	2.23 / 0.000
S_7	2.67 / 0.000	2.63 / 0.000	2.52 / 0.000	2.24 / 0.145
S_8	2.78 / 0.000	2.71 / 0.000	2.78 / 0.509	2.46 / 0.449
S_9	2.79 / 0.361	2.73 / 0.004	2.83 / 0.000	2.52 / 0.000
S_{10}	2.89 / 0.002	2.82 / 0.366	2.94 / 0.015	2.52 / 0.013
AntAz-C				
S_1	1.91 / 0.002	2.11 / 0.001	1.89 / 0.000	1.79 / 0.000
S_2	1.91 / 0.019	2.13 / 0.014	1.91 / 0.007	1.81 / 0.006
S_3	1.96 / 0.007	2.18 / 0.001	1.95 / 0.006	1.85 / 0.006
S_4	2.01 / 0.015	2.22 / 0.030	2.01 / 0.028	1.90 / 0.027
S_5	2.61 / 0.004	2.75 / 0.002	2.78 / 0.001	2.59 / 0.004
S_6	2.73 / 0.000	2.79 / 0.002	2.89 / 0.009	2.61 / 0.004
S_7	2.80 / 0.012	2.88 / 0.002	2.92 / 0.005	2.62 / 0.019
S_8	2.85 / 0.036	2.91 / 0.014	2.97 / 0.004	2.65 / 0.001
S_9	2.89 / 0.009	2.92 / 0.003	2.98 / 0.017	2.78 / 0.009
S_{10}	2.93 / 0.012	3.00 / 0.008	3.03 / 0.001	2.91 / 0.001
AntAz-D				
S_1	1.82 / 0.017	2.07 / 0.025	1.83 / 0.028	1.71 / 0.026
S_2	1.85 / 0.001	2.08 / 0.010	1.84 / 0.011	1.74 / 0.010
S_3	1.99 / 0.002	2.22 / 0.007	1.98 / 0.009	1.89 / 0.009
S_4	2.03 / 0.001	2.27 / 0.002	2.02 / 0.003	1.93 / 0.003
S_5	2.56 / 0.003	2.65 / 0.002	2.77 / 0.008	2.46 / 0.011
S_6	2.61 / 0.009	2.69 / 0.018	2.81 / 0.013	2.65 / 0.008
S_7	2.74 / 0.003	2.83 / 0.001	2.81 / 0.000	2.66 / 0.004
S_8	2.80 / 0.019	2.89 / 0.009	2.89 / 0.000	2.69 / 0.103
S_9	2.84 / 0.034	2.93 / 0.040	2.92 / 0.009	2.69 / 0.008
S_{10}	2.89 / 0.176	2.98 / 0.061	2.93 / 0.004	2.69 / 0.000

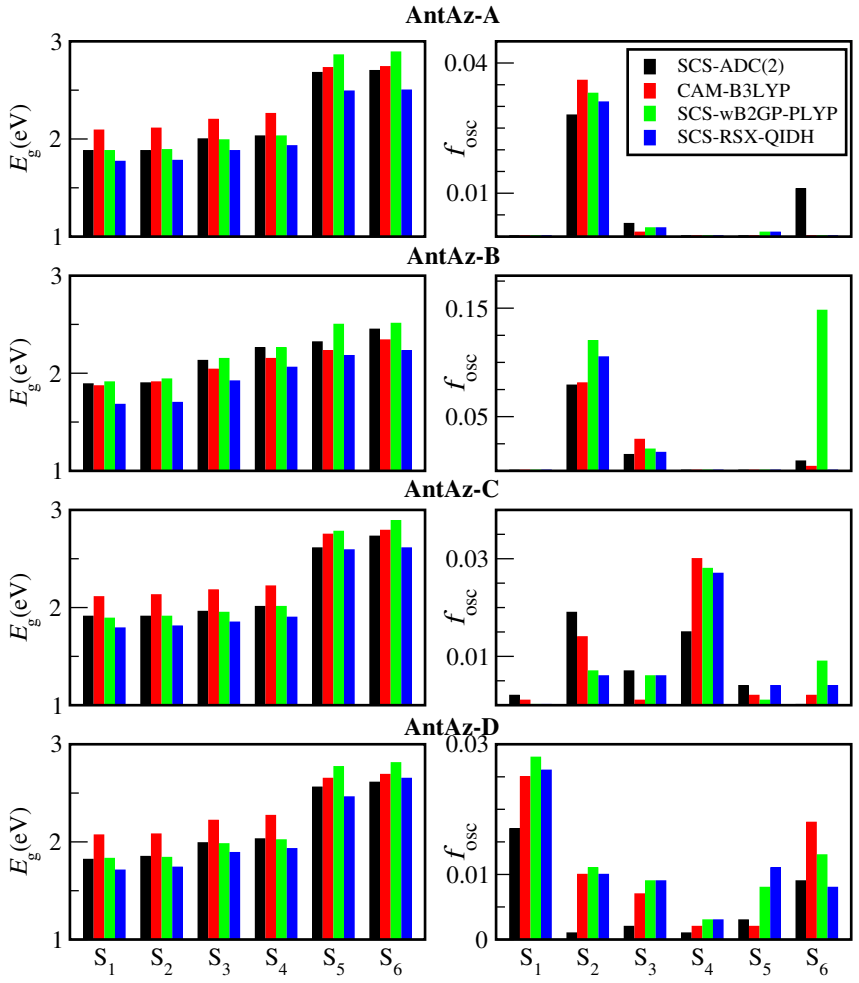

FIGURE D4: Comparison of TD-DFT excitation energies (E_g) and oscillator strengths (f_{osc}) corresponding to the first six excited states with the SCS-ADC(2) results for the dimers of **AntAz** isomers.

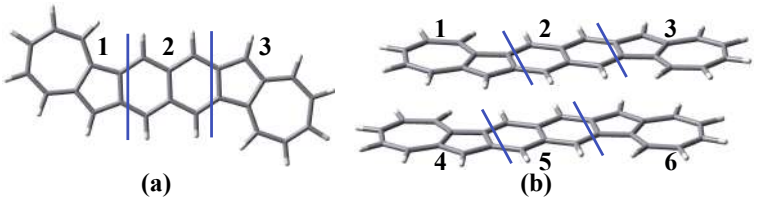

FIGURE D5: Fragmentation scheme of (a) monomer and (b) π-stacked dimer .

TABLE D5: Values of three descriptors, charge transfer parameter (ω_{CT}), exciton size (d_{exc}), and participation of natural transition orbitals (PR_{NTO}) for the monomers of **NapAz** and **AntAz** isomers. The values are computed at SCS-ADC(2)/def2-TZVP level

State	**NapAz-A**	**NapAz-B**	**NapAz-C**	**NapAz-D**	**AntAz-A**	**AntAz-B**	**AntAz-C**	**AntAz-D**
				ω_{CT}				
S_1	0.41	0.48	0.38	0.41	0.37	0.51	0.37	0.39
S_2	0.26	0.36	0.31	0.32	0.30	0.39	0.34	0.32
S_3	0.47	0.57	0.64	0.54	0.49	0.56	0.58	0.53
S_4	0.37	0.45	0.62	0.44	0.45	0.40	0.53	0.49
S_5	0.93	0.82	0.47	0.59	0.54	0.69	0.49	0.60
S_6	0.55	0.58	0.62	0.85	0.61	0.59	0.58	0.53
S_7	0.65	0.47	0.66	0.56	0.87	0.63	0.53	0.82
S_8	0.50	0.61	0.64	0.59	0.50	0.46	0.68	0.57
S_9	0.72	0.82	0.71	0.65	0.64	0.75	0.63	0.69
S_{10}	0.65	0.58	0.60	0.67	0.53	0.71	0.68	0.58
				d_{exc}				
S_1	4.50	5.05	4.31	4.42	4.63	5.43	4.39	4.42
S_2	3.79	4.38	3.95	4.10	4.03	4.76	4.21	4.10
S_3	5.00	5.54	5.81	5.07	5.43	5.75	6.11	5.15
S_4	4.34	4.88	5.90	4.67	5.03	4.88	5.97	4.92
S_5	7.93	7.60	4.96	5.20	5.60	7.35	5.18	5.45
S_6	5.38	5.28	5.36	6.86	6.16	6.47	5.69	5.22
S_7	5.75	4.75	6.06	5.17	8.22	6.14	5.64	7.56
S_8	5.10	5.62	5.68	5.25	5.35	4.99	6.45	5.67
S_9	6.11	7.21	5.74	5.38	6.45	7.39	5.90	6.23
S_{10}	5.75	5.53	5.80	6.19	4.97	6.67	6.24	6.04
				PR_{NTO}				
S_1	1.52	1.22	1.98	1.42	1.74	1.29	2.17	1.71
S_2	2.09	1.89	2.02	1.82	2.14	1.92	2.08	2.02
S_3	2.21	1.76	2.08	2.29	2.11	1.59	2.27	2.16
S_4	3.27	3.05	2.11	2.86	3.07	3.13	1.99	2.52
S_5	1.89	2.00	2.33	2.12	2.24	2.01	2.41	2.07
S_6	2.43	1.86	3.50	2.00	2.30	2.44	2.29	2.06
S_7	2.30	2.57	3.03	2.48	2.14	1.79	3.72	2.19
S_8	1.47	1.54	2.18	1.65	1.80	2.14	2.99	2.59
S_9	2.13	2.12	2.35	3.00	1.91	2.41	2.36	2.57
S_{10}	2.30	1.84	2.64	1.96	1.92	2.67	1.61	2.45

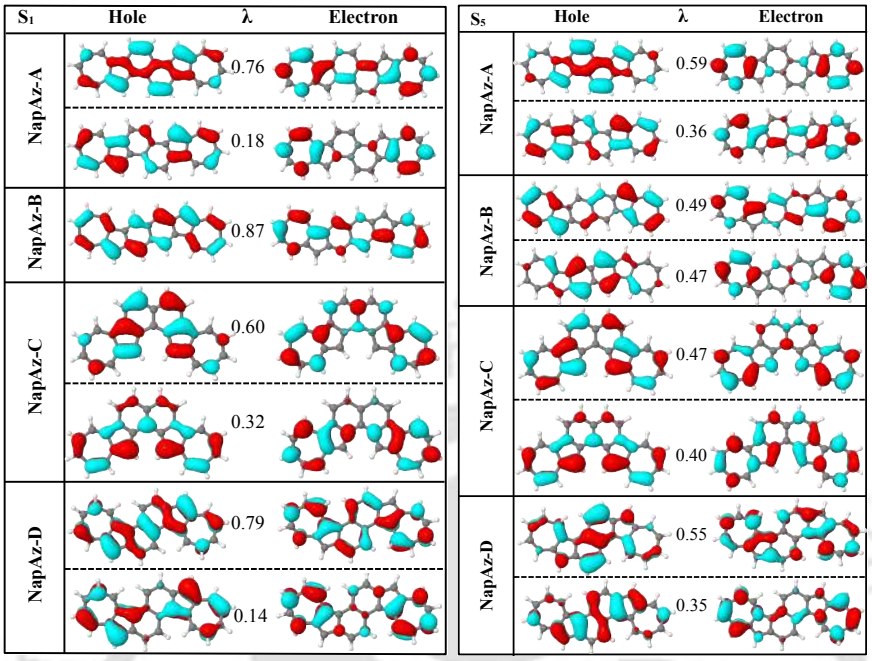

(A) (B)

FIGURE D6: Natural transition orbitals (NTOs) for (a) S_1 and (b) S_5 states of the monomers of the **NapAz** isomers obtained at SCS-ADC(2)/def2-TZVP level. The eigenvalue λ indicates the weight of the pair's contribution.

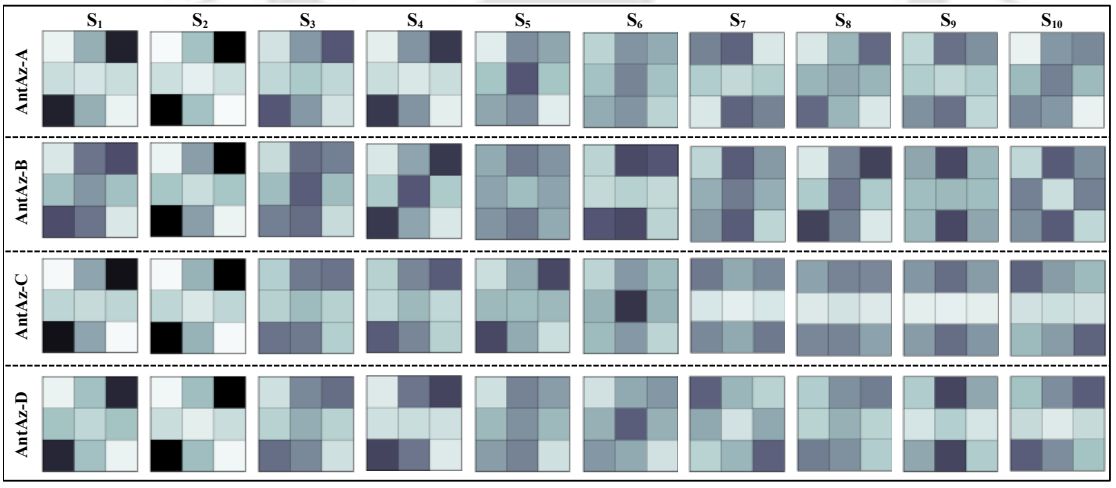

FIGURE D7: Electron-hole (e-h) correlation plots for the first ten excited states of the monomers of **AntAz** isomers computed at SCS-ADC(2)/def2-TZVP level.

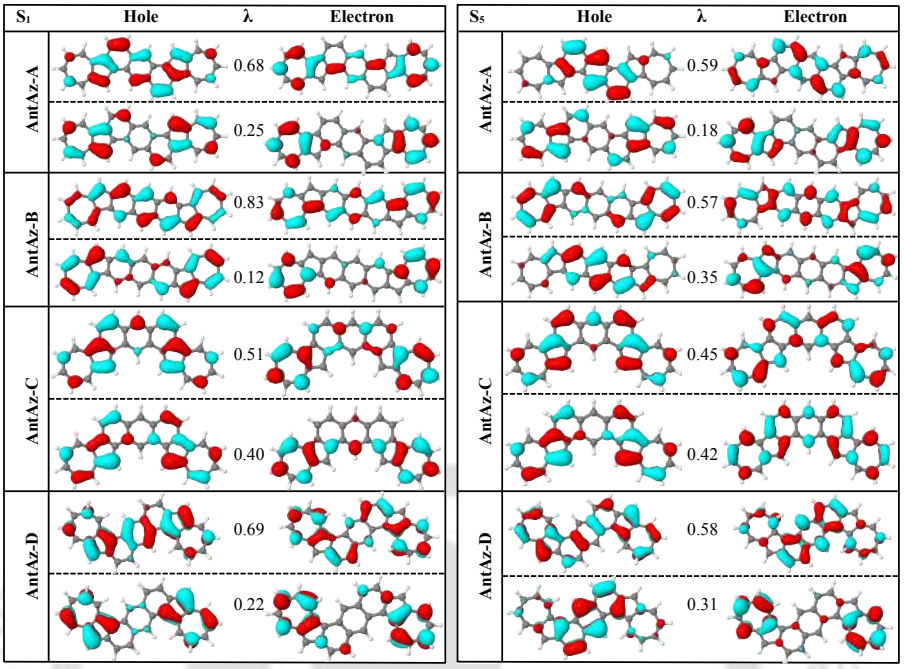

(A) (B)

FIGURE D8: Natural transition orbitals (NTOs) involved in (a) S_1 and (b)S_5 states for the monomers of the **AntAz** isomers obtained at SCS-ADC(2)/def2-TZVP level. The eigenvalue λ indicates the weight of the pair's contribution.

TABLE D6: ω_{CT} values corresponding to the ten excited states of the monomers of **NapAz** isomers computed at SCS-ADC(2) level and using three DFT functionals

	NapAz-A				**NapAz-B**			
State	SCS-ADC(2)	CAM-B3LYP	SCS-ωB2GP-PLYP	SCS-RSX-QIDH	SCS-ADC(2)	CAM-B3LYP	SCS-ωB2GP-PLYP	SCS-RSX-QIDH
S_1	0.41	0.36	0.29	0.29	0.48	0.45	0.38	0.37
S_2	0.26	0.23	0.19	0.19	0.36	0.30	0.24	0.24
S_3	0.47	0.45	0.35	0.35	0.57	0.54	0.47	0.47
S_4	0.37	0.32	0.24	0.24	0.45	0.82	0.29	0.78
S_5	0.93	0.91	0.46	0.46	0.82	0.37	0.78	0.29
S_6	0.55	0.60	0.54	0.54	0.58	0.46	0.46	0.47
S_7	0.65	0.67	0.60	0.59	0.47	0.58	0.46	0.46
S_8	0.50	0.80	0.63	0.64	0.61	0.79	0.49	0.49
S_9	0.72	0.53	0.44	0.44	0.82	0.55	0.62	0.60
S_{10}	0.53	0.47	0.72	0.72	0.58	0.65	0.42	0.44
	NapAz-C				**NapAz-D**			
S_1	0.38	0.31	0.26	0.26	0.41	0.37	0.31	0.30
S_2	0.31	0.26	0.21	0.21	0.32	0.25	0.21	0.21
S_3	0.64	0.58	0.40	0.40	0.54	0.48	0.38	0.38
S_4	0.62	0.47	0.25	0.25	0.44	0.36	0.25	0.25
S_5	0.47	0.61	0.52	0.52	0.59	0.85	0.50	0.49
S_6	0.62	0.61	0.52	0.51	0.85	0.59	0.50	0.70
S_7	0.66	0.69	0.61	0.61	0.56	0.58	0.72	0.50
S_8	0.64	0.68	0.46	0.46	0.59	0.62	0.48	0.48
S_9	0.71	0.77	0.53	0.68	0.65	0.68	0.47	0.48
S_{10}	0.60	0.78	0.68	0.52	0.67	0.79	0.45	0.43

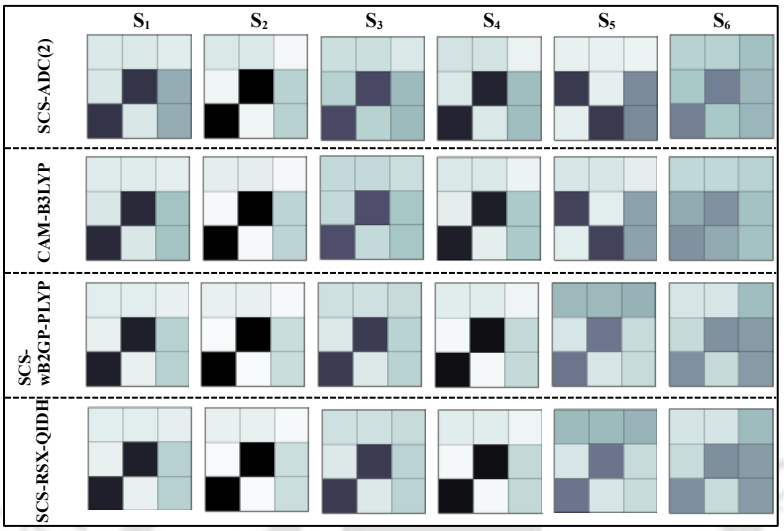

FIGURE D9: Electron-hole (e-h) correlation plots corresponding to the first six excited states of **NapAz-A** monomer computed at SCS-ADC(2) level and using three DFT functionals.

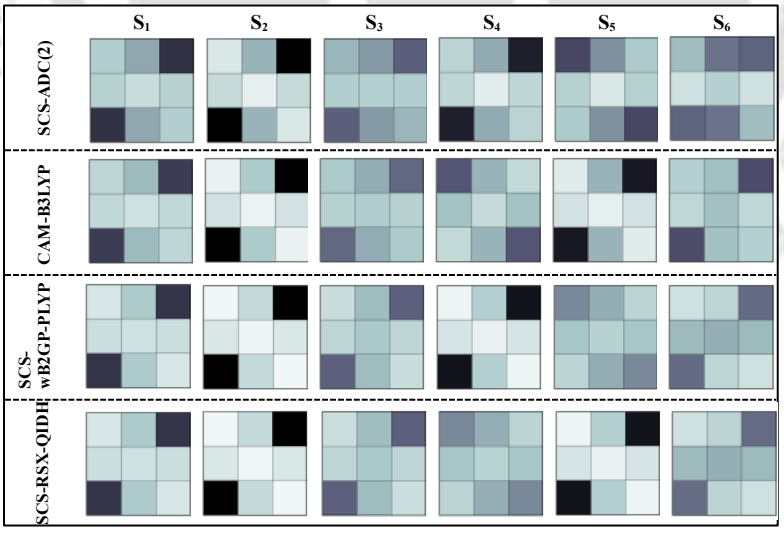

FIGURE D10: Electron-hole (e-h) correlation plots corresponding to the first six excited states of **NapAz-B** monomer computed at the SCS-ADC(2) level and using three DFT functionals.

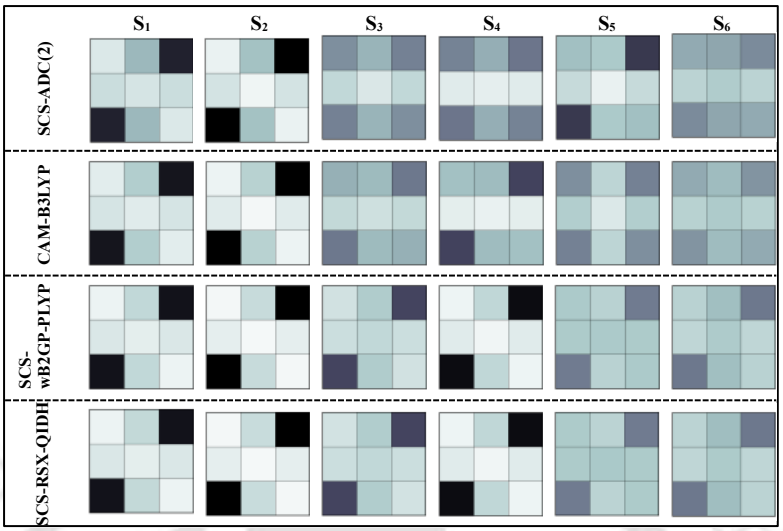

FIGURE D11: Electron-hole (e-h) correlation plots corresponding to the first six excited states of **NapAz-C** monomer computed at the SCS-ADC(2) level and using three DFT functionals.

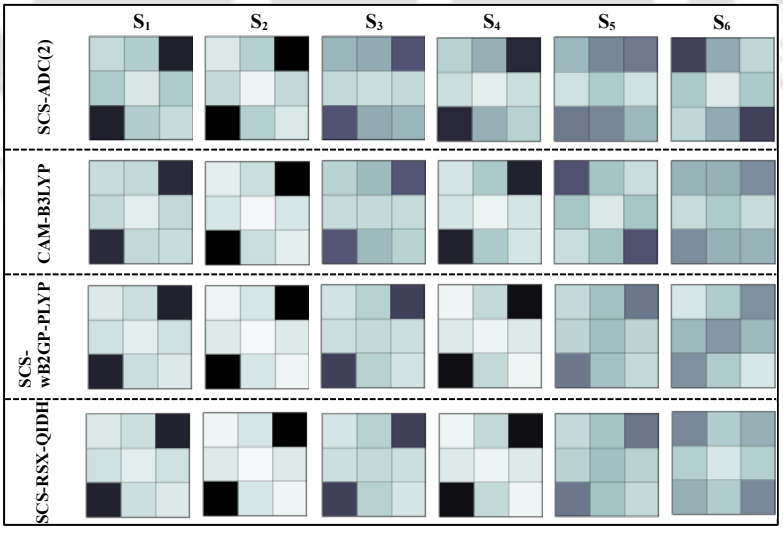

FIGURE D12: Electron-hole (e-h) correlation plots corresponding to the first six excited states of **NapAz-D** monomer computed at SCS-ADC(2) level and using three DFT functionals.

TABLE D7: ω_{CT} values corresponding to the first ten excited states for the monomers of **AntAz** isomers computed at the SCS-ADC(2) level and using three DFT functionals

	AntAz-A				**AntAz-B**			
State	SCS-ADC(2)	CAM-B3LYP	SCS-ωB2GP-PLYP	SCS-RSX-QIDH	SCS-ADC(2)	CAM-B3LYP	SCS-ωB2GP-PLYP	SCS-RSX-QIDH
S_1	0.37	0.38	0.33	0.33	0.51	0.51	0.48	0.48
S_2	0.30	0.29	0.27	0.27	0.39	0.39	0.32	0.32
S_3	0.49	0.49	0.40	0.40	0.56	0.53	0.48	0.48
S_4	0.45	0.42	0.34	0.34	0.40	0.83	0.39	0.78
S_5	0.54	0.59	0.49	0.49	0.69	0.46	0.40	0.39
S_6	0.61	0.90	0.51	0.51	0.59	0.47	0.78	0.40
S_7	0.87	0.63	0.63	0.62	0.63	0.66	0.53	0.53
S_8	0.50	0.58	0.43	0.42	0.46	0.45	0.47	0.47
S_9	0.64	0.80	0.54	0.81	0.75	0.81	0.51	0.51
S_{10}	0.53	0.56	0.63	0.53	0.71	0.76	0.62	0.58
	AntAz-C				**AntAz-D**			
S_1	0.37	0.29	0.24	0.24	0.39	0.33	0.27	0.27
S_2	0.34	0.26	0.21	0.21	0.32	0.25	0.21	0.21
S_3	0.58	0.53	0.37	0.37	0.53	0.49	0.37	0.37
S_4	0.53	0.40	0.25	0.25	0.49	0.40	0.27	0.27
S_5	0.49	0.64	0.48	0.48	0.60	0.54	0.45	0.45
S_6	0.58	0.53	0.45	0.45	0.53	0.55	0.44	0.44
S_7	0.53	0.59	0.37	0.37	0.82	0.86	0.39	0.81
S_8	0.68	0.61	0.44	0.44	0.57	0.58	0.43	0.39
S_9	0.63	0.65	0.40	0.39	0.69	0.71	0.80	0.43
S_{10}	0.68	0.77	0.51	0.48	0.58	0.62	0.46	0.43

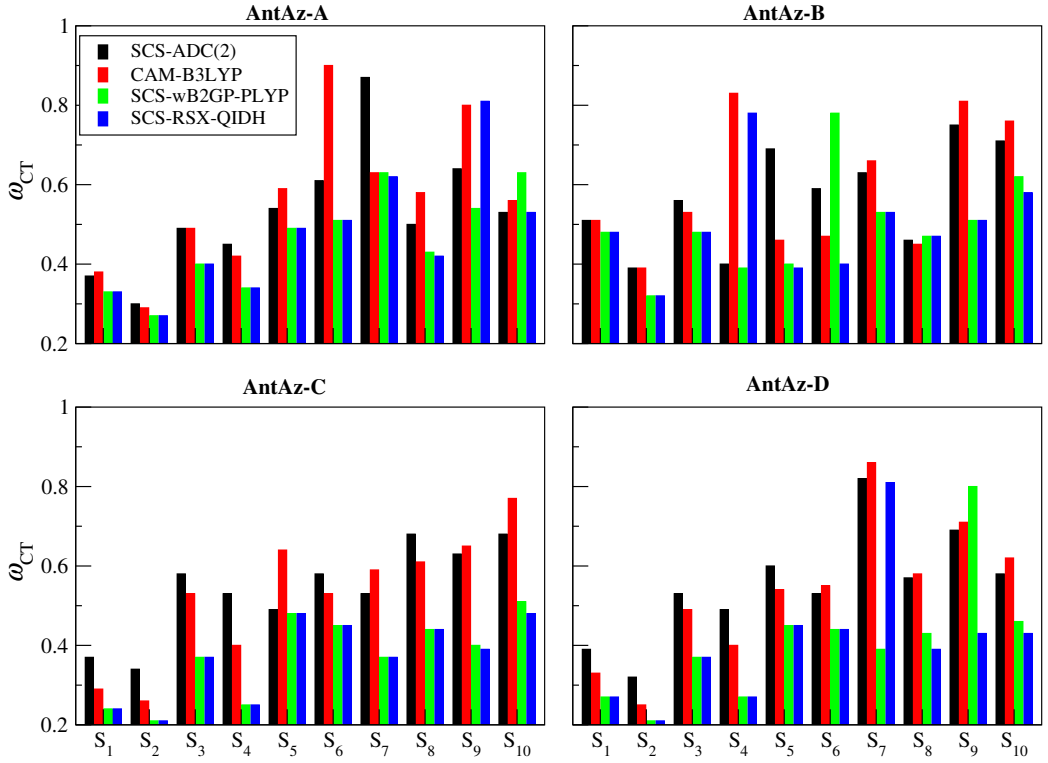

FIGURE D13: Comparison of TD-DFT ω_{CT} values of the first six excited states with the SCS-ADC(2) results for the monomers of **AntAz** isomers.

TABLE D8: Values of three descriptors, charge transfer parameter (ω_{CT}), exciton size (d_{exc}), and participation of natural transition orbitals (PR_{NTO}) for the π-stacked dimers of **NapAz** and **AntAz** isomers. The values are computed at the SCS-ADC(2)/def2-TZVP level

State	**NapAz-A**	**NapAz-B**	**NapAz-C**	**NapAz-D**	**AntAz-A**	**AntAz-B**	**AntAz-C**	**AntAz-D**
				ω_{CT}				
S_1	0.50	0.47	0.46	0.50	0.46	0.59	0.49	0.49
S_2	0.47	0.48	0.48	0.49	0.44	0.57	0.47	0.48
S_3	0.39	0.48	0.44	0.43	0.39	0.65	0.48	0.47
S_4	0.37	0.37	0.44	0.42	0.37	0.52	0.46	0.45
S_5	0.93	0.84	0.77	0.95	0.96	0.93	0.75	0.91
S_6	0.86	0.70	0.75	0.89	0.93	0.80	0.81	0.87
S_7	0.64	0.54	0.83	0.83	0.77	0.63	0.83	0.77
S_8	0.65	0.61	0.92	0.73	0.62	0.85	0.94	0.81
S_9	0.76	0.78	0.94	0.76	0.92	0.69	0.87	0.83
S_{10}	0.86	0.86	0.94	0.90	0.72	0.97	0.91	0.87
				d_{exc}				
S_1	5.01	5.45	4.69	4.80	4.92	5.88	5.12	5.01
S_2	4.83	5.47	4.76	4.83	4.97	5.94	5.05	4.87
S_3	4.33	5.48	4.54	4.60	4.49	6.19	5.10	4.93
S_4	4.18	4.76	4.50	4.63	4.36	5.53	4.99	4.88
S_5	6.73	6.85	6.11	6.50	7.06	7.19	6.94	6.51
S_6	6.25	6.32	6.21	6.18	6.96	6.71	6.59	6.35
S_7	6.14	5.79	6.03	5.83	5.96	6.23	7.10	6.01
S_8	5.87	6.16	6.24	5.67	6.17	6.45	6.47	6.50
S_9	5.97	5.98	6.61	6.01	5.73	6.47	6.97	6.49
S_{10}	5.94	6.20	5.96	5.92	6.22	6.82	6.76	6.21
				PR_{NTO}				
S_1	1.89	2.01	1.79	1.88	2.78	2.37	2.71	1.73
S_2	2.19	2.26	1.84	2.34	3.12	2.27	1.83	1.95
S_3	3.18	2.34	1.87	2.09	3.23	2.35	2.16	1.55
S_4	2.94	3.25	1.90	1.91	3.77	3.16	1.36	1.50
S_5	1.74	2.07	1.92	1.82	2.27	2.12	1.22	1.67
S_6	2.05	2.25	2.54	1.84	2.24	2.31	2.21	2.10
S_7	2.91	2.60	1.98	2.55	2.73	2.34	2.40	1.72
S_8	3.50	2.95	2.42	1.86	3.93	3.02	2.02	2.80
S_9	3.03	2.92	1.99	2.74	3.58	2.88	2.54	2.82
S_{10}	2.84	2.75	3.19	3.27	2.88	2.81	1.96	2.58

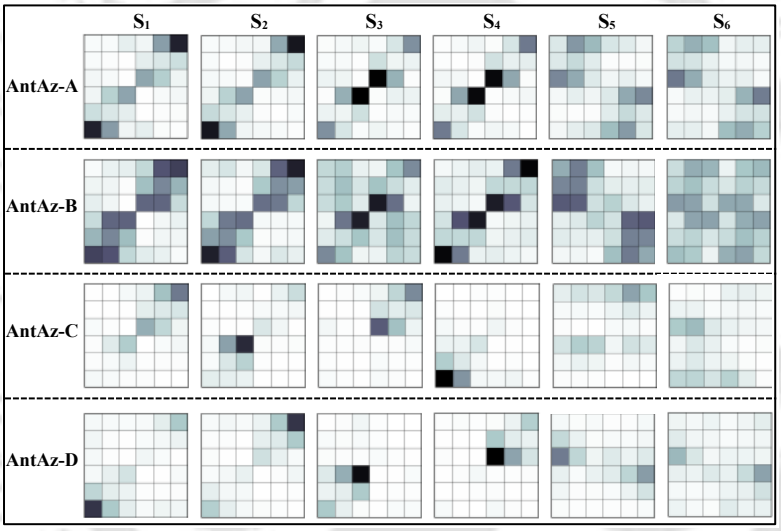

FIGURE D14: Electron-hole (e-h) correlation plots for the first six excited states of the π-stacked dimers of **AntAz** isomers computed at the SCS-ADC(2)/def2-TZVP level.

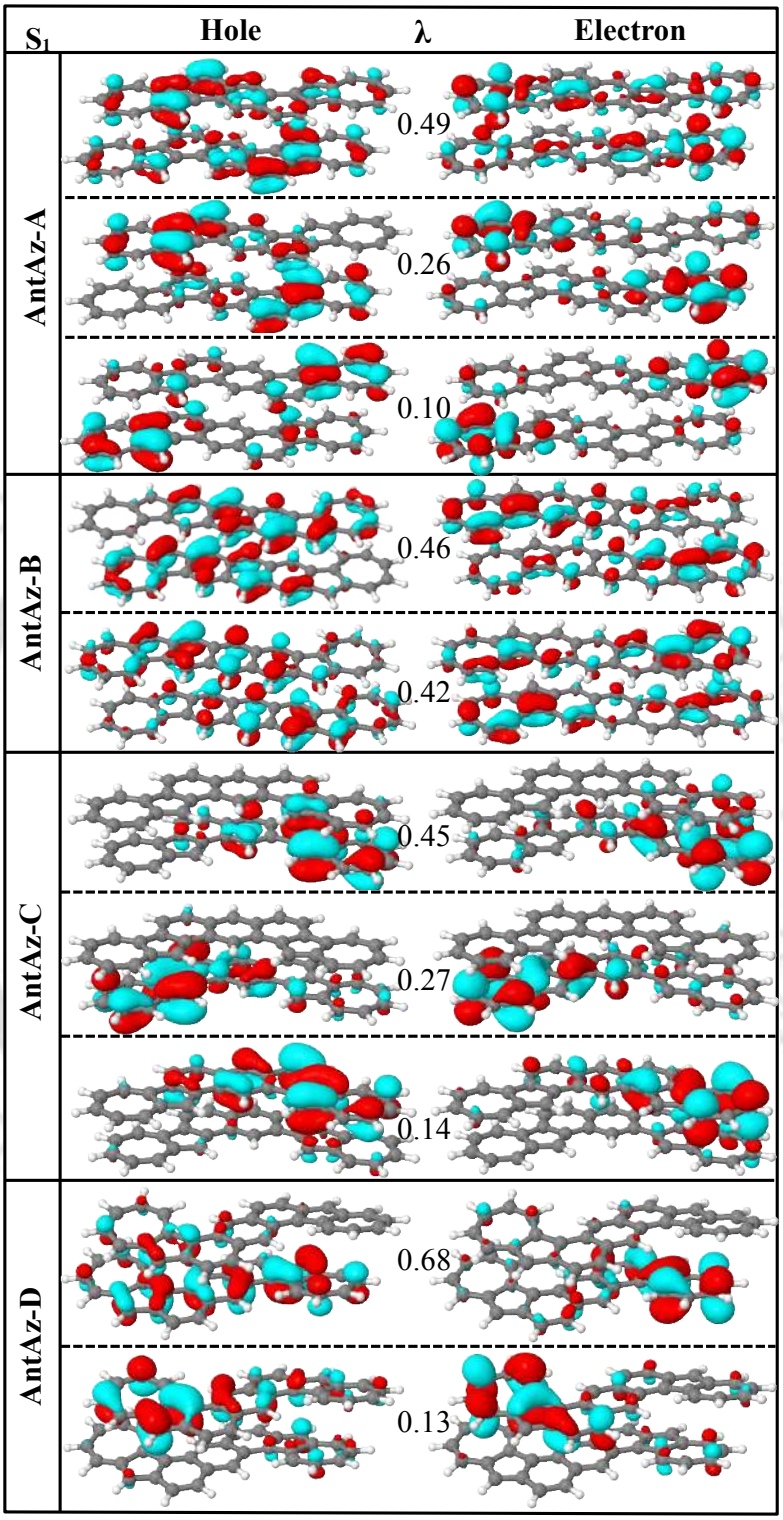

FIGURE D15: Natural transition orbitals (NTOs) of S_1 state for the π-stacked dimers of the **AntAz** isomers obtained at SCS-ADC(2)/def2-TZVP level. The eigenvalue λ indicates the weight of the pair's contribution.

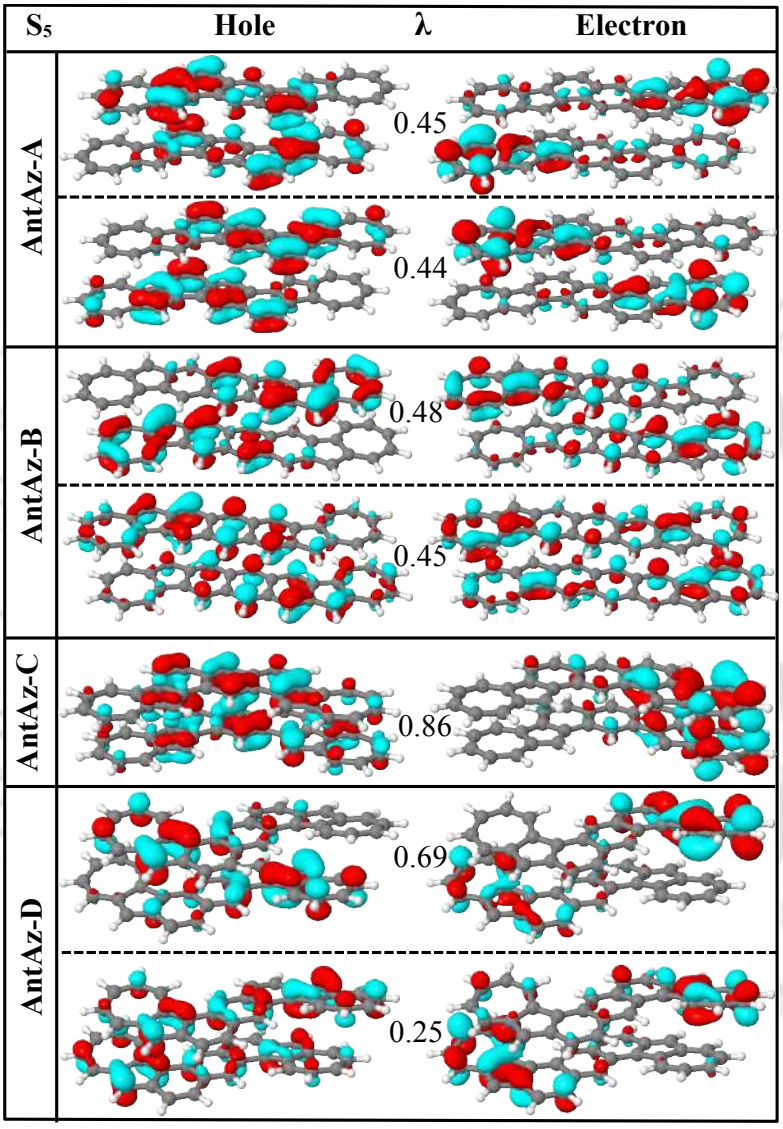

FIGURE D16: Natural transition orbitals (NTOs) of S_5 state for the π-stacked dimers of the **AntAz** isomers obtained at the SCS-ADC(2)/def2-TZVP level. The eigenvalue λ indicates the weight of the pair's contribution.

TABLE D9: ω_{CT} values corresponding to the first ten excited states for the π-stacked dimers of **NapAz** isomers computed at the SCS-ADC(2) level and using three DFT functionals

	NapAz-A				**NapAz-B**			
State	SCS-ADC(2)	CAM-B3LYP	SCS-ωB2GP-PLYP	SCS-RSX-QIDH	SCS-ADC(2)	CAM-B3LYP	SCS-ωB2GP-PLYP	SCS-RSX-QIDH
S_1	0.50	0.43	0.33	0.33	0.47	0.43	0.35	0.34
S_2	0.47	0.43	0.31	0.31	0.48	0.42	0.34	0.35
S_3	0.39	0.32	0.27	0.27	0.48	0.50	0.27	0.27
S_4	0.37	0.31	0.26	0.25	0.37	0.80	0.23	0.76
S_5	0.93	0.80	0.42	0.73	0.84	0.32	0.75	0.22
S_6	0.86	0.87	0.83	0.83	0.70	0.61	0.54	0.53
S_7	0.64	0.58	0.63	0.42	0.54	0.59	0.46	0.70
S_8	0.65	0.58	0.38	0.83	0.61	0.68	0.69	0.45
S_9	0.76	0.71	0.68	0.68	0.78	0.76	0.61	0.82
S_{10}	0.86	0.85	0.42	0.37	0.86	0.67	0.83	0.60
	NapAz-C				**NapAz-D**			
S_1	0.46	0.35	0.29	0.29	0.50	0.43	0.35	0.35
S_2	0.48	0.35	0.29	0.29	0.49	0.41	0.33	0.33
S_3	0.44	0.31	0.26	0.27	0.43	0.35	0.26	0.26
S_4	0.44	0.31	0.26	0.26	0.42	0.31	0.25	0.25
S_5	0.77	0.74	0.47	0.90	0.95	0.95	0.79	0.78
S_6	0.75	0.86	0.44	0.47	0.89	0.82	0.48	0.80
S_7	0.83	0.72	0.51	0.85	0.83	0.82	0.44	0.48
S_8	0.92	0.93	0.90	0.85	0.73	0.64	0.78	0.44
S_9	0.94	0.89	0.88	0.44	0.76	0.76	0.49	0.82
S_{10}	0.94	0.79	0.50	0.51	0.90	0.80	0.49	0.47

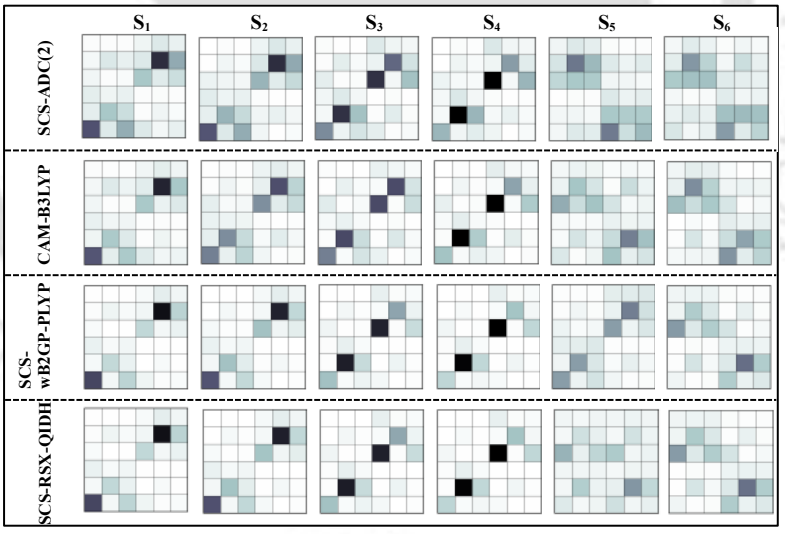

FIGURE D17: Electron-hole (e-h) correlation plots corresponding to the first six excited states for the π-stacked dimer of **NapAz-A** computed at the SCS-ADC(2) level and using three DFT functionals.

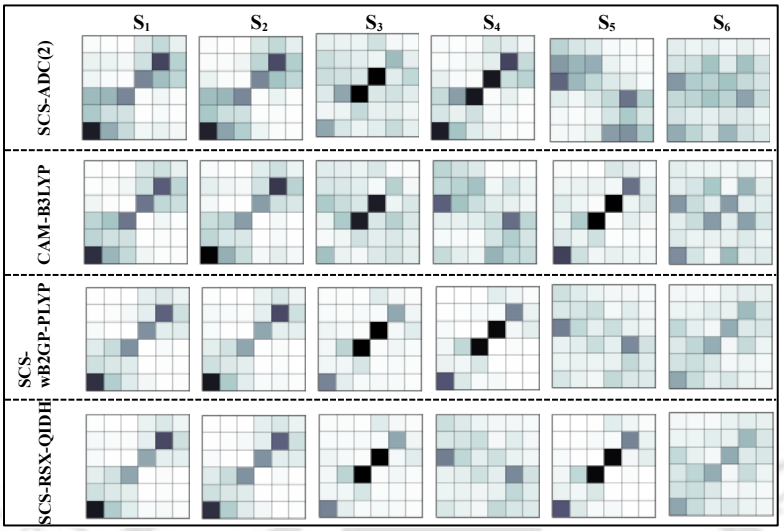

FIGURE D18: Electron-hole (*e*-*h*) correlation plots corresponding to the first six excited states for the π-stacked dimer of **NapAz-B** computed at SCS-ADC(2) level and using three DFT functionals.

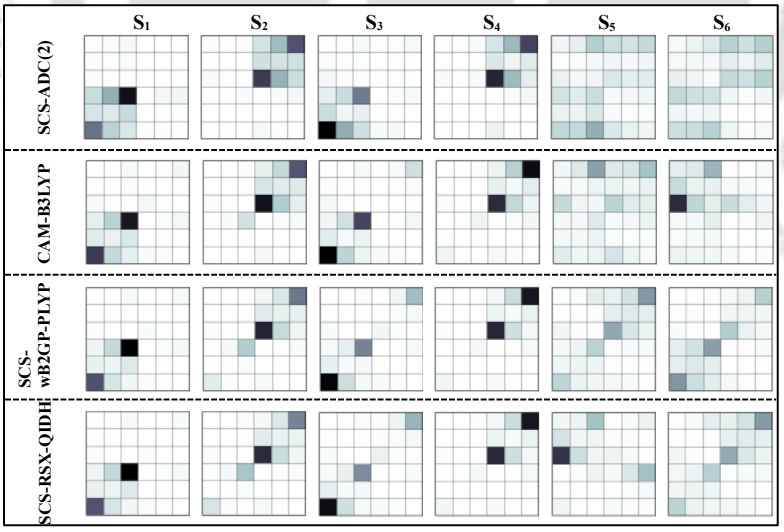

FIGURE D19: Electron-hole (*e*-*h*) correlation plots corresponding to the first six excited states for the π-stacked dimer of **NapAz-C** computed at SCS-ADC(2) level and using three DFT functionals.

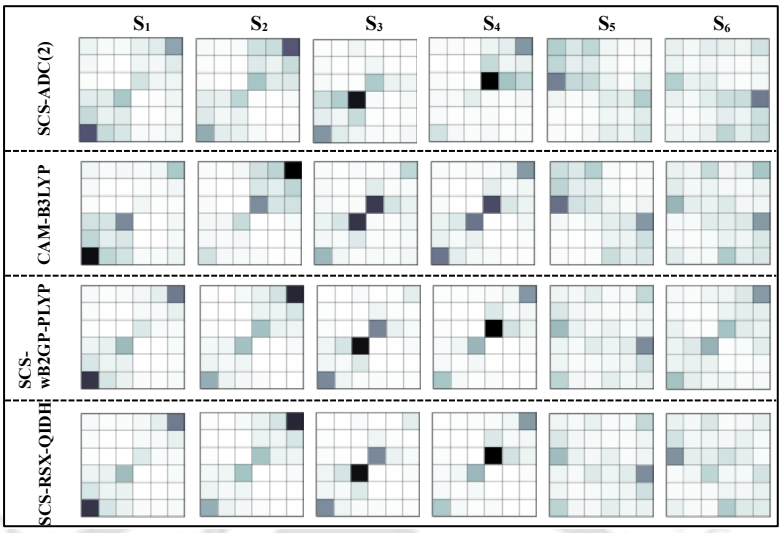

FIGURE D20: Electron-hole (e-h) correlation plots corresponding to the first six excited states for the π-stacked dimer of **NapAz-D** computed at the SCS-ADC(2) level and using three DFT functionals.

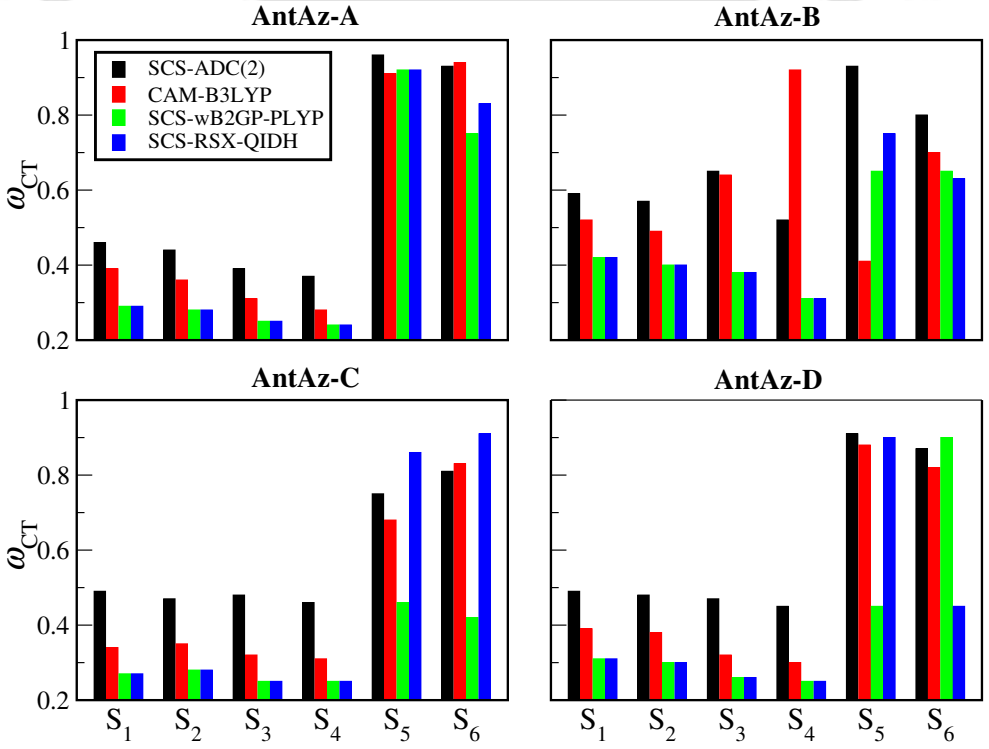

FIGURE D21: Comparison of TD-DFT ω_{CT} values of first six excited states with the SCS-ADC(2) results for the dimers of **AntAz** isomers.

TABLE D10: ω_{CT} values corresponding to the first ten excited states for the π-stacked dimers of **AntAz** isomers computed at the SCS-ADC(2) level and using three DFT functionals

	AntAz-A				**AntAz-B**			
State	SCS-ADC(2)	CAM-B3LYP	SCS-ωB2GP-PLYP	SCS-RSX-QIDH	SCS-ADC(2)	CAM-B3LYP	SCS-ωB2GP-PLYP	SCS-RSX-QIDH
S_1	0.46	0.39	0.29	0.29	0.59	0.52	0.42	0.42
S_2	0.44	0.36	0.28	0.28	0.57	0.49	0.40	0.40
S_3	0.39	0.31	0.25	0.25	0.65	0.64	0.38	0.38
S_4	0.37	0.28	0.24	0.24	0.52	0.92	0.31	0.31
S_5	0.96	0.91	0.92	0.92	0.93	0.41	0.65	0.75
S_6	0.93	0.94	0.75	0.83	0.80	0.70	0.65	0.63
S_7	0.77	0.82	0.40	0.79	0.63	0.79	0.73	0.64
S_8	0.62	0.92	0.40	0.56	0.85	0.66	0.70	0.71
S_9	0.92	0.62	0.64	0.40	0.69	0.97	0.68	0.66
S_{10}	0.72	0.54	0.79	0.40	0.97	0.61	0.93	0.92
	AntAz-C				**AntAz-D**			
S_1	0.49	0.34	0.27	0.27	0.49	0.39	0.31	0.31
S_2	0.47	0.35	0.28	0.28	0.48	0.38	0.30	0.30
S_3	0.48	0.32	0.25	0.25	0.47	0.32	0.26	0.26
S_4	0.46	0.31	0.25	0.25	0.45	0.30	0.25	0.25
S_5	0.75	0.68	0.46	0.86	0.91	0.88	0.45	0.90
S_6	0.81	0.83	0.42	0.91	0.87	0.82	0.90	0.45
S_7	0.83	0.86	0.86	0.93	0.77	0.71	0.45	0.68
S_8	0.94	0.91	0.91	0.45	0.81	0.76	0.52	0.84
S_9	0.87	0.94	0.93	0.42	0.83	0.76	0.59	0.57
S_{10}	0.91	0.75	0.38	0.38	0.87	0.90	0.66	0.44

Appendix E

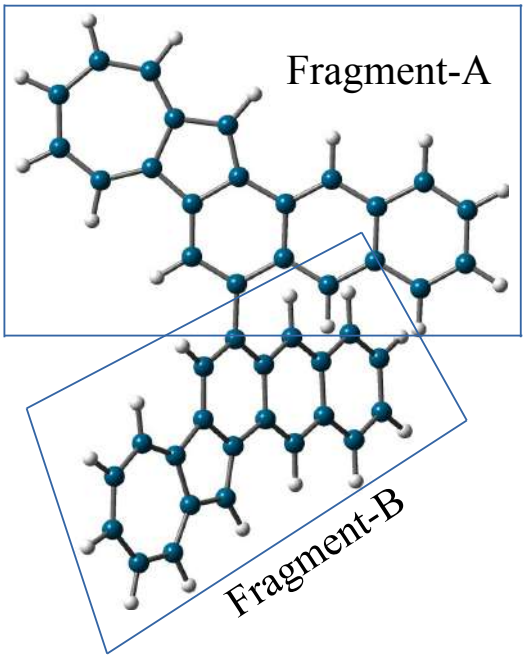

FIGURE E1: Fragmentation scheme for excitonic analysis in conformer **M2**.

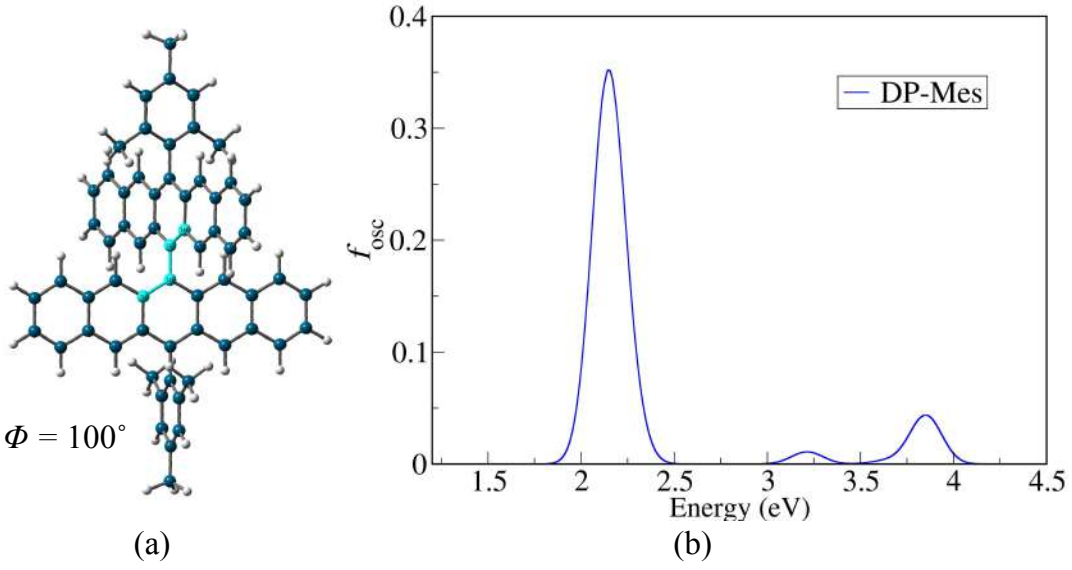

FIGURE E2: (a) Ground state optimized geometry of DP-Mes at RI-MP2/def2-SVP and (b) Absorption spectra of DP-Mes at the RI-ADC(2)/def2-SVP levels.

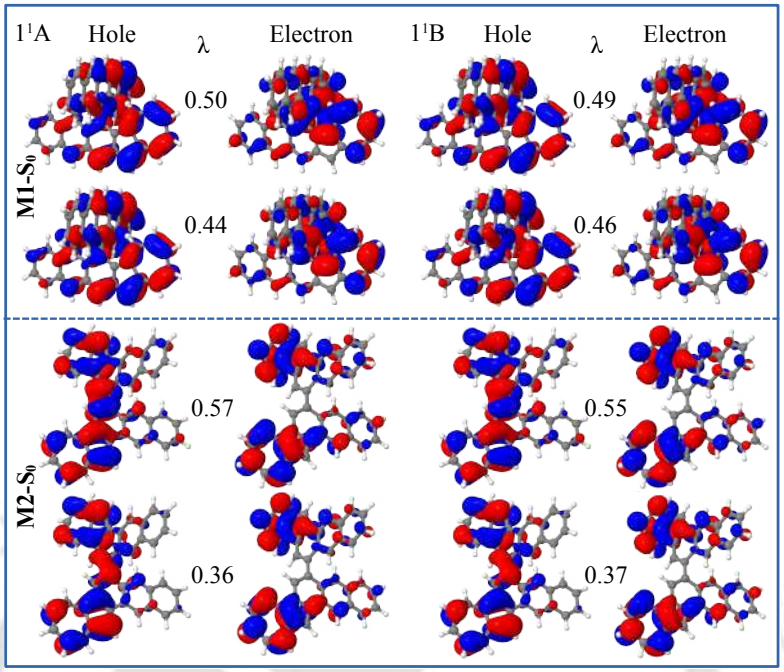

FIGURE E3: Natural transition orbitals (NTOs) involved in $S_0 \rightarrow 1^1A$ and $S_0 \rightarrow 1^1B$ transitions for the S_0 optimized geometries at the RI-ADC(2)/def2-SVP level.

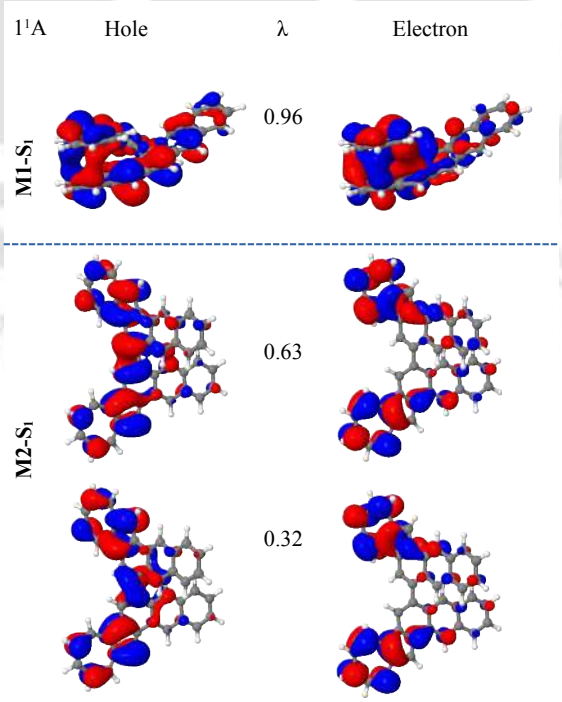

FIGURE E4: NTOs involved in $S_0 \rightarrow 1^1A$ transitions for **M1-1^{1}A** and **M2-1^{1}A**..

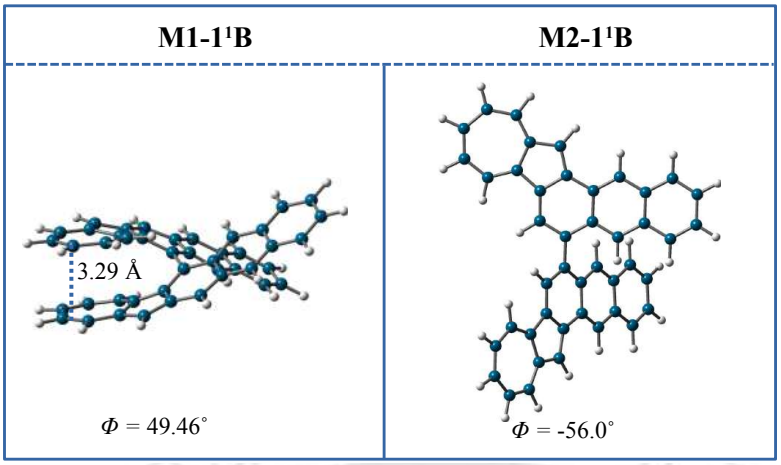

FIGURE E5: 1^1B state optimized geometries of **M1** and **M2** at the RI-ADC(2)/def2-SVP level.

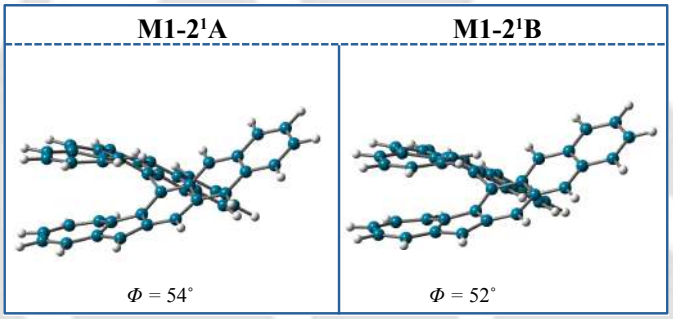

FIGURE E6: 2^1A and 2^1B states optimized geometries of **M1** at the RI-ADC(2)/def2-SVP level.

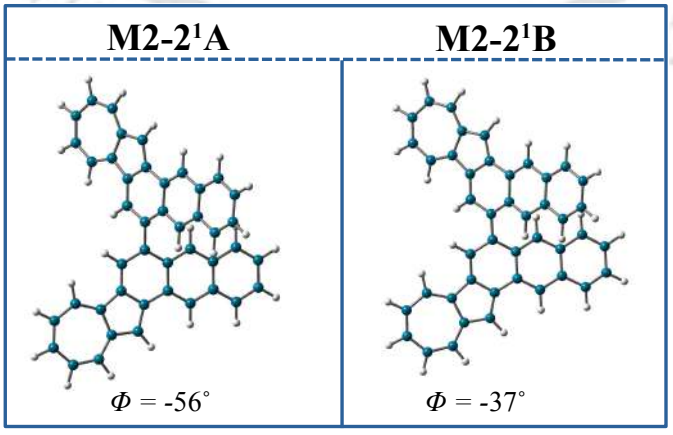

FIGURE E7: 2^1A and 2^1B states optimized geometries of **M2** at the RI-ADC(2)/def2-SVP level.

TABLE E1: Vertical excitation energy/oscillator strength (E_g/f_{osc}) and corresponding ω_{CT} values for the first six excited states computed for the 2^1A and 2^1B optimized geometries at RI-ADC(2)/def2-SVP level

		M1-2^{1}A			**M1-2^{1}B**	
state		E_g/f_{osc}	ω_{CT}		E_g/f_{osc}	ω_{CT}
S_1	1^1A	1.07 / 0.006	0.19	1^1A	0.81 / 0.003	0.40
S_2	1^1B	1.12 / 0.012	0.08	1^1B	1.08 / 0.008	0.10
S_3	2^1B	1.49 / 0.000	0.93	2^1B	1.39 / 0.008	0.89
S_4	2^1A	1.55 / 0.015	0.80	2^1A	1.64 / 0.017	0.63
S_5	3^1A	2.39 / 0.065	0.15	3^1B	2.30 / 0.167	0.35
S_6	3^1B	2.40 / 0.171	0.16	3^1A	2.31 / 0.044	0.30
		M2-2^{1}A			**M2-2^{1}B**	
S_1	1^1A	1.66 / 0.007	0.06	1^1A	1.63 / 0.010	0.14
S_2	1^1B	1.66 / 0.010	0.06	1^1B	1.63 / 0.009	0.15
S_3	2^1B	2.88 / 0.109	0.12	2^1B	2.54 / 0.760	0.40
S_4	2^1A	2.93 / 0.029	0.13	2^1A	2.87 / 0.039	0.34
S_5	3^1B	3.03 / 0.013	0.91	3^1B	3.02 / 0.092	0.78
S_6	3^1A	3.04 / 0.009	0.84	3^1A	3.07 / 0.028	0.63

TABLE E2: Ground state(S_0) energies, and excitation energy (E_g) and ω_{CT} values for the first four excited states at different dihedral angles of **M1-S$_0$** geometry calculated at RI-ADC(2)/def2-SVP level

Angle	Energy (eV)					ω_{CT}			
	S_0	1^1A	1^1B	2^1A	2^1B	1^1A	1^1B	2^1A	2^1B
45.7	3.35	4.41	4.88	5.49	5.34	0.50	0.40	0.54	0.60
47.7	2.62	3.81	4.17	4.85	4.71	0.50	0.38	0.57	0.62
49.7	2.09	3.38	3.66	4.40	4.26	0.50	0.35	0.56	0.65
51.7	1.63	3.01	3.24	4.01	3.87	0.44	0.33	0.58	0.67
53.7	1.27	2.73	2.90	3.68	3.56	0.43	0.31	0.62	0.69
57.7	0.76	2.33	2.44	3.21	3.12	0.34	0.27	0.68	0.72
61.7	0.45	2.11	2.17	2.91	2.85	0.29	0.24	0.71	0.76
65.7	0.26	2.00	2.03	2.73	2.69	0.23	0.20	0.77	0.80
69.7	0.15	1.95	1.96	2.62	2.60	0.18	0.15	0.83	0.84
73.7	0.08	1.93	1.93	2.56	2.55	0.14	0.12	0.85	0.88
77.7	0.05	1.93	1.92	2.53	2.52	0.10	0.09	0.90	0.91
81.7	0.02	1.94	1.92	2.51	2.51	0.07	0.07	0.93	0.94
85.7	0.01	1.94	1.93	2.50	2.50	0.05	0.04	0.95	0.96
89.7	0.00	1.95	1.93	2.49	2.49	0.03	0.03	0.97	0.97
93.7	0.00	1.95	1.93	2.49	2.49	0.02	0.02	0.96	0.97
97.7	0.00	1.95	1.94	2.49	2.49	0.03	0.03	0.97	0.97
101.7	0.01	1.95	1.94	2.49	2.50	0.04	0.04	0.96	0.96
105.7	0.04	1.96	1.94	2.51	2.51	0.06	0.05	0.95	0.95
109.7	0.08	1.98	1.97	2.54	2.54	0.09	0.08	0.92	0.93
113.7	0.15	2.02	2.01	2.61	2.61	0.13	0.10	0.86	0.90

TABLE E3: Ground state(S_0) energies, and excitation energy (E_g) and ω_{CT} values for the first four excited states at different dihedral angles of **M2-S_0** geometry calculated at the RI-ADC(2)/def2-SVP level

Angle	Energy (eV)					ω_{CT}			
	S_0	1^1A	1^1B	2^1A	2^1B	1^1A	1^1B	2^1A	2^1B
-31.4	1.60	3.43	3.43	4.49	4.43	0.09	0.09	0.39	0.36
-35.4	1.00	2.85	2.85	3.97	3.90	0.09	0.08	0.23	0.23
-39.4	0.61	2.46	2.46	3.62	3.54	0.08	0.07	0.18	0.22
-43.4	0.32	2.18	2.19	3.36	3.29	0.07	0.07	0.14	0.19
-47.4	0.18	2.05	2.06	3.25	3.17	0.07	0.06	0.11	0.17
-51.4	0.08	1.96	1.97	3.17	3.10	0.06	0.06	0.09	0.14
-55.4	0.03	1.92	1.92	3.13	3.07	0.06	0.05	0.07	0.12
-59.4	0.01	1.90	1.90	3.12	3.06	0.05	0.04	0.06	0.10
-63.4	0.00	1.90	1.90	3.12	3.07	0.04	0.04	0.04	0.08
-67.4	0.00	1.91	1.91	3.13	3.09	0.04	0.04	0.03	0.06
-71.4	0.01	1.92	1.92	3.14	3.11	0.03	0.03	0.02	0.04
-75.4	0.03	1.93	1.94	3.16	3.13	0.03	0.03	0.02	0.03
-79.4	0.04	1.95	1.95	3.17	3.15	0.03	0.03	0.02	0.02
-83.4	0.05	1.96	1.96	3.18	3.16	0.02	0.02	0.02	0.02
-87.4	0.06	1.97	1.97	3.19	3.17	0.03	0.02	0.03	0.03
-91.4	0.07	1.97	1.97	3.19	3.17	0.03	0.02	0.05	0.04
-95.4	0.07	1.98	1.97	3.19	3.17	0.03	0.03	0.08	0.05
-99.4	0.08	1.98	1.97	3.19	3.16	0.03	0.03	0.09	0.09
-103.4	0.08	1.97	1.97	3.18	3.15	0.04	0.04	0.10	0.11

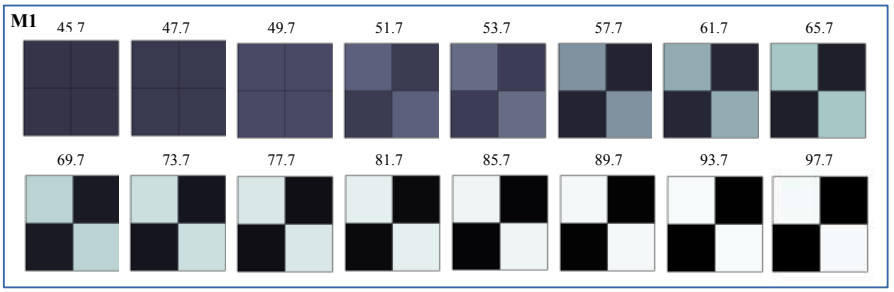

FIGURE E8: Electron-hole correlation plots for the 1^1A state along the dihedral angle of **M1**.

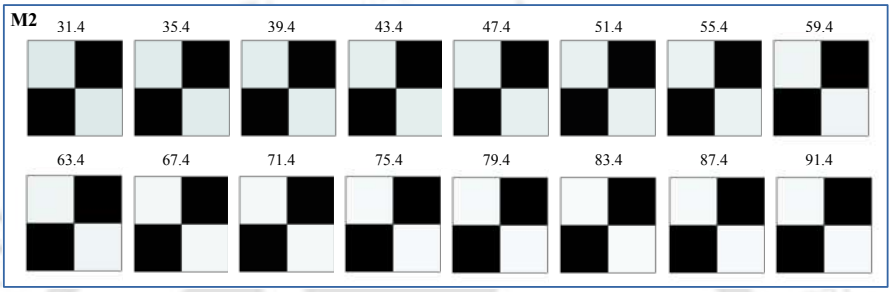

FIGURE E9: Electron-hole correlation plots for the 1^1A state along the dihedral angle of **M2**.

TABLE E4: Ground state(S_0) energies, and excitation energy (E_g) and ω_{CT} values for the first four excited states at different dihedral angles of **M1-1^1A** geometry calculated at the RI-ADC(2)/def2-SVP level

Angle	Energy (eV)					ω_{CT}			
	S_0	1^1A	1^1B	2^1A	2^1B	1^1A	1^1B	2^1A	2^1B
43.5	0.36	0.81	1.28	2.38	2.14	0.50	0.45	0.68	0.56
45.5	0.12	0.59	1.05	2.07	1.76	0.50	0.42	0.56	0.60
47.5	0.00	0.53	0.95	1.85	1.52	0.50	0.33	0.51	0.66
49.5	0.00	0.63	0.99	1.76	1.45	0.50	0.26	0.58	0.73
51.5	-0.06	0.67	0.96	1.63	1.36	0.42	0.18	0.62	0.80
53.5	-0.09	0.75	0.96	1.55	1.34	0.38	0.12	0.67	0.86
55.5	-0.09	0.84	0.98	1.52	1.36	0.29	0.07	0.72	0.92
59.5	-0.08	0.98	1.02	1.49	1.43	0.15	0.05	0.84	0.93
63.5	-0.03	1.09	1.1	1.55	1.54	0.04	0.06	0.94	0.94
67.5	0.02	1.16	1.18	1.64	1.64	0.04	0.03	0.96	0.97
71.5	0.09	1.23	1.24	1.75	1.74	0.04	0.05	0.96	0.95
75.5	0.15	1.3	1.31	1.86	1.84	0.07	0.04	0.94	0.95
79.5	0.22	1.37	1.38	1.96	1.93	0.09	0.05	0.92	0.95
83.5	0.31	1.45	1.47	2.08	2.03	0.11	0.05	0.90	0.95
87.5	0.42	1.55	1.59	2.21	2.15	0.13	0.06	0.88	0.94
91.5	0.56	1.69	1.74	2.38	2.31	0.15	0.08	0.86	0.93
95.5	0.77	1.91	1.96	2.6	2.53	0.17	0.09	0.84	0.92
99.5	1.09	2.23	2.29	2.93	2.85	0.19	0.11	0.82	0.90

TABLE E5: Ground state(S_0) energies, and excitation energy (E_g) and ω_{CT} values for the first four excited states at different dihedral angles of **M2-1^{1}A** geometry calculated at the RI-ADC(2)/def2-SVP level

Angle	Energy (eV)					ω_{CT}			
	S_0	1^1A	1^1B	2^1A	2^1B	1^1A	1^1B	2^1A	2^1B
-32	0.84	2.28	2.29	3.59	3.51	0.10	0.10	0.82	0.27
-36	0.50	1.96	1.96	3.28	3.21	0.10	0.10	0.51	0.26
-40	0.28	1.75	1.75	3.09	3.01	0.09	0.09	0.47	0.24
-44	0.14	1.62	1.62	2.97	2.90	0.08	0.08	0.46	0.22
-48	0.06	1.54	1.55	2.90	2.84	0.07	0.07	0.46	0.22
-52	0.02	1.51	1.52	2.87	2.82	0.07	0.07	0.46	0.20
-56	0.00	1.50	1.51	2.86	2.82	0.06	0.06	0.46	0.18
-60	0.00	1.51	1.51	2.87	2.84	0.05	0.05	0.46	0.20
-64	0.01	1.52	1.53	2.89	2.86	0.04	0.04	0.46	0.20
-68	0.02	1.54	1.55	2.91	2.89	0.04	0.04	0.46	0.21
-72	0.03	1.56	1.56	2.93	2.92	0.03	0.03	0.47	0.21
-76	0.05	1.58	1.58	2.96	2.94	0.03	0.03	0.48	0.20
-80	0.06	1.60	1.60	2.98	2.96	0.03	0.02	0.54	0.14
-84	0.07	1.61	1.61	2.99	2.98	0.03	0.02	0.65	0.04
-88	0.08	1.62	1.62	2.99	2.98	0.02	0.02	0.58	0.37
-92	0.09	1.62	1.62	2.98	2.98	0.02	0.02	0.57	0.45
-96	0.09	1.62	1.62	2.97	2.97	0.03	0.03	0.57	0.46
-100	0.10	1.62	1.62	2.96	2.96	0.03	0.03	0.57	0.44
-104	0.10	1.62	1.62	2.95	2.95	0.03	0.04	0.56	0.42
-108	0.11	1.62	1.61	2.95	2.94	0.04	0.04	0.56	0.39